Polymers in aligned carbon nanotube arrays

Zur Erlangung des Grades eines Doktors der Naturwissenschaften (Dr. rer. nat.)
genehmigte Dissertation von Ing.-Phys. Marina Khaneft aus Kurgan (Russland)
Dezember 2013 — Darmstadt — D 17

TECHNISCHE
UNIVERSITÄT
DARMSTADT

Fachbereich Physik
Institut für Festkörperphysik

Polymers in aligned carbon nanotube arrays

Genehmigte Dissertation von Ing.-Phys. Marina Khaneft aus Kurgan (Russland)

1. Gutachten: Prof. Dr. B. Stühn
2. Gutachten: Prof. Dr. R. Feile

Tag der Einreichung: 11.10.2013
Tag der Prüfung: 25.11.2013

Darmstadt — D 17

Erklärung zur Dissertation

Hiermit versichere ich, die vorliegende Dissertation ohne Hilfe Dritter nur mit den angegebenen Quellen und Hilfsmitteln angefertigt zu haben. Alle Stellen, die aus Quellen entnommen wurden, sind als solche kenntlich gemacht. Diese Arbeit hat in gleicher oder ähnlicher Form noch keiner Prüfungsbehörde vorgelegen.

Darmstadt, den 29. November 2013

(M. Khaneft)

Abstract

In the present experimental study we investigate polymer behavior in aligned carbon nanotube (CNT) arrays. We analyze the polymer filling mechanism in composite materials containing highly ordered and vertically aligned carbon nanotubes. CNTs are obtained by a template assisted chemical vapor deposition (CVD) method. Porous aluminum oxide (PAOX) is used as template. PAOX is obtained by electrochemical anodization of aluminum substrates and contains arrays of hexagonally arranged pores. Different forms of the CNT arrays are studied: fully and partially closed tubes having one or two carbon layers on one or both sides of the array, and open tubes in a freestanding CNT arrays. Investigation is performed by Small Angle X-ray Scattering (SAXS) in combination with transmission and scanning electron microscopy (TEM and SEM) and atomic force microscopy (AFM). The tubes being used are of 40 μm length and 40/90 nm diameter. Different polymers are infiltrated into CNT arrays – glassy polystyrene (PS), polymethylmethacrylate (PMMA) and semicrystalline polydimethylsiloxane (PDMS) of different molecular weight. Infiltration is performed in polymer solution and in melt. It was found that the original order of the template is only locally preserved in the CNT array. Imbibition of polymer melts is achieved in the interior of CNTs as well as in between tubes, modifying the local order in the array. We compare structural changes of different CNT arrays caused by polymer infiltration. The filling kinetics is followed with time-resolved SAXS in the whole array and in tube interior only. We find that the polymer flow into CNT arrays deviates from the Lucas-Washburn equation and can be described with compressed exponentials. During the imbibition of polymers into CNT arrays a depletion layer is formed in vicinity of the CNT surface.

To investigate the influence of the CNT surface on the polymer behavior we apply differential scanning calorimetry (DSC) and study polymers at the glass transition as well as melting and crystallization. We fill arrays with two different polymers – PS in tube interior and PDMS in interstices between tubes. The glass transition for inner and outer polymer is analyzed and compared. We also investigate the crystallization behavior of PDMS in bulk and in CNT arrays. Isothermal and nonisothermal crystallization kinetics are considered. Both experiments show the enhanced crystallization of the polymer in the presence of CNTs.

The dynamical aspects of the polymer behavior are further probed by Brillouin light spectroscopy (BLS). We observe Brillouin scattering of acoustic excitations in two porous systems: randomly distributed parallel pores in ion-track-etched polycarbonate (ITPC) and highly ordered parallel pores in the PAOX template. ITPC is produced by irradiating the polycabonate film with an ion beam and subsequent wet-chemical etching of the ion beam tracks. Both systems have a pore radius of $R \approx 20$ nm and differ with respect to order and density of pores. In the experiment we follow the changes of BLS spectra depending on the angle between the template surface and the incident laser beam. BLS spectra of emtpy porous templates and templates filled with PDMS are compared. We observe two types of Brillouin modes: bulk modes of PDMS and the templates as well as surface modes.

Zusammenfassung

In der vorliegenden experimentellen Studie untersuchen wir das Verhalten von Polymeren in Arrays ausgerichteter Kohlenstoffnanoröhrchen (carbon nanotubes, CNT). Der Füllmechanismus des Polymers in Verbundwerkstoffen mit hochgradig geordneten und senkrecht ausgerichteten Kohlenstoffnanoröhrchen wird charakterisiert. Die CNT Arrays wurden mittels chemischer Gasphasenabscheidung (chemical vapor deposition, CVD) in einer Matrize aus nanoporösem Aluminiumoxid (porous anodic aluminum oxide, PAOX) hergestellt. PAOX besteht aus hexagonal angeordneten Poren, die bei elektrochemischer anodischer Oxidation enstehen. Wir untersuchen CNT Arrays in verschiedenen Formen: entweder als freistehendes Array oder mit durchgehenden Kohlenstoffschichten auf einer oder beiden Seiten. Als experimentelle Methoden verwenden wir eine Kombination aus Röntgenkleinwinkelstreuung (small angle X-ray scattering, SAXS), Transmissions- und Rasterelektronenmikroskopie (transmission and scanning electron microscopy, TEM and SEM) sowie Rasterkraftmikroskopie (atomic force microscopy, AFM). Die untersuchten CNTs besitzen eine Länge von 40 μm und haben einen Durchmesser von 40 und 90 nm. Verschiedene Polymere – glasartiges Polystyrol (PS), Polymethylmethacrylat (PMMA) und teilkristallines Polydimethylsiloxan (PDMS) – in verschiedenen Molekulargewichten werden in die CNT Arrays infiltriert, wobei die Infiltration entweder in einer Lösung von Polymer oder in der Polymerschmelze durchgeführt wird. Es wird gezeigt, dass die ursprüngliche Ordnung der Poren der Matrize im resultierenden CNT Array nur lokal erhalten bleibt. Die Imbibition von Polymerschmelzen findet sowohl im Inneren der Kohlenstoffnanoröhrchen als auch in Zwischenräumen des Arrays statt, so dass die lokale Ordnung im Array beeinflusst wird. Wir vergleichen die durch die Infiltration von Polymer verursachten Strukturänderungen in den verschiedenen Arten von CNT Arrays. Die Kinetik des Füllprozesses wird mit zeitaufgelöster Röntgenkleinwinkelstreuung untersucht, sowohl für das gesamte Array als auch nur für das Innere der Kohlenstoffnanoröhrchen. Es stellt sich heraus, dass das Fließverhalten von Polymer in CNT Arrays von der Lucas-Washburn Gleichung abweicht und mit gestauchten Exponentialfunktionen beschrieben werden kann. Während der Imbibition des Polymers entsteht eine Verarmungszone in der unmittelbaren Umgebung der Oberfläche der CNT.

Um den Einfluss der Oberfläche der CNTs auf das Polymerverhalten zu studieren wird mittels dynamischer Differenzkalorimetrie (differential scanning calorimetry, DSC) der Glasübergang sowie der Schmelz- und Kristallisationprozess von Polymeren in CNT Arrays untersucht. Die Arrays werden dabei mit zwei verschiedenen Polymeren gefüllt – PS im Inneren der Röhrchen und PDMS in ihren Zwischenräumen. Der Glasübergang für das innere und das äußere Polymer kann so getrennt ausgewertet und verglichen werden. Weitherhin untersuchen wir das Kristallisationverhalten von PDMS im Bulk und in CNT Arrays, wobei isotherme und nicht isotherme Kristallisationskinetik betrachtet werden. In beiden Fällen zeigt sich eine verstärkte Kristallisation der Polymere in Gegenwart von Kohlenstoffnanoröhrchen.

Die dynamischen Aspekte des Polymerverhaltens werden weiter mit Brillouin-Lichtstreuung (Brillouin light scattering, BLS) untersucht. Wir messen akustische Anregungen in zwei verschiedenen porösen Systemen: zufällig angeordnete, parallele Poren in ionenspurgeätztem Polycarbonat (ion track etched polycarbonate, ITPC) und hochgradig geordnete Poren in PAOX Matrizen. ITPC wird durch Bestrahlung einer Polycarbonatfolie mit Schwerionen und anschließendem Ätzen der Ionenspuren hergestellt. Beide Systeme besitzen einen Porenradius von $R \approx 20$ nm, unterscheiden sich aber in Anordnung und Dichte der Poren. Im Experiment untersuchen wir BLS Spektren als Funktion des Winkels zwischen Probenoberfläche und einfallendem Laserstrahl. Wir vergleichen leere und mit PDMS gefüllte Matrizen, wobei wir zwei Arten von Moden im Brillouin-Spektrum beobachten: Bulkmoden von PDMS und der Matrizen einerseits und Oberflächenmoden andererseits.

Contents

1 Introduction

Polymeric nanocomposites are a new class of materials which have been intensively studied in the recent years. The combination of polymers with nanoparticles results in new physical and chemical properties of the obtained materials [1]. The thermal, electrical and mechanical properties of such composites open new possibilities for technology and engineering. One type of these composite materials are polymeric composites based on fibers. They consist of strong fibers included in polymeric matrices. Fibers play a functional role in composites depending on their properties. Using different types of fibers the mechanical stability and thermal conductivity of polymeric matrices can be significantly improved [2]. Using metallic fibers polymers which are originally not conducting can carry electrical currents [3]. The polymer itself is used to protect fibers and keep them at fixed positions.

Composite materials are interesting not only for industrial applications, but also for scientific research. It is well known that materials can have different properties at nanoscales [4, 5]. Polymers confined to a size which is comparable to the size of polymer chains demonstrate different kinetics and dynamical behavior [6–8]. Moreover, in nanocomposites the interface starts to play an important role. The physics of interfaces is not yet well understood and contains a lot of open questions. The interaction of polymers with solid surfaces [9] leads to an interphase layer of polymer in the vicinity of the surface, which has a different behavior than the bulk polymer. The size and polymer properties in the interphase strongly depend on many parameters and internal properties of the polymer and the surface. Composite materials are an ideal candidate for studying the interfacial phenomena. The surface ratio in composites is very high and the interphase can occupy up to 80% of the material volume.

One of the most interesting composite materials are polymeric composites based on carbon nanotubes (CNTs). Since CNTs have been discovered in the beginning of the 1990s [10], many researchers reported on their extraordinary properties and possible applications [11, 12]. Beside single nanotubes, CNT arrays [13] and forests [14] can be synthesized. Tailoring of CNT based composites is one of the ”hot” topics nowadays. However, having been discovered two decades ago, CNTs are still not widely used in applications. Fabrication of CNT/polymer composites contain many physical and chemical problems, like dispersion of CNTs in the matrix, orientation and alignment of tubes in composites and the interaction of CNTs with matrices. CNTs are hollow fibers and have two areas for polymer location: inside and outside the tubes. Which confinement do polymers prefer and can polymers essentially flow into the tube interior? Thus, during the fabrication of composites polymer location is also an open question. Since the inner and the outer surface have different geometrical shapes they provide different confinement for polymers. The conformation, dynamics and kinetics of infiltration of polymers can differ on the inner and outer surfaces of CNTs.

The aim of this thesis is the characterization of CNT/polymer composites based on dense, well ordered and vertically aligned CNT arrays in order to understand the specialities of their structure and the fabrication process as well as the interaction between CNTs and the polymeric matrix.

1.1 Carbon nanotubes: structure and properties

CNTs are long thin cylinders of carbon and can be thought of as a sheet of graphene rolled into a cylinder. Graphene has a 2-D structure of carbon atoms arranged in a hexagonal lattice. Each carbon atom has three nearest neighbors. Rolling sheets of graphene to tubes forms CNTs. They can be considered as large macromolecules with unique size, shape and physical properties. The properties of nanotubes depend on the atomic arrangement of carbon in respect of the tube axis as well as on the diameter and the length of tubes. Moreover, CNTs can be either single-walled (SWCNTs) or multi-walled (MWCNTs) structures

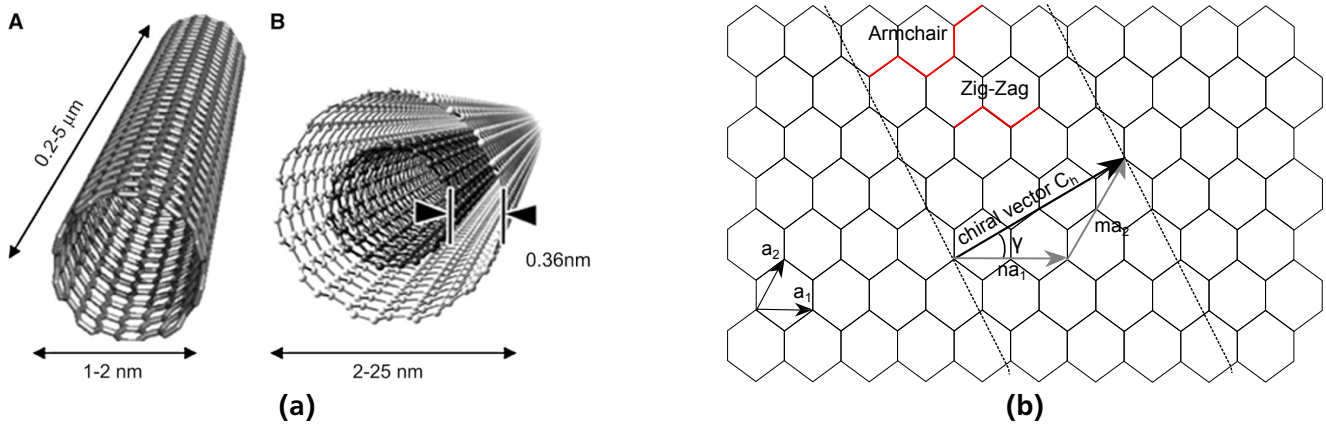

Figure 1.1.: (a) SWCNTs and MWCNTs (taken from [15]); **(b)** Schematic plot of the graphite sheet showing how the CNT is rolled (adapted from [12]) γ is the chiral angle.

(fig. 1.1a). SWCNTs are formed as a single rolled sheet of graphene. MWCNTs consist of several layers of carbon tubes which are arranged in concentric cylinders: one tube inside the other with an interlayer spacing of 0.34-0.36 nm.

The atomic structure of CNTs depends on the way of wrapping of the sheet of graphene which is described in terms of chirality. The direction of wrapping or rolling is defined by the chiral vector $\mathbf{C}_h$:

$$\mathbf{C}_h = n\mathbf{a}_1 + m\mathbf{a}_2 \tag{1.1}$$

where integers n and m denote the number of unit vectors $\mathbf{a}_1$ and $\mathbf{a}_2$ along two directions in the honeycomb crystal lattice of graphene. The schematic structure of a sheet of graphene is shown in figure 1.1b. Two limiting cases exist where $m = 0$ and $n = m$ which correspond to the chiral angles $\gamma = 0°$ and $30°$ respectively. These structures are called "zig-zag" and "armchair". The chiral vector also defines the diameter of CNTs. The diameter of CNTs varies in a broad range. Originally SWCNTs have a diameter of a few nm and MWCNTs can be obtained in the range of 20-25 nm. Nowadays, different techniques allow to synthesize MWCNTs up to a few hundreds nm in diameter.

The chirality of CNTs strongly influences the material properties, for example density and electrical conductivity. Although graphene structures, for example graphite, are considered to be semimetallic, CNTs can be either metallic or semiconducting, depending on the chirality [12]. For metallic tubes the value $n - m$ is divisible by three, in all other cases CNTs are semiconducting [16].

CNTs have unique mechanical properties. Young's modulus and the maximum tension are several times higher than for steel [17, 18]. At the same time CNTs are very light and flexible, they can be used for improving mechanical stability of many composite materials without loosing the elastic properties. CNTs as well as graphite are thermodynamically stable in a very broad range of temperatures under normal ranges of pressure [19, 20]. The extraordinary properties of CNTs make them attractive for many applications: in medicine, nanoscale electronics and material research.

1.2 CNT/polymer composites: achievements and perspectives

Many works have focused on preparation of polymer composites based on CNTs which can result in new functional materials with nanoscale structure and significantly improved physical properties. Nowadays the mechanical properties of such composites are well studied. These studies were inspired by the unique mechanical stability of CNTs since they have been discovered. With decreasing CNT diameter the tensile strength of CNT increases due to less defects of the surface. Smaller tubes provide higher mechanical stability, however even CNTs with large diameter demonstrate higher tensile strength than steel. The

flexibility of CNTs allows to enhance the mechanical properties of composite materials [11]. For example including CNTs into an epoxy matrix increases the tensile modulus to 300% [21]. The elastic modulus, storage modulus and thermo-mechanical properties of CNT/epoxy composites are also significantly improved [22]. Together with mechanical properties the electrical conductivity and shielding effectiveness of composites increase [21]. However, depending on the way of preparation and combination of polymeric matrices with different types of CNTs some properties of the composites can degrade. For example, functionalization and covalent modification of MWCNT with PMMA significantly improves thermal stability but leads to reduced electrical conductivity[22].

Thus, the strategy of fabrication of CNT based polymeric composites is very important and has to be studied. Since the beginning of the research on nanocomposites, CNTs with various diameters and lengths were incorporated in various types of polymers using different techniques: from simple mixing methods in solution to in-situ synthesis of polymers in CNT structures. General strategies of the fabrication of CNT/polymer composites and their developments were summarized in a review by Barrera [21]. They can be compiled in at least five approaches: (1) Nanotube dispersion into polymers by various mixing means; (2) Low-concentration approaches to impact shear loading and z-axis properties in laminate structures; (3) New resin formulation for hybrid polymer formation; (4) Forming interpenetrating polymers and (5) Full integration of nanotubes into polymeric matrices. The first method is most elaborated nowadays. Various composites are prepared using mixing methods depending on mixing viscosity and porosity. In the second method, laminate composites have shown enhancements, for example, in double cantilever beam testing. In the third method, new curing agents have been produced as hybrid systems. The fourth method is focused on network polymers which have advantages in tangled nanotube systems. Finally, in the last method, the integration of CNTs leads to the strengthening for various alloys and thermoplastics [21].

Various aspects of nanocomposites have already been studied. In the case of mixing CNTs with polymer solutions or melts the dispersion and homogenization of CNTs in mixtures are an important factor. Due to the strong agglomeration of CNTs in clusters it is hard to achieve a homogeneous composite material with high concentration of CNTs. Agglomeration can significantly decrease the electrical properties of composites [23]. To prevent the agglomeration and create chemical bonds between CNTs and polymers in composites, nanotubes can be functionalized. The way of functionalization and application of the obtained CNTs in composites are reported in a review by Byrne [24]. Polymer composites based on chemically modified nanotubes demonstrate the best mechanical results.

One of the important factors of the morphology of composites is the orientation of CNTs in the matrix. The alignment of nanotubes in polymer composites is the only way to optimize the anisotropic behavior of the composite in its electrical, mechanical properties [25, 26] and thermal transport [27]. At the same time it is a critical factor and is difficult to control experimentally. Methods during preparation of the composites have to be developed and the achieved distribution has to be determined. Using mixing methods, it is difficult to achieve a preferred orientation and alignment of CNTs in the matrix. In this case alignment can be achieved after mixing of composites by applying an electrical or magnetic field [26, 28]. Another way can be the infiltration of polymers into already aligned CNT structures (arrays or forests). These structures are very dense and have a high concentration of CNTs in composites.

Most works on CNT/polymer composites considered low-concentration systems in order to avoid the agglomeration of CNTs while there are still a lot of open questions and possibilities for advanced properties of high-concentration system. Some works have shown that increasing the concentration of CNTs in a polymeric matrix leads to enhancement of some physical properties, for example tribological properties [29] and electrical transport [30]. Polymer composites with high concentration of CNTs can be prepared using arrays or forests which have a vertical alignment of tubes in respect of the surface. Using CNT arrays necessitates a different way of composite preparation: instead of dispersing CNTs in the polymeric matrix, the polymer must be infiltrated into arrays. Infiltration of polymers can be carried out in melt and in solution [31, 32]. However, the infiltration of polymers into dense CNT arrays contains

several technical and physical problems based on the interaction between polymers and CNTs which will be considered in this thesis.

1.3 The role of interface in composites

Polymers in composites show properties different from bulk polymer. The reason for this is considered as an effect of a polymer interphase near the solid wall of particles or fibers. These interfacial regions are created when two or more materials come in contact. The border between materials is called interface, which is defined by properties of contacting surfaces. The interface exists on all scales ranging from macro to nano. Since the surface-to-volume ratio in nanocomposites can be very large, the surface properties cannot be neglected and play a fundamental role in nanocomposite properties. Experimental results have shown that including nanoparticles into polymeric matrices changes the crystallization behavior of polymers [33–36]. Many researchers reported a shift of the glass transition of polymers in composites and thin films [37–39], and change in conformation and chain dynamics under the nanoscopic confinement [40, 41]. Understanding of interface properties could clarify the composite behavior. Dynamical and statical studies of polymers under confinement have shown that mobility of polymer chains in vicinity of the surface is significantly changed. The factors which influence the chain mobility are the length of the polymer chain, particle surface morphology, the polymer-surface interaction and the chemical bonding between the surface and the polymer [42].

The interface phenomena revolve around the effect of surface forces. They define the interaction between polymers and particles, wetting and capillary flow of polymers into composites. van der Waals forces play a central role in the interaction at the surface. They define repulsive or attractive intermolecular interactions. For example, for two molecules with small radius the energy W of van der Waals interaction can be written as:

$$W = -\frac{C}{D^6} \tag{1.2}$$

where D is the distance between particles and C corresponds to the coefficient of atom-atom pair interaction. In case of a spherical particle at a flat planar surface the van der Waals energy can be expressed as [43]

$$W = -\frac{A_H R}{6D}, \quad D \ll R \tag{1.3}$$

where R is the radius of the sphere, D the distance between surface and sphere and $A_H = \pi^2 C \rho_1 \rho_2$ the Hamaker constant with ρ_1 and ρ_2 being the numbers of atoms per unit volume in the two interacting bodies (sphere and planar surface in our example). The Hamaker constant characterizes the interaction between molecules. The value of A_H depends on the chemical structure of interacting molecules and medium where they interact. The Hamaker constant can be either positive or negative. In the first case the interaction is called ”attractive”; a negative value of A_H leads to ”repulsive” interaction. As we can see, the ”strength” of van der Waals forces depends not only on the distance between interacting bodies but also on their geometry. Thus, van der Waals forces can be effective on a rather long range, greater than 10 nm [44]. However, with increasing distance between bodies the van der Waals interaction decreases. In nanocomposites with polymers having chain sizes in the range of few nanometers confined inside tubes or around particles with comparable size, van der Waals forces play an important role in composite structure and behavior of the polymeric matrix. For example the wetting of CNTs with polymers in composites depends on the surface energy γ_S of the polymer and CNT surface, which is also defined by atomic interaction [43]:

$$\gamma_S = \frac{A_H}{24\pi D_0}. \tag{1.4}$$

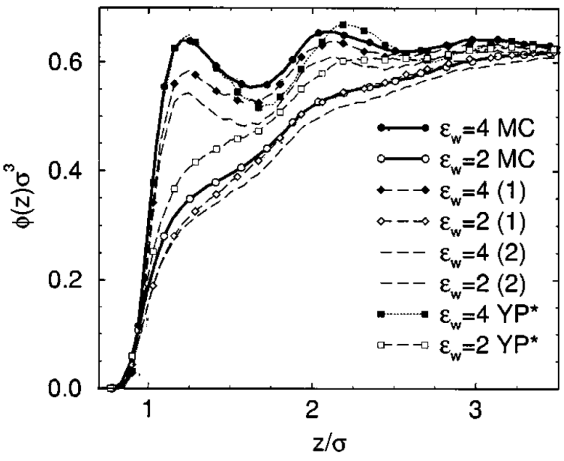

Figure 1.2: Monomer number density profile as a function of attraction ε_w between the monomers and surface. Figure is taken from [45]. Label "MC" corresponds to data obtained by Monte-Carlo simulation, (1) and (2) denote the results with different weighting function and label "YP" shows the result of the adjusted van der Waals approximation.

Here D_0 is the distance between two atoms of the surface material. Details of wetting phenomena will be briefly presented in section 4.4.1.

The surface interaction is also a reason for different conformation and mobility of polymer chains near the interface. Experimental and theoretical studies of confined polymers have shown that polymers form a layer at the surface with different structure and dynamics than bulk polymers. It is the so-called interphase. The size and the structure of the interphase depends on the surface interaction as well. For example, solid particles dispersed in polymeric solution can demonstrate adsorption of polymers to the surface in case of attractive interaction between particles and polymer. In case of a repulsive interaction the depletion zone is formed in vicinity of particles. A similar situation can be observed in polymer melts. Polymer can be adsorbed to the surface or form a depletion layer. Both of these layers (adsorbed and depleted) have sizes comparable to the segment length of polymer. However, theoretical works on polymer confined on nanoscale have shown that the polymer interphase near the solid surface has a more complex structure which results in an oscillating density profile (fig. 1.2 [45]). In the case of strong attractive interaction the density of polymer increases at the surface, then decreases and reaches the bulk density. Depending on the interaction potential the density of the polymer can also be depleted near the surface.

The conformation of polymer chains at the surface and under confinement is restricted and differs from the bulk. The van der Waals forces do not only describe the attraction of molecules to the surface, they also play a role in orientation of molecules in vicinity of the surface as well as in the bulk. Of course, this orientation is weaker than with dipole interaction which occurs between two polar molecules [44]. Thus, polymer can be stretched or compressed depending on many factors like concentration of polymer at the surface, the interaction of chains with the surface and the interchain interaction. For strong interaction with the surface polymer chains will be stretched along the surface. The size and shape of confinement also play an important role. For example, if the size of a cylindrical pore is much smaller than the radius of gyration of the polymer, polymer chains will be stretched in pores [46]. The stretching decreases with increasing pore size.

The interfacial interactions and the size of confinement also affect the polymer dynamics. As was mentioned before, the mobility of polymer chains in vicinity of the surface is changed. The polymer at the interface is immobilized and solidified [47] which is considered as a primary reinforcing mechanism of tailoring composites. It can explain peculiarities in the viscoelastic response of polymers near the solid surface. However, the specific interactions of certain polymers and surfaces play an important role as well. Some works have shown less restricted dynamics of polymers under confinement at long times [41, 48].

For the past decades the interaction between polymer and nanoparticles in composite materials have been extensively studied and have shown the importance of interface phenomena for the preparation and final properties of composites.

1.4 Outline of the thesis

The aim of this thesis is to investigate the structure of CNT/polymer composites as a promising composite material as well as a potentially good system for the study of polymer interphase phenomena in cylindrical confinement. For these purposes we chose vertically aligned CNT arrays and infiltrated different polymers – glassy polystyrene (PS), polymethylmethacrylate (PMMA) and semicrystalline polydimethylsiloxane (PDMS). The length and diameter of CNTs as well as the arrangement of tubes in arrays can be experimentally controlled during the CVD (chemical vapor deposition) process which is used for synthesis of arrays.

The thesis consists of 7 chapters. The main experimental method – small angle scattering – is described in the second chapter of the thesis. The theoretical background of X-ray scattering and its experimental realization as well as instrumental details are given in section 2.1. The model function applied for description of the experimental data is also presented therein. Section 2.2 summarizes the theory and experimental details of small angle neutron scattering (SANS) which is used for investigation of the polymer chain conformation in CNT arrays.

Chapter 3 is focused on characterization of CNT arrays at each step of the preparation procedure. First of all the structure of PAOX (porous aluminum oxide) will be discussed. The PAOX template is used for synthesis of CNTs and defines the size of tubes and their arrangement. We follow the preparation process step by step: from empty PAOX templates to PAOX with CNTs grown inside the pores and finally to the CNT array with the PAOX removed by etching. We will characterize arrays depending on preparation conditions – time of the synthesis and parameters of templates. Three possible structures of arrays can be achieved: freestanding, one side closed and both sides closed tubes. All three structures will be analyzed.

The structure of CNT/polymer composites as well as imbibition of polymers into arrays will be considered in the fourth chapter of the thesis. In the first two sections (4.1 and 4.2) of this chapter we will discuss two ways of infiltration of polymers into CNT arrays: infiltration of polymeric solutions and melt infiltration.

After a complete investigation of the structure of CNT/polymer composites we will focus on polymer properties in the arrays. In section 4.3 the conformation of polymer chains inside CNTs which is studied by SANS will be described. Section 4.4 discusses the filling kinetics of polymer into CNT arrays. Using time-resolved SAXS the polymer flow into the whole array as well as only into the CNT interior are studied. The filling is described in terms of variation of electron density inside and outside CNTs in the arrays. The formation of a polymer interphase in vicinity of the CNT surface will be also discussed there.

In the following chapter 5, the study of phase transitions of polymers in CNT arrays will be presented. This chapter will give an idea about the change of dynamical behavior of polymers confined in CNT arrays. First of all a short introduction of the experimental method – differential scanning calorimetry (DSC) – will be given in section 5.1. Glass transitions of polymers in the whole array as well as separately inside and outside tubes are subject of section 5.2. We will investigate the effect of tube diameter and molecular weight of polymer on the glass transition. Melting and crystallization of PDMS confined in between CNTs in arrays will be discussed in section 5.3. We compare isothermal and nonisothermal crystallization of polymer in arrays with the bulk properties.

A detailed study of dynamics of polymers can be performed by inelastic scattering experiments. As a first step in the investigation of polymer dynamics in cylindrical confinement similar to CNT arrays the polymer confined in cylinders of nanoporous templates is probed by Brillouin light scattering (BLS). The sound propagation through the hard templates filled with polymer will be presented in chapter 6 of the thesis. The principles of BLS and the experimental setup will be explained in section 6.1. The two templates with different porosity –ITPC (ion-track etched polycarbonate) and PAOX – will be discussed in section 6.2. We will present the influence of the polymer infiltration on sound propagation in the bulk and along the surface of templates. Finally, all aspects will be summarized in the last chapter 7 of the thesis.

2 Small angle scattering: theory and experiment

2.1 Small angle X-ray scattering

Small Angle X-ray Scattering (SAXS) enables to measure structural features on length scales between 1 nm up to hundreds of nanometers by analyzing the scattering pattern at very low angles (typically at 2θ less than 5°) from the direct X-ray beam. The technique is used in various applications to get access to different parameters such as polymer molecular mass and supramolecular structure, pore size distribution and shapes of colloids.

The section summarizes basic principles of scattering theory. To give an idea of scattering in soft matter and X-ray scattering in particular key points of the theory will be introduced. A more detailed description of the scattering theory can be found elsewhere [49–51]. Since the scattering on highly dense and anisotropic samples has a number of peculiarities, they will be discussed as well after the general section. The used instrument will be presented together with an introduction of the model function for data treatment due to the strong dependency of the function on the orientation of the sample with respect to the primary X-ray beam.

2.1.1 Basic principles of X-ray scattering

X-rays are transverse electromagnetic waves with shorter wavelength compared to visible light. The range of wavelengths is about 10^{-2} to 10^{2} Å. Usually laboratory studies of polymers are performed mostly with K_α characteristic radiation from a copper anode tube having a wavelength of 1.5418 Å. Similarly to visible light, X-rays can be represented in terms of a wave-particle duality. Some experiments are better understood in a wave interpretation, while others require to consider a beam of X-rays as a stream of photons. As the stream of particles X-rays can be characterized by their energy E and momentum p:

$$E = h\nu \tag{2.1}$$

and

$$p = \frac{h}{\lambda} \tag{2.2}$$

where $h = 2\pi\hbar = 6.626 \cdot 10^{-34}$ Js is the Planck constant, and ν and λ are frequency and wavelength of X rays correspondingly. The typical energy of X-ray photons is $E \sim 10$ keV and they can exchange energy during the scattering process. However, the inelasticity of the scattering is neglected in the type of experiments described here due to negligible energy transfer compared to the photon energy.

A sketch of the scattering experiment is shown in figure 2.1. We assume that the distance between sample and source and the distance between sample and detector are much bigger than the sample size. Moreover, we assume that the source emits radiation of one given energy, i.e. monochromatic radiation and we consider scattering without energy exchange (elastic scattering). In this case, the incident wave can be described by a wave vector $\mathbf{k}$ of the incident wave and the scattered wave $\mathbf{k}'$:

$$k = \mid \mathbf{k} \mid = \mid \mathbf{k}' \mid = k' = \frac{2\pi}{\lambda}. \tag{2.3}$$

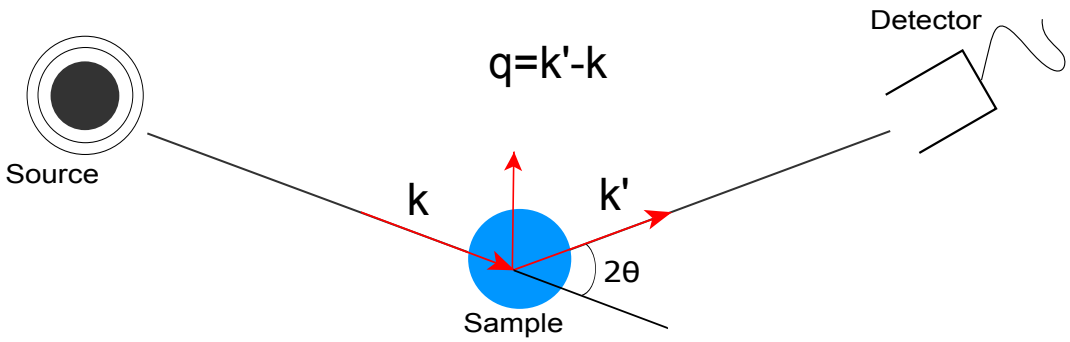

Figure 2.1.: Sketch of the scattering process. The incoming X-ray photons with incident wave vector $\mathbf{k}$ interact with the sample and are detected at an angle 2θ with scattered wave vector $\mathbf{k}'$. The scattering vector $\mathbf{q}$ is the difference in wave vector: $\mathbf{q} = \mathbf{k}' - \mathbf{k}$.

The difference between the wave vectors of scattered and incident wave is defined as scattering vector $\mathbf{q}$:

$$\mathbf{q} = \mathbf{k}' - \mathbf{k}. \tag{2.4}$$

The magnitude of the scattering vector can be calculated from wavelength λ and scattering angle 2θ:

$$|\,\mathbf{q}\,| = \frac{4\pi}{\lambda}\sin\theta. \tag{2.5}$$

A scattering experiment comprises the measurement of the intensity distribution as a function of the scattering vector. The intensity of an approximately parallel beam of X-rays is the flux of energy which crosses a unit surface normal to the average ray of the beam per second. In the case of monochromatic plane waves the intensity is proportional to the squared amplitude:

$$I = |A|^2 = AA^* \tag{2.6}$$

where the amplitude A of a wave of frequency ω and wave vector $\mathbf{k}$ at the position $\mathbf{r}$ and time t can be described as

$$A = A_0 e^{i(\mathbf{k}\cdot\mathbf{r}-\omega t)}. \tag{2.7}$$

In the case of spherical waves, when the intensity of radiation is emitted by a point source in a given direction, the intensity can be expressed as the number of X-ray photons transmitted per solid angle $d\Omega$ per second. In this way the measure of the intensity becomes independent of the distance from source to the detector. To investigate the structure of a sample we have to measure the number of X-ray photons scattered into the solid angle $d\Omega$. This quantity is related to the differential scattering cross section:

$$\frac{d\sigma}{d\Omega} = \frac{J}{J_0}, \tag{2.8}$$

where J is the scattered X-ray flux into a unit of the solid angle in a given direction and J_0 is the flux of the incident beam. Experimentally one measures the intensity I of the scattered beam as a function of scattering angle. The result may be converted to the differential scattering cross section if the incident beam flux J_0 is known, otherwise the result can be measured in arbitrary units, such as counts per second.

2.1.2 Total scattering intensity

The diffraction of X-rays by matter results from the combination of two phenomena: (1) scattering by individual electrons in the sample, and (2) interference between the waves scattered by these electrons. X-rays, being electromagnetic radiation, interact with charged particles in the matter – electrons. The differential scattering cross section of a free electron is given by the Thomson formula:

$$\left(\frac{d\sigma}{d\Omega}\right)_e = r_e^2 \frac{1+\cos^2 2\theta}{2} = b_e^2, \tag{2.9}$$

where r_e is the classical radius of the electron and defined as $r_e^2 = e^2/mc^2 = 2.818 \cdot 10^{-15}$ m. b_e is the scattering length of an electron that expresses the efficiency of scattering by the particle. The magnitude of the scattering length depends on the nature of the radiation and the scattering particle. By integrating equation (2.9) over the solid angle Ω we find the total scattering cross section:

$$\sigma_{tot} = \int_\Omega \left(\frac{d\sigma}{d\Omega}\right) d\Omega. \tag{2.10}$$

The total scattering cross section of an electron is found to be $\sigma_e = 8/3\pi r_e^2 = 6.65 \times 10^{-29}$ m^2= 0.665 barn.

We now consider matter with the density distribution of electrons $\rho_e(r)$. The scattered amplitude at the position r is proportional to the scattering length density distribution $\rho(r)$ at that position. $\rho(r)$ depends on the type of radiation and the interaction of this radiation with the matter. In case of X-ray scattering, the scattering density is equal to the electron density of the sample $\rho_e(r)$ multiplied by b_e:

$$\rho(r) = \rho_e(r) b_e. \tag{2.11}$$

The total scattering amplitude is given by a superposition of scattering from all positions r within the sample, taking into account the phase factor $e^{i\mathbf{qr}}$:

$$A(q) = A_0 \int b_e \rho_e(r) e^{-i\mathbf{qr}} d^3r, \tag{2.12}$$

where A_0 is the amplitude of the incident beam. It can be seen from (2.12) that the amplitude of the scattered radiation is connected to $\rho_e(r)$ by a simple spatial Fourier transformation.

Now we consider that the sample consists of a large numbers of identical unit cells arranged regularly in space. The information contained in the observed intensity can be separated into two factors, one relating to the lattice structure of the sample and another one relating to the internal content of the unit cell. In this case the electron density can be represented as a convolution of these two terms:

$$\rho_e(r) = \rho_F(r) \otimes \rho_S(r), \tag{2.13}$$

where $\rho_F(r)$ is the electron density distribution in a single unit cell, for example cylinders, and $\rho_S(r)$ is defined by specifying the positions of all unit cells in the sample.

According to the general equation (2.12), the amplitude scattered by the object is represented by the Fourier transform of its electron density. Using the convolution theorem, the amplitude can be written as:

$$A(\mathbf{q}) = A_F(\mathbf{q}) \cdot A_S(\mathbf{q}), \tag{2.14}$$

Where $A_F(\mathbf{q})$ is the scattering amplitude of the geometrical shape of every unit cell in the sample and called form factor $F(\mathbf{q})$. The second factor, $A_S(\mathbf{q})$ is the scattering amplitude corresponding to the scattering coming from correlation between unit cells in the sample. The form factor $F(\mathbf{q})$ is in general a smoothly varying function defined over the whole range of reciprocal space. The product of $F(\mathbf{q})$ and $A_S(\mathbf{q})$, however, produces a scattering amplitude which is nonzero only in the immediate neighborhood of the nodes of the reciprocal lattice. The intensity of scattering observed at these various lattice points is "modulated" by the form factor, which is governed by the atomic content of the unit cell only. Thus the interpretation of scattering patterns separates into two aspects: the scattering from lattice structure and scattering giving information about the placement of atoms in the unit cell.

Hence, the scattering intensity is

$$I(\mathbf{q}) = \mid A(\mathbf{q}) \mid^2 = S(\mathbf{q}) \cdot \mid F(\mathbf{q}) \mid^2 . \tag{2.15}$$

where $S(\mathbf{q})$ is the structure factor which describes the correlation between unit cells. In the general case when the lattice is not ideal and contains some imperfections every unit cell can be replaced by an average cell and the total scattering intensity can be rewritten as

$$\langle I(\mathbf{q}) \rangle = C(\langle F(\mathbf{q}) \rangle^2 S(\mathbf{q}) + \langle F(\mathbf{q})^2 \rangle - \langle F(\mathbf{q}) \rangle^2). \tag{2.16}$$

The difference $\langle F(\mathbf{q})^2 \rangle - \langle F(\mathbf{q}) \rangle^2$ is called Laue scattering, or diffuse scattering. It is due to variations in the form factors for the different positions on the lattice and provides a continuous but q-dependent background. The constant C is a scaling factor and defined as $C = (b_e \cdot \Delta\rho_e \cdot V_p)^2 \cdot N$, where V_p is the volume of the unit cell and N is the total number of unit cells.

2.1.3 Small angle scattering of cylindrical nanotubes — model function

According to the Bragg law $\sin\theta = \lambda/2d$ the information about relatively large objects (large d) is contained in $I(\mathbf{q})$ at relatively small θ. The relationship between the wavelength and the scattering vector $q = 4\pi \sin\theta/\lambda$ means that small angle experiments entail the low-q.

The principles of SAXS are based on general concepts of scattering. Here we will focus on the particular case of SAXS on particles with strong anisotropy having cylindrical form and describe the model function for CNT/polymer composites.

In the case when particles are stretched axially and have small aspect ratio R/L (where R is the radius and L is the tube length), the structure is no longer isotropic and the scattered intensity $I(\mathbf{q})$ is not only a function of scattering vector $\mathbf{q}$, but also a function of the sample orientation. Let us consider axial orientation of tubes in the primary beam. Then the tube is tilted to the angle γ as shown in figure 2.2.

Vertically aligned CNT arrays can be considered as long hollow cylinders. They are ordered on a hexagonal lattice (fig. 2.3) as a consequence of the hexagonal order of pores in PAOX. The shell thickness is the thickness of the multi-walled CNT. We only quote results for the scattering from such an array of cylindrical particles. Details of the model function can be found in the work of Engel [52].

Similar to the scattering from crystals the scattering pattern of the two dimensional array of CNTs is given as product of squared form factor of the scattering particle, the CNT, and the structure factor, which takes correlations between CNTs into account. The form factor $F(\mathbf{q})$ is the Fourier transform of the electron density distribution of a single CNT. The form factor for scattering from a single solid cylinder, described with the cylinder coordinates r' and ϕ and with z as cylinder axis, is given by

$$F(q) = b_e \rho_0 \int_{-L/2}^{L/2} \int_0^R \int_0^{2\pi} e^{-i\mathbf{q}\mathbf{r}} r' d\phi\, dr' dz, \tag{2.17}$$

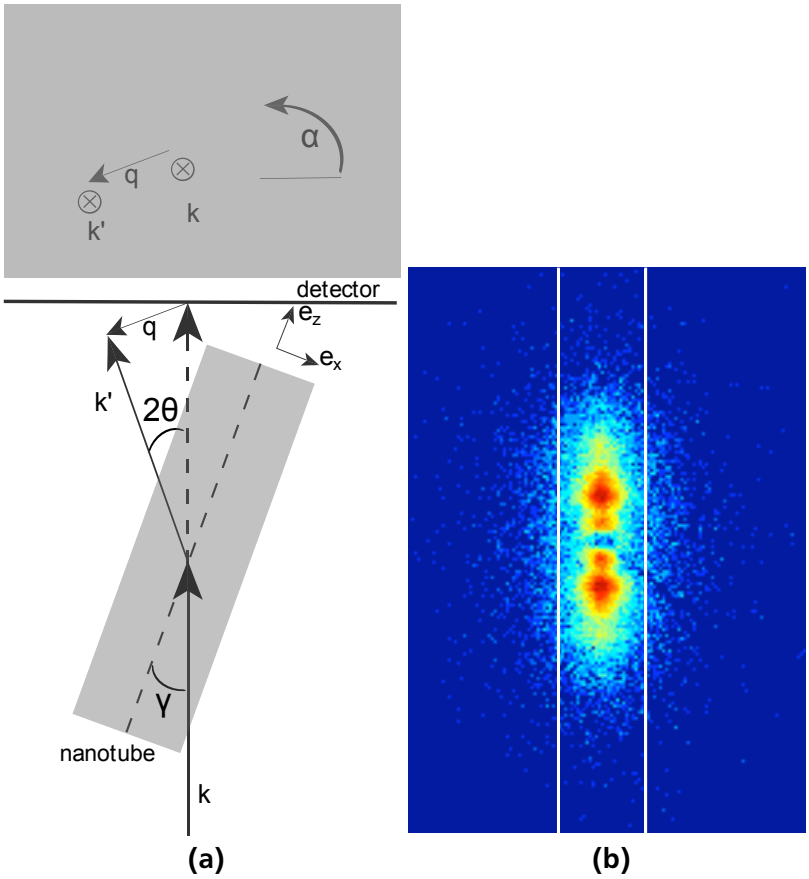

Figure 2.2.: a) Orientation of the sample in the X-ray beam: top view and on detector plane, α is azimuthal angle in the detector plane, γ is the tilting angle of the goniometer sample holder, 2θ is the scattering angle. b) Scattering pattern(2D detector image) of CNT at $\gamma = 20°$. White lines represent the rectangular filter used for data evaluation.

where $b_e\rho_0$ is scattering length density of the thin cylinder, which does not depend on length and radius of the cylinder. The scattering vector $\mathbf{q} = q_x\mathbf{e}_x + q_y\mathbf{e}_y + q_z\mathbf{e}_z$ needs to be expressed in spherical coordinates as well [52]:

$$q_x = q(\cos\alpha\cos\gamma\cos\theta + \sin\gamma\sin\theta) \tag{2.18}$$

$$q_y = -q\sin\alpha\cos\theta \tag{2.19}$$

$$q_z = q(\cos\alpha\sin\gamma\cos\theta - \cos\gamma\sin\theta), \tag{2.20}$$

where α is azimuthal angle in the detector plane, 2θ is scattering angle and γ is tilting angle of cylinders against primary beam. In the case of small angle scattering we can apply approximations for analytically solving the integral: $\cos\theta \approx 1$ and $\sin\theta \approx 0$, thus the direction of the scattering vector $\mathbf{q}$ depends only on γ and α. Since the CNTs have high aspect ratio (L/R) the scattering intensity strongly depends on tilting angle γ. When cylinders are parallel to the primary beam ($\gamma = 0$) the intensity is distributed isotropically around the primary beam. If $\gamma = 90°$ the scattering pattern results in a straight strip of scattering intensity. For long tubes ($L \gg R$) the straight strip of the intensity distribution is also observed at $\gamma < 90°$. Experiments described in this work are performed at $\gamma = 20°$ since this angle already results in the straight strip of the scattering pattern, and at the same time provides sufficient scattered intensity.

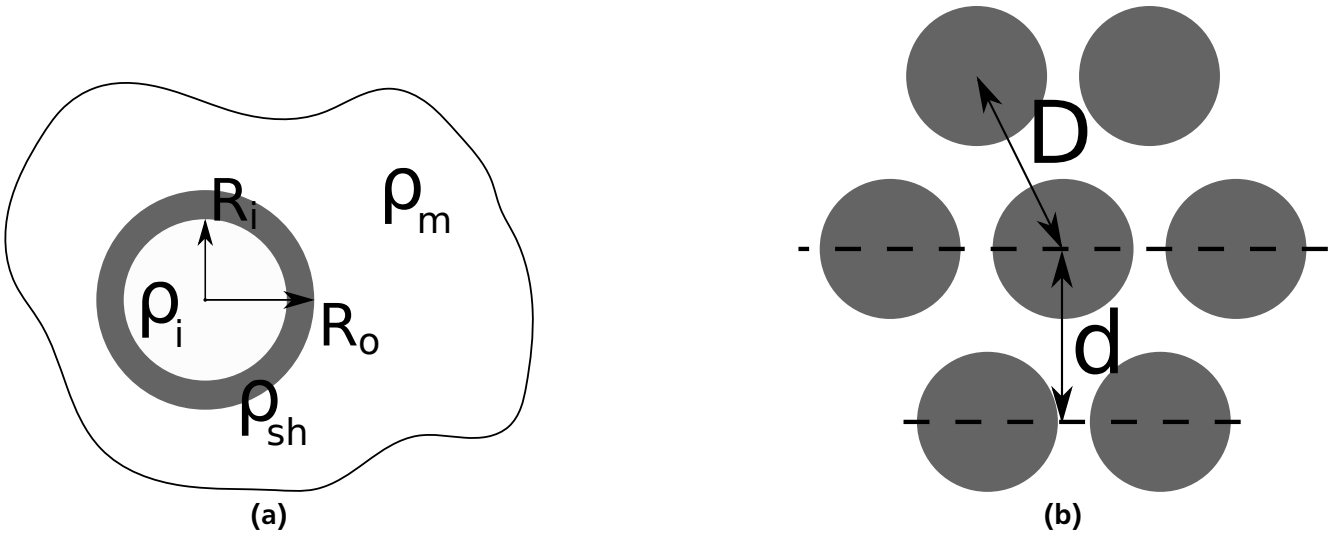

Figure 2.3.: Schematic view of structure of the CNT array for understanding the SAXS model function: a) Core-shell cylindrical structure of one tube; b) Hexagonal arrangement of CNTs in the array where D is mean distance between two nearest tubes.

Since the nanotubes have a constant electron density distribution along the long axis, ρ is independent of z. Correspondingly the integration along z in equation (2.17) can be performed independently:

$$\int_{-L/2}^{L/2} e^{iq_z z} dz = \frac{2}{q_z} \cdot \sin\left(q_z \frac{L}{2}\right). \tag{2.21}$$

The remaining two integrals in equation (2.17) can be calculated numerically for every azimuth angle. Due to specific orientation of the scattering pattern along the vertical direction in the detector plane the azimuth angle is fixed, $\alpha = 90°/270°$. In this case the ϕ and r' integration can be calculated analytically:

$$F(q, \alpha = 90°/270°) = 2\pi L R^2 \cdot b_e \rho_0 \frac{J_1(qR)}{Rq} \tag{2.22}$$

where J_1 is the first order Bessel function. This equation was given by Mittelbach and Porod [53] and applied for the analysis of scattering from cylindrically shaped particles. The prefactor $\pi L R^2$ is the volume of the cylinder.

As was mentioned before the carbon nanotube can be modeled as hollow cylinder and has three different electron density regions – core with electron density ρ_{core}, shell ρ_{shell} and matrix ρ_{matrix}. The form factor can be expressed as superposition of two cylinders:

$$F(\mathbf{q}, R_i, R_o) = C\left(R_i(\rho_{\text{core}} - \rho_{\text{shell}})\frac{J_1(R_i q)}{q} + R_o(\rho_{\text{shell}} - \rho_{\text{matrix}})\frac{J_1(R_o q)}{q}\right) \tag{2.23}$$

where ρ_{core}, ρ_{shell} and ρ_{matrix} are electron densities of inner part of the tube (core), the tube wall and surrounding area of the tube respectively. R_i and R_o are inner and outer radius of the cylindrical tube. The shell thickness is the difference between outer and inner radii ($R_o - R_i$). The constant C is the combination of all remaining constants and called prefactor.

Real CNTs have some deviations from ideal core-shell cylinders given in equation (2.23) like statistical distribution of the radius – polydispersity – and a smooth transition region from electron density of the

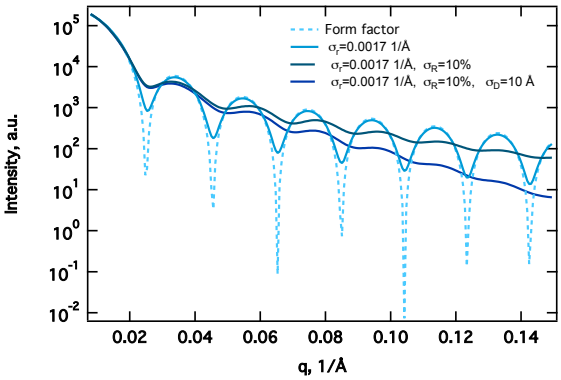

Figure 2.4: Form factor according to equation (2.23) and real form factor with included instrument resolution σ_r, polydispersity σ_R and roughness of tube surface σ_D. Curves show the influence of every parameter.

matrix to the core - roughness [52]. All these effects should be taken into account as well in order to get a realistic model function. Polydispersity is described by a normalized Schultz-Zimm distribution function:

$$g(R,\sigma_R,\langle R\rangle) = \left(\frac{z_1}{\langle R\rangle}\right)^{z_1} R^z \exp\left(-\frac{z_1}{\langle R\rangle}R\right)\frac{1}{\Gamma(z_1)} \tag{2.24}$$

where $z = (\langle R\rangle/\sigma_R)^2 - 1, z_1 = z + 1$, Γ is the Gamma function and σ_R the width of the distribution. This function has an advantage over a Gaussian function for large values of σ_R as there is no unphysical negative radii contribution to the average. Therefore, the averaged form factor is given as

$$\langle F(q)\rangle = F(q,\langle R\rangle) = \int_0^\infty F(q,R)g(R,\sigma_R,\langle R\rangle)dR. \tag{2.25}$$

Another additional factor which should be taken into account is roughness of the tube walls, or in other words, the smooth transition region from the electron density of the core to the matrix. This is realized by a convolution of the electron density distribution with Gaussian function:

$$I(q) = \tilde{I}(q)\cdot e^{-\sigma_D^2 q^2} \tag{2.26}$$

where is σ_D is the width of the transition region. The effect on the scattering profile is shown in figure 2.4.

Finally, we need to consider the resolution of the instrument which is usually taken into account by convolution of the intensity with a Gaussian smearing function. The width of this function is determined and kept fixed. In summary, the scattering intensity from a single cylindrical tube at azimuth angle in the detector plane at $\alpha = 90°/270°$ is given as

$$I(\mathbf{q}) \sim \int \langle F(\tilde{q})^2\rangle \cdot e^{-\sigma_D^2\tilde{q}^2}\frac{1}{\sqrt{2\pi}\sigma_r}e^{-\frac{(\tilde{q}-q)^2}{2\sigma_r^2}}d\tilde{q} + I_{\text{bkg}} \tag{2.27}$$

where I_{bkg} is q-independent background scattering. All convolutions of the Laue term in equation (2.16) are performed in an analogous manner. Influence of all described parameters is shown in figure 2.4.

As a consequence of the high density of nanotubes in the array structural correlations between tubes are quite strong and the structure factor $S(\mathbf{q})$ is not a constant and has to be taken into account in the total scattering intensity (eq. (2.16)).

In case of strong orientation and strictly parallel long tubes the system may be modelled as a two dimensional polycrystalline powder. Just as in 3D crystallography one would then expect a scattering

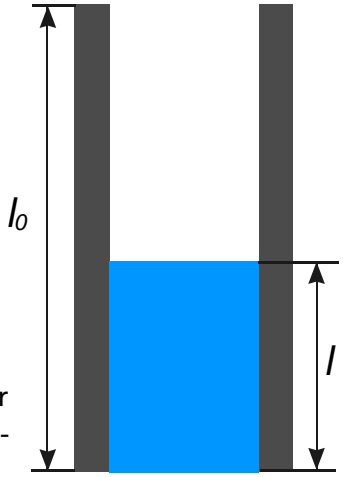

Figure 2.5: Schematic view of modeled form factor in case of capillary flow inside the nanotube

pattern consisting of Bragg peaks at positions defined by the lattice. This situation has been analysed in the work of Ruland [54]. Taking into account that CNTs are grown into nanopores of PAOX templates (fig. 3.1) having hexagonal arrangement of pores the structure factor is that for a two dimensional hexagonal lattice (TDHL)(fig. 2.3). The scattered intensity is then given as:

$$S_{TDHL}(\mathbf{q}) = \frac{K}{A} e^{-q^2\sigma_{DW}^2} \sum_{h,k,0} \frac{m_{h,k,0}}{\sqrt{2\pi}\sigma_B} \frac{1}{q} \exp\left(-\frac{(\mathbf{q}^*_{h,k,0} - \mathbf{q})^2}{2\sigma_B^2}\right) \tag{2.28}$$

where $A = \frac{D^2\sqrt{3}}{2}$ is the 2D surface of the unit cell and D the lattice parameter or the mean distance between tubes (see fig. 2.3b). σ_{DW} is the Debye-Waller factor describing the effect of positional disorder of the lattice on intensity. m_{hk0} is multiplicity, σ_B is the constant width of the Bragg peaks at the position q^*_{hk0} and K is combination of all further constant contributions and called structural prefactor. Typical variation of K is from 1 to 10 and does not play a critical role in fitting. This parameter is fixed while fitting and adjusted in the end after definition of all important parameters.

2.1.4 Form factor of tubes filled by capillary flow

Let us consider the situation when a polymer film is placed on the top of the porous structure. At high temperature polymer melts and flows into nanotubes. In this case the electron density distribution along the long axis of tubes is not a constant, and equation (2.21) needs to be modified. Now we have to consider ρ as a function of z, $\rho(z)$. On the other hand, according to the scattering geometry (fig.2.2) when the tubes are tilted to 20° from their parallel position against the primary beam the scattering intensity is concentrated along a straight vertical line. The model function is calculated for azimuthal angle $\alpha = 90°/270°$. In this case the variation of electron density along the long axis of the tube does not play any role since the q_z component is equal to zero (see equation (2.20)). Therefore, the model function is sensitive to radial variation of electron density distribution. Any variation of electron density along the long axis can be taken into account by variation of an average electron density inside the tube, but cannot be separated from the radial component. The filling height considered in Lucas-Washburn theory (see chapter 4.4) cannot be fitted in terms of the presented model function.

To be able to directly analyze the continuous filling of the nanotube along z direction we consider $q_z \neq 0$. This condition is satisfied when in equation (2.20) $\cos\alpha \neq 0$ or $\alpha = 0°/180°$.

Consider that in the beginning of the filling process, at time $t = 0$, the tube of height l_0 is empty and electron density inside the tube is zero. After the filling process has been started at time $t = \tau$, the tube is partially filled and the filling height is l with inner electron density ρ_p. This situation is shown in

figure 2.5. The form factor of the whole cylinder is a superposition of the form factor of the empty part of the tube and the filled one:

$$F(\mathbf{q}) = l \cdot F_{\text{filled}}(\mathbf{q}) + (l_0 - l) \cdot F_{\text{empty}}(\mathbf{q}). \tag{2.29}$$

For both form factors $F_{\text{filled}}(\mathbf{q})$ and $F_{\text{empty}}(\mathbf{q})$ the expression (2.21) is used since electron density of empty and polymer filled cylinders is a constant. For the azimuthal angle $\alpha = 0°/180°$ the ϕ and r' integration in expression (2.17) can be done analytically:

$$F_{\text{filled}}(q, \gamma > 0, \alpha = 0°/180°) = \frac{4V_{\text{filled}} b_e \rho_0}{lq^2 \sin\gamma \cos\gamma} \sin\left(\frac{lq\sin\gamma}{2}\right) \frac{J_1(qR\cos\gamma)}{qR\cos\gamma}, \tag{2.30}$$

$$F_{\text{empty}}(q, \gamma > 0, \alpha = 0°/180°) = \frac{4V_{\text{empty}} b_e \rho_0}{(l_0 - l)q^2 \sin\gamma \cos\gamma} \sin\left(\frac{(l_0 - l)q\sin\gamma}{2}\right) \frac{J_1(qR\cos\gamma)}{qR\cos\gamma} \tag{2.31}$$

where V_{filled} and V_{empty} are volumes of filled and empty cylinder correspondingly. According to the core-shell structure of every tube both equations can be rewritten as

$$F_{\text{filled/empty}}(\mathbf{q}, R_i, R_o) \sim B(q) \cdot \left(2R_i(\rho_{\text{core}} - \rho_{\text{shell}}) \frac{J_1(R_i q\cos\gamma)}{q\cos\gamma} + 2R_o(\rho_{\text{shell}} - \rho_{\text{matrix}}) \frac{J_1(R_o q\cos\gamma)}{q\cos\gamma}\right) \tag{2.32}$$

where the q-dependent coefficient B(q) is defined as

$$B(q)_{\text{filled}} = \frac{4\pi}{q^2 \sin\gamma\cos\gamma} \sin\frac{lq\sin\gamma}{2}, \tag{2.33}$$

$$B(q)_{\text{empty}} = \frac{4\pi}{q^2 \sin\gamma\cos\gamma} \sin\frac{(l_0 - l)q\sin\gamma}{2}. \tag{2.34}$$

The sine term is a rapidly oscillating function of q as l and l_0 are large quantities. Since $l \gg 1/q$ the oscillations can be averaged in terms of intensity and equations (2.33) and (2.34) can be simplified to

$$B(q) = \frac{2\sqrt{2}\pi}{q^2 \sin\gamma\cos\gamma}. \tag{2.35}$$

Intensity along the horizontal axis in the detector plane ($\alpha = 0°/180°$) scales with q^{-4} which means stronger decrease than the intensity along the vertical axis ($\alpha = 90°/270°$) with q^{-2} scaling. Due to the very high aspect ratio ($R/L \ll 1$) intensity at $\alpha = 0°/180°$ is very low and its analysis is possible only in the case of high scattering intensity. Thus, the analysis of the filling kinetics in section 4.4 will only be performed in terms of the average electron density of the core for intensity scattered along $\alpha = 90/270$.

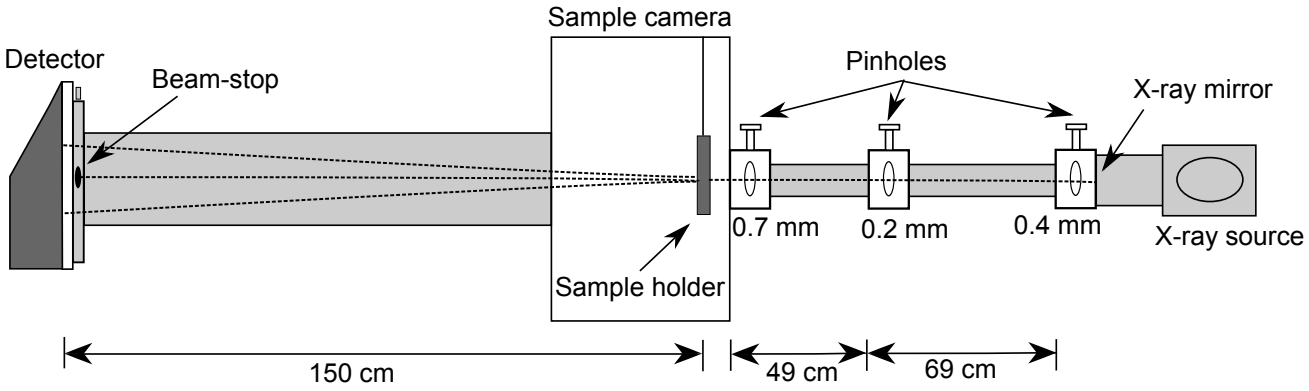

Figure 2.6.: Schematic view of SAXS setup

2.1.5 Experimental setup

All X-ray experiments were performed using a laboratory scattering instrument. The setup is schematically shown in figure 2.6.

A sealed X-ray tube (Panalytical) with Göbel mirror is used yielding CuK_α radiation with $\lambda = 1.54$ Å. The beam is collimated by three pinholes. The sample is mounted on a goniometer-like sample holder which allows to rotate the sample around the two axes perpendicular to the incoming beam with high accuracy (better than 0.01 degree). The sample holder is located inside a vacuum chamber ($5 \cdot 10^{-2}$ mbar).

Scattered intensity is recorded with a two-dimensional detector (Molecular Metrology) at 150 cm distance from the sample providing an accessible range of scattering vectors 0.008 Å$^{-1} < q < 0.25$ Å^{-1}.

Figure 2.2 shows the positioning of the sample with respect to the primary beam. The nanotubes were tilted to 20° from their parallel position with respect to the primary beam. The strongly anisotropic scattering pattern is analyzed in terms of the projections q_x and q_y of the scattering vector $\mathbf{q}$ on the detector. For a tilting angle $\gamma = 20°$ intensity is concentrated along a nearly straight line and is denoted as $I(q)$ with $q = \mid \mathbf{q} \mid$ [52]. A typical scattering pattern is shown in figure 2.2b. Calibration of q-vector was done by silver behenate, which has a characteristic peak at 0.108 Å^{-1}. Data are evaluated by a vertical rectangular filter with a width of 21 pixels which is shown in figure 2.2b.

The sample was fixed between two Kapton foils with thickness of 0.1 mm each. This is necessary due to the very small size and the high fragility of samples. Kapton foil scatters very low and produces only insignificant constant background.

2.2 Small angle neutron scattering

In addition to X-ray scattering, neutrons are a useful tool for investigation of soft matter probes. A neutron is an uncharged elementary particle with a mass of $1.675 \cdot 10^{-24}$ g, spin 1/2 and magnetic moment of -1.923 nuclear magnetons. Due to weak interaction inside the particle, free neutrons are not stable and decay into a proton, electron and antineutrino with a half life of approximately 10 minutes. The kinetic energy of neutrons is

$$E = \frac{1}{2}m\upsilon^2 = h\nu = \frac{h^2}{2m\lambda^2} \tag{2.36}$$

where υ is velocity of the neutron, ν, λ and m are frequency, wavelength and mass of the neutron correspondingly. Thus corresponding to the kinetic energy $E = k_B T$ and wavelength neutrons can be classified as cold, thermal and hot neutrons with average temperatures of 25K, 330K and 2000K correspondingly. The wavelength of these neutrons is in the same order as X-rays (Å) which is comparable

to interatomic distances. The energy range of neutrons covers the range of excitations in soft matter. Therefore, neutron scattering is a powerful tool for investigating structure and dynamics of soft matter probes.

The advantage of neutron scattering compared to X-rays is the possibility of contrast variation. Cross section in X-ray scattering is invariably bounded to the atomic number. In neutron scattering, the cross section can be varied by isotopic substitution which allows to create a scattering contrast between chemically identical molecules. This is widely used in small angle neutron scattering to investigate for example single polymer chain conformation.

This chapter will discuss peculiarities of small angle neutron scattering (SANS). The general scattering theory as well as theory of small angle scattering described in chapter 2.1 applies to neutrons as well as to X-rays. Here the key points which are special for neutron scattering only will be given. All SANS experiment were performed at Institut Laue-Langevin (ILL) in Grenoble, France. The experimental setups and primal data correction will be described in the end of the chapter.

2.2.1 Elastic neutron scattering: deviation from X-rays

Similar to X-ray scattering (eq. (2.9)) the differential cross section for neutrons can be expressed as

$$\frac{d\sigma}{d\Omega} = b^2 \tag{2.37}$$

where b is the scattering length of the nucleus. The value b is usually independent of the wavelength of incident neutrons. It depends not only on the element but also on the spin state of the nucleus-neutron system. In contrast to X-rays where the interaction of X-rays with an atom depends directly on the atomic number, the strength of the nucleus-neutron interaction depends on details of the nuclear structure, which is not simply related to the atomic number. Moreover, b differs between isotopes of the same element. The magnitude of the scattering length b is experimentally determined and can be found in special tables.

Another significant difference between X-rays and neutrons is the difference of size of atomic nucleus and electron cloud. In the case of neutrons, the wavelength of neutrons being scattered is orders of magnitudes bigger than the size of the nuclei it is scattered on. This results in a spherical symmetry of the scattering process on a single nucleus, and the scattering length does not depend on scattering angle. In the case of X-ray scattering, the equivalent to b is a product of the atomic scattering form factor $f(q)$ and the X-ray scattering length b_e which is θ-dependent (see eq. (2.9)). The atomic scattering factor decreases with q because the range of the atomic electron clouds is comparable to the X-ray wavelength. X-rays scattered from different parts of the atom have a phase difference which increases with increasing scattering angle [50].

Coherent and incoherent scattering

Since the nuclear interaction depends on the nuclear structure the scattering length b is different for isotopes of a certain element and also for different nuclear spin states. The scattered intensity can contain two components: one reflects the structure and the other one arises from random distribution in the scattering lengths of the individual nuclei. Consider the neutron scattering on one kind of atoms with scattering length b_j on fixed positions $\mathbf{r}_j$. The scattering amplitude as a function of scattering vector $\mathbf{q}$ can be written as

$$A(\mathbf{q}) = A_0 \sum_j b_j e^{i\mathbf{q}\mathbf{r}_j}. \tag{2.38}$$

Since the different isotopes are randomly distributed and spin orientation is random as well, we have to average over the random distribution of the scattering length in the sample. Taking into account that intensity is $I = A(\mathbf{q})A^*(\mathbf{q})$, the differential cross section can be expressed as

$$\frac{d\sigma}{d\Omega} = \sum_{k,j} \langle b_k b_j \rangle e^{-i\mathbf{q}(\mathbf{r}_k - \mathbf{r}_j)}. \tag{2.39}$$

The distribution of the scattering length on the different sites is completely uncorrelated unless $k = j$ which gives additional terms describing the mean quadratic deviation from the average:

$$\langle b_k b_j \rangle = \langle b \rangle^2 + \delta_{k,j} \left(\langle b^2 \rangle - \langle b \rangle^2 \right) \tag{2.40}$$

where $\delta_{k,j}$ is the Kronecker delta, which is equal to 1 if $k = j$ and equal to 0 if $k \neq j$. Therefore, the cross section can be rewritten as

$$\frac{d\sigma}{d\Omega} = b_{coh}^2 \sum_{k,j} e^{-i\mathbf{q}(\mathbf{r}_k - \mathbf{r}_j)} + N \cdot b_{inc}^2 = \left(\frac{d\sigma}{d\Omega} \right)_{coh} + \left(\frac{d\sigma}{d\Omega} \right)_{inc} \tag{2.41}$$

where

$$b_{coh} = \langle b \rangle \tag{2.42}$$

is the so-called coherent scattering length. The corresponding cross section $\left(\frac{d\sigma}{d\Omega}\right)_{coh}$ is called coherent differential cross section. This term contains the structure information and describes the scattering intensity in the case when all nuclei are identical and have identical scattering length.

The second term $\left(\frac{d\sigma}{d\Omega}\right)_{inc}$ is called incoherent differential cross section and has no structure information. It contains only the variance of scattering length which is called incoherent scattering length:

$$b_{inc} = (\langle b^2 \rangle - \langle b \rangle^2)^{1/2}. \tag{2.43}$$

Therefore, the total scattered intensity is a superposition of coherent and incoherent scattering. In neutron scattering experiments both are measured. The contribution of both components depends on the chemical structure of the sample. The strength of coherent and incoherent scattering can be adjusted by selective deuteration. Due to the big difference between cross sections of ^{1}H and ^{2}D certain contrast situations with a different contribution of coherent and incoherent scattering can be achieved.[1] Replacing protons by deuterons in the chemical structure of the samples is a widely used method in investigations of soft matter samples by neutron scattering. Depending on the aim of the experiment the sample can be mainly protonated or deuterated. Thus, for structure investigations of polymers by SANS the "useful" signal is contained in the coherent scattering component, while the incoherent scattering results in background only and should be minimized.

2.2.2 Experiments and instruments

SANS instruments

The general scheme of a SANS diffractometer is shown in figure 2.7. The incoming neutron beam is monochromatized by a velocity selector which transmits only neutrons with certain wavelength. After monochromatization the beam is collimated; the sample size is defined by an aperture with chosen shape to match the specific sample geometry. The scattered intensity from the sample is recorded by a position sensitive detector which is located inside an evacuated tube. Depending on the requested q-range the detector can be moved to a certain distance.

[1] ^{1}H: $\sigma_{coh} = 1.76 \cdot 10^{-24}$ cm^2, $\sigma_{inc} = 80.27 \cdot 10^{-24}$ cm^2; ^{2}D: $\sigma_{coh} = 5.59 \cdot 10^{-24}$ cm^2, $\sigma_{inc} = 2.05 \cdot 10^{-24}$ cm^2

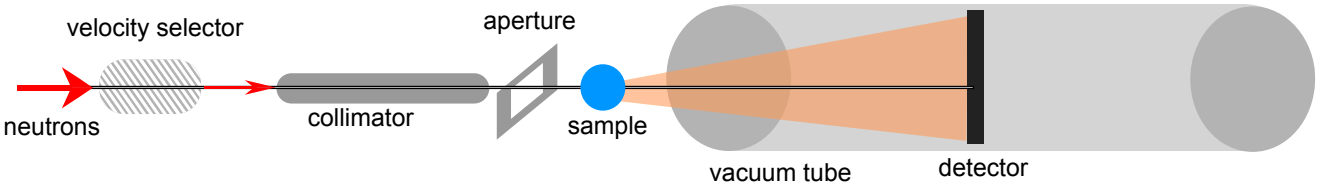

Figure 2.7.: Schematic illustration of SANS instrument

D11

D11 is a pinhole geometry instrument for SANS using cold neutrons and installed at the neutron guide H15 at the ILL. The neutron beam is monochromated by a helical slot velocity selector which selects neutrons in the range of $\Delta\lambda/\lambda = 9\%$. By varying the speed of the velocity selector neutrons with a wavelength λ between 4.5 Å and 40 Å can be obtained. Then the neutrons are collimated by a series of movable glass guides. The horizontal sample changer is situated 40 m from the velocity selector. Typical sample size is 10×10 mm^2. Neutrons scattered from the sample are detected by a position sensitive 96×96 cm^2 ^{3}He multi-detector at distances between 1.2 m and 39 m behind the sample. The accessible q range is $3 \cdot 10^{-4} \leq q[\text{ Å}^{-1}] \leq 1$. Maximum neutron flux at the sample is $1 \cdot 10^8$ n·cm^{-2}s^{-1}.

D22

D22 is a SANS instrument with a maximum flux at the sample of $1.2 \cdot 10^8$ n·cm^{-2}s^{-1}. D22 is situated at the cold neutron guide H512 at the ILL. The neutrons are monochromated by the velocity selector which consists of a 25 cm long rotating drum with helical lamellae shaped in a three dimensional mould. By varying the speed of the velocity selector neutrons with wavelength $4.5 \leq \lambda[\text{Å}\,] \leq 40$ with $\Delta\lambda/\lambda \sim 10\,\%$ can be obtained. The collimation system consists of eight guide selectors. Each selector has three tubes; any tube can be positioned on the beam axis. The collimation length can be varied in the range from 1.4 m to 19.1 m. The typical sample size is 10 to 300 mm^2. The ^{3}He multi-detector with an active area of 96×96 cm^2 movable in an evacuated tube with diameter of 2.5 m and length 20 m counts neutrons at variable distances from the sample from 1.1 m to 17.6 m. The accessible q-range is from $4.5 \cdot 10^{-4}$ Å^{-1} to 0.44 Å^{-1} without detector offset and 0.85 Å^{-1} with detector offset.

Data correction

The measured neutron intensity has to be corrected for background, detector efficiency, cell scattering and normalized to the standard scatterer in order to obtain the differential cross section. The coherent part of the differential cross section contains the structural information about the sample. Obtained data has to be normalized to the sample volume V to obtain the macroscopical cross section which is independent of the sample size.

$$I(cm^{-1}) = \frac{d\Sigma}{d\Omega} = \frac{1}{V}\frac{d\sigma}{d\Omega}. \tag{2.44}$$

For the normalization of scattering intensity the instrumental background, for example electrical noise or scattering from instrumental environment has to be taken into account. It is measured using B_4C instead of the sample. B_4C is a strong absorber of neutrons and stops the incident neutron beam. The obtained value is subtracted from the measured intensity of empty cell I_{cell} as well as from the total intensity (sample + cell) I_{total}.

To correct for the variation in the cell efficiency and normalize the scattering intensity in absolute units a standard (water) with known cross section is used. The typical standard for SANS is water which has a predominant incoherent scattering independent from the scattering angle. Scattering from the sample cell is taken into account by measuring scattering and transmission of the empty cell. The scattering intensity of the sample can be calculated using the following equation

$$I_{sample} = I_{total} - \frac{T_{total}}{T_{cell}} I_{cell} \tag{2.45}$$

where I_{sample}, I_{cell} and I_{total} are correspondingly scattering from sample, empty cell and total scattering of sample and cell together. T_{cell} and T_{total} are transmission of empty cell and cell with sample.

All experimental data was corrected by using ILL software LAMP and GRASP. Both programs include several steps [55]:

- Calculating the beam center for different configurations used
- Creating a detector mask
- Calculating transmission
- Creating radial filter in order to treat anisotropic scattering or perform radial averaging in the case of isotropic scattering
- Background subtraction and normalization to absolute units
- Merging the data from different configurations to get intensity over the full q-range.

Experimental details

The first experiment was carried out on the D22 diffractometer using a neutron wavelength of $\lambda = 6$ Å with three sample to detector distances 17.6m , 8 m and 2 m. (Collimations were 17.6m, 8 m and 2 m respectively). The chosen configurations covered a range of scattering vectors q from 0.003 to 0.45 $Å^{-1}$. Samples were measured in 1 mm thick standard quartz cells at room temperature. Data was not calibrated to absolute units due to very small size of samples and the undefined thickness of samples. Average size of the sample piece is 3×3 mm^2 with a thickness of around 100 μm. To maximize the scattered intensity several pieces of the sample were stacked in the sample cell. Data were radially averaged, corrected for electronic background and empty cell scattering using standard ILL software. Data from different detector configurations were merged without further transformations.

The second experiment was performed on the D11 diffractometer using a wavelength of $\lambda = 4.5$ Å with three sample to detector distances 20 m, 8 m and 1.2 m which covered a q-range from 0.007 to 0.7 $Å^{-1}$. Samples have a size of around 10×10 mm^2 but rather different geometrical shape. In order to obtain absolute intensity a cadmium mask was created. The mask represents a diaphragm of 4 mm diameter in a sheet of cadmium of 1 mm thickness. A single piece of sample was fixed on the cadmium mask and placed in the horizontal sample changer at room temperature. Data were corrected for electronic background, empty diaphragm scattering and normalized to absolute units. Data from different detector configurations were merged without further transformations. Correction for incoherent background is described in section 4.3.3.

3 Development of structure from PAOX template to CNT array

The alignment of CNTs in the array is a particularly important factor in fundamental studies and in applications, for example in microelectronics [56–58] and composite materials [59] including polymer composites[60–62].

One of the methods allowing to produce vertically aligned CNTs is chemical vapor deposition (CVD). The advantage of the CVD technique is its ability to control diameter and length of the CNTs during the synthesis of aligned CNT arrays. This technique allows to obtain CNT arrays with a size of several centimeters on different substrates [14, 63], for example silica, glass or quartz. Before the synthesis the substrate is covered by metal nanoparticles which serve as a catalyst. The size of nanotubes is controlled by the size of nanoparticles. Another promising way to obtain aligned CNT arrays is template assisted CVD [64]. Nanotubes are formed within each pore of the template. Subsequently, the template can be etched leaving a freestanding, aligned CNT array. Template assisted synthesis is a widely used method to achieve a certain arrangement of nanotubes in the array. Another advantage of this technique is the possibility of catalyst-free synthesis. The final nanotube arrays or composites do not contain metallic catalyst particles and do not need extra purification which can cause disorientation of CNTs [65, 66]. In this process a template of porous anodic aluminum oxide (PAOX) can be used [67].

After the CVD process, the CNTs are arranged in the array according to the arrangement of pores in the template. However, removing the template can introduce disorder in the structure of the CNT array due to interaction between CNTs. Additionally, amorphous carbon layers forming during the CVD process on the top and bottom of the array influence the structure as well. The tubes in the array can be prepared to be closed, partially closed or fully open.

In this chapter the structural characterization of carbon nanotube arrays grown in porous alumina templates will be discussed. We will follow the preparation process starting from the PAOX template. First, a short overview of the preparation of the PAOX template will be given since the structure of this template defines the structure of the CNT array and its polymer composites. PAOX templates are well known and have been investigated before, a more detailed description of preparation of PAOX can be found in literature [68, 69]. All these samples were provided by collaborators from the research group of inorganic and physical chemistry from TU Darmstadt. We will focus mostly on characterization of PAOX membranes by means of small angle X-ray scattering using the TDHL model function presented in chapter 2.1.3. The SAXS analysis is complemented by scanning electron microscopy (SEM).

Following the sequence of the sample preparation, after the PAOX template we will discuss the structure of the template with CNTs grown in its pores, the CNT array after etching of the template and finally the effect of removing the top and bottom carbon layers.

3.1 Nanoporous aluminum oxide templates - PAOX

The PAOX template is stable at high temperatures, which is important for the high-temperature synthesis of CNTs. It has high chemical resistance against organic solvents, but can be selectively etched with aqueous acids. Moreover, PAOX is transparent, flexible and contains mostly parallel straight aligned nanopores. Another advantage of using a PAOX membrane as a template for growing CNTs is the possibility to vary the size of individual alumina pores in a wide range between 10 and 300 nm. Arrangement, pore density and thickness of the template are controlled by the electrochemical synthesis conditions as

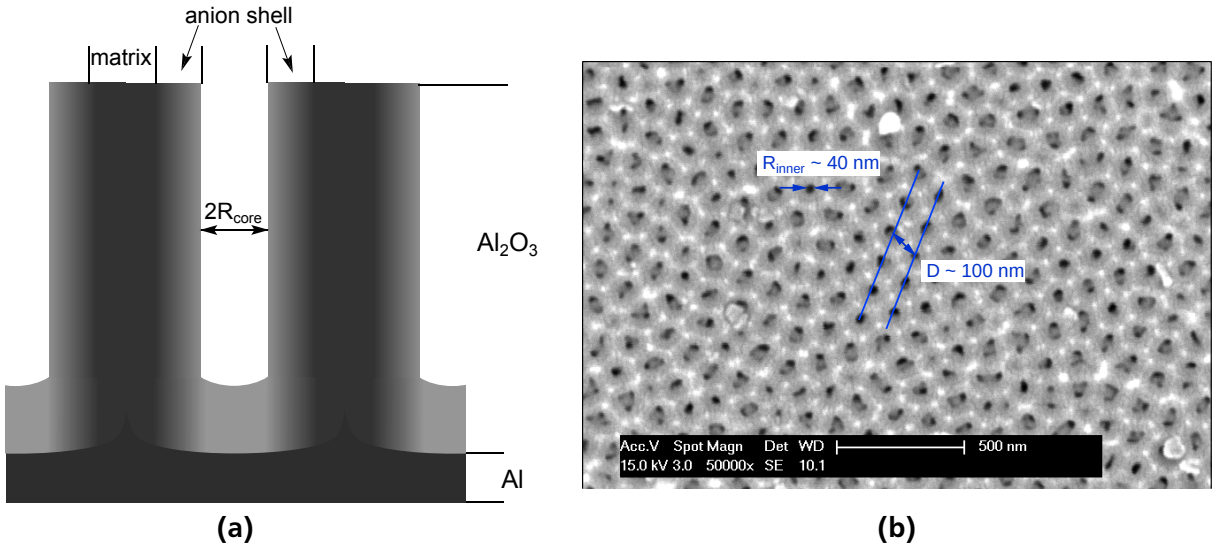

Figure 3.1.: Left: Schematic view of characteristics of the PAOX membrane according to the TDHL model function (see section 2.1.3). The pore radius is R_{core}, anion-contaminated alumina is R_{shell}, anion-free alumina corresponds to the matrix. **Right:** SEM image of the PAOX membrane representing hexagonal arrangement of pores.

well. Therefore, the morphology of the PAOX membrane can be completely specified during the preparation which enables the fabrication of a well defined vertical array of CNTs with a certain tube diameter, length and tube arrangement.

3.1.1 Preparation and structure of PAOX template

The PAOX template consists of highly ordered cylindrical pores with one pore in the center of each unit cell (fig. 3.1b) of a hexagonal lattice. Therefore, the arrangement of pores can be described in terms of the TDHL model function. In the first step of the preparation, an aluminium sheet (99.93%) with approximate thickness of 1 mm is degreased with acetone and annealed at 400 °C for one hour. This process smoothes the surface of the Al sheet from defects. Then the metal surface is electropolished in a solution of perchloric acid ($HClO_4$) in ethanol at 0 °C within 5 minutes. The typical current density for the electropolishing process is between 0.25 and 0.40 A/cm^{-2}. The voltage is the same as for the following anodization. Electropolishing is used for removing the roughness of the Al surface introduced during annealing. Anodization is performed in a mixture of 4% oxalic acid ($H_2C_2O_4$) and 4% sulfuric acid (H_2SO_4) in water under a voltage between 20-60 V. The concentration of acids as well as voltage can be varied in order to obtain porous templates with a different pore diameter and distance between them. The diameter of pores is directly proportional to the applied anodization voltage and can be controlled during the preparation. The anodization time varies between 12-24 hours, depending on the degree of pore opening. The anodization procedure can be repeated in order to obtain better arrangement of pores.

The pore walls consist of two different types of alumina. The first one is relatively anion pure alumina which forms the matrix of the hexagonal cell. In figure 3.1a this type of alumina is shown as dark gray area between pores. The region located directly around the pores contains less dense alumina contaminated with electrolyte anions since it is in direct contact with electrolyte during anodization. This alumina forms the pore wall and is represented in figure 3.1a as light gray anion shell. The structure

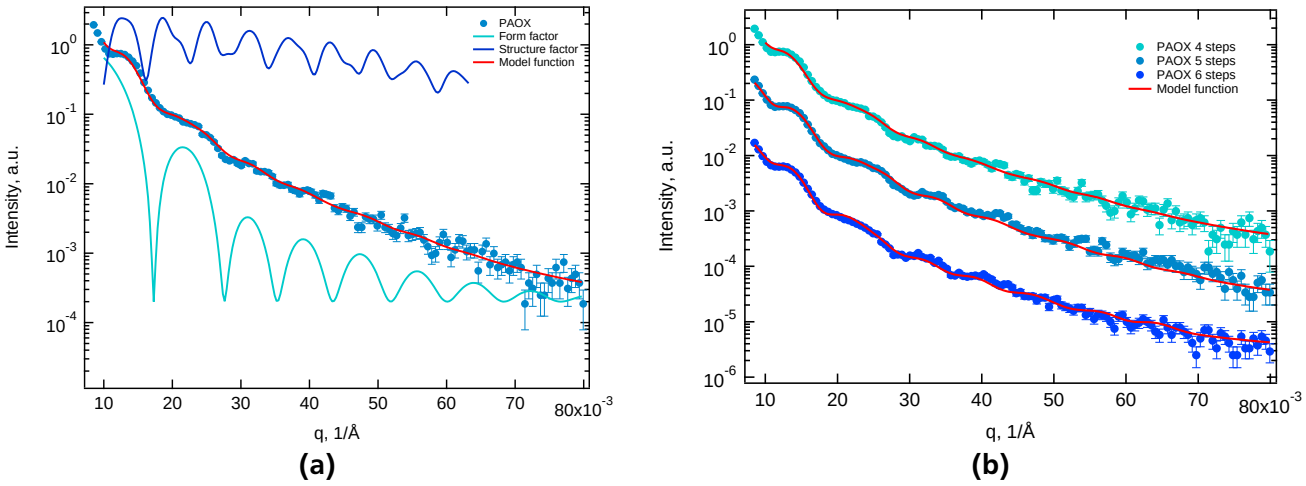

Figure 3.2.: PAOX template: a) Scattering pattern of PAOX with 4 steps anodization including form and structure factor; b) Scattering curves of PAOX template with 4, 5 and 6 steps anodization with fit according to model function described in section 2.1.3.

of the PAOX template is shown in figure 3.1b[1]. Therefore, PAOX consists of core-shell cylinders arranged in a hexagonal lattice and can be described by the TDHL model function.

Using SAXS we correspondingly find a profile displaying three well resolved maxima which represent a superposition of Bragg peaks of the structure factor (eq. (2.28)) and peaks of Bessel functions in the form factor (eq. (2.23)). This result is displayed in figure 3.2. The full red line in this plot corresponds to a fit of the model described before. Figure 3.2a shows form and structure factor together with the total scattering profile. This plot demonstrates that observed maxima can be clearly identified as a result of form and structure factors. The intensity between peaks is caused by the contribution of Laue scattering that depends on form factor only. The contribution of the structure factor is stronger at low q and the first observable peak mostly corresponds to the hexagonal arrangement of pores and can be used for preliminary estimation of distance between pores. According to SEM data (fig. 3.1b) the expected distance between pores is 100 nm which corresponds to the first Bragg-peak at $q_{max} = 4\pi/\sqrt{3}D \approx 0.0072$ Å^{-1} situated below the lower limit of the laboratory instrument. Figure 3.2a thus shows the scattering curve starting from the second Bragg peak which is well resolved in the scattering pattern. At high q the contribution of form factor is getting stronger and the single pore dominates the scattering.

The PAOX membrane is well described by the model of cylindrical pores of 23 nm radius. Structural parameters[2] of this fit are compiled in table 3.1. The outer radius – the radius of anion shell – is around 36 nm. The width of the radius distribution σ_i is around 25% of the inner radius. Such a high polydispersity can be explained by not ideal cylindrical shape of pores which can be seen in figure 3.1b. The fitted distance between pores is around 92 nm which is in good agreement with SEM results. In particular, for the fitting procedure we use a fixed electron density of the matrix, $\rho_{matrix} = 825$ e/nm^3 [31, 52]. The electron density of the cylinder shell ρ_{shell} is a fitted parameter and corresponds to the anionic shell caused by the electrolyte between pore and alumina itself [67]. As expected, ρ_{shell} is higher than ρ_{matrix} due to extra anions in the material. The value varies depending on anodization time and

[1] In contrast to figure 3.1a the gray scale is inverted. Black cycles corresponds to the pores and light gray color to the matrix.

[2] This is not a complete list of fit parameters. The fitting function also contains the parameters roughness, scaling factor (prefactor), structural prefactor, instrumental resolution and background. Last three parameters are fixed. The scaling factor correlates to electron densities. This problem is discussed in the text. Roughness varies in the range of 1-3 nm depending on the sample.

Parameter	4 steps	5 steps	6 steps
R_i, nm	22.9 ± 0.5	23.3 ± 0.5	23.5 ± 0.5
R_o, nm	36.5 ± 0.5	35.8 ± 0.5	37.8 ± 0.5
σ_{R_i}	0.3 ± 0.01	0.28 ± 0.01	0.25 ± 0.01
σ_D, nm	1.9 ± 0.1	1.8 ± 0.1	1.8 ± 0.1
D, nm	96.9 ± 2	96.0 ± 2	99.3 ± 2
σ_{DW}, nm	2.09 ± 0.3	1.68 ± 0.3	0.94 ± 0.2
ρ_{core}, e/nm^3	(0)	(0)	(0)
ρ_{shell}, e/nm^3	1187 ± 5	1192 ± 5	1198 ± 5
ρ_{matrix}, e/nm^3	(825)	(825)	(825)

Table 3.1.: Fitting parameters of model fuction of core-shell cylinder particles (equation (2.23)) with TDHL structure factor (equation (2.28)) for PAOX templates: R_i – mean inner radius, R_o - outer radius, σ_{R_i} – polydispersity of inner radius, σ_D – roughness of the pore wall, D is mean cylinder distance, σ_{DW} is Debye-Waller factor, ρ_{core} – electron density of the core is fixed to 0 e/nm^3 for empty pores, ρ_{matrix} – electron density of the matrix is calculated and fixed during fitting $\rho_{\mathrm{matrix}} = 825 e/nm^3$. Electron density of the shell (ρ_{shell}) is fit parameter.

type of anions: the longer the time, the more anions are contained in the shell. Typical values are in the range of $\rho_{\mathrm{shell}} = 960 - 1200$ e/nm^3.

Another important parameter which describes the deviation of the pore arrangement from the ideal hexagonal lattice is the Debye-Waller factor σ_{DW}. Smaller values of σ_{DW} indicate a better arrangement of pores. The PAOX template has a relatively low σ_{DW} around 1-2 nm. This value as well as the "quality" of the hexagonal lattice depends on steps of anodization. Consequently, the PAOX template consists of parallel pores with broad radius distribution of around 25% of the mean radius. The pores are packed in a well defined hexagonal arrangement.

3.1.2 Impact of number of anodization steps on arrangement of pores

The morphology of the PAOX template is completely defined by parameters of the electro-chemical anodization like time, applied voltage, temperature and type of electrolytes. For example, anodization with sulfuric acid at a voltage of about 25 V yields self-ordered PAOX membranes with a pore diameter of 25 nm and distance between pores of 65 nm [70]. Using oxalic acid solution at anodization voltages of about 40V yields membranes with a pore diameter of 35 nm and distance of around 100 nm [70]. At the same time the arrangement of pores depends on the amount of anodization steps. The first anodization step is carried out in such a way that initially disordered nanopores self-assemble into a hexagonal lattice. The upper layer containing disordered pores is removed by selective wet-chemical etching. In this step, a prestructured aluminium sheet is obtained. In the next steps, it is anodized to the PAOX template [68, 70]. The long range order of the lattice of pores is usually increased with the number of anodization steps. Here the structure of PAOX templates prepared with four, five and six anodization steps will be compared. Scattering patterns of these membranes are shown in figure 3.2b and fitting parameters are compiled in table 3.1. SEM images (fig. 3.3) suggest a pore radius of around 40 nm for all three templates and distance between pores of around 100 nm. Moreover, a locally improving hexagonal arrangement of pores with increasing number of anodization steps is observed.

Comparing all three curves in figure 3.2b we can observe that more peaks are resolved with increasing number of anodization steps. The upmost scattering curve has three well pronounced maxima at 0.013 Å^{-1} and 0.0238 Å^{-1} correspondingly and one broad, weak peak at higher q. The other two curves represent five and six anodization steps and have four well resolved peaks each. The first two are situated at the same q as before, while the third maximum is shifted to lower q. A possible reason why more maxima can be resolved could be increasing long range order of pores or increasing electron

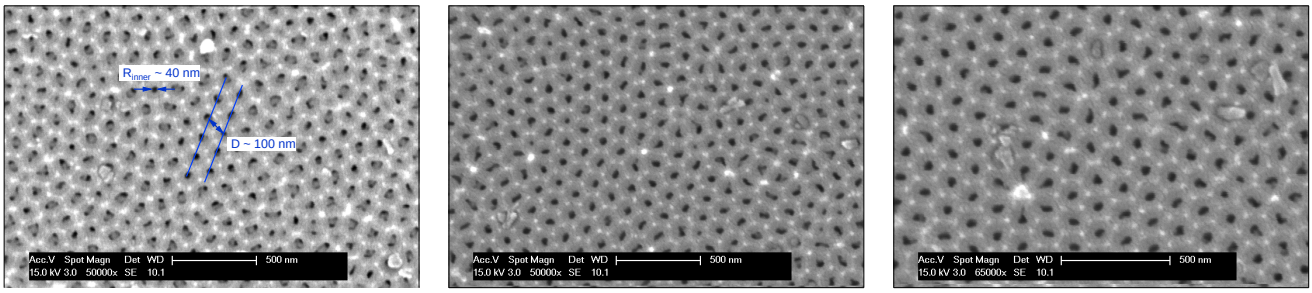

(a) **(b)** **(c)**

Figure 3.3.: SEM images of the PAOX template with four (a), five (b) and six (c) anodization steps. The scale mark is 500 nm.

density contrast because of longer contact of pore walls with electrolytes. On the other hand, according to fitting parameters (see table 3.1) the electron density of shell ρ_{shell} has almost the same value for all three templates and has no clear dependency on anodization time and steps. Other important factors which influence the shape and the amount of resolved maxima are polydispersity σ_{R_i} and roughness σ_D of the pores. As was shown in section 2.1.3, high values of σ_{R_i} smooth the maxima, and increasing σ_D results in an additional decay of intensity at high q. Both polydispersity and roughness are part of the form factor. A similar effect of intensity decay can be observed with variation of the Debye-Waller factor σ_{DW} which resembles to the disorder of the pores. σ_{DW} is contained in the structure factor and affects mostly the low q range (lower than the roughness in the form factor). Indeed within the narrow variation of these parameters they correlate to each other and simultaneous fitting can result in uncertain values[3] of σ_{DW}, σ_{R_i} and σ_D.

As we can see in table 3.1, all three templates have similar radii for core and shell with similar polydispersity. The number of anodization steps of the etching process does not affect the pore structure. The distance between pores does not change as well and is close to 100 nm for each template. At the same time the structure factor varies from curve to curve by a decreasing Debye-Waller factor with increasing number of anodization steps. Taking into account the correlation between σ_{DW}, σ_D and σ_{R_i} the same quality of the fit can be achieved with a slightly lower polydispersity and roughness, and correspondingly a higher Debye-Waller factor. For example, the six steps template can be fitted with σ_{DW} around 2 nm, $\sigma_{R_i} = 0.2$ and $\sigma_D = 1.4$ nm. Even though SEM images suggest increase of the hexagonal arrangement of the pores with increasing number of anodization steps, we can not directly conclude a significant difference in the pore arrangement between four, five and six steps of anodization from SAXS experiments. However, improving arrangement of pores in PAOX from two to four anodization steps was clearly observed using SAXS and reported by Engel [52]. Extending this result up to six anodization steps one observes that the hexagonal arrangement of the pores is not proportional from step to step. There is a clear difference between two and four steps, but we do not observe a significant indication of improving arrangement from four to six anodization steps.

[3] Uncertainties are expected to be higher than the ones shown in table 3.1. The uncertainty from the fitting process which is shown in table 3.1 are linear estimations, but the parameters have non-linear effect, due to correlations. Thus, a relative uncertainty of the range of σ_R is most probable inaccurate. Further if the "real" uncertainties strongly deviate from the fitting ones, they will be additionally discussed.

3.2 Preparation and structure of CNT arrays

3.2.1 CNTs grown inside PAOX templates

The aligned and parallel pores of the PAOX membrane can be used as 2D structured template for the growth of arranged CNT arrays by the non-catalytic CVD method [13, 67]. During synthesis of CNTs within the PAOX template, carbon precursors are deposited directly on the pore walls of PAOX by decomposition of hydrocarbons. One would expect the diameter of CNTs formed inside the PAOX template pores to be the same as the pore diameter of the template. However, certain PAOX properties like high polydispersity, roughness of the pore wall and not ideal cylindrical shape of pores can introduce some deviation of the CNT diameter from the diameter of pores in the template. The CVD process of CNT formation depends on a variety of experimental parameters such as pressure, temperature, reaction time, precursor gas flow rate and others. The importance of these parameters were discussed in many publications and can be found elsewhere [71–73]. Here a short explanation of the growth of CNTs will be given and some features of the CVD process which can influence the structure analysis of the CNT array will be pointed out.

A schematic overview of the growth of CNTs and obtaining the CNT/polymer composite is shown in figure 3.4. In a typical experiment of synthesis of CNTs inside a PAOX membrane by the CVD method the PAOX membrane is placed in a graphitic sample holder and introduced in an induction furnace. The PAOX template is fixed in the reactor tube perpendicular to the gas flow. Within 20 min the temperature is raised to 750 °C under Ar-atmosphere. After reaching the synthesis temperature, propene, the so called precursor gas, is added as a carbon source. The precursor gas transported by a carrier gas (Ar) is decomposed inside the hot-wall tube reactor. Propene penetrates into the PAOX pores, decomposes and forms nanotubes. Together with the growth of CNTs inside the PAOX template the deposition of amorphous carbon on the template surface is observed. The amorphous carbon layer is shown on the left side of the figure 3.4. This carbon layer is dense and hardly removable by chemical etching. It can prevent tubes from filling with polymer, but it helps to keep the hexagonal arrangement of CNTs in the array. Depending on reaction time two different types of structure can be realized: with short reaction time (5 min) CNT arrays with only a bottom layer of carbon (see right side fig. 3.4) can be obtained, while long reaction times (10 min) result in ordered CNT structures with a bottom and a top layer of carbon (see left side fig. 3.4). After switching off the flow of reaction gas, the system is cooled down to room temperature under argon gas flow. The bottom and/or top carbon layers can be removed by chemical/mechanical polishing, by ion beam milling, selective oxidation method [67] or plasma etching with oxygen leaving the CNTs [31].

The CNT/PAOX sample can then be characterized by SAXS in terms of the model function presented in section 2.1.3 with TDHL structure factor since all structure parameters like pore arrangement, radii and distance between pores corresponds to the PAOX template as described in the previous section. Nevertheless, growing CNTs inside pores of the template has a strong influence on the scattering curve. This is seen in the series of scattering patterns displayed in figure 3.5a. The observed maxima shift and change in their relative peak intensities. These changes are the consequence of the changes in the electron density contrast between core, shell and matrix when the CNTs are grown in the pores.

Ideally, for a precise description of the CNT/PAOX system an additional shell would have to be included in the model function. This shell would take into account the thickness of the CNT wall. On the other hand, including an extra shell in the model necessitates at least two additional fit parameters: thickness of CNT wall and electron density of this shell. Since the polydispersity of pore radius of the PAOX template is high and the model function already contains roughness and prefactor C (see eq (2.23)) as free fit parameters, including the extra shell does not significantly improve the model function, but makes the fitting procedure more complex. Moreover, in order to keep a consistent sequence of data analysis starting form the empty PAOX template up to CNT/polymer composites and for the sake of simplicity, it is good to use exactly the same model function in the fitting procedure. Thus, CNTs grown inside

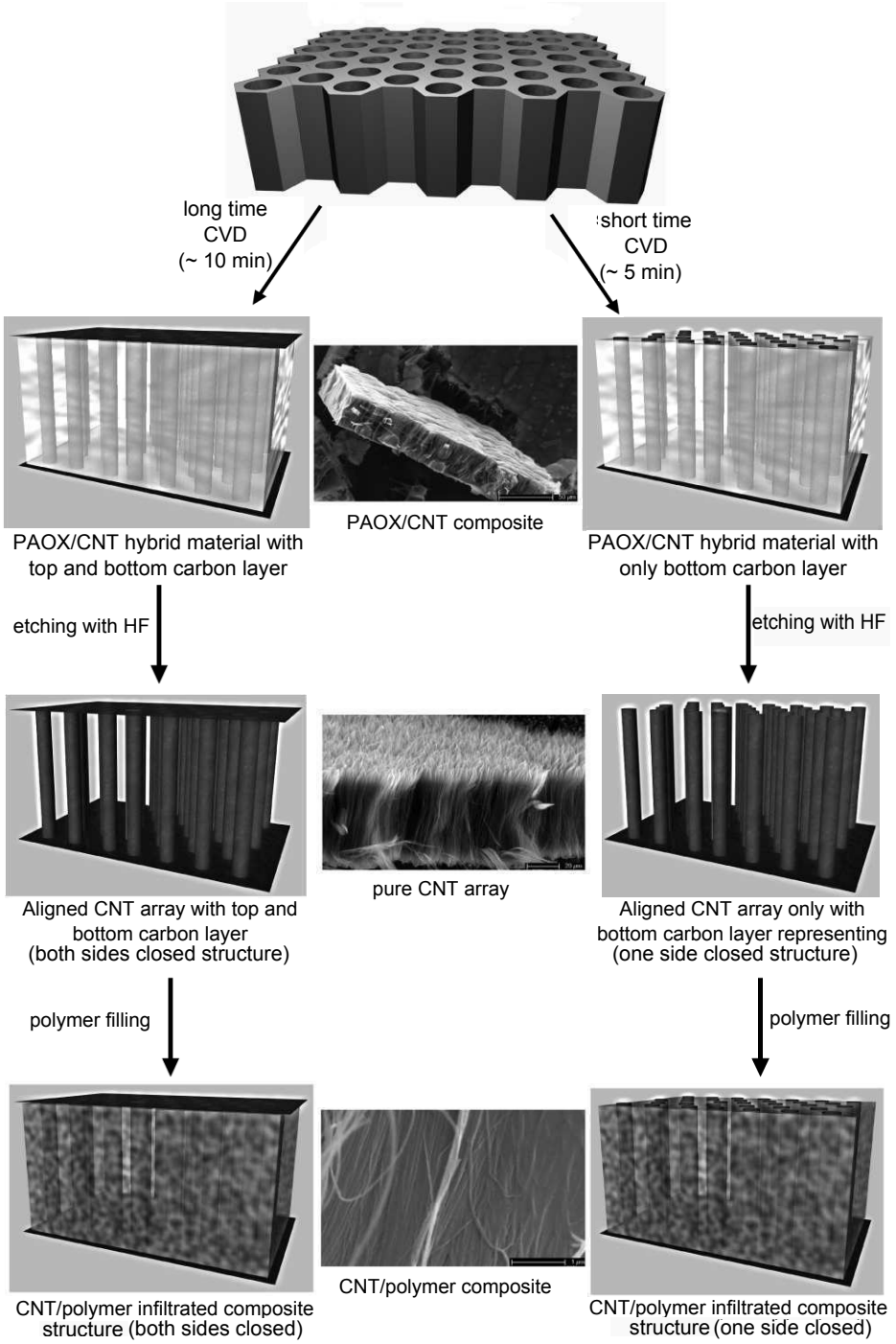

Figure 3.4.: The sketch shows the synthesis strategy for infiltration of aligned CNT arrays with polymer. Starting with the pure PAOX membrane (top) CNTs can be synthesised via a CVD process inside the pores of the PAOX template. Depending on the synthesis time a CNT array with only a bottom layer (right side) or with top and bottom layers of carbon (left side) is produced resulting in a PAOX/CNT hybrid material (step 1). Removing the PAOX template by etching with HF produces pure CNT arrays (step 2) which can then be infiltrated with polymer (step 3) giving the CNT/polymer composite. The different stages of synthesis process are illustrated by SEM micrographs in the center of the scheme.

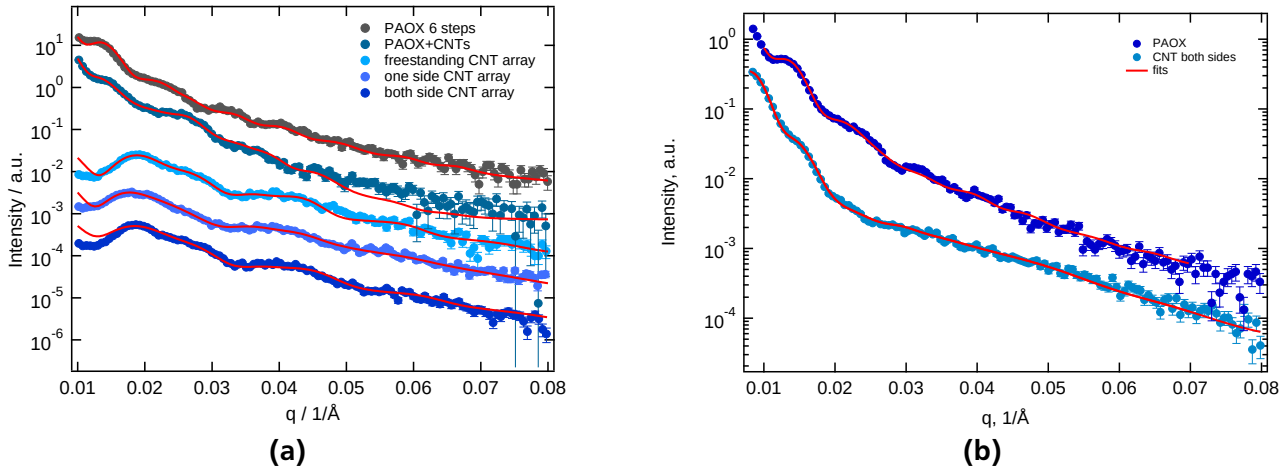

Figure 3.5.: SAXS curves with fit according to the model function: (a) (top to bottom) PAOX template, PAOX containing CNT into pores, freestanding CNT array, CNT array with one remaining carbon layer, CNT array with both remaining carbon layers. (b) (top to bottom) PAOX template anodized with oxalic acid, CNT array with both remaining carbon layers synthesized in oxalic PAOX . This array has tube separation of 87 nm which is close to the pore separation of the PAOX template.

pores are only taken into account by a modified electron density of the core ρ_{core}. We assume ρ_{core} to be homogeneous and close to the electron density of CNTs. However it is kept as fitted parameter in order to account for the internal core-shell structure of the CNT itself. The resulting ρ_{core} is 588 e/nm^3. This value is lower than the one expected for the carbon structure alone (632 e/nm^3) [74]. Additionally it should be remarked that the calculated electron density of CNTs corresponds to the electron density of CNT wall and does not include the empty core. Since the CNTs prepared by CVD are multi-walled (MWCNT) and structure of the wall is close to the structure of pyrolytic graphite the electron density of CNTs is calculated according to the general equation $\rho_e = n\rho_m N_a/M$. Here ρ_m is the mass density of pyrolytic graphite, N_a is the Avogadro constant, M is the molar mass of carbon and n is the number of electrons per carbon atom. ρ_m differs slightly in various literature, thus the expected value of the electron density of the CNT wall can be different. The deviation is around 15% of the mean value. In this work the mean value of mass density $\rho_m = 2.10$ g/cm^3 given in the work of Bose [74] is used. Moreover, the scale factor is not fixed in the fitting procedure which influences the absolute value of electron densities. In this way the uncertain definition of ρ_e of CNTs can be covered by the scaling factor.

3.2.2 Vertically aligned CNT arrays

Following the sequence of preparation of the aligned CNT array (fig. 3.4) we will now discuss the structure of the CNT array after removing the PAOX template. Depending on preparation conditions two different types of CNT arrays can be obtained during the CVD process: with carbon layer on one side (right side of the fig. 3.4) or with layers on the both sides of the array (left part of fig. 3.4). These carbon layers formed in the CVD process can be completely removed by plasma etching which allows to obtain a freestanding CNT array (center image in fig. 3.4). After removing of carbon layers the CNT/PAOX material is immersed into 48 % HF at room temperature for 3 hours and then into 24 % HF for several days. This process etches the PAOX template. The obtained CNT array is washed in distilled water and dried in air at 80 °C. Here, all three types of CNT arrays will be compared: freestanding and with remaining carbon layers on one or both surfaces of the array.

Parameter	freestanding CNT	one side closed CNT	both sides closed CNT
R_i, nm	16.9 ± 0.5	17.5 ± 0.8	17.8 ± 0.4
R_o, nm	20.6 ± 0.5	20.6 ± 0.5	21.5 ± 0.4
σ_{R_i}	0.25 ± 0.01	0.3 ± 0.02	0.3 ± 0.03
D, nm	42.0 ± 2	45.0 ± 2	51.6 ± 4.1
σ_{DW}, nm	3.4 ± 0.5	4.6 ± 0.1	12.2 ± 0.4
ρ_{core}, e/nm^3	(0)	(0)	(0)
ρ_{shell}, e/nm^3	(632)	(632)	(632)
ρ_{matrix}, e/nm^3	76 ± 6	76 ± 6	34 ± 5

Table 3.2.: Fitting parameters of model fuction for core-shell cylinder particles (equation (2.23)) with TDHL structure factor (equation (2.28)) for different types of CNT arrays: R_i - mean inner radius, R_o - outer radius, σ_{R_i} - polydispersity of inner radius, D mean cylinder distance, ρ_{core} - electron density of the core, ρ_{matrix} - electron density of the matrix. Electron density of the shell (ρ_{shell}) is the calculated electron density of CNT walls and kept fixed during fitting. σ_{DW} is Debye-Waller factor.

At first we consider the freestanding CNT array shown in figure 3.6a. One can observe that CNTs are not arranged in a precise hexagonal lattice anymore. The scattering pattern of the freestanding CNT array is shown as the third curve from the top in figure 3.5a. Comparing this pattern to those of the PAOX and PAOX+CNTs one observes a strong shift of the first maximum to larger q values. This maximum is related to the distance between CNTs as $q_{max} = 4\pi/\sqrt{3}D$. Therefore the mean intertube distance D is dramatically decreased. The pattern may be fitted with a model using a fixed electron density for the shell $\rho_{shell} = 632e/nm^3$ where ρ_{shell} is the electron density of the CNT wall. Ideally, the inner part of tubes and the space between CNTs should be described with $\rho_{core} = 0$ and $\rho_{matrix} = 0$. In order to simplify the fit procedure ρ_{core} is fixed to zero and ρ_{matrix} is left as free fit parameter. In table 3.2 ρ_{matrix} is not equal zero (76 e/nm^3). This could be due to some etched materials and organic products of the etching process which are not completely removed from the system. Another contribution to the non-zero ρ_{matrix} could be from broken parts of CNTs which can have random orientation in the array. These factors can contribute to ρ_{matrix} only, but not to ρ_{core}. The inner part of tubes can contain only some inhomogeneity of the inner surface of the wall due to decomposition of amorphous carbon which can be taken into account by roughness in the fitting function. Therefore, as the space between tubes is more likely to be perturbed than the core of CNTs, ρ_{matrix} is used as a free fit parameter while ρ_{core} is kept fixed.

The fit shows a separation of freestanding CNTs which is slightly above their diameter (table 3.2). This means that tubes bundle together and therefore long range order is lost. The bundling of CNTs is shown in figure 3.7a. Due to the strong van der Waals interaction between the tubes, CNTs are incorporated in micro clusters. Inside each cluster, the tubes can be modeled as hexagonally arranged, but at the same time the arrangement of CNTs in the total volume of the array could be far from hexagonal. In accordance with this picture we can observe that the Bragg peak is six times broader for the freestanding CNTs and for their composites than for the PAOX template, which is an indication of decreased ”quality” of the hexagonal arrangement. In contrast to bundling, a dense packing of CNTs without forming clusters is shown in figure 3.7b. This situation can be achieved by using CNTs with larger tube diameter or remaining carbon layers on top and bottom sides of the array.

A remaining carbon layer on one or both sides of the CNT array (see fig. 3.6b) can improve the separation between tubes, prevent bundling and keep their vertical alignment. Comparing the third and the last curve in figure 3.5a we observe that the first maximum of the both sides closed CNT array is sharper than the same maximum of freestanding CNTs. This shows that the long range order of the two-dimensional lattice in this system is slightly better. Fitting the scattering profile results in a mean intertube distance that is 10 nm larger than in the freestanding array (see table 3.2). Nevertheless,

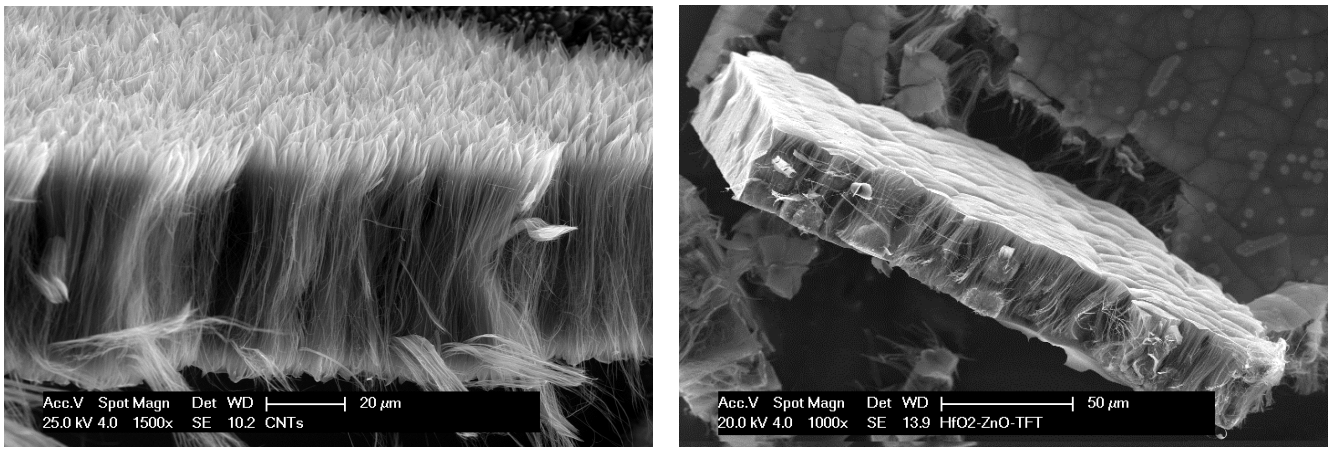

(a) (b)

Figure 3.6.: SEM images of (a) freestanding CNT array, (b) CNT array with a carbon layer on both surfaces of the CNT array.

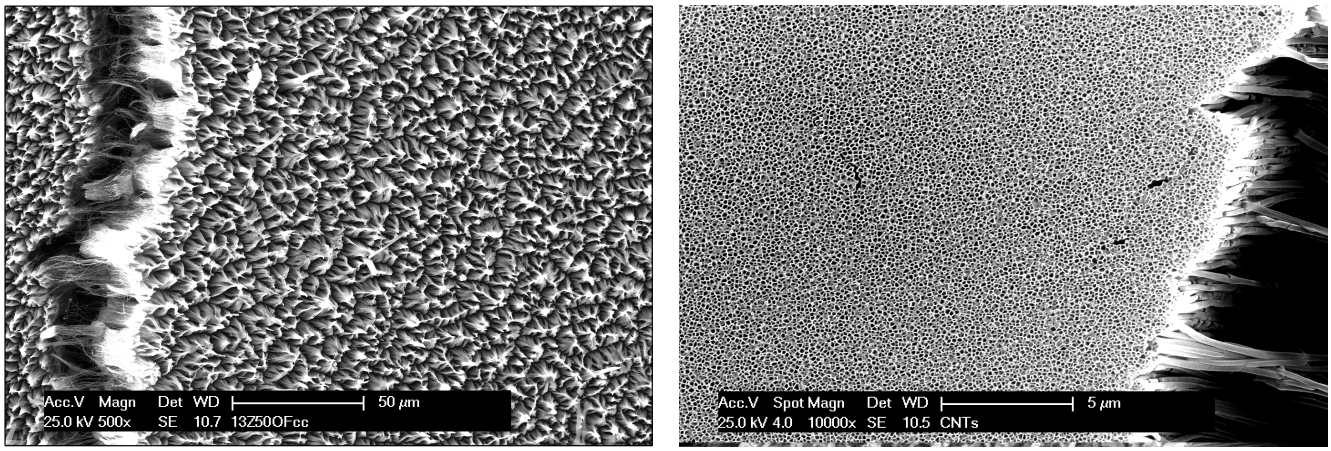

(a) (b)

Figure 3.7.: SEM images of (a) bundling of the freestanding CNT array (top view), (b) CNT array without bundling.

this distance is twice smaller than for PAOX. Obviously, without the PAOX matrix CNTs are attracted by van der Waals interaction. They may bend resulting in a reduced mean separation. The Debye-Waller factor for this CNT array is relatively large (12.2 nm) which indicates a strong deviation of the tube arrangement from hexagonal order. This can be explained by van der Waals attraction in the middle of the tube length. Since the tube aspect ratio is very high, CNTs are flexible along their length and tend to be bundled. Remaining carbon layers on the surfaces of the CNT array prevent bundling and keep tubes apart at both ends. Nevertheless, the centers of the tubes still attract each other, and due to very long length of tubes the CNTs can be curved in the middle of the length. The separation between tubes in this case is not constant along the length: near the carbon layers tubes stay apart, in the center the distance between them is decreased. The average distance between tubes was determined from the scattering profiles, and a detailed investigation of the tube separation was done using SEM.

Another situation is shown in figure 3.5b. The first curve represents the PAOX template anodized with a oxalic acid ($H_2C_2O_4$) only. This template has almost the same structural parameters as templates prepared with a mixture of oxalic and sulfuric acids. The inner pore radius is around 21 nm and the separation between tubes is 93 nm. The second curve represents the CNT array with a remaining carbon

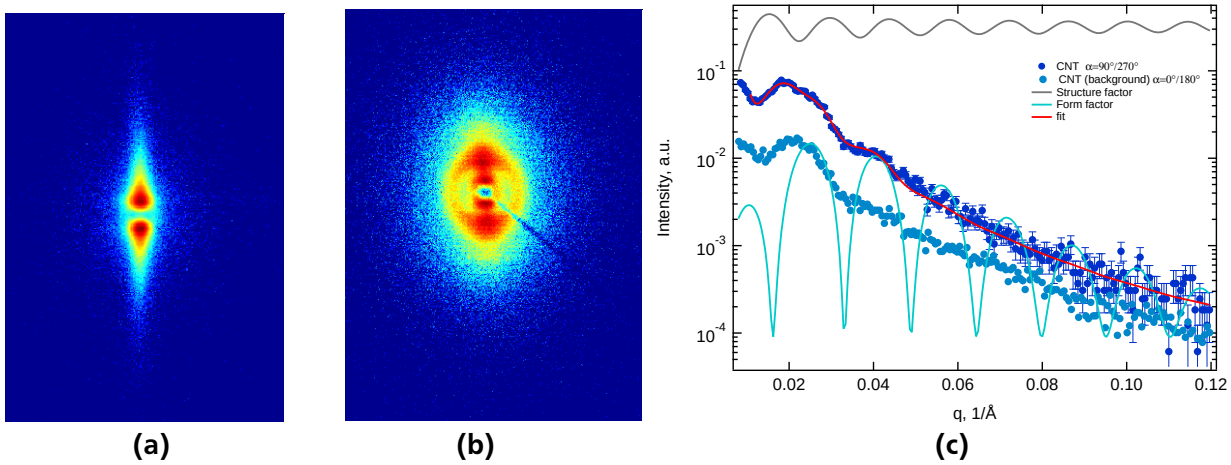

Figure 3.8.: **(a)** Detector image of PAOX template containing CNT inside pores; **(b)** Detector image of freestanding CNT array after removing PAOX template; **(c)** Scattering curves of CNT array along q_y ($\alpha = 90°/270°$) and background scattering along q_x ($\alpha = 0°/180°$) together with fit according to model function, form and structure factor.

layer on both sides prepared in this PAOX template. CNTs have smaller tube diameter than before ($R_{inner} = 7$ nm) and relatively thick walls ($R_{outer} = 17$ nm, thickness of tube wall is 10 nm respectively). In other words, these CNTs have more layers in their multi-wall. The separation between CNTs is around 87 nm which is very close to the original distance between pores of the PAOX template. CNTs with thick walls are less flexible and are not curved in the middle of their length. The disadvantage of this kind of arrays is a very high polydispersity of the inner radius (around 50%) which makes the array less attractive for polymer filling since tubes are not uniform. Another reason is the very small inner radius which can make future polymer infiltration more difficult.

With only one remaining carbon layer we obtain a result close to the freestanding CNT array (table 3.2). The separation between tubes is larger than for freestanding CNTs but still slightly above tube diameter. This means that tubes are bundled as well. Thus, all three types of CNT arrays keep a similar arrangement of nanotubes as nanopores in the PAOX template. Depending on remaining carbon layers CNTs have different long range order. Their mean separation increases in the presence of one or two layers of carbon.

Another important remark concerns a comparison of the detector image obtained for the CNT array and PAOX containing CNTs in its pores as shown in figure 3.8. The CNT array has a stronger contribution of isotropic scattering, and the scattering maxima are broader. This isotropic background comes from carbon layers on array surfaces and misorientation of a fraction of CNTs. Figure 3.8c compares the scattering curves of CNT array and isotropic background scattering that lies outside the q_y line. The background scattering is evaluated by a rectangular filter similarly to the "main" scattering of the array, but along the horizontal axis of the detector image ($\alpha = 0°$ and $180°$). The background scattering shows the q-dependence of the form factor and appears for all types of CNT arrays. Since the background scattering reproduces mostly the form factor, it indicates a small fraction of misoriented CNTs.

3.3 Summary and conclusions

In this chapter, the preparation sequence starting from the PAOX template to the pure CNT array was investigated by SAXS and described in terms of a model function of core-shell cylindrical tubes arranged in a hexagonal 2D lattice. We found good agreement of the resulting parameters for the PAOX template obtained by SAXS with data obtained by SEM: radii, tube separation and local order of CNTs. The

investigation of PAOX templates with four, five and six anodization steps shows that the quality of order has a limit. We do not observe a clear dependency between arrangement of the pores and the number of investigated anodization steps. The structure of templates does not significantly vary with increasing number of anodization steps.

Aligned CNT arrays were prepared inside the hexagonally ordered pores of the PAOX template using CVD. Three different types of arrays were synthesized: freestanding, and with a carbon layer on one or both surfaces of the array. Structure of CNT arrays as well as PAOX templates was investigated using SEM and SAXS. Scattering profiles of PAOX templates as well as CNT arrays were described using the TDHL model function. Although the hexagonal packing of the CNTs is only preserved on local scale we were able to describe the SAXS profiles based on this model. The structural changes during the preparation process from the empty PAOX templates to aligned CNT arrays could thus be consistently described. The separation between CNTs decreases dramatically after etching away the PAOX template. We have found that tubes are affected by van der Waals attraction and bundled into clusters. This effect is stronger for freestanding tubes than for CNTs with remaining carbon layers. The remaining carbon layers on the array surfaces preserve part of the original order.

4 Imbibition of polymers in CNT arrays

In order to make use of the exceptional properties of CNTs they can be applied in fabrication of composite materials, especially in polymeric matrices [60–62]. Their large aspect ratio serves to promote stress transfer from the polymer matrix to CNTs. Moreover, CNT/polymer composites have improved physical properties and have a great potential for applications in electronics. For example only 1% by weight of nanotubes can increase the elastic modulus by 25% [75, 76]. The distribution of the nanotubes in the material is a critical parameter for its performance. It is therefore of great importance to understand the mechanisms governing the mixing process. As was already mentioned, the alignment of nanotubes is a critical factor and difficult to control experimentally.

This chapter summarizes the preparation and structure of CNT/polymer composites based on aligned CNT arrays which were analyzed in the previous chapter. After characterization of the structure of composites the imbibition of polymer into CNT arrays and filling kinetics will be presented.

In the last decade the problem of preparation of oriented CNT/polymer composites has been extensively studied. Oriented CNT/polymer composites have been prepared using different methods, like capillary-driven wetting, spinning, electric and magnetic fields, and solution or melt infiltration of CNT arrays that are nearly perfectly aligned [26, 28, 31, 32, 77, 78]. This part of the thesis is focused on the two last-metioned methods: filling in solution and in melt.

Following the analysis from the previous chapter, the filling of freestanding and of one or both sides closed CNT arrays will be described. In the first section the characterization of filling of CNT arrays with polymeric solution will be presented. The second section will be focused on the infiltration in melt. A combination of scattering techniques and microscopy is used for detailed description of the structure of composites. In the last section the filling kinetics of CNT arrays will be considered. We will discuss in-situ SAXS measurements during polymer infiltration in the whole array as well as into the tube interior only.

4.1 Polymer infiltration in solution

In principle, the infiltration of polymeric solutions into CNT arrays is a sufficiently simple experiment: the array is immersed in solution with subsequent evaporation of the solvent. In order to attempt to infiltrate polymers into CNT arrays in our first experiments this way of infiltration was used. However, it is not trivial to predict the properties of this mixture. The problem of infiltration of solutions occurs due to the complex behavior of polymeric solutions. They consist of the polymer itself and a low molecular mass solvent. Therefore, the properties of polymeric solutions filled in CNT arrays can correspond to the polymer melt or to the low molecular mass liquid. In general, if the solution at first completely fills the tube, a polymer layer forms on the tube walls due to adsorption from solution [70]. The concentration of the polymer will affect the formation of polymeric nanostructures inside the array. Evaporation of the solvent will change the nature of the adsorbed polymer layer on the wall. If the solution behaves like a polymer melt, tubes are thought to be filled according to the precursor wetting mechanism [70]. In any case, this infiltration process is hardly controlled and will influence the morphology of the nanocomposites.

In this part of the work CNT/polymer composites are prepared by the solution infiltration method using a solution of polymer in tetrahydrofuran (THF). The used polymers are poly(methylmethacrylate) (PMMA) and polystyrene (PS) with molecular weights of 120 000 g/mol and 290 000 g/mol correspondingly. Different amounts of polymer are solved in the same amount of solvent (approx. 10 ml), yielding a series of different inital weight concentrations and initial viscosity. The amount of polymer used was 50 mg, 100 mg and 150 mg. It is not possible to determine the exact volume fraction of the polymer in

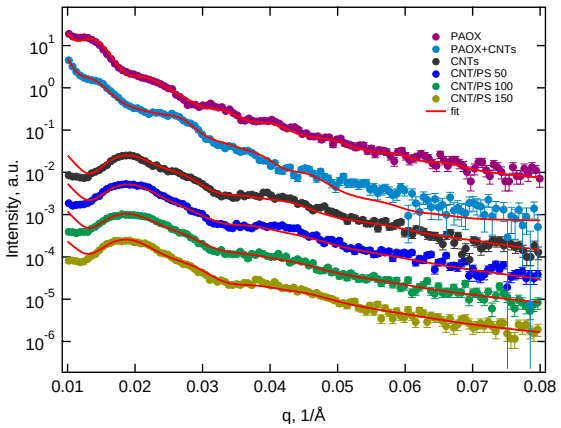

(a)

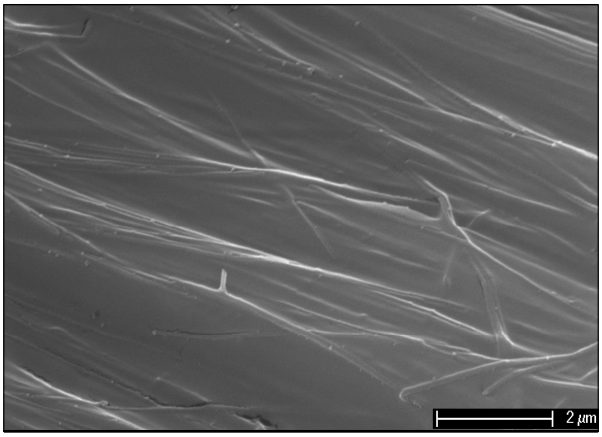

(b)

Figure 4.1.: (a) SAXS patterns of freestanding CNT array filled with PS solution. Quantity of PS in solution is 50 mg, 100, mg and 150 mg; **(b)** SEM image of freestanding CNT/PS composite filled with solution. Quantity of PS is 150 mg.

CNT arrays due to the initial low mass of CNTs. The polymer fraction in the CNT array corresponds to the electron density in the tube interior and in interstices between tubes, and therefore, it is determined only qualitatively. For this reason the concentration of polymer will be taken as the amount of polymer in the solution. After dissolving the polymer in THF, CNT arrays are immersed therein for 24-48 hours. In the next step CNT/polymer composites are dried at 50 °C for several hours in air.

4.1.1 Infiltration into freestanding CNT arrays

In this section we consider completely open tubes, without any carbon layers on top or bottom surfaces immersed in polymeric solution. In this case the array can be filled from any side (parallel and perpendicular to the tubes). Figure 4.1 shows the sequence of scattering patterns from the empty PAOX template to the CNT/PS composites filled with polymeric solutions at three different initial concentrations after drying. As was discussed in the previous chapter, after etching of the PAOX template CNTs are attracted to each other by van der Waals interaction forming clusters of freestanding tubes. This effect can be seen as the dramatical change from second to third curve from the top in figure 4.1. Usually clusters of CNTs do not have enough space between tubes and remain free from polymer. During the infiltration in solution the interaction between tubes can be reduced. In this case polymer flows inside the clusters. The last three curves represent the final CNT/PS composites dried in air. Infiltration causes an additional change of scattering curves. There is no variation of the pattern with the concentration of the polymer solution used. Again the same model function is applied (see section 2.1.3). We recover the same inner and outer radii of the CNT as for the empty array. The important change with polymer filling is the scattering contrast and the corresponding electron densities of matrix and core. The densities are much lower (see table 4.1) than the calculated electron density of PS, which is 340 e/nm^3. Therefore, polymer does not completely fill the CNT array in all three cases. In addition to SAXS, microscopy was performed by SEM shown in figure 4.1b It can be seen that the CNTs form clusters coated by polymer. Since the electron density of the matrix is lower than the density of PS we suppose that polymer does not flow inside clusters forms only a coating around the cluster as a whole. The Debye-Waller factor is twice as high as for the pure CNT array which indicates an increased static disorder with respect to the initial hexagonal arrangement of CNTs.

Another situation is observed in figure 4.2 showing results for CNT/PMMA composites. The scattering curve changes with different concentration of the PMMA solution. For the lower concentration the

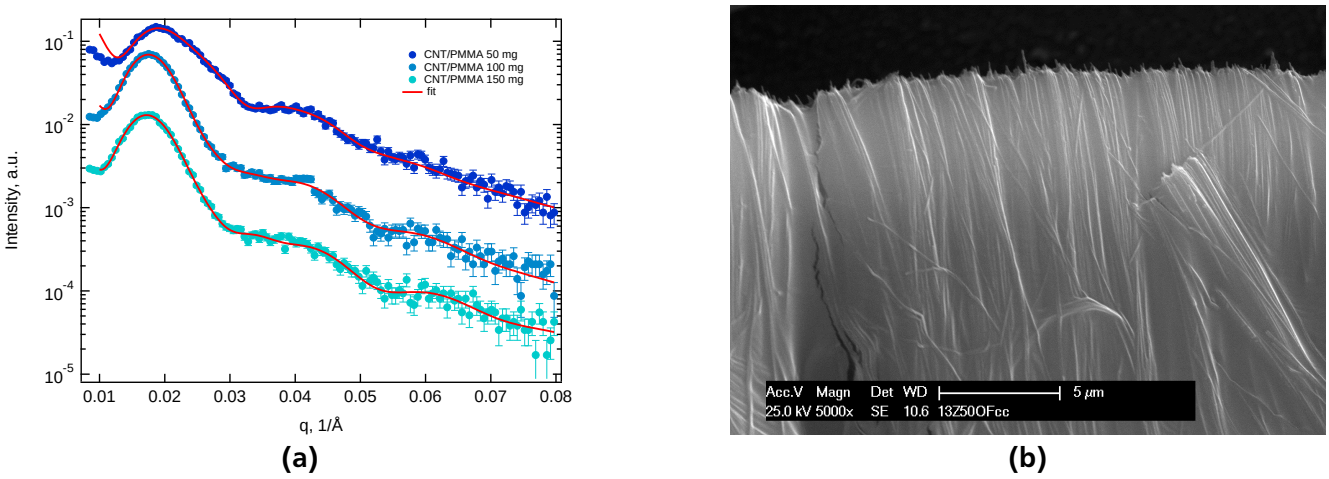

(a) **(b)**

Figure 4.2.: (a) SAXS patterns of freestanding CNT array filled with PMMA solution after drying. Quantity of PMMA in solution is 50 mg, 100 mg and 150 mg.; **(b)** SEM image of freestanding CNT/PMMA composite filled with solution after drying. Quantity of PMMA is 150 mg.

electron density of core is close to the electron density of PMMA (390 e/nm^3). In contrast to PS, PMMA fills the tube interior. A reason of this can be the smaller molecular weight of PMMA compared to PS. The smaller the molecular weight of polymer, the lower the viscosity of the solution is. The electron density of the matrix is higher than 390 e/nm^3 (tab. 4.1). A possible explanation of this result is the influence of the uncertain definition of the electron density of CNTs. This point was already discussed in chapter 3.2. Another possible reason is the contribution of broken fragments of CNTs to the average electron density of the matrix.

With increasing concentration of PMMA in solution both electron densities decrease. In figure 4.2 this effect can be seen as an increase of the relative peak height due to the higher electron density contrast between core, shell and matrix. At high concentrations we observe less polymer in the arrays. Possible reasons for this will be discussed in section 4.1.3. The tube separation is close to zero (difference between D and $2R_i$ is less than 1 nm). Therefore, tubes are strongly bundled even in solution, the polymer flows only between clusters and coats them. Since the tube separation for PMMA filled CNT arrays is smaller than for PS filled arrays, the matrix contains less polymer free volume and the average electron density is closer to the electron density of polymer than in case of PS. In other words, the coating layer of PMMA which is formed due to adsorption of the polymer from solution occupies more volume between tubes than the same layer of PS due to the smaller tube separation of the arrays filled with PMMA.

There is also a difference between the scattering profile of CNT/PMMA 50 and the ones obtained for the other two polymer concentrations which is caused by a different structure of tubes and not by the polymer infiltration. As shown in table 4.1 the wall thickness of CNTs in the CNT/PMMA 50 composite is 3 nm smaller than the thickness of the CNT wall for the other two samples (with 100 and 150 mg of PMMA). This results in the different shape of form factor as well as the total scattering profile.

In both experiments scattering curves are well described by the considered model function and do not show any evidence of the capillary flow. If the solvent behaves like a polymer melt, the solvent concentration affects only early stages of infiltration due to the different viscosity, and should not significantly influence the structure of the final composites. We suppose that polymer adsorption from solution is a very fast process and occurs as soon as polymer comes in contact with the CNT surface. A detailed discussion of the infiltration mechanism will be presented in section 4.1.3.

	PS			PMMA		
Parameter	**50 mg**[a]	**100 mg**	**150 mg**	**50 mg**	**100 mg**	**150 mg**
R_i, nm	16.2 ± 0.4	16.4 ± 0.5	16.4 ± 0.4	16.4 ± 0.5	16.3 ± 0.4	16.0 ± 0.5
R_o, nm	18.6 ± 0.8	18.6 ± 0.8	18.7 ± 0.8	19.6 ± 0.7	23.7 ± 0.8	22.3 ± 0.8
σ_{R_i}	0.25 ± 0.01	0.25 ± 0.01	0.28 ± 0.01	0.26 ± 0.01	0.24 ± 0.01	0.25 ± 0.01
D, nm	41.4 ± 2	44.4 ± 3	41.2 ± 3	41.1 ± 3	47.8 ± 5	46.8 ± 5
σ_{DW}, nm	7.8 ± 0.8	6.9 ± 0.6	8.0 ± 0.8	3.5 ± 0.3	5.4 ± 0.5	5.0 ± 0.5
ρ_{core}, e/nm^3	73 ± 4	42 ± 5	47 ± 5	388 ± 12	345 ± 15	297 ± 10
ρ_{shell}, e/nm^3	(632)	(632)	(632)	(632)	(632)	(632)
ρ_{matrix}, e/nm^3	166 ± 9	142 ± 8	172 ± 10	446 ± 17	415 ± 15	400 ± 15

Table 4.1.: Fitting parameters of the model fuction for core-shell cylinder particles (equation (2.23)) with TDHL structure factor (equation (2.28)) for freestanding CNT/polymer composites filled in solution: R_i - mean inner radius, R_o - outer radius, σ_{R_i} - polydispersity of inner radius, D is mean cylinder distance, σ_{DW} is Debye-Waller factor, ρ_{core} - electron density of the core, ρ_{matrix} - electron density of the matrix. Electron density of the shell ρ_{shell} is the calculated density of CNT walls and fixed during fitting.

[a] labels 50 mg, 100 mg and 150 mg correspond to the initial amount of the polymer in solution.

4.1.2 Infiltration into both sides closed CNT arrays

Now we consider CNT arrays closed from both sides. In this case the polymer infiltration is performed perpendicular to the long axis of the tube. The tube interior is not filled since the tubes are completely closed. Polymer can flow between CNTs only. Figure 4.3a shows the structural changes of the both sides closed CNT array after polymer infiltration. No variation of the scattering profile with the concentration of PMMA is observed. The first scattering maximum is getting broader due to increased broadness of the bragg peak indicating a decrease of the long range order. We do not observe a shift of the maxima and conclude that the separation between tubes does not change. According to the fit parameters the electron density of the matrix is much lower than the expected value of PMMA. This indicates that the polymer does not flow into the CNT array. This is supported by the SEM image shown in figure 4.4. The figure shows that the interspace between tubes is free from polymer.

A similar experiment was done with a CNT array synthesized inside pores of oxalic PAOX described in chapter 3.2 and shown in figure 3.5b. In this case the nanotubes have larger separation between each other (87 nm). Nevertheless, polymer does not fill this array either, according to table 4.2 the electron density of the matrix is again much lower than the electron density of PMMA and takes similar values as for above discussed composites.

4.1.3 Discussion

As was shown before, the polymer infiltration in solution proceeds in different ways depending on the structure of CNT arrays. No infiltration was observed in the case of both sides closed arrays. Apparently, the direction of infiltration plays an important role in the filling process. In the direction perpendicular to the long tube axis the CNT array has a nanoscopic porous structure and the infiltration should proceed due to the acting of capillary forces, which should drive the solution into the system. However, this could not be observed. A possible reason of this could be the adsorption of polymer near the entrance of the CNT array. Adsorbed polymer chains would block the volume in the beginning of the infiltration process and the solution could not penetrate into the array anymore. Polymer would be situated around the whole CNT array. However, this situation does not occur for the freestanding CNT array. In this case polymer is also adsorbed inside the array. The separation between tubes in the freestanding array is comparable to the both sides closed array shown in figure 4.3a and smaller compared to the CNT array

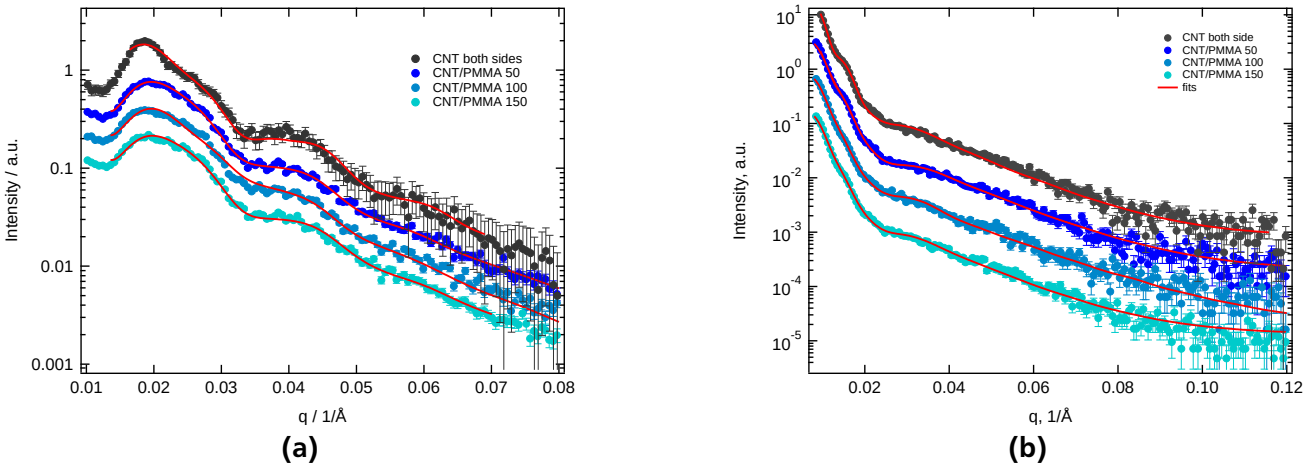

Figure 4.3.: **(a)** SAXS patterns of CNT array with remaining carbon layers on both surfaces of the array filled with PMMA solution after drying. Quantity of PMMA in solution is 50 mg, 100 mg and 150 mg; **(b)** same type of CNT/PMMA composites, but CNTs were synthesized in the oxalic PAOX (see fig. 3.5b).

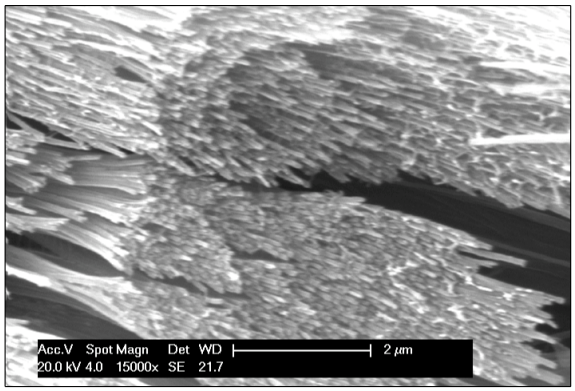

Figure 4.4.: SEM image of a cut through the both sides closed CNT/PMMA composite filled in solution. Quantity of PMMA is 150 mg.

synthesized in oxalic PAOX shown in figure 4.3b. The dramatic difference in the filling behavior could be due to the much slower speed of infiltration into the both sides closed system. During infiltration in solution two processes occur simultaneously: imbibition of solution into the array and solvent evaporation. The polymeric solution is getting more and more viscous over time and adsorption is expected to proceed faster and faster. In case of the freestanding CNT array the solution flows inside before adsorption starts. The flow perpendicular to the tube axis is much slower and adsorption starts before the infiltration takes place. The difference in the flow velocity can be explained in terms of different geometry of the filled volume. When the filling starts from the top of the CNT array (freestanding case) the volume to be filled can be assumed as a straight capillary, which means that the radius of the capillary does not change with filling height. If the filling process proceeds from the side of the array (closed tubes) the shape of capillaries is not constant along the length. In this case the "effective" radius of capillaries is smaller than the radius of the straight ones. It is well known that the flow is a balance between the capillary force ($\propto 1/r_{\text{eff}}$) and the viscous retarding force ($\propto 1/r_{\text{eff}}^2$) where r_{eff} is the effective radius of the capillary. As we can see, when the radius of the capillary becomes smaller the viscous retarding force increases faster than the capillary force and flow velocity decreases [79]. Moreover, the solution becomes more viscous

	CNT/PMMA shown in fig.4.3a			CNT/PMMA shown in fig.4.3b		
Parameter	**50 mg**[a]	**100 mg**	**150 mg**	**50 mg**	**100 mg**	**150 mg**
R_i, nm	17.5 ± 0.8	17.0 ± 0.6	17.4 ± 0.8	6.2 ± 0.1	6.5 ± 0.2	6.4 ± 0.2
R_o, nm	21.5 ± 0.4	21.5 ± 0.4	21.1 ± 0.4	16.4 ± 0.5	17.1 ± 0.7	17.3 ± 0.5
σ_{R_i}, nm	10.1 ± 1	10.0 ± 1	10.1 ± 1	4.0 ± 0.1	4.2 ± 0.1	4.0 ± 0.1
D, nm	41.4 ± 2	51.6 ± 4	51.1 ± 3	52.0 ± 4	87.6 ± 5	86.0 ± 5
σ_{DW}, nm	7.4 ± 0.5	7.1 ± 0.5	7.8 ± 0.5	11.1 ± 0.5	11.3 ± 0.5	11.4 ± 0.5
ρ_{core}, e/nm^3	(0)	(0)	(0)	(0)	(0)	(0)
ρ_{shell}, e/nm^3	(632)	(632)	(632)	(632)	(632)	(632)
ρ_{matrix}, e/nm^3	75 ± 5	80 ± 5	71 ± 4	68 ± 5	78 ± 5	80 ± 15

Table 4.2.: Fitting parameters of the model fuction for core-shell cylinder particles (equation (2.23)) with TDHL structure factor (equation (2.28)) for both sides closed CNT/PMMA composites filled in solution: R_i - mean inner radius, R_o - outer radius, σ_{R_i} - polydispersity of inner radius, D is mean cylinder distance, σ_{DW} is Debye-Waller factor, ρ_{core} - electron density of the core, ρ_{matrix} - electron density of the matrix. Electron density of the shell ρ_{shell} is the calculated density of CNT walls fixed during fitting.

[a] labels 50 mg, 100 mg and 150 mg correspond to the initial amount of the polymer in solution.

with time due to evaporation of the solvent, which additionally increases the viscous term in the force balance.

Now we consider the freestanding CNT array in detail. First of all we take a closer look on the fitting parameters of CNT/PMMA composites (see table 4.1). The electron density of core and matrix decrease with increasing initial concentration of the solution, which again can be explained in terms of the increased viscosity and the resulting decreased flow velocity. More polymer is adsorbed around the CNT array than inside the structure. Adsorbed polymer blocks the way to the tube interior and to the interstices between tubes. Since the infiltration is carried out at the room temperature which is lower than the glass transition temperature of the polymer, the adsorbed polymer chains immediately form solid polymer layer and prevent further infiltration.

If we consider CNT/PS composites, there is no systematic dependence on initial polymer concentration. PS solution does not fill the CNT array completely. However, Mahanandia at el. [31] have shown that infiltration with PS in solution gives results of an almost completely filled structure. This discrepancy can be explained by different preparation conditions. In general the CNT array is immersed into polymeric solution at room temperature for 24 hours. The fluctuation of temperature can significantly influence the rate of the solvent evaporation. The evaporation rate as well as the viscosity can be different from sample to sample and from experiment to experiment, that results in a different filling quality of the CNT array. Exactly the same situation is observed in the case of infiltration with PMMA solution. Different experiments give different results. All experiments on polymer infiltration in solutions are not well reproducible and the filling process is hardly controllable.

To summarize all observations on infiltration of polymeric solutions into CNT arrays we suppose that adsorption is the dominating mechanism of formation of the polymeric matrix in composites. Polymer adsorbed on walls of CNTs forms coating layers around clusters of nanotubes. The amount of polymer inside the arrays depends on many external factors as well as on the structure of empty CNT arrays.

4.2 Polymer infiltration in melt

This section summarizes results on filling of CNT arrays with polymer melt. This method is described in detail in the work of Boncel [32]. The advantage of filling in melt is the absence of any solvents in the final composite. No solvent evaporation has to be considered in this filling method. There is no adsorption mechanism, polymer is directly infiltrated into nanopores due to capillary forces. The filling

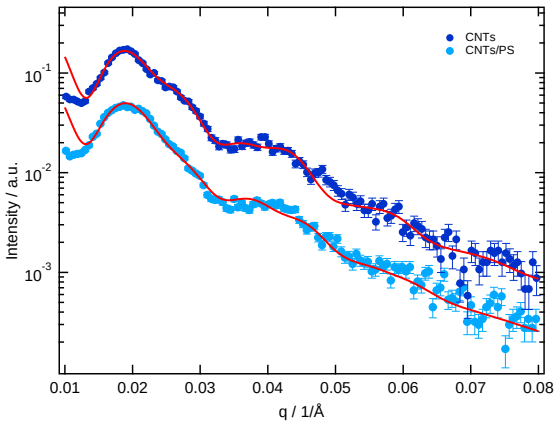

Figure 4.5: Scattering profiles of the empty freestanding CNT array and the array filled with molten PS.

process is well controlled and more reproducible. Moreover, filling in melt allows to apply time resolved SAXS and to analyze kinetics of the filling process.

Generally, for the melt infiltration with polymers into CNT arrays a thin polymer film is placed on top of the array. The system is then heated above the glass transition temperature of the polymer. For the infiltration with PS this temperature varies from 150°C to 200°C depending on molecular weight of the polymer. The polymer film is prepared from powder in advance by a high temperature press. CNT arrays filled with PS of molecular weights from 2000 g/mol to 290 000 g/mol with corresponding radius of gyration from 1 nm to 4.7 nm (calculated according to [80]) will be discussed here.

In this section we will focus on freestanding and one side closed CNT arrays since both sides closed arrays did not show any signs of polymer infiltration in solution earlier.

4.2.1 Freestanding CNT/PS composite

Freestanding CNT arrays contain fully open nanotubes, polymer can flow inside tubes as well as between CNTs. The infiltration of polymer in melt proceeds from one side of the array along the long axis of the tube. The polymer is expected to fill nanotubes continuously from top to bottom.

In the first experiment on freestanding CNTs, PS with molecular weight of 290 000 g/mol was used. The infiltration time was 24 hours in vacuum at 180 °C. Results of filling of the freestanding CNT array with molten PS is shown in figure 4.5. The top curve represents the scattering from the empty CNT array and the bottom curve shows results for the CNT/PS composite. By comparing this scattering pattern with the pattern of the empty CNT array no shifts of maxima are observed. This suggests that the polymer filling does not have any influence on the arrangement of tubes. We obtain the same intertube distance for the composite (see table 4.3) as for the empty CNT array. We recover the same inner and outer radii of nanotubes as well. However, the scattering profiles of the empty CNT array and CNT/PS composite are different due to the different electron density contrast. This is observed in the ratio between peak intensities and corresponds to the variation of the electron density of the core and the matrix. In particular, the second peak is slightly weaker and not well pronounced anymore. The fitted electron density of core and matrix are close to the calculated value for PS (340 e/nm^3). This indicates almost complete polymer filling of the array.

Since the empty freestanding CNT array shows clusters of the bundled tubes, one can expect that the polymer melt fills the CNT array in a similar way as a polymeric solution between clusters of the tubes. Since the separation distance between tubes does not change after the polymer infiltration, the polymer does not flow to the space inside clusters of CNTs which confirms that polymer successfully fills interspaces between small clusters and also flows inside nanotubes.

	freestanding		One side closed (fig. 4.6a)		One side closed (fig. 4.6c)	
Parameter	**CNT**	**CNT/PS**	**CNT**	**CNT/PS**	**CNT**	**CNT/PS**
R_i, nm	16.9 ± 0.5	16.2 ± 0.5	17.5 ± 0.8	17.8 ± 0.8	14.8 ± 0.7	15.1 ± 0.5
R_o, nm	20.6 ± 0.5	19.8 ± 0.5	20.6 ± 0.5	22.4 ± 0.7	22.5 ± 0.5	22.6 ± 0.8
σ_{R_i}	0.25 ± 0.01	0.27 ± 0.02	0.33 ± 0.03	0.25 ± 0.02	0.30 ± 0.03	0.33 ± 0.03
D, nm	42.0 ± 2	42.2 ± 2	45.0 ± 2	47.8 ± 4	44.5 ± 3	44.5 ± 2
σ_{DW}, nm	3.4 ± 0.5	3.6 ± 0.5	4.6 ± 0.1	7.4 ± 0.1	3.9 ± 0.1	4.1 ± 0.2
ρ_{core}, e/nm^3	(0)	342 ± 5	(0)	152 ± 10	(0)	292 ± 6
ρ_{shell}, e/nm^3	(632)	(632)	(632)	(632)	(632)	(632)
ρ_{matrix}, e/nm^3	76 ± 6	357 ± 5	76 ± 6	338 ± 20	97 ± 11	302 ± 15

Table 4.3.: Fitting parameters of model function for core-shell cylinder particles (equation (2.23)) with TDHL structure factor (equation (2.28)) for different CNT arrays and their polymer composites prepared by melt infiltration: R_i – mean inner radius, R_o – outer radius, σ_{R_i} - polydispersity of inner radius, D mean cylinder distance, ρ_{core} - electron density of the core, ρ_{matrix} – electron density of the matrix, ρ_{shell} – electron density of the shell, σ_{DW} – Debye-Waller factor

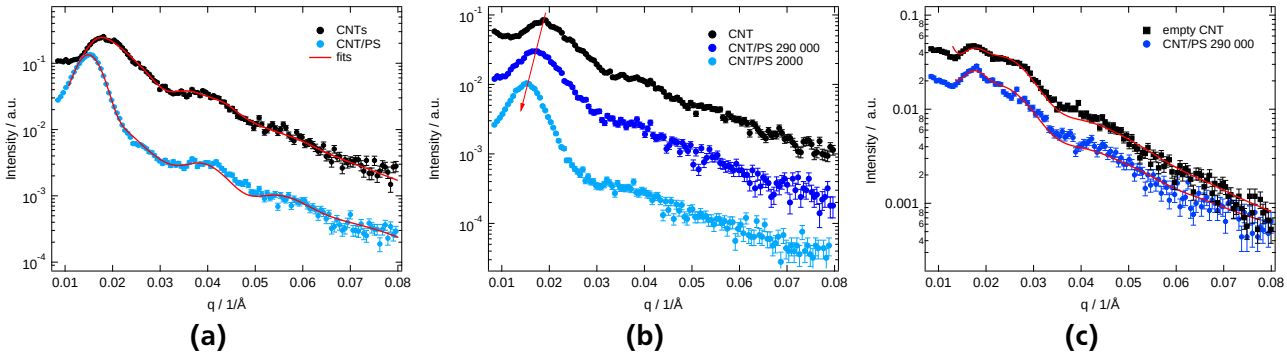

Figure 4.6.: SAXS profiles of **(a)** CNT arrays with a carbon layer on one side filled with molten PS M_{w} (2000 g/mol). Curves are shifted in vertical direction for better visualization; **(b)** Comparison of CNT/PS composites with high M_{w} (290 000 g/mol) and low M_{w} (2000 g/mol) of the polymer. The arrow shows the direction of the peak shift; **(c)** CNT arrays with a carbon layer on one side filled with molten PS (M_{w} 290 000 g/mol) (different experimental set). Curves are presented without vertical shift.

4.2.2 One side closed CNT/PS composite

CNT arrays with one side closed tubes were filled with PS of three different molecular weights: 2000 g/mol, 21 800 g/mol and 290 000 g/mol. Figure 4.6a displays SAXS data obtained for the one side closed CNT array and its composite filled with PS 2000 g/mol. In contrast to the freestanding array, the polymer infiltration into the one side closed array has a strong influence on the scattering pattern. First of all, the first maximum is shifted to lower q correspondingly indicating an increase of the separation between nanotubes in the array. CNTs are fixed on the carbon layer on one side which partially prevents the bundling of tubes. However, the tubes still attract each other due to van der Waals forces. Polymer flows into interstices between single tubes and reduces the attraction between them, correspondingly keeping the CNTs straight which increases the mean intertube distance. This effect is well observed in the SEM image shown in figure 4.7. The results of SAXS data analysis gives a difference of approximately 3 nm in intertube distance between the empty and filled system (table 4.3). The SEM image shows a quite homogeneous distribution of tubes and polymer in the composite. Less bundled clusters of CNTs than in freestanding arrays are observed. Looking back to the SAXS pattern, one observes that the shape of the first peak changes dramatically. The peak width becomes smaller indicating an improved alignment of

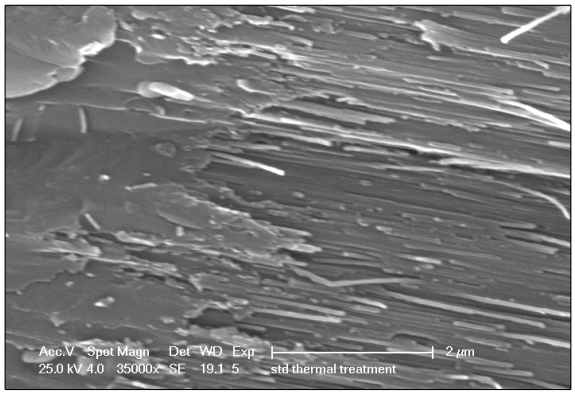

Figure 4.7: SEM images showing the cracked one side closed CNT/polymer composite to inspect the filling of CNT interstices with polymer. The CNT array is filled with PS 21 800 g/mol. In this sample with only one side closed tubes a compact structure can be observed after filling.

tubes. The peak intensity becomes significantly higher. As mentioned before, these changes are related to the variation of electron density contrast and give evidence of the polymer infiltration. Nevertheless, the fitted electron density of the core is lower than the electron density of PS. This indicates that the array is not completely filled, most probably due to insufficient filling time. At the same time, the electron density of the matrix is close to the value for bulk PS and we observe differences in filling of the inner part of tubes and interstices between tubes. The differences in polymer behavior inside and outside the tube occur due to differences in tube radius R and separation D between them. The separation between tubes is smaller than the radius of nanopores: $R_{inner} = 17.8$ nm, $R_{outer} = 22.4$ nm, and the mean distance is $D = 47.8$ nm. Since D is center-to-center distance (see fig. 2.3b) the separation between tubes is around 3 nm only. This means that capillary forces are stronger in matrix than in core and the polymer fills interstices between tubes more effectively. We note that the Debye-Waller factor (σ_{DW}) increases significantly as a result of polymer infiltration. We suppose that the polymer pushes nanotubes and introduces extra disorder in the hexagonal arrangement of tubes in the array.

A similar situation is observed in figure 4.6b representing the CNT array and its composites filled with PS of $M_w = 2000$ g/mol and 290 000 g/mol. After polymer infiltration the first maximum in both profiles is again shifted to lower q. The peak width becomes smaller and the peak intensity is higher. The shift and narrowing are even more pronounced for the polymer of the small molecular weight. PS of the low molecular weight has a lower viscosity and a higher mobility of polymer chains than the polymer of the high molecular weight . Thus, it fills the CNT array more effectively. However, investigation of large polymer chains confined inside CNT arrays is more interesting for the study of the conformation of polymer chains and their mobility under confinement.

Figure 4.6c displays CNT and CNT/PS composite filled again with high molecular weight (290 000 g/mol) of the polymer. This sample was prepared independently from the others in a different experimental series under the same preparation conditions. Now the scattering curve of CNT/PS 290 000 shows less changes than before (see figure 4.6b). The peak is not shifted, which means that the separation between tubes is unchanged after polymer infiltration. But changes of the scattering curve still have the same tendency as before: the first peak is slightly sharper and the second one decreases. However, we do not observe an increase of the first peak, the overall intensity decreases after polymer infiltration. The decrease of the scattering intensity corresponds to the decreasing electron density contrast and indicates filling of the array. Infiltration of polymer does not produce any structural changes of the CNT array in that sample. Tubes are strongly bundled which is shown in the very low separation between tubes ($D \approx 2R_{outer}$ within errors). The electron density of core and matrix is close to the value of the electron density of bulk PS, but still does not reach it. The rather high electron density of the matrix can occur mostly due to external contributions like broken fragments of CNTs and the arbitrary prefactor rather than due to polymer infiltration.

Although decreasing of the electron density contrast corresponds to the filling, in figures 4.6 (a) and (b) one observes growth of the first maximum, which also was interpreted as a change of the electron density contrast due to the polymer infiltration. Differences in the shape of scattering curves in figures

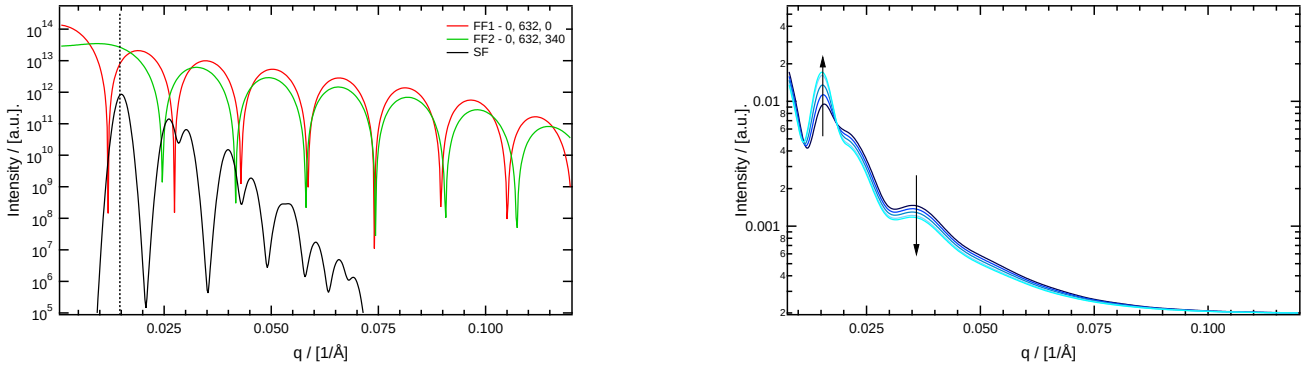

(a) **(b)**

Figure 4.8.: (a) Unsmeared form factor (eqn. (2.23)) with different electron densities of matrix: $\rho_{matrix} = 0e/nm^3$ for red curves and $\rho_{matrix} = 340e/nm^3$ for green curves with fitting parameters $R_{inner} = 17.8$ nm, $R_{outer} = 22.4$ nm, $D = 47.8$ nm which correspond to the CNT/PS composite shown in figure 4.6b; **(b)** The total scattering profile corresponding to the form factor shown in the left graph. Arrows show the direction of the change of the scattering curve with increasing electron density of core and matrix.

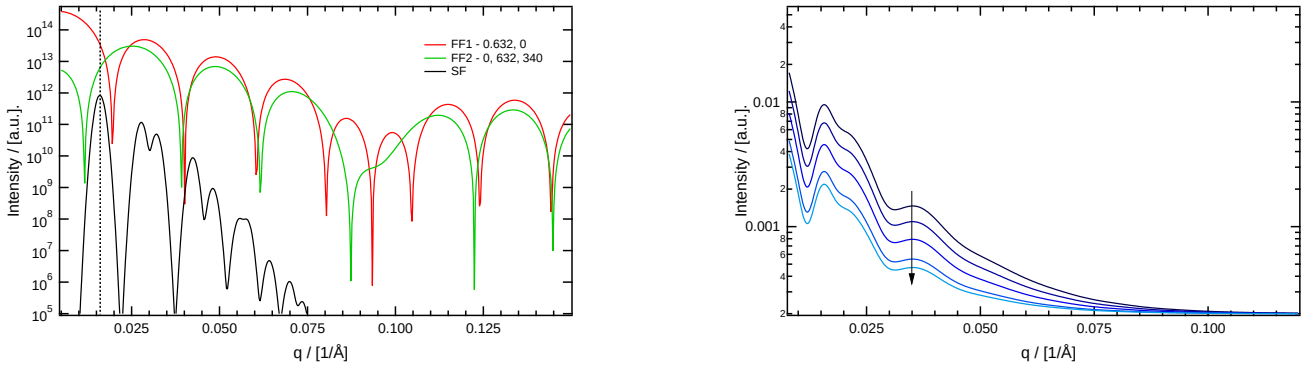

(a) **(b)**

Figure 4.9.: (a) Unsmeared form factor (eqn. (2.23)) with different electron densities of matrix: $\rho_{matrix} = 0e/nm^3$ for red curves and $\rho_{matrix} = 340e/nm^3$ for green curves with fitting parameters $R_{inner} = 15.1$ nm, $R_{outer} = 22.6$ nm, $D = 44.5$ nm which correspond to the CNT/PS composite shown in figure 4.6c, **(b)** The total scattering profile corresponding to the form factor shown in the left graph. The arrow shows the direction of th change of the scattering curve with increasing electron density of core and matrix.

4.6b and 4.6c can occur due to differences in inner and outer radii of initial nanotubes (see table 4.3) and correspondingly the differences in position of maxima of the form factor with respect to the first maximum of the structure factor. The total scattering intensity is a superposition of form and structure factors. The first observed maximum of the scattering profile is mostly defined by the first Bragg peak. The rest of the curve has a dominant contribution from the form factor. First of all, we consider the form factor only. Polymer infiltration results in the change of electron densities ρ_{core} and ρ_{matrix}. Both densities increase with infiltration which leads to the decrease of the density contrast between core, shell and matrix. Lower contrast results in lower intensity and the scattering intensity decreases with infiltration. This effect can be seen in figures 4.8a and 4.9a as a decrease of the green curve (after polymer infiltration) with respect to the red curve (before infiltration). One can observe that together with decreasing intensity the form factor is shifted along the q-axis after infiltration of the polymer. At

this point we consider the structure factor which is shown in figures 4.8a and 4.9a as solid black line. As we mentioned above, the first Bragg peak mostly contributes to the first maximum of the total scattering profile. This peak is marked as dashed black line. Since the structure of the CNT array does not change dramatically after polymer infiltration, the position of the first Bragg peak is almost the same [1].

Now we consider the filling situation shown in figure 4.6b which corresponds to form and structure factors shown in figure 4.8. Comparing the form factor before and after infiltration at the position of the first Bragg peak (dashed black line) we observe that in figure 4.8a the green curve has a plateau which has higher intensity than the slope of the red curve. It means that the product of form and structure factors after the polymer infiltration results in higher intensity than before the polymer infiltration, and subsequently the first maximum of the total scattering profile increases. The variation of the total scattering intensity for the described situation is shown in figure 4.8b. One observes that with increasing electron density of the matrix, the first maximum increases and the rest of the curve decreases correspondingly to the decrease of the form factor. Increase of the first maximum is observed only if $\rho_{\text{matrix}} > \rho_{\text{core}}$ because this difference results in the q-shift of the filled form factor with respect to the unfilled one. In all other cases the total scattering curve decreases uniformly with increasing electron densities.

Now we switch to figure 4.9 which corresponds to the filling of the CNT array shown in figure 4.6c. In contrast to the situation described above, we observe that both form factors – before and after the polymer infiltration – have a high slope at the position of the first Bragg peak (red and green curves in figure 4.9a). In this case the green curve has lower intensity than the red curve, this corresponds to lower intensity of the total scattering curve after infiltration. It means that after polymer infiltration the first maximum of the scattering curve as well as the rest of the curve decreases, which is shown in figure 4.9b.

These simulations of the behavior of the model function show that the total scattering curve depends on parameters of single tubes and relative positions of maxima of form and structure factors. The same physical process of polymer filling can lead to a different behavior of the scattering curve.

Although the fabrication of CNT/polymer composites via melt infiltration is also not perfectly reproducible and depends on the initial structure of CNT arrays, the filling process can be controlled and adjusted. Experiments on melt infiltration have shown that the remaining carbon layer allows to achieve a more homogeneous polymer filling with better distribution of the nanotubes in polymeric matrices.

4.2.3 Impact of tube diameter on filling mechanism

This section is focused on the discussion of polymer distribution inside the composite depending on tube diameter. Results for two different radii of gyration of the polymer will be presented. Here CNTs with relatively large diameter are considered and compared with the above described small tubes. We suppose that larger tubes keep better alignment and have larger separation between each other. As shown in the section above, smaller tubes have a small tube to tube distance and thus have less matrix volume available for polymer filling. At the same time the radius of gyration of the polymer also plays an important role in the filling process. The long chain polymer flows slower into the nanopores than the short one.

We use the one side closed CNT arrays with a tube diameter of around 90 nm. They are filled by PS of two different molecular weights (21 800 and 88 000 g/mol) with calculated radii of gyration $R_g = 1.26$ nm and 2.59 nm, correspondingly. The polymer infiltration is done at 180°C within 8 days in vacuum.

[1] In figure 4.6a and 4.6b we observe a significant shift of the maximum. It should be taken into account that this maximum consists not only of the Bragg peak, but also contains the peak of the form factor. Simply speaking, it is a double peak which contains the Bragg peak on the left side and form factor peak on the right side. The real shift of the structural peak is less pronounced than the shift observed in the figure and results in 3 nm increase of D. The dashed line in figure 4.8a represents the position of the Bragg peak before the polymer infiltration. This peak is expected to be at slightly lower q after polymer infiltration which does not affect the further discussion due to the constant level of the form factor (green line in figure 4.8a) in this q range.

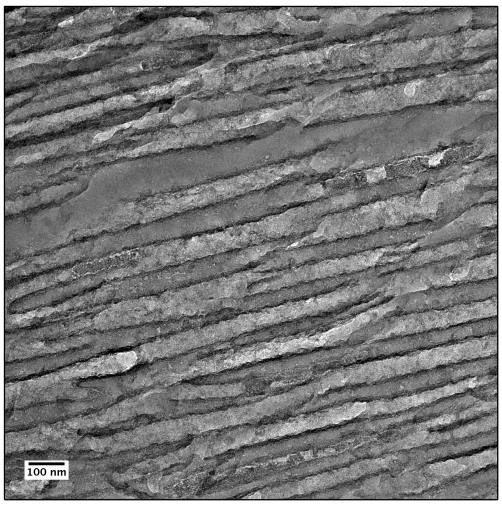

Figure 4.10: TEM of a cross section of CNT/PS composite material (tube diameter of 90 nm, M_w of PS is 88 000 g/mol) prepared by ultramictrotome cutting along the CNT tube axis. The parallel alignment of the tubes and the filling with polymer are observable.

Due to complexity of the model function we support the SAXS experiment with direct visualization methods like TEM and AFM which allow to obtain a local information about size and shape of tubes and polymer location. Moreover, the mean distance between tubes with $2R_{inner} = 90$ nm is over 100 nm and the first structural peak is situated below the limit of the SAXS instrument. Nevertheless, the experiment is sensitive to the form factor of the composites giving information about tube size and electron densities.

Figure 4.10 shows the cutting edge obtained by microtoming a CNT/polymer sample in vertical direction. In this way the CNT polymer interlayer structure becomes visible as well as the quality of polymer infiltration. It can be seen that the CNTs are fully embedded in the polymer and a good wetting has been achieved by the infiltration process. Some misalignment of the CNT/polymer structure is due to the mechanical cutting process of the sample which partly destroys some of its alignment.

For a more detailed investigation of the composite with large tubes we apply AFM (fig. 4.11a, 4.11b). Here we consider CNTs with PS 21 800 g/mol. In order to be able to look into the sample at various depths, we cleaved the sample diagonally at approximately 20 degrees to the surface. Fig. 4.11a and 4.11b show the topography and phase image of the same area of the sample, respectively. The topography image shows almost round objects with 20-60 nm in diameter (slight deformations might be caused by the cutting procedure). This is smaller than the sizes found in the TEM images for the tubes. As was reported before [72, 81], CNTs with large diameter are very flexible and can collapse along their length. This can result in bundling of tubes in an ideal parallel arrangement or in deformations at the end. A typical collapse pattern is the formation of one or two parallel tubelike arrangements caused by a collapse of the flat inner part. Typical sizes of such structures are 15-20 nm, consistent with structures seen in the AFM height image. Voids in between the tubes are clear to see, showing that filling of the matrix was not completely homogeneous. Since the center of nanotubes is filled by polymer, the collapse took place even before filling.

The AFM phase image (Fig. 4.11b) is sensitive to the elasticity of the material and therefore gives clear contrast between CNTs and the filler. The center of the tubes (PS) has a large phase shift (white), while the CNT wall shows up as a dark (low phase shift) ring of approximately 8 nm. This is only a rough approximation, as the true size is a deconvolution with the AFM tip shape (which is not known in detail). Further a second white ring with a larger diameter and thickness can be observed. This might be the precursor film of PS. Finally, the remaining black areas are the voids already visible in the height image. Several tubes show a double white center, again indicating that a considerable amount of tubes collapsed. Although we expect to observe a somewhat regular spacing in SAXS, the AFM images do not show a hexagonal packing. Some deviations might be caused by the preparation process.

Comparing microscopy and SAXS which is presented in figure 4.12 we observe that despite considerable disorder of CNTs in the array the scattering pattern can be fitted by our model function with a

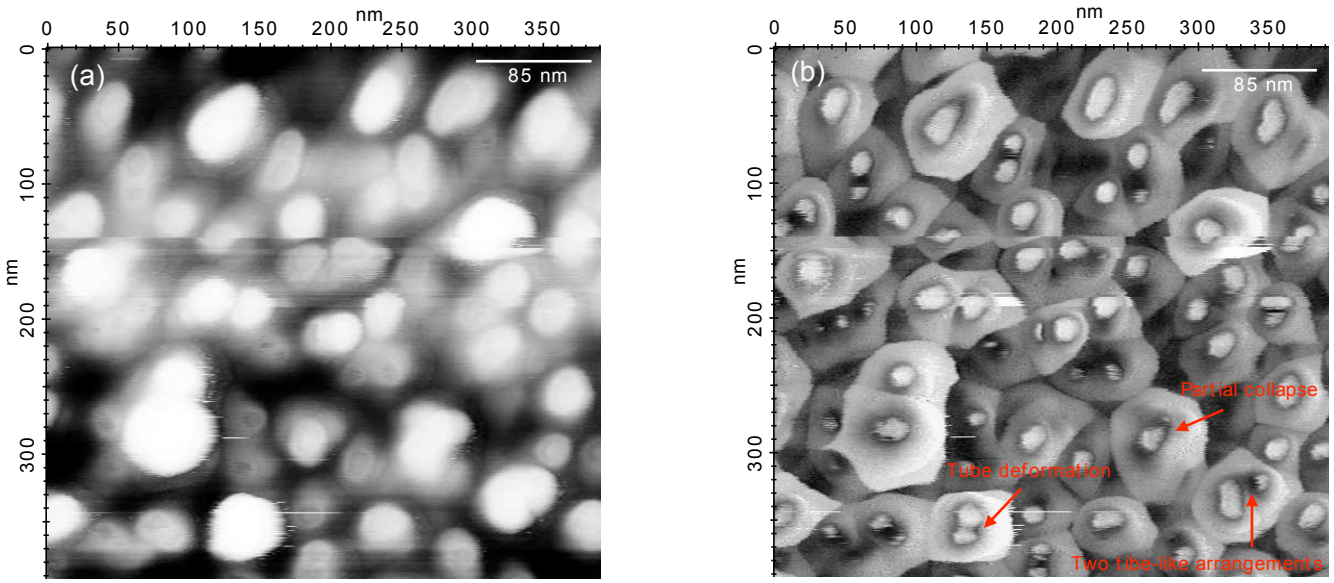

(a) (b)

Figure 4.11.: Polymer location in the composite: AFM of CNT 90/PS 21 800: a) height image b) phase image. The white mark of 85 nm in the upper right corner represents the average diameter obtaining by SAXS.

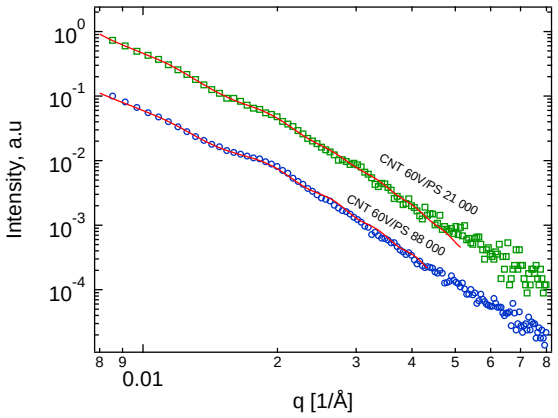

Figure 4.12: SAXS profiles of CNT/PS composites with diameter 85 nm and different M_w of PS

hexagonal structure factor. As we discussed above, the first structure peak is not visible due to large separation between tubes. The observable peaks in the scattering patterns are mainly caused by scattering of single tubes. For precise fitting the inner and outer tube radii are fixed based on TEM data (fig. 4.10). The collapse of tubes is taken into account by polydispersity of the inner radius, which is relatively high (approx. 35%). The deviation from hexagonal order results in a high Debye-Waller factor (6.5 nm). The fitted electron density of core is close to PS in all cases which indicates complete filling of the inner part of tubes. The electron density of matrix is close to the calculated value for PS as well, that means the matrix is almost completely filled.

In summary, CNTs with large tube diameter have an intertube distance comparable to the outer tube diameter. Comparing to smaller CNTs described in the previous section we observe the opposite situation in the filling process: the polymer fills the inner part of the tube more effectively than interstices between CNTs in the case of larger tubes. Since the tubes can be collapsed to tubelike arrangements with smaller diameter while the tube separating stays large (over 100 nm), the capillary forces are stronger in the core than in the matrix which supports filling of the inner part of the tube. At the same time the radius of gyration does not play an important role since it is still much smaller than the dimensions of the filled

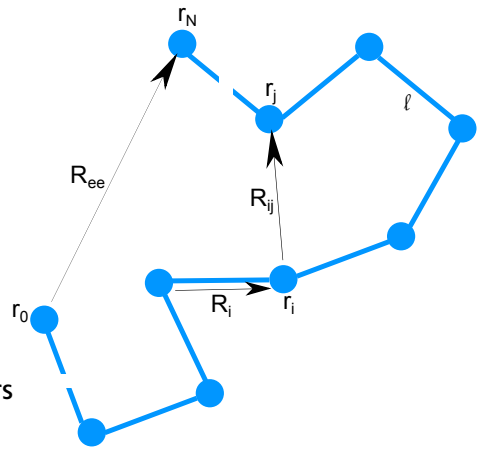

Figure 4.13: Sketch of the ideal polymer chain. All bond vectors have a constant length l

.

volume. Nevertheless we suppose that for small CNTs the size of the polymer chain is getting more significant due to smaller separation between tubes which is comparable to the radius of gyration.

4.3 Polymer chain conformation in CNT arrays

The conformation of a polymer describes the spatial arrangement of monomers of the chain and is governed by the interaction between monomers and the interaction of the chain with its environment. When the available volume (e.g., in pores of CNTs) is comparable to the size of the polymer chain the conformation is restricted [82]. Due to flexibility of the polymer chain the conformation can change under external conditions, the polymer chain can adopt to a variety of restrictions imposed by the confinement.

Typical polymers have a size in the nanometer range which is comparable to the radius of CNTs and separation between them in arrays. We can expect to see a difference in conformation between bulk polymer and polymer confined in the tubes. In this chapter the study of conformation of polystyrene chains in the CNT array will be presented. The conformation of PS chains is studied by SANS in order to investigate influence of CNT surface on conformation of polymer chains in the CNT arrays. Two experiments will be discussed: in the first experiment the CNT array is filled with PS inside the tubes and between them; in the second we will focus only on conformation of PS chains in the tube interior.

The first section will outline major theoretical aspects of chain conformation used in the experimental study later on. A detailed description and models of polymer conformation can be found in literature [83–86]. The subsequent section will explain the scattering from polymer chains which is directly applied in the SANS experiment. Finally in the last section the experiment and results on polymer chain conformation in the CNT array will be discussed. Experimental details and description of instruments can be found in chapter 2.2.

4.3.1 Characterization of polymer structure

The structure of a typical linear polymer chain is schematically shown in figure 4.13. The polymer chain is usually flexible and due to the flexibility monomers can be arranged differently in space. The arrangement of the monomers depends on the chemical structure as well. All possible arrangements of a polymer of its given chemical structure are called chain conformation. In order to describe the structure of the polymer chain we define positions of the independent segments which form the backbone of the polymer chain. Assume that the first segment is situated at the position $\mathbf{r_0}$ (fig. 4.13), the next one at position $\mathbf{r_1}$ and so on. The chain can be described by N bond vectors $\mathbf{R_i}$ which are defined as

$$\mathbf{R_i} = \mathbf{r_i} - \mathbf{r_{i-1}} \quad \text{with} \quad i = 1, 2, ..., N. \tag{4.1}$$

There are several parameters which can characterize the conformation of the polymer chain. One of them is the end-to-end distance R_{ee} which is simply the vector sum of all bond vectors:

$$\mathbf{R_{ee}} = \sum_{i=1}^{N} \mathbf{R_i}. \tag{4.2}$$

$\mathbf{R_{ee}}$ can vary from one individual chain to another as well as fluctuate over time for each of the chains. Usually the average end-to-end distance $\mathbf{R_{ee}}$ is a parameter which describes the structural features of the chain. For completely disordered systems without any preferential orientation the thermal average of $\mathbf{R_{ee}}$ is zero. The next moment of the end-to-end distance distribution (second moment $\langle R_{ee}^2 \rangle$) is nonzero after averaging:

$$\langle R_{ee}^2 \rangle = \langle \mathbf{R}_{ee} \cdot \mathbf{R}_{ee} \rangle = \sum_{i,j=1}^{N} \langle \mathbf{R}_i \cdot \mathbf{R}_j \rangle \tag{4.3}$$

which can be further rewritten as

$$\langle R_{ee}^2 \rangle = \sum_{i=1}^{N} \langle R_i^2 \rangle + 2 \sum_{1 \le i < j \le N} \langle \mathbf{R}_i \cdot \mathbf{R}_j \rangle. \tag{4.4}$$

The quantity $\langle R_{ee}^2 \rangle$ is usually used for characterization of the spatial extension of a linear polymer chain. The first term in equation (4.4) equals to the squared length of a single bond l^2 multiplied by the number of the bonds N. The second term describes the correlation between different bonds. In case of an ideal polymer chain these correlations are zero and the end-to-end distance can be simply expressed as:

$$\langle R_{ee}^2 \rangle = N l^2. \tag{4.5}$$

Another quantity which is widely used for description of the structure of the polymer chain is the radius of gyration, R_g. It measures the size of a polymer similar to a moment of inertia. The radius of gyration characterizes the average extension of a chain relative to the center of mass:

$$R_g^2 = \frac{1}{N+1} \sum_{1 \le i < j \le N}^{N} \mathbf{R}_{i,j}^2 \tag{4.6}$$

Where $\mathbf{R}_{i,j}$ is a vector between $\mathbf{r}_i$ and $\mathbf{r}_j$ bonds of the same polymer chain. The detailed mathematical calculation of the radius of gyration can be found in literature [50, 83, 84]. In case of the ideal polymer chain (no interactions between monomers) R_g can be written in the simple form:

$$\langle R_g^2 \rangle = \frac{N l^2}{6} = \frac{\langle R_{ee}^2 \rangle}{6} \tag{4.7}$$

R_g is smaller than R_{ee} since it describes the size of the polymer relative to the center of mass, whereas the end-to-end distance is the size of the whole chain.

4.3.2 Form factor of the gaussian chain

Definition of the gaussian chain

The simplest model to describe polymer structure is the model of the ideal chain. It assumes that the polymer follows a random walk and that there are no interactions between monomers. The polymer does not have specific shape, monomers are oriented randomly but still have bonds between them. The length of segments is assumed to be unique and equal to l. The gaussian assumption is that the local nature of the chain segments does not play a role in the global structure of the polymer chain. It is still possible to replace the chain segment in the model by any other kind of segments as long as the global structural properties are conserved [83]. In this case, the gaussian chain assumes that the segment length l_i which corresponds to the length of the bond vector $\mathbf{R}_i$, is not a constant and follows a gaussian distribution, where the standard deviation of the distance between the end points of the segments is identical to the effective segment length l [83] :

$$P(\mathbf{R}_1, ..., \mathbf{R}_N) = \left(\frac{3}{2\pi l^2}\right)^{3N/2} \exp\left(-\frac{3}{2l^2}\sum_i^N R_i^2\right). \tag{4.8}$$

Using the model of the gaussian chain allows us to easily calculate characteristic values of the polymer chain like radius of gyration and end-to-end distance.

Scattering from the gaussian chain

The structure of polymer chains is often studied by scattering techniques, for example neutron scattering. We assume that the polymer is well diluted[2]. In this case, there are no correlations between different polymer chains and the structure factor $S(\mathbf{q})$ equals one. The scattering intensity is proportional to the form factor of a single polymer chain, $F(\mathbf{q})$. This form factor considers interferences of all possible pairs of chain segments.

$$F(\mathbf{q}) = \frac{1}{N}\sum_{i=0}^{N}\sum_{j=0}^{N}\langle\exp\left(i\mathbf{q}(\mathbf{R}_i - \mathbf{R}_j)\right)\rangle. \tag{4.9}$$

In case of the gaussian chain, all bond vectors are distributed according equation (4.8) and the form factor can be rewritten as

$$F(\mathbf{q}) = \frac{1}{N}\sum_{i=0}^{N}\sum_{j=0}^{N}\exp\left(-\frac{q^2l^2}{6}|i-j|\right). \tag{4.10}$$

When N is a large, the sums in the equation can be replaced by integrals:

$$F(\mathbf{q}) = \frac{1}{N}\int_0^N \mathrm{d}i \int_0^N \mathrm{d}j \exp\left(-\frac{q^2l^2}{6}|i-j|\right) = N \cdot f_D(q^2R_g^2) \tag{4.11}$$

with

$$f_D(x) = \frac{2}{x}(x - 1 + e^{-x}). \tag{4.12}$$

[2] for SANS on polymer melt "diluted" means that we have only a small fraction of protonated polymer in the deuterated one.

The function $f_D(x)$ is called Debye function which is often observed in scattering experiments on polymers. Thus, the form factor $F(\mathbf{q})$ has two important regions arising from asymptotic behavior of the Debye function:

$$\begin{array}{ll} F(\mathbf{q}) \propto N(1-\frac{q^2R_g^2}{3}) & \text{for} \quad qR_g \ll 1 \\ F(\mathbf{q}) \propto \frac{2N}{q^2R_g^2} & \text{for} \quad qR_g \gg 1. \end{array} \tag{4.13}$$

The scattering intensity has a maximum at $q = 0$ and continuously decreases towards larger q. The intensity at small q is governed by the radius of gyration R_g of the polymer chain and describes the chain as a whole. At large q, intensity is proportional to q^{-2} with a prefactor which relates to the segment length $l = \sqrt{6R_g^2/N}$. This scattering corresponds to the correlations between chain segments [84]. Since the wavelength of neutrons is a few Å and R_g for typical polymers is in the range of nm, the conformation of the polymer chain can be observed by small angle scattering techniques only.

The scattering intensity is proportional to the form factor with a scale factor which depends on the volume fraction of the polymer ϕ, scattering contrast Δb, volume of a monomer V_m, and number of monomers per chain N:

$$I(q) = \text{scale} \cdot f_D(q^2R_g^2) + \text{bkg} \tag{4.14}$$

where the scale factor is $\phi(\Delta b)^2 N \cdot V_m$.

The real polymer has a certain polydispersity which should be taken into account in the intensity distribution. For polydisperse gaussian coils equation (4.12) can be expressed as

$$f_D(x) = \frac{2[(1+\sigma x)^{-1/\sigma} + x - 1]}{(1+\sigma)x^2} \tag{4.15}$$

with

$$x = \frac{q^2R_g^2}{1+2\sigma}, \tag{4.16}$$

and the polydispersity

$$\sigma = \frac{M_w}{M_n} - 1 \tag{4.17}$$

where M_w is the weight average molecular weight and M_n is the number average molecular weight.

4.3.3 Radius of gyration and stiffness of the polystyrene chain in the tube interior

In this section experimental results on the conformation of polystyrene chains in CNT arrays investigated using SANS will be presented. The technical details of the experiments are described in section 2.2.2. Here we will focus on results obtained for PS of $M_w = 21800$ g/mol measured in the CNT 60 V array with large tube diameter.[3] Results for CNTs with small tube diameter (CNT 40V) can be found in appendix A.2. CNT 40V has smaller tube diameter and the form factor of single CNTs is overlapping with scattering from the polymer coil which hinders the extraction and analysis of the scattering from the polymer.

[3] These CNTs are named in the text CNT 60V and have the inner radius $R_{inner} \approx 45$ nm. The alternative CNTs with small tube diameter are named CNT 40V and have $R_{inner} = 20$ nm. The labels 40V and 60V correspond to the preparation voltage of the PAOX template used for synthesis of CNTs.

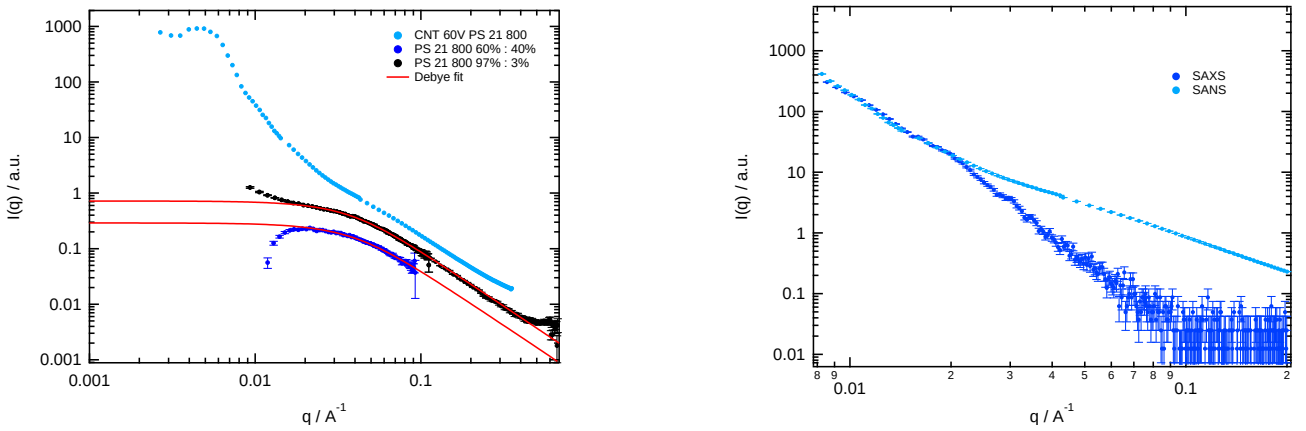

Figure 4.14.: (a): SANS curves of CNT 60V (85 nm in diameter) filled with PS (M_w=21800 g/mol) with mixing ratio of d-PS : p-PS is 60 : 40 and bulk PS with the same mixing ratio (experiment is performed at D22) and bulk PS with the ratio of d-PS : p-PS is 97 : 3 (experiment is performed at D11) ; **(b)**: Comparison of SANS and SAXS curves of CNT 60V filled with PS of M_w=21800 g/mol.

PS infiltrated into CNT array inside and between the tubes

The first experiment was performed on the D22 diffractometer. PS was infiltrated into the one side closed CNT array by melt infiltration (see chapter 4.2). The remaining polymer layer on top of the array was removed by plasma etching in order to reduce the contribution of the bulk polymer. Samples were measured without preferred orientation since several ”pieces” of the sample were stacked together in the sample holder. The average orientation of CNTs in the measured sample volume has a broad distribution and is considered to be random. The mixing ratio of d-PS and p-PS is 60:40 since the volume fraction of polymer is much lower than the volume fraction of CNTs and the scattering intensity of the polymer chains was expected to be low. The aim of the experiment was to observe a clear separation of the signal from tube scattering and polymer scattering. The high mixing ratio can significantly increase the contribution of polymer scattering to the total signal due to high volume fraction of p-PS in the sample volume[4]. The result is shown in figure 4.14a. CNT 60V (light blue curve) exhibits two features at low q: one is a structure peak at 0.005 $Å^{-1}$ and second is a small shoulder at 0.013 $Å^{-1}$. The first peak describes the correlation between CNTs. The average correlation distance is around 125-130 nm. The second peak corresponds to a distance of around 47 nm, which is close to the tube radius. The structure of the CNT 60V was described in detail in section 4.2.3. As was discussed before the polydispersity of these CNTs is relatively high (more than 35%), the deviation from the hexagonal lattice is also significant. This can produce extra smearing of the scattering curve and other features like structural peaks and peaks of the form factor are hidden. Moreover, CNTs are randomly oriented with respect to the incident beam.

At larger q the scattering profile shows a broad shoulder which is usually not observed in SAXS. A comparison of SANS and SAXS scattering profiles is shown in figure 4.14b. The shoulder can be caused by scattering contrast between d-PS and p-PS which is observable in SANS only. Moreover, this peak disappears in the case of filling CNTs with PS of higher molecular weight (88 000 g/mol). This data is shown in appendix A.2 (fig. A.2). Therefore, we can consider this shoulder as the scattering from the polymer coil. If so, the peak should be described by the Debye function (eq. (4.14)). Since the data is presented in arbitrary units and the scattering profile does not reach a flat background, we cannot

[4] Scattering from polymer coils also depends on SLD contrast of d-PS and p-PS (SLD(d-PS)=5.96 $e^{-6}Å^{-2}$, SLD(p-PS)= 1.4 $e^{-6}Å^{-2}$)

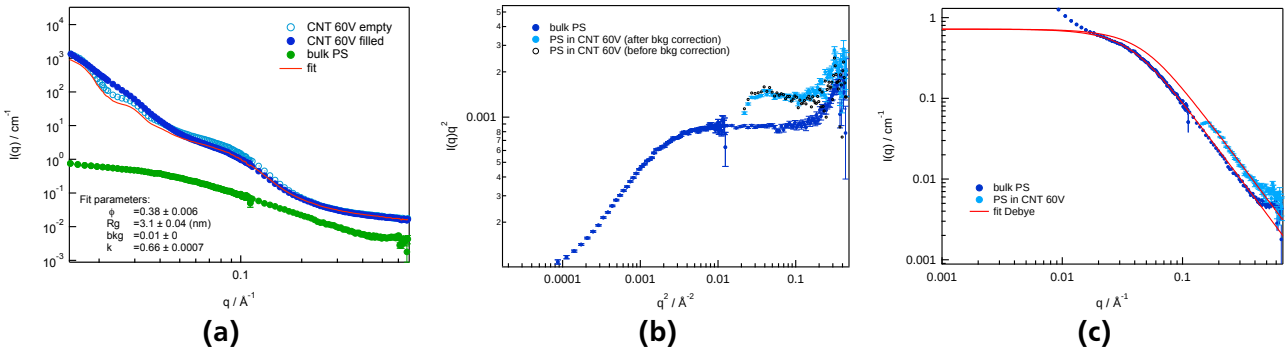

Figure 4.15.: (a): Data treatment of the SANS experiment performed on D11 in order to separate polymer scattering from CNTs. Tube diameter is around 85 nm and M_w of PS is 21800 g/mol; **(b)**: Kratky representation of the polymer scattering shows the background correction; **(c)**: Scattering from bulk PS and PS in the CNT arrays together with fit. Obtained R_g is 3.8 nm and 3.1 nm for bulk PS and PS in the CNT array.

directly apply the Debye function because the total scattered intensity also contains the contribution from CNT structure. Figure 4.14a shows the bulk PS blend with a mixing ratio of 60:40 (d-PS : p-PS) (dark blue line) and the same polymer with the ratio of 97 : 3 (black line). Both curves can be described with the Debye function and the fitting in both cases results in $R_g = 3.80 \pm 0.03$ nm. Comparing these curves with the scattering profile of CNT 60V filled with PS shown in the same plot one observes that the form of the scattering curves in the q range higher than 0.04 $Å^{-1}$ is similar for all profiles. In other words, the scattering at high q is caused mostly by the scattering from the polymer chain and can be separated from the scattering at low q which is caused by form and structure factor of the CNT array. Therefore, we are able to separate scattering from polymer chains and the CNT structure. The best separation can be achieved for CNT 60V filled with PS of $M_w = 21800$ g/mol.

PS infiltrated in the tube interior

As was shown above, the scattering from polymer chain and CNTs can be well separated in SANS experiments. In the next step, polystyrene of the same molecular weight (21 800 g/mol) with mixing ratio of d-PS : p-PS of 97 : 3 was infiltrated in the tube interior only. This can be achieved by infiltration of the polymer before etching of the PAOX template. In order to obtain a sample with relatively large surface area and to be able to cover the neutron beam by one large continuous sample, the PAOX template is not etched away. The sample consists of CNTs with polymer filled interior situated in the pores of PAOX. Speaking in terms of the scattering model we have polymer in the core, CNT as the shell and alumina as the matrix. Keeping CNTs in the solid matrix allows to preserve the precise orientation of the pores of PAOX. Avoiding the polymer in matrix – between tubes – enables us to investigate the polymer chain conformation under a certain geometrical confinement.

The experiment was carried out on the D11 difractometer. The first two curves from the top in figure 4.15a show scattering profiles of the empty and the polymer filled CNT array. Differences at low q are caused by the different orientation of CNTs with respect to the incident neutron beam. As was discussed above, the low q region corresponds to the structure of the single CNTs and structure of the whole array. The higher q range presented here corresponds to the scattering from polymer coils. In the range of 0.1 $Å^{-1}$ one can observe a broad shoulder in both scattering profiles. This shoulder has the same position, shape and intensity for filled and empty CNTs. We suppose that the shoulder arises due to weak scattering length density (SLD) contrast between CNTs and PAOX (see appendix A.2 fig. A.3). The observed shoulder overlaps with the scattering from polymer coils (Scattering from bulk PS is shown in green in figure 4.15a). In order to extract the scattering from the polymer the curve obtained for the empty array is subtracted from the filled one with corrections for differences of the orientation of CNTs in

the primary beam. The correction has to be performed because the orientation of the CNTs was to some extent arbitrary. Samples were fixed in the sample holder such that the sample surface is perpendicular to the incident beam. In case of ideal orientation, the tubes, initially oriented perpendicular to the sample surface, should be parallel to the incident beam. In reality the tubes can be slightly tilted with respect to the sample surface and the neutron beam correspondingly. Moreover, the sample surface can be curved which influences the sample volume in the neutron beam. Another factor which contributes to the discrepancy between filled and empty CNTs is fact that the two measured samples — filled and empty — are not exactly the same. They were produced under the same conditions but might have local differences. All these factors have to be taken into account before analysis of the scattering from the polymer chain.

Since the fitting with the core-shell model function which was used for fitting of SAXS profiles is not directly applicable due to arbitrary orientation of tubes with respect to the primary beam, SANS profiles were fitted according to the following approach:

$$I_{\text{filled}}(q) = k \cdot I_{\text{empty}}(q) + \phi \cdot I_{\text{chains}}(q) \tag{4.18}$$

where $I_{\text{filled}}(q)$ is the scattered intensity of the sample containing PS inside the pores, $I_{\text{empty}}(q)$ the intensity of the empty sample and $I(q)_{\text{chains}}$ is the scattered intensity of polymer chains described by equation (4.14). The coefficient k corresponds to the correction factor which has to be applied for subtraction of the scattering profile of the empty sample from the filled one. Polymer filled CNTs show an additional scattering component due to polymer scattering. This component corresponds to the scattering from polymer chains and is described by the Debye function. The coefficient ϕ is the volume fraction of polymer in the sample. First of all, due to correlation between all fit parameters, some of them must be fixed. We can fix parameters in the Debye function (see eq (4.14)) — scale factor and background. The scale factor for bulk PS can be theoretically calculated. The background corresponds to the incoherent scattering intensity I_{inc} which is known for PS[5]. The background can be calculated as $I_{\text{bkg}} = \phi \cdot I_{\text{inc}}$, where is ϕ is the volume fraction of polymer in the sample. For the bulk polymer $\phi = 1$, and $I_{bkg} = I_{\text{inc}}$. In case of the polymer scattering in the CNTs, the volume fraction of the polymer is a priori not known and can be estimated using SEM. From the SEM image one can recover the porosity of the PAOX template containing CNTs. The estimated porosity is around 40%. Another factor which affects ϕ is the filling factor. The filling factor is the volume fraction of the tube interior filled with polymer. It equals one in case of complete filling. In the previous chapters it was shown that CNTs are not filled completely. Thus the filling factor is expected to be lower than 1. Moreover, the sample can contain some polymer on the surface of the array, which can increase the volume fraction of polymer in the sample volume. In order to simplify the fitting procedure, we fixed scale factor and background in the Debye function to the values for the bulk PS. The coefficients ϕ and k in equation (4.18) are free fit parameters together with radius of gyration R_g in the Debye function[6].

Since filled and empty CNTs have different orientation at low q, which does not strongly affect high q the fit was performed at high q only where both samples show the same features in the scattering profiles. The fit region is $0.06\,\text{Å}^{-1}$ to $0.7\,\text{Å}^{-1}$. The resulting fit curve is shown in figure 4.15a in red. The fit parameters are also shown in the figure. The obtained volume fraction of polymer ϕ is 38% and radius of gyration is 3.1 nm which is 0.7 nm lower than for the bulk PS. The correction factor is $k = 0.66$.

In the next step we subtract the scattering from empty CNTs from the filled ones and check the background correction. This step is necessary to check that the calculated background is correct. Since all scattering profiles in figure 4.15a do not show a clear plateau the direct estimation of the background is impossible. The scattering from polymer coils can be obtained by the following equation:

$$I_{\text{polymer}} = I_{\text{filled}} - k \cdot I_{\text{empty}}. \tag{4.19}$$

[5] For bulk PS: $I_{\text{inc}} = 0.03 \cdot I_{\text{inc}}^{p-PS} + 0.97 \cdot I_{\text{inc}}^{d-PS}$ ($I_{inc}^{p-PS} = 3.9\ \text{cm}^{-1}$ and $I_{inc}^{d-PS} = 0.042\ \text{cm}^{-1}$).

[6] ϕ in equation (4.18) is not exactly the same as in scale factor of equation (4.14). In eq. (4.18) is a total volume fraction of the polymer while in eq. (4.14) ϕ is a fraction of protonated chains only.

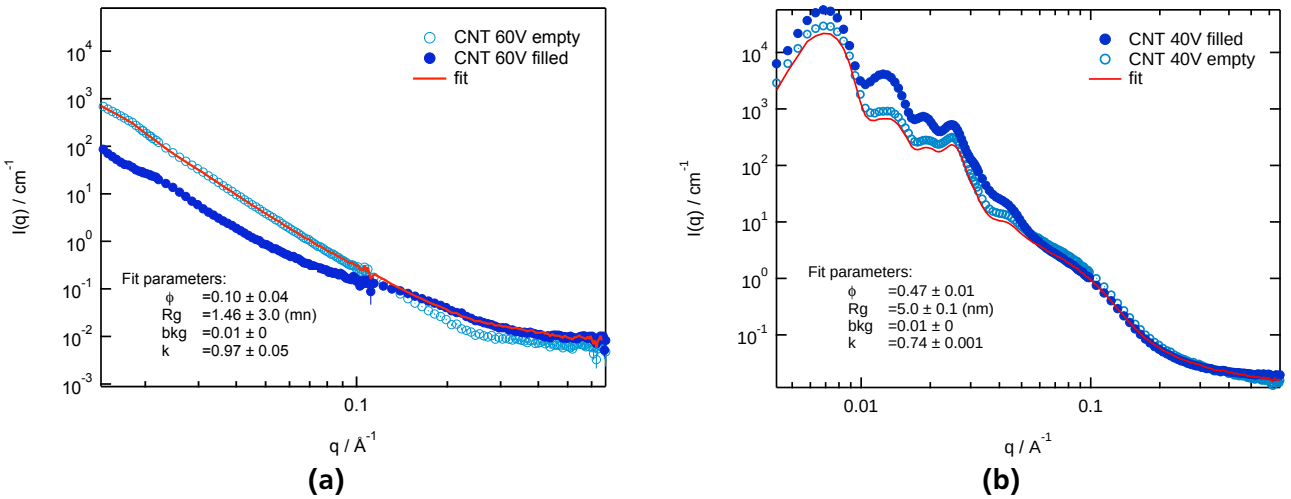

Figure 4.16.: Fitting of scattering profiles of filled CNT arrays in order to separate the polymer scattering: **(a)**: Tube diameter is around 85 nm and M_w of PS is 21800 g/mol; **(b)**: Tube diameter 40 nm and M_w of PS is 21800 g/mol.

It is then normalized to the volume fraction ϕ of polymer in the sample which was obtained in the fit.

The obtained scattering from the polymer as well as the scattering from bulk polymer will be corrected for background. In order to estimate the background correction, the scattering profile of the polymer is presented in a Kratky plot ($I(q) \cdot q^2$ vs q^2) which is shown in figure 4.15b. The ideally subtracted background should lead to a plateau at high q. This is well observed for the bulk polymer (dark blue curve). Moreover, the plateau indicates that the PS chain can be described in terms of a gaussian chain. The black circles in figure 4.15b correspond to the polymer scattering in CNTs. We observe a small negative slope in the range of 0.05–0.12 Å^{-2} which indicates that the subtracted background was too large in the case of PS in CNTs. The subtracted background is adjusted such that the points at high q are parallel to the points of the scattering curve of the bulk polymer. The real background is 10% less than estimated before. It also means that the volume fraction of polymer in CNTs is 10% less than the value obtained by the fit. The result after all corrections is shown as light blue curve in figure 4.15b.

In figure 4.15b one observes that at very high q all scattering profiles have an increase of $I(q)q^2$ with q^2. Since all points between $q = 0.01$ Å^{-2} and $q = 0.1$ Å^{-2} are situated in the plateau already, this additional scattering does not arise due to background. The extra "tail" is caused by the segment-segment correlation of the polymer chain since this region is close to the wide angle scattering. The intersegmental correlation of PS is observed in WANS at 0.7 Å^{-1} [87]. In figure 4.15c the scattering profiles of bulk PS and PS in the CNTs are shown. Both curves have a small peak at 0.65 Å^{-1}, which is in good agreement with literature and considered as intersegmental correlation.

Now we obtained the scattering from polymer chains and can precisely determine the radius of gyration R_g. For this purpose scattering curves are fitted according to equation (4.15). The obtained radius of gyration for bulk PS is $R_g = 3.8 \pm 0.03$ nm and $R_g = 3.2 \pm 0.06$ nm for PS in the CNTs. The polymer chain in CNTs seems to be compressed with respect to the bulk PS. However, the data evaluation and subsequently the results are very sensitive to the coefficient k. To be able to conclude that conformation of polymer chains changes inside CNTs we have to check reproducibility of data and analysis.

Figure 4.16 shows a different data set. The left plot corresponds to CNTs with the same diameter as discussed above but prepared independently. One observes a significant difference between the filled and empty CNTs at high q which can be due to a weak similarity of the local structure of the filled and empty samples (as was discussed above the filled and empty templates are not exactly the same and could have local differences). A fit according to equation (4.18) results in a very small radius of gyration which is

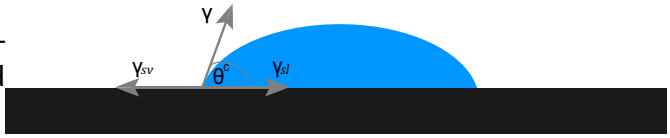

Figure 4.17: A sketch of the wetting phenomenon illustrating the force balance for a liquid droplet on a solid surface.

not realistic for this experiment[7]. The right plot (fig. 4.16b) shows CNT of 40 nm in diameter again with a fit according to equation (4.18). In this case the obtained R_g is much bigger which is also not realistic. The low reproducibility indicates that the orientation of samples as well as the local structure can play a significant role in data analysis and thus strongly influence the results. In order to conclude the change of the polymer chain conformation in CNT arrays more accurate experiments have to be performed. For example, the template can be filled in situ without removing the sample from the sample holder. The sample can also be fixed on a goniometer in order to measure at a well defined orientation of the sample with respect to the incident beam which allows to fit the complete scattering profile.

In situ filling should be first studied by SAXS in order to determine the kinetics of the polymer filling and explore possible evidence of formation of an interphase near the CNT surface which can produce a difference in the conformation of polymer chains.

4.4 Filling kinetics of CNT/Polymer composites

The analysis of the composite structure described in chapter 4.2 has shown that the electron density in the core and matrix respectively does not change simultaneously during the infiltration. This implies a different filling kinetics of the polymer inside the nanotubes and between them. In the present chapter the filling process of the CNT array will be considered in detail. Experiments on the system with one remaining carbon layer will be considered. The first section will overview the different possibilities of the polymer infiltration, for example wetting which leads to formation of a precursor film and the Lucas-Washburn theory of capillary flow. In the next section the filling kinetics studied by in-situ SAXS will be discussed.

4.4.1 Wetting of nanotubes

Basic principles of wetting phenomena

Wetting is the ability of a liquid to maintain contact with a solid surface. The wettability is determined by a force balance (see figure 4.17). This case of a liquid droplet on a flat surface is described by Young's equation which connects three interfacial tensions, γ_{sl}, γ_{sv} and γ with the equilibrium contact angle, θ^c:

$$\cos\theta^c = (\gamma_{sv} - \gamma_{sl})/\gamma \tag{4.20}$$

where γ_{sl}, γ_{sv} and γ are solid-liquid, solid-vapor and liquid-vapor interfacial tensions. Measuring of the contact angle is a typical way to measure wettability of the surface by a liquid. The system will adopt a state where the overall interfacial energy is minimized. It means that the acting forces have a specific balance for specific combinations of surface and liquid. When all forces cannot be compensated at any contact angle, that is $\gamma_{sv} > \gamma_{sl} + \gamma$, the droplet spreads completely over the surface. This situation is called complete wetting. If the surface energies of the solid and the liquid converge, the contact angle will be larger than zero. This case is called partial wetting and corresponds to $0 < \cos\theta^c < 1$. The third possibility is the nonwetting case, when the contact angle is bigger than $\pi/2$.

For a total equilibrium of the system three conditions have to be fullfilled [88]: (a) Liquid must be in equilibrium with its own vapor; (b) liquid must be in equilibrium with the solid and (c) vapor must be in

[7] One might expect a significant decrease of R_g in case when tube radius R_{tube} is smaller than R_g. Since in our experiment $R_{\text{tube}} \gg R_g$ the change of R_g should not be so dramatic.

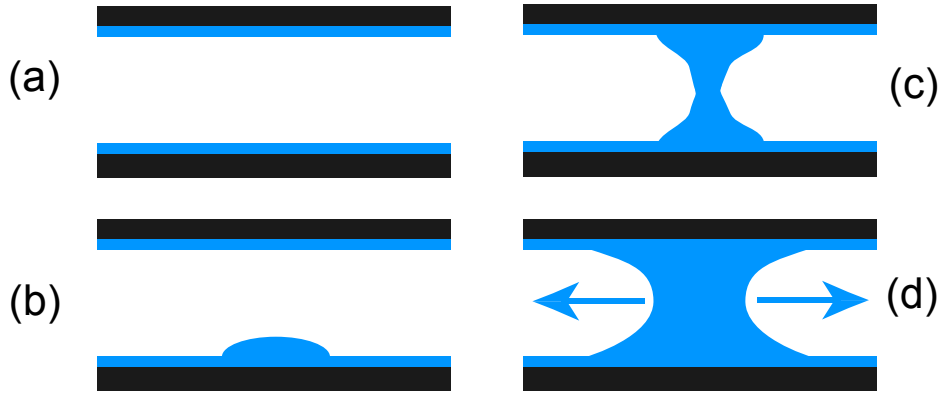

Figure 4.18.: Filling the nanotubes due to instability of precursor film: (a) wetting of walls of nanotubes; (b) formation of instability; (c) snap-off; (d) interface movement

equilibrium with the solid. The first condition requires equal chemical potentials of the liquid molecules in vapor and inside the droplet. This means that the liquid must be in equilibrium with the oversaturated vapor. If we take into account the equilibrium between the vapor, which is oversaturated now, and the solid surface the adsorption of molecules of the liquid on the surface cannot be avoided. This results in formation of an adsorption liquid film on the surface, the so called precursor film.

The infiltration of liquids into nanotubes is more complex than spreading of a droplet on a surface. Depending on the size of the tube different physical mechanisms can dominate, for example hydrodynamics or interfacial phenomena [70]. The precursor filling of the nanotube is schematically shown in figure 4.18. First of all, a precursor film of liquid covers the tube walls. Instabilities in this film may occur, and as more and more liquid flows into the tube, this instability begins to grow and connects to the film on the other surface of the tube wall – a so-called "snap off" takes place [70]. The formed meniscus grows in both directions and the tube volume is completely filled with the liquid.

One of the important factors which influence the wettability of surfaces and pores is the surface free energy. If polymer has a surface energy lower than the solid surface, it will spread on the surface and form the precursor layer. The larger the difference between surface energies, the faster the polymer covers the surface. The pore radius also plays an important role in the filling process. Due to flexibility of polymer chains, they can adapt many conformations, even in pores having a smaller radius than the radius of gyration. The radius of pores affects the filling behavior of polymers. In general, if liquid or polymers are brought into contact with porous materials having surface energies higher than the polymer and radius of the pores is larger than radius of gyration of the polymer, the precursor layer rapidly covers the pore walls and forms a stable polymer film. If the radius of pores is smaller or comparable to the radius of gyration the polymer fills the pores completely forming polymer rods inside.

Capillary flow in nanotubes

The interest in properties of liquids in tubes or channels has already started in the nineteenth century. Navier and Stokes formulated the fundamental equation of the motion of fluids. The Navier-Stokes equation [89] is based on Newton's second law. Another fundamental law describing the flow of liquids was found by Hagen and Poiseuille, and can be derived from Navier-Stokes equation. First experiments on determination of the time dependency of the filling height of liquids in pores resulted in a power law behavior with an exponent in the range of 0.5. Lucas [90] and Washburn [91] described the dynamics of capillary flow theoretically, using the Hagen-Poiseuille law, and confirmed the experimental finding of a $\sqrt{t}$-dependency of the filling height.

Here the key points of capillary flow which are important for analysis of polymer filling of nanotubes will be summarized.

The flow rate (dV/dt) of a simple (Newtonian) liquid driven through a long narrow cylindrical pipe by pressure can be described by the Hagen-Poiseuille equation:

$$\frac{dV}{dt} = \frac{\pi R^4}{8\eta}\frac{\partial p}{\partial z}, \tag{4.21}$$

where $\partial p/\partial z$ is the pressure gradient along the cylinder, R is the radius of the cylinder and η is the viscosity of the liquid. The pressure gradient consists of different contributions to the pressure, for example, capillary pressure $p_{cap} = 2\gamma\cos(\theta^c)/R$ with contact angle θ^c and surface tension γ. Furthermore, there can be a gravitational or hydrostatic pressure $p_g = \rho g h$, where ρ is the density of the liquid, g is the gravitational constant and h is the height of the liquid column. It is also possible to apply external pressure p_{ext}. In our case the polymer infiltration proceeds without any external force. Moreover, for nanotubes the capillary pressure is dominating since the radius is very small. In this case the equation of the force balance can be significantly simplified and results in:

$$z(t) = \sqrt{\frac{\gamma}{\eta}\frac{\cos(\theta^c)}{2}Rt} = \sqrt{at} \tag{4.22}$$

with $a = \gamma\cos(\theta^c)R/2\eta$. This equation shows the time dependence of the filling height and is often referred to as Lucas-Washburn law. It describes well the experimental findings of the filling process starting fast and subsequently slowing down. This law makes it possible to determine the value of the contact angle in porous media. Since the filling rate is not constant one can only calculate an average velocity over time interval $\Delta\tau$ to obtain the filling speed [92]:

$$\bar{v}(\Delta\tau) = \frac{z(\Delta\tau)}{\Delta\tau} = \sqrt{\frac{a}{\Delta\tau}}. \tag{4.23}$$

The total length of the capillary l_0 will be completely filled within the time interval τ:

$$\tau = \frac{l_0^2}{a}. \tag{4.24}$$

If this time interval is inserted in equation (4.23) as $\Delta\tau$, we obtain an expression for the average speed to fill the capillary completely

$$v_\tau = \frac{a}{l_0}. \tag{4.25}$$

4.4.2 Filling kinetics of PS in CNT arrays

The flow of the polymer into the CNT array is monitored with time-resolved SAXS. For this experiment the CNT array with small tube diameter is chosen in order to be able to observe form and structure factor and to avoid the tube collapse. We also take a small molecular weight of 21800 g/mol for PS. It turned out that larger molecular weights gave rise to very long filling times whereas for shorter chains the first part of the filling process could not be observed. A polymer film is placed on top of the CNT array and positioned in the evacuated sample chamber of the SAXS instrument. The sample holder is heated to 180°C. Scattering profiles are accumulated continuously for 2500 sec each. The experiment is run for a total of 8 days as far as change of the curve is observed. Such a slow polymer filling can be explained by very small differences in surface energy between the polymer and nanotubes (40.7 mN/m and $40-45$ mJ/m^2 for PS and CNT correspondingly [9])[8]. The primary beam intensity is monitored and all profiles are corrected for possible changes. Variations are smaller than 15 %.

The result of this experiment is displayed in figure 4.19. The overall form of the scattering profiles is the same as discussed in previous sections. A clear variation of intensity in both scattering maxima with time is seen. The position of the maxima on the q-axis remains unchanged.

[8] Usually the surface energy for solids is given in mJ/m^2 and in mN/m for liquids. These units are convertible.

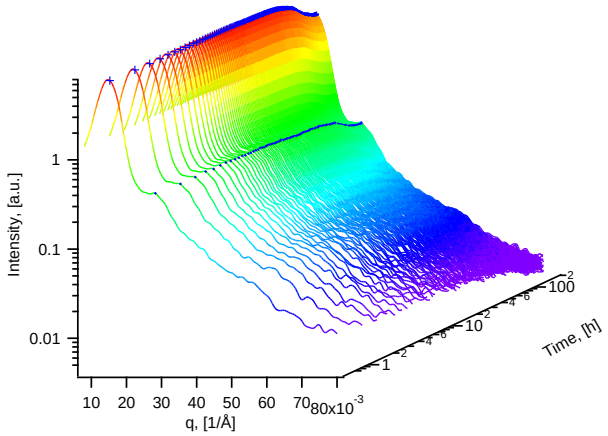

Figure 4.19.: In situ time-resolved SAXS measurement of the imbibition of PS 21800 into the CNT array.

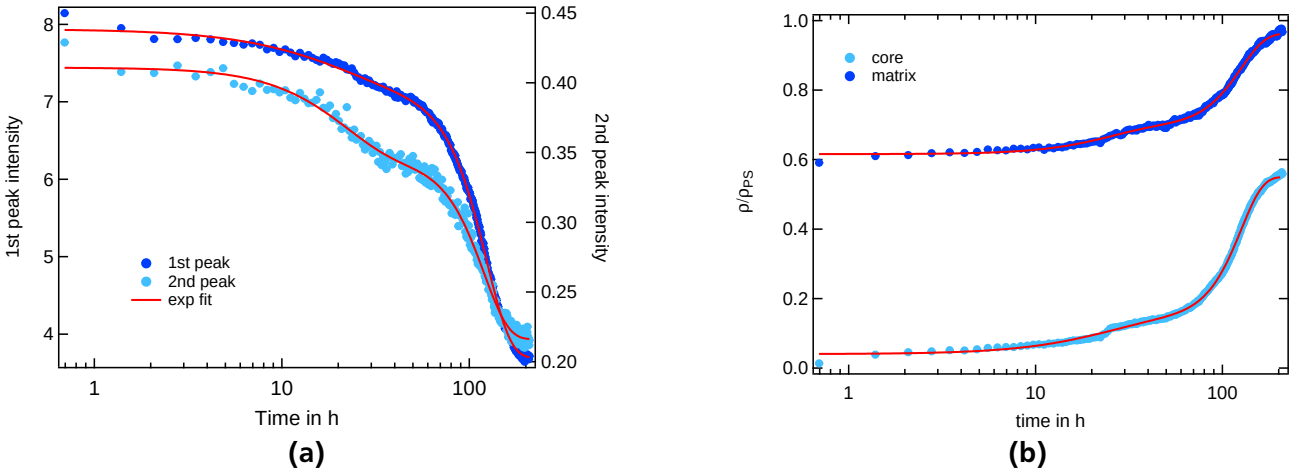

Figure 4.20.: a) Intensity of peaks depending on filling time, b) Electron density of core and matrix as obtained from a fit of SAXS model function. Full lines: fit of exponential power law (equation (4.26))

In a first step we analyze the kinetics by directly following the intensity of both scattering maxima with time. These results are shown in figure 4.20a. The data clearly show the decay of intensity in both maxima occuring on two well separated time scales. It is possible to fit the time variation of peak intensity with the following phenomenological equation:

$$F(t) = Ae^{-\left(\frac{t}{\tau_1}\right)^{\beta_1}} + Be^{-\left(\frac{t}{\tau_2}\right)^{\beta_2}} \tag{4.26}$$

The full lines in figure 4.20a show the quality of the fits. A short time process at $\tau_1 \approx 27\,\mathrm{h}$ is seen as a small step in the first and as a stronger effect in the second peak. It is followed by a long time decay at $\tau_2 \approx 120\,\mathrm{h}$ with large amplitude. The detailed form of both decays is a compressed exponential with $\beta_1 \approx 1.7$ and $\beta_2 \approx 3.5$.

Close inspection of figure 4.20a reveals that at very early times there is an additional decay of intensity. We suppose this decay is a relict of relatively fast wetting of the outer wall of CNTs within the first 20 min which is also the reason of the observed shift of the first maximum between the empty and the polymer filled array. Thus, structural changes of the CNT array caused by polymer infiltration occur only in the early stage of the filling.

In order to relate the peak intensity to structural properties of the CNT/polymer composite we analyse in detail the contributions to the scattering intensity. As seen in equation (2.16) the scattered intensity is related to a product of structure and form factor. Both contributions display a marked variation with q. In figure 4.21 we show a scattering profile from the time series. The red line corresponds to a fit using the model function. Also included in the figure are the contributions from structure factor (black line) and form factor (green line). It is seen that both scattering maxima are influenced by both contributions. However, the second maximum is clearly dominated by the form factor. As this maximum displays the more pronounced effect we are led to conclude that the imbibition of polymer is changing the form factor scattering. What is seen in the variation of peak intensity must be related to a change of electron density outside and inside the carbon nanotubes.

We therefore use the model function as described above and fit it to every scattering profile of our time series. The only parameters varied in these fits are the electron densities inside the CNT and in the matrix. Every profile was corrected for transmission. The detailed description of the fitting procedure is given in appendix A.3.

The description of the data with this model is very good and allows to determine the time variation of the electron density in the CNT core and in the matrix. The results are displayed in figure 4.20b. The figure displays electron density divided by the electron density of polystyrene. We find both electron densities grow exponentially with time. The time variation is again very well described with exponential functions. For the fitting of electron densities equation (4.26) is modified in order to account that $I(q) \propto \rho^2(r)$:

$$\rho(t) = A\left(1 - e^{-\frac{1}{2}\left(\frac{t}{\tau_1}\right)^{\beta_1}}\right) + B\left(1 - e^{-\frac{1}{2}\left(\frac{t}{\tau_2}\right)^{\beta_2}}\right) \tag{4.27}$$

Times τ as well as the exponents β are found to be nearly the same as those obtained before from the variation of the peak intensity.

Closer inspection of figure 4.20b shows that the electron density found in the interstices between tubes, the matrix, starts from a rather high value compared to the apparently empty interior of the CNTs. A small fraction is added on the time scale of 20 hours. The final value for the matrix is reached after 120 hours and correponds to a complete filling of space with polystyrene. The interior of the CNT saturates at the same time at nearly 60% filling. Such high value of the electron density of the matrix in the beginning of the experiment indicates a third, rather fast process, which corresponds to the fast wetting of the outer wall of CNTs. Note that the obtained electron density is an average density in the volume between tubes. 60% of filling indicates inhomogeneous filling of the volume and does not correspond to the filling height. Thus, the matrix (as well as the core) can contain polymer along the full length of tubes but with some polymer free voids in volume which leads to the lower average electron density. However, the absolute value of this electron density should not be taken as 60% filled volume, due to external contributions to the electron density of the matrix, which were already discussed in chapter 4.1 and 4.2. The average electron density of the core only reaches 60% of the electron density of bulk PS. Therefore, the tubes are not filled homogeneously.

In general the imbibition process of straight nanopores is found to follow the well-known Lucas Washburn law [92], which predicts a variation of filling height l with time as $l \propto \sqrt{t}$. This is not in accordance with our data. The exponential variation (eq. (4.26)) suggests a kinetics that is analogous to an Avrami law which well describes polymer crystallization kinetics.

The fast process may therefore be related to the formation of a precursor film on the internal surfaces of the CNT array. The low difference in surface energy between CNT and polystyrene (less then 5 mN/m) results in a rather long time for this process. In case of low difference in surface energy the contact angle can be larger than zero [70] and wetting of CNT walls can be partial. According to Lavi et al.[93], in this case variation of filled area of the sample surface with time can follow an exponential law.

On a slower time scale we also find the volume inside the CNT and in the interstices to fill according to an exponential law. The processes contributing here are capillary flow as well as instabilities of the

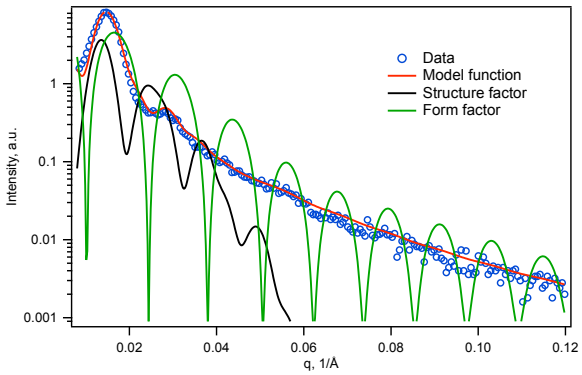

Figure 4.21.: Scattering curve of CNT/PS 21 800 composites with fit (red line) according to model function, form (green line) and structure (black line) factors

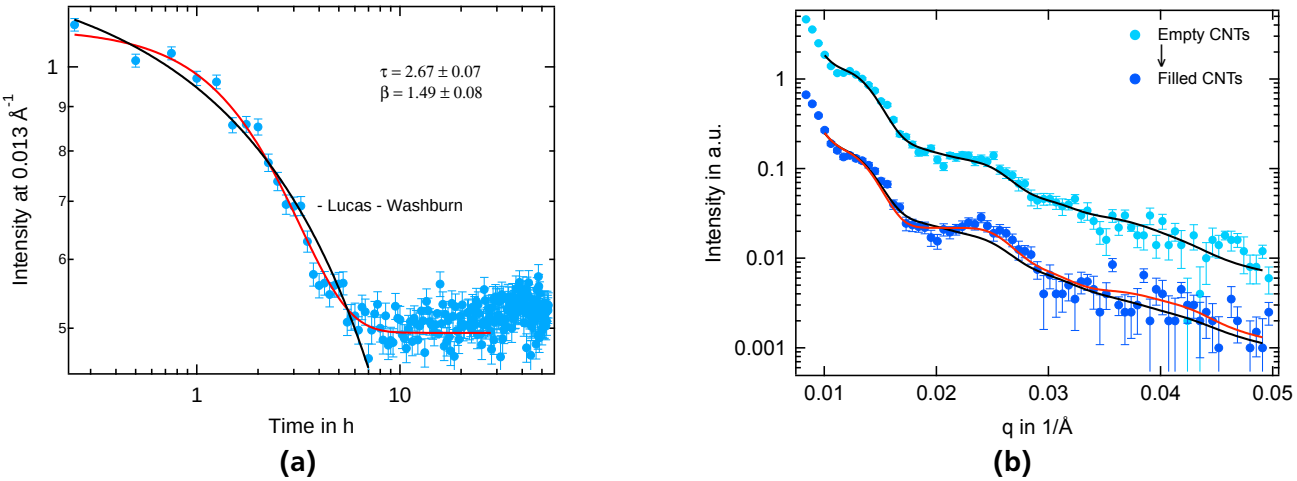

Figure 4.22.: **(a)** Intensity variation of the first maxima during the time-resolved SAXS on the filling of the CNT interior. Red line corresponds to the exponential fit, black line represents Lucas-Washburn fit; **(b)** Scattering profiles of the empty and filled CNT array after 50 hours from the beginning of the infiltration. The black lines correspond to the fit with core-shell cylindrical form factor. The red line shows fit by model with double shell cylindrical form factor.

precursor film [70] as sketched in figure 4.18. If we assume that instabilities occur randomly on the surface and that the surface dominates in the sample volume due to the small tube radius and separation between tubes, β can be interpreted in terms of Avrami's law as dimensional factor. Hence the slow process with $\beta \approx 3.5$ relates to a three dimensional filling, which means that polymer fills the volume in all three directions: radially and along the tubes.

4.4.3 Filling kinetics of tube interior

In order to get more information about filling kinetics of the CNT array, the filling processes inside and outside tubes (in the core and in the matrix) have to be investigated separately. The basic idea of the separation of these two filling processes is to close the matrix and fill the inner part of the tubes only. Subsequently, using a different polymer with lower glass transition temperature, the matrix can be filled without polymer flow in the core. The glass transition temperature of both polymers should be well separated and the inner polymer must have a higher T_g and stay solid during infiltration of the outer

polymer. For example, the CNT array can be filled inside with polystyrene having $T_g = 100°C$ and outside with polydimethylsiloxane (PDMS) which has $T_g = -125°C$.

This section will be focused on the filling of the inner part of CNTs only. This can be achieved by performing polymer infiltration before the etching of the PAOX template. The matrix is closed and polymer flows into the tube interior only. The experiment is done under the same conditions as described above: a PS film of molecular weight 21 800 g/mol is placed on the top of the CNT array with tubes of 40 nm diameter and heated to 180 °C inside the sample chamber of the SAXS instrument. The result is shown in figure 4.22a. Here we again observe a variation of intensity of the scattering maximum with filling time. First of all, the filling proceeds on a different time scale than before, the intensity decreases to a plateau within ten hours which is one order of magnitude faster than observed for filling of the whole array. This discrepancy can be explained by a deviation of the surface energy contrast between CNT and PS for different samples. Since the CNT has surface energy in the range of 40-45 mJ/m^2 depending on the exact structure of the wall, the difference between surface energies of CNT and PS can be slightly larger[9] than before which can result in faster wetting of the CNT surface. On the other hand, the structure of the array is different from the one used above. Now the CNT array has a solid matrix (alumina) which keeps tubes straight and better aligned. Polymer flows into the straight, mostly uniform cylindrical capillaries; this can enhance the infiltration speed as well. The third possible reason can be the contact of the sample with heating plate of the sample holder. CNTs included in PAOX have a larger sample surface due to the higher stability of the sample, and subsequently have a better contact to the heating plate. The contact affects the real temperature of the polymer. The better the contact, the closer the sample temperature is to the temperature of the heating plate, which affects the viscosity of the polymer. The red line in figure 4.22a shows the fit according to the exponential function (eq. (4.26)). The data can be described by a single compressed exponential with $\tau = 2.67\,\text{h}$ and $\beta = 1.5$. Comparing this β with the one obtained above for filling the array as whole, one observes that filling of the inner part of the tube corresponds to the fast filling process of the whole array ($\beta_{\text{fast}} = 1.7$). The process with $\beta = 3.5$ is not observed for filling of the tube interior.

At the same time data points before the plateau can be described according to Lucas-Washburn (LW) theory. Analysis of the scattering intensity in terms of the LW law was discussed in the literature [92]. The polymer flow in nanotubes can be modeled as a superposition of two cylinders: one cylinder is empty and another one is filled. In the beginning of the infiltration the empty cylinder has length l_0 which equals to the length of the CNT. The length of the filled cylinder varies with time according to Lucas-Washburn law (eq. (4.22)). Thus, the variation of the intensity with time can be described by the following equation:

$$I(q,t) = C(q)\left(l_0\rho_{\text{CNT}} - \rho_{\text{polymer}}\sqrt{at}\right)^2 \tag{4.28}$$

where $C(q)$ is a q-dependent prefactor corresponding to the core-shell form factor of the CNTs. ρ_{CNT} and ρ_{polymer} are electron densities of the CNT and the polymer correspondingly.

A fit according to this equation is shown in black in figure 4.22a. Before the plateau we cannot distinguish between an exponential and Lucas-Washburn, both fits can be applied for the description of the data. According to the LW fit, the filling process is finished after 10 hours because the intensity does not decrease any more. However, the scattering profile is slowly changing during 50 hours[10]. The scattering profiles of the empty (at $t = 0$) and the polymer filled (after 50 hours) CNT array are shown in figure 4.22b. The shape of the scattering profile changes during infiltration. The ratio of intensities of the first and second observed maxima becomes different. The second peak is more pronounced and increases after polymer infiltration. This observation leads to consider structural changes of the tube interior during infiltration, for example formation of a precursor film on the internal surface of the tube. Moreover, data cannot be described anymore with the considered model function with fixed radius of core and shell. The fit according to the considered core-shell model is shown in black in figure 4.22b.

[9] Surface energy depends on the exact structure of the graphite layer: armchair or zig-zag.

[10] Variation of the scattering profile with time is shown in appendix A.3, fig. A.4a

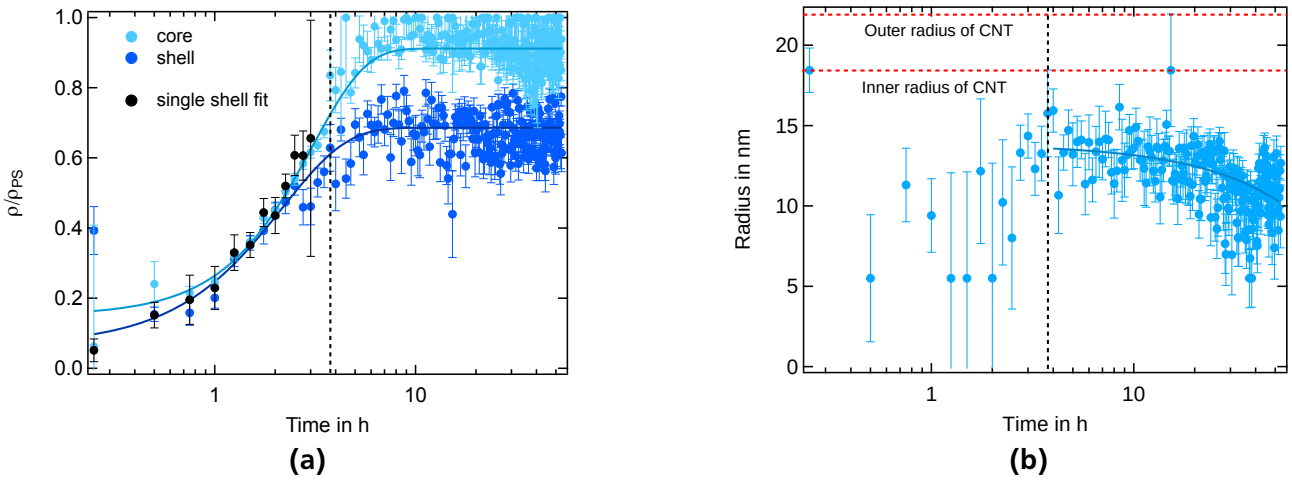

Figure 4.23.: (a) Variation of the electron density of core and shell (extra layer on the surface of the CNT wall) with time. Black circles correspond to the electron density inside tubes obtained by fitting with single shell form factor; **(b)** Variation of the radius of the core with filling time. Broken red lines represent the inner and outer radii of the CNT.

One observes that this model does not account for the deformation of the second observed maxima. The model function has to be extended in order to take into account the formation of the precursor film. For this reason an extra shell is included in the model function (see appendix A.1). The fit according to the double-shell model is shown in red in figure 4.22b. Comparing black and red curves we observe that including the extra shell is necessary and significantly improves quality of the fit. Every scattering profile of the time series is fitted with the double-shell model function. The TDHL structure factor remains the same. Free fit parameters in these fits are the electron density of core ρ_{core}, which corresponds to the central part of the tube interior, electron density of the first shell ρ_{shell}, which is now the precursor film on the internal surface of the tube and radius of the core R_{core}. By variation of this radius we can observe the variation of the thickness of the precursor film; the radius of the tube itself is fixed. Fitting results are displayed in figure 4.23 (details of fitting is given in appendix A.3).

The left plot represents the variation of the electron density of the core and the shell (precursor layer). We observe that at early times of the infiltration both electron densities grow simultaneously from zero. This indicates that there is no precursor film in the usual way of understanding. Usually, ”precursor film” means a thin layer which covers the surface relatively fast or at least faster than the rest of the polymer which flows into the tube. In this case the variation of the electron density of the shell would be different from the variation of the electron density of the core. However, this is not observed. In the experiment the polymer flows into the core and the shell at the same time. Thus infiltration of PS into the CNT proceeds without a precursor film. However, after approximately four hours both electron densities slowly reach a plateau and do not show any change after 8-10 hours from the beginning of the infiltration. The electron density of the core is close to the electron density of the bulk PS while the shell reaches only 65% of the bulk value. Thus, the layer at the CNT wall has lower density than in the bulk, a so-called depletion layer. The obtained difference of electron densities between core and shell is around 40%. Since the prefactor (scaling factor) is not exactly determined and measured in arbitrary units, both electron densities are only defined relatively. In the fitting procedure, the prefactor is assumed to be unchanged and corrected only for intensity of the primary beam which passes through the sample. Moreover, there is one more fit parameter — the core radius, which corresponds to the radius of the bulk polymer in the center of the nanotube. The simultaneous fit of two electron densities and the radius together with an arbitrary prefactor can affect the values of these densities. Thus, the value of electron densities should not be taken as absolute, but they clearly show the tendency of lower electron density

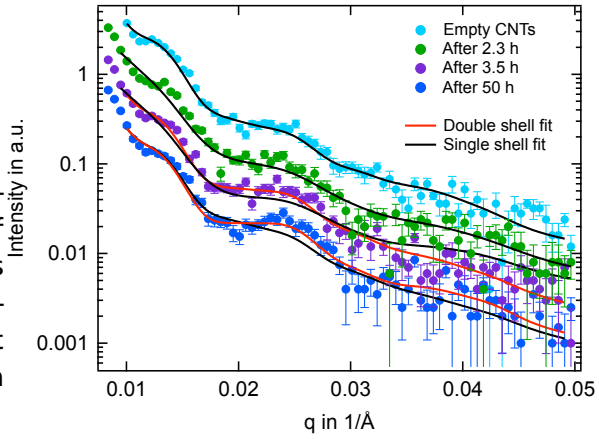

Figure 4.24: Scattering profiles of CNT arrays during infiltration demonstrating the changing of model function with filling. The black lines correspond to the fit with core-shell cylindrical form factor. The red line shows fit by model with double-shell cylindrical form factor.

near the wall[11]. Figure 4.23b shows the variation of the core radius with time. During the first four hours we observe no layer at the wall and consequently the radius cannot be determined. Since the radius is a free fit parameter during the fitting procedure the error bars of the data points which are corresponding to the missing depletion layer are large. Moreover in this region scattering profiles still can be fitted with the "simple" core-shell model (black circles in fig. 4.23a). The difference between double-shell and single-shell model occurs after approximately three hours from beginning of infiltration. Figure 4.24 shows few scattering profiles during infiltration fitted with single shell and double shell model for comparison.

We find that appearance of the depletion layer is observed after the same time as the second shell, which is well shown by the narrowing of the distribution of the core radius and the decreasing uncertainties of the fit parameter. At the time when electron densities have reached the plateau, the radius starts to decrease. The decrease is observed during the last 40 hours of the filling experiment. This means that beside the filling process, there is one more process which changes the arrangement of the polymer in nanotubes. This process is relatively slow compared to the filling and leads to the reconformation of polymer chains near the surface of the CNTs. The thickness of the depletion layer can be obtained as difference between inner tube radius and core radius, thus the thickness of the depletion layer is around 7-8 nm with a relative uncertainty of around 10%. The relatively high thickness of the layer also indicates that this layer is not a precursor film which occurs due to a possible wetting mechanism of the surface by the polymer. The typical size of this layer is in the order of the segment length of the polymer [94]. The presence of a depletion layer of simple liquids and polymers near CNTs was reported in the literature. For example water in CNTs with a diameter of less than 100 nm shows a depletion layer near the surface [95]. The simulation of the density profile of a polymer melt according to self-consistent field theory (SCFT) around CNTs leads to a depletion layer around the tubes [96]. The thickness of the depletion layer depends on the interaction between the polymer chain and the CNT wall. The depletion layer can be considered as an interphase near the wall. In general, the thickness of this interphase depends on the interaction of the polymer with the surface and can be different for different combinations of polymer and surface.

Polymer in a cylinder with repulsive interaction has increased density close to the center of the tube [46]. Generally, the density profile in thin films at the surface has an oscillating density profile [45]. Even attractive surfaces can cause depletion near the wall. The density profile is very sensitive to the free energy density and details of the chemical structure of the surface [97]. For very strong interaction the density profile has strong oscillations near the surface which can lead to high density near the wall. When the interaction decreases, the amplitude of the density oscillations is reduced and a depletion layer builds up near the surface [45]. The thickness of the depletion layer depends sensitively on the

[11] Indeed we also cannot conclude about absolute values of filling. Electron densities are determined in respect of zero electron densities in the beginning of the filling process.

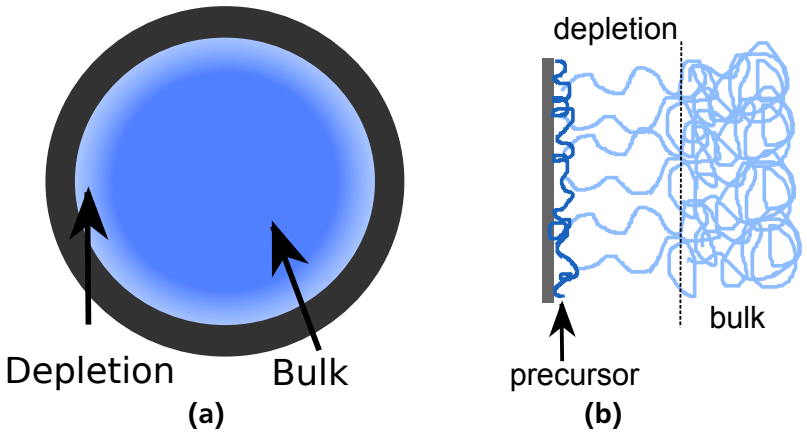

Figure 4.25.: (a) Schematic view of the density profile inside the CNT. **(b)** A possible structure of the interphase inside the CNT.

chemical potential in the vicinity of the surface and in the bulk. In the case of weak interaction and small difference in the chemical potential the depletion layer can be significantly thick. However, some researchers reported that flexible polymers like PMMA and PS strongly interact with SWCNT [9] and adsorb on the CNT wall. Assuming this fact and taking into account that we need a weak interaction to form a thick depletion layer, we can suggest that another layer between the CNT wall and the depletion zone could exist. This could be a strongly adsorbed polymer layer (fig. 4.25b) with a thickness of 1-2 nm.[12] This adsorbed layer creates a neutral surface for the rest of the polymer and depletion can occur. Moreover this layer can play the role of a precursor film on the CNT wall in the filling process. The idea of two different layers in the vicinity of the pore wall has been recently discussed [48]. The authors investigated PDMS dynamics in PAOX pores and suggested that the polymer has three different dynamical zones: a strongly absorbed layer at the pore wall, a transition phase between the polymer adsorbed on the surface and the bulk polymer, and the bulk phase itself. Similar to this we suggest that PS has three zones in the CNTs: an adsorbed (precursor) layer on the surface which is expected to be stretched along the surface, the depletion layer containing radially stretched polymer chains and the bulk phase. In our experiments we did not directly observe the thin adsorbed layer.

In the study of the filling kinetics the precursor layer should be visible in principle. However, the expected size of the layer is relatively small and the considered roughness of the CNT wall is around 2 nm which together with the large polydispersity can conceal this thin layer. In conclusion, the interpretation of two interphase layers based on theoretical findings and comparable experiments on the interaction between polymer and CNTs has to be substantiated by future experiments.

4.5 Summary and conclusions

It was shown that aligned CNT arrays can be filled with polymer in different ways: using polymer solution and by melt infiltration. Freestanding and both sides closed CNT arrays were filled with solution of PMMA and PS. A SAXS study shows that polymers flows inside the tubes and between clusters of tubes of freestanding CNT arrays. The amount of polymer in CNT arrays depends on the initial concentration of polymer in solution. The higher the concentration of the solution, the lower the obtained electron density is inside and outside CNTs. This dependency is well observed in the case of the infiltration of PMMA solution. Polymer filling does not improve the structure of the array, tubes remain bundled and polymer flows between clusters of CNTs.

[12] The segment length of PS is around 1 nm

The remaining carbon layers on both sides of the arrays prevent filling of the tube interior. The polymer can flow into the array only perpendicular to the long tube axis. No polymer is observed in the array in this case. The both sides closed CNT arrays keep their structure and stay unfilled. It is suggested that adsorption of the polymer from solution is the dominant mechanism of the infiltration.

Infiltration of the polymer melt proceeds due to the acting of capillary forces. This method is better controlled. Freestanding and one side closed CNT arrays were filled by molten PS. Depending on the initial structure of the array polymer has a different location in the array. In freestanding CNT arrays polymer fills the tube interior and forms a layer around clusters of CNTs. Similar to polymeric solutions, infiltration of the melt does not affect the structure of arrays. A completely different situation is observed for arrays with one carbon layer. Filling affects the order of the array, increases tube separation, and improves alignment. The obtained CNT/PS composites have an average tube separation which is increased by 3 nm with respect to the empty array. The inner part of the tubes is filled by polymer as well.

Combining SAXS with microscopy (TEM/AFM) allows to characterize CNT arrays and their composites on a wide range of scales. Tube separation, inner and outer radii can be determined in a combination of SAXS and TEM results. Using AFM we have found that tubes of 90 nm in diameter are not stable along their length. CNTs may collapse to smaller tube-like arrangements with a diameter of 15-20 nm.

Studies of the kinetics of the filling process show that imbibition of polymers into CNT arrays proceeds on two separate, rather long time scales. They are related to the formation of a precursor film and subsequent partial filling of the volume of the array. The filling kinetics deviates from the well known Lucas-Washburn flow and is described by compressed exponentials with the exponents 1.7 and 3.5 which can correspond to the dimension of the expansion of the polymer filled volumes in the array.

Keeping CNTs inside the PAOX template allows to investigate filling kinetics in the tube interior only. In this case tubes are kept straight and parallel like pores of the template. Investigation of the filling kinetics only in the tube interior shows only one filling process with the exponent 1.5. The early stage of the kinetics can be described in two ways: using a compressed exponential or the Lucas-Washburn equation. Analysis of the electron density inside tubes shows no formation of a precursor film. The difference in results of the first and second experiments could be due to the different morphology of the two systems. CNT arrays in their PAOX matrix have straight tubes and a more precise arrangement which might affect not only the time of infiltration but also the filling kinetics. The formation of a possible precursor layer can be much faster, and at the same time, the filling of the volume of tubes can be also enhanced. The fitting process is another possible reason for the discrepancies between the two experiments. In the first experiment the filling of the tube interior and interstices between CNTs cannot be separated. Variation of both electron densities with fixed arbitrary prefactor leads to correlations between the parameters, that could influence the absolute values at each step of the fitting procedure. In the second experiment fitting of the electron density of the tube interior is independent of the density of matrix.

At the late stage of the kinetics there are two different phases of the polymer: the density depletion layer in vicinity of the CNT wall and the bulk phase in the center of the tube. The thickness of the depletion layer slowly grows over time and reaches 7-8 nm.

Based on theoretical approaches of the interaction of the CNTs and polymers we suggest that the interphase near the CNT wall has a complex structure. It consists of a thin adsorbed layer, which plays the role of a precursor film during the polymer infiltration and a rather thick depletion layer.

5 Glass transition and crystallization of polymers inside the CNT array

The detailed study of structure of CNT/polymer composites and filling kinetics of polymer in the tube interior have shown that CNTs affect the polymer properties in composites. Thus, the tube diameter and the separation between CNTs influence the polymer location in CNT arrays. In situ SAXS experiments have shown the existence of an interphase in the vicinity of the CNT wall with a probably complex structure. The interphase leads to a change in dynamical properties of polymers in composites. For example, the glass transition and crystallization of polymers near the CNT wall can significantly differ from the bulk.

The purpose of this chapter is the investigation of thermal properties of polymers in CNT arrays. We will focus on glass transition and crystallization behavior of polymer inside and between the tubes. The first section in this chapter will introduce the experimental method — differential scanning calorimetry (DSC) which is used for this study. The next section will discuss experiments on glass transition of polystyrene (PS) and polydimethylsiloxane (PDMS) infiltrated in CNT arrays of different tube diameter. The last section will present the study of melting and crystallization behavior of PDMS in the bulk and in composites.

5.1 Introduction to the thermal analysis of polymers

5.1.1 Experimental method — DSC

Differential scanning calorimetry (DSC) is a thermal analysis technique that measures heat flow associated with transitions in materials as a function of time and temperature. Such measurements provide qualitative and quantitative information about physical and chemical changes that involve endothermic or exothermic processes or changes in heat capacity. Typically DSC is used to measure melting/crystallization points, glass transitions, heat of fusion and reactions as well as thermal and oxidization stability.

In a standard DSC, the sample material, encapsulated in a pan, and an empty reference pan sit on a thermoelectric disk surrounded by a furnace. As the temperature of the furnace is changed (usually by heating at a linear rate), heat is transferred to the sample and reference through the thermoelectric disk. As heat is transfered through the disk, the differential heat flow between sample and reference is measured. The heat flow $\mathrm{d}H$ is defined as

$$\mathrm{d}H = C_p \mathrm{d}T \tag{5.1}$$

where C_p is the heat capacity and $\mathrm{d}T$ is the heating/cooling rate. The temperature changes linearly during the DSC scan and can be controlled in a broad temperature range. The temperature can also be kept constant in order to obtain information about isothermal behavior of the sample. In these experiments the variation of the heat flow with time can be observed. Isothermal measurements allow to investigate the isothermal crystallization kinetics of polymers.

Conventional and modulated DSC

Modulated DSC (MDSC) is a technique which also measures the difference in heat flow between a sample and a reference as a function of time and temperature. However, in MDSC a different heating profile is applied. The temperature is not only a linear function of time anymore. A sinusoidal modulation (oscillation) is overlaid on the linear heating ramp:

$$T(t) = T_0 + \phi_0 t + T_\alpha \sin \omega_0 t \tag{5.2}$$

where T_0 is the starting temperature and ϕ_0 is a constant scanning rate. These two components represent the linear contribution which are similar to a standard (conventional) DSC scan. The last term represents the modulation with an amplitude T_α and an angular frequency $\omega_0 = 2\pi/t_p$ where t_p is the modulation period.

The idea of modulation of the temperature profile was introdued in 1970 by Gobrecht [98]. This method was improved and published by Reading [99–101] and alternatively evaluated by Schawe [102, 103], the theory of MDSC was summarized later by Garden in a review [104]. In modulated DSC the measured heat flow is separated into the underlying heat flow rate Φ_{dc} and a "reversing" component Φ_{rev}. Φ_{dc} is approximately equal to the conventional heat flow rate as observed in a standard DSC scan and Φ_{rev} contains information about processes which are able to follow the alternating heating or cooling. The difference between these two is called "non-reversing" component Φ_{non}, which contains all other processes.

The general case of a time dependent thermal event can be described with a time-dependent heat capacity $C(t)$. If the time dependent process is not far from equilibrium, the enthalpy H can be described in terms of the linear response approximation as a convolution product:

$$\partial H(t) = \int_{-\infty}^{t} \psi(t - t')\partial T(t')dt' \tag{5.3}$$

where $\psi(t)$ is the retardation function characterizing molecular fluctuations.The frequency dependent heat capacity $C(\omega)$ which is the Fourier transform of $C(t)$ is defined as

$$C(\omega) = \int_{0}^{\infty} \psi(t)e^{i\omega t}dt \tag{5.4}$$

where $C(\omega)$ is the complex heat capacity containing the real part $C'(\omega)$, the so-called storage heat capacity, and the imaginary part $C''(\omega)$ named loss heat capacity. The real part describes molecular motion and corresponds to C_p if the system is in equilibrium. The imaginary part corresponds to dissipation.

Thus, the heat flow rate can be expressed as the time derivative of the heat Q at constant pressure P:

$$\Phi(t) = \left(\frac{\mathrm{d}Q}{\mathrm{d}t}\right)_P = \frac{\mathrm{d}H}{\mathrm{d}t} = \int_0^t \psi(t - t')\phi(t')\mathrm{d}t' \tag{5.5}$$

with

$$\phi(t) = \frac{\mathrm{d}T}{\mathrm{d}t}. \tag{5.6}$$

In the classical or conventional DSC when the last term in equation (5.2) equals zero, the heat flow rate is

$$\Phi(t) = C_p\phi_0 \tag{5.7}$$

In MDSC when the temperature profile contains the modulation term (eq. (5.2)) the heat flow rate is a superposition of oscillating and non-oscillating components. Now we assume that the non-oscillating component is a constant during one period of oscillations. This requires a slow scanning rate, meaning that $\phi_0/\omega_0 \ll 1$K. The typical scanning rate in MDSC experiments is less than 1 K/min. Inserting equation (5.2) in equation (5.5) we obtain the expression for the heat flow rate:

$$\Phi(T(t)) = C_\phi(T)\phi_0 + \omega_0 T_a |C(T,\omega_0)| \cos(\omega_0 t - \xi) \tag{5.8}$$

with

$$|C| = \sqrt{C'^2 + C''^2}. \tag{5.9}$$

$C_\phi(T)$ is the apparent heat capacity which, in a standard DSC, is determined at a heating rate ϕ_0, but different from the equilibrium heat capacity C_p. The constant scanning rate can be connected to a certain average frequency ω_ϕ. ξ is the phase shift between heat flow and temperature change.

At relatively small scanning rate ($\omega_\phi \ll \omega_0$) and an equally small temperature amplitude the obtained heat flow is a superposition of two independent signals: underlying heat flow Φ_{dc} and oscillating heat flow. The last component can be separated into "reversing" and "non-reversing" heat flow. Φ_{rev} corresponds to the modulus of the heat capacity [102]:

$$\Phi_{rev}(T,\omega_0) = |C(T,\omega_0)|\phi_0 \approx \sqrt{C_p(T)C'(T,\omega_0)}\phi_0 \tag{5.10}$$

The non-reversing component results from the difference between C_ϕ and $|C(\omega_0)|$. From the physical point of view the non-reversing component does not contain any additional information.

MDSC is used to study the same material properties as conventional DSC including: transition temperatures, melting and crystallization, and heat capacity. However, MDSC provides unique capabilities that increase the amount of information that can be obtained from a single DSC experiment, thereby improving the quality of interpretation.

From an experimental point of view parameters such as scanning rate, period and amplitude of modulation should be chosen carefully. The sample must be able to follow the chosen temperature profile. The scanning rate should be relatively slow: at least 4-5 modulations must localized within one thermal event. The amplitude increases sensitivity for the transitions, for example the glass transition. A large amplitude allows to increase the signal in case of low sample mass. However, a too large amplitude may result in a situation where the sample cannot follow the modulation. All parameters can be adjusted experimentally for a certain sample.

5.2 Glass transition of polymers in the CNT array

The physical properties of polymers in confined geometry are not necessarily the same as for bulk polymers. Fundamental investigations of polymer properties in nanoconfined materials have been performed since the early 1990s when the change of glass transition of polymer in thin films was reported by McKenna [105] and the same effect was observed in porous silica [106]. In the last decades many experiments were done in different systems, like thin films [37, 38, 107–109], nanopores [110, 111] and polymer containing particles [39]. Glass transitions of glass-forming polymers are found to decrease [112–116], increase[39, 109, 117] or remain unchanged [118–120].

As was shown in the previous chapters, CNT arrays are nanostructured materials with large surface area and nanoscale confinement may have a strong influence on polymer properties. Polystyrene in CNT composites, dispersed in solution [121] or grafted on SWCNTs [122] has been found to decrease the glass transition temperature by several degrees. The T_g shift depends on molecular weight of the polymer and on volume fraction of nanotubes. McCoy and Curro [123] formulated a theory explaining

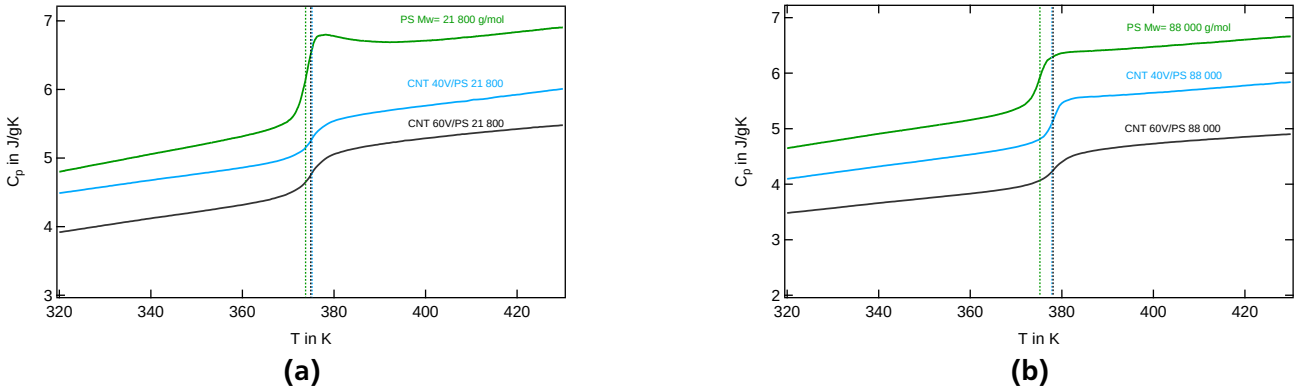

Figure 5.1.: Glass transition of bulk PS and PS in the CNT array with different tube diameter. Heating rate 40 K/min. **(a)** PS M_w = 21 800 g/mol; **(b)** PS M_w = 88 000 g/mol. Curves have been shifted vertically for better visualization.

the variety of T_g changes in confined geometries using results of Reiter [124] that T_g depends on the effective density of polymer thin films. They have shown that for polymer confined in a narrow slit the shift of T_g is negative for most cases where the interaction between wall and polymer is weak or comparable to the intermolecular interactions between polymer chains. Only for strong wall-polymer interactions T_g can be larger than the corresponding bulk T_g.

Some works on CNT/polymer composites have reported an increase of the glass transition temperature[125, 126] as well as broadening of the transition temperature range [127]. The heat capacity C_p near T_g decreases in the presence of CNTs [122] due to immobilization of polymer by the nanotube surface which also contributes to a higher T_g. On the other hand, Grady et al.[121] have reported an increasing C_p in the presence of CNTs.

This chapter summarizes results of investigation of glass transition of polymers in aligned CNT arrays using differential scanning calorimetry. First of all, CNTs filled with PS will be discussed. In the next section results for CNTs filled with two different polymers simultaneously will be shown: polystyrene inside the tubes and polydimethylsiloxane (PDMS) between.

5.2.1 CNT/PS composites: filling the whole array

In this chapter, the glass transition of polystyrene inside aligned CNT arrays will be discussed. We will compare CNT arrays with two different tube diameters of 40 nm (40V CNT) and 90 nm (60V CNT[1]). PS of two different molecular weights will be investigated.

CNT/PS composites were prepared in the same way as was discussed in previous chapters: by infiltration of polymer melt at high temperature in vacuum. Figure 5.1 shows the DSC heating scan with heating rate 40K/min in the temperature range corresponding to the glass transition. Figure 5.1a and 5.1b represent the glass transition of PS in bulk and in the CNT array for two different molecular weight of PS: 21 800 g/mol and 88 000 g/mol correspondingly.

The experiment was performed in a cycle consisting of three temperature scans: heating-cooling-heating with equilibration time of 5 min before every scan. The first heating scan was used to bring the sample in contact with the DSC pan in order to achieve good thermal contact. The second heating scan is shown in figure 5.1. Calculation of all parameters of the transition region (T_g, ΔT and ΔC_p) is explained in appendix B.1.

[1] The labels 40V and 60V correspond to the voltage applied during preparation of PAOX template which is used for synthesis of CNTs. The voltage influences the final pore diameter and consequently the CNT diameter (see chapter 3.1)

PS M_w = 21 800 g/mol			
parameter	**bulk PS**	**CNT 40V**	**CNT 60V**
T_g, K	273.7	375.0	375.1
ΔT, K	3.8	6.8	6.9
ΔC_p, J/gK	1.1	0.56	0.64

PS M_w = 88 000 g/mol			
parameter	**Bulk**	**CNT 40V**	**CNT 60V**
T_g, K	275.3	377.8	378.0
ΔT, K	4.6	4.1	7.35
ΔC_p, J/gK	0.98	0.67	0.60

Table 5.1.: Parameters of glass transition of bulk PS and PS in CNT arrays. T_g is the glass transition temperature, ΔC_p the difference of heat capacity at the glass transition and ΔT the broadness of the glass transition.

The glass transition temperature depends on the molecular weight of the polymer. PS is one of the most investigated polymers and T_g is well known to increase with increasing molecular weight of the polymer[128]. Comparing the green curves on the left and right plots of figure 5.1 and the values of T_g listed in table 5.1[2] one observes that for PS 88 000 $T_g = 275.3K$ which is around 1.5 K higher than T_g of PS 21 800. The other two curves in both graphs represent PS in CNT arrays with 40V and 60V tubes. One observes that inside CNT arrays T_g is shifted to the higher temperature range for both molecular weights of polymer. This shift is larger for the polymer with higher molecular weight. For low molecular weight the shift of T_g (ΔT_g) is around 2K and for high molecular weight of PS $\Delta T_g = 4K$. At the same time tube diameter does not significantly influence T_g, as the glass transition of PS in 60V tubes and in 40V tubes is observed at almost the same temperature.

Together with shift of T_g we observe that the temperature range ΔT of the glass transition is broader for the CNT/PS composites compared to bulk PS (see table 5.1) although there is no systematic change of ΔT with molecular weight and tube diameter.

The heat capacity of polymer in the CNT array decreases compared to the bulk PS. It means that polymer near the CNT wall is immobilized and does not change its mobility at T_g [122]. The difference in C_p at T_g is shown in table 5.1. The heat capacity of polymer inside the CNT array is approximately 40% smaller than for bulk PS. We observe no systematic change in C_p depending on the tube diameter and the molecular weight of polymer. In the presented experiment the heat capacity is normalized to the total mass of the sample and not only to the mass of PS. Indeed, this introduces a systematic error in the calculation of ΔC_p. Nevertheless, the sample mass is defined by polymer mass mostly, since the mass of CNTs is much smaller than the mass of the polymer. For example, the investigated mass of the sample is around 4 mg, the corresponding volume of pure CNTs has a mass lower than 0.1 mg and cannot be precisely determined with the laboratory balance. We can assume that the error of the mass is 0.1 mg. Another factor which can affect the change of heat capacity is the contact between sample and DSC pan. The sample is made as thin film which remains solid in the measured temperature range. Due to curvature of the film the contact between the pan and the sample can be weak and a part of heat can be lost. However, the sample always contains a thin polymer layer on top which creates a good thermal contact to the pan. Moreover, we do not observe a curvature of the thermogram which is a possible indication of bad contact. Thus, systematic errors in this experiment are significant and only large difference in ΔC_p and ΔT should be taken as indication of the change of polymer properties. As we can see in table 5.1 ΔC_p is 40% smaller that for bulk PS. This difference is large enough to suggest

[2] Usually in DSC the recorded thermograms contain no uncertainties of the measured values. For this reason all parameters directly obtained from the thermogram are presented without error bars. Possible uncertainties will be discussed in the text.

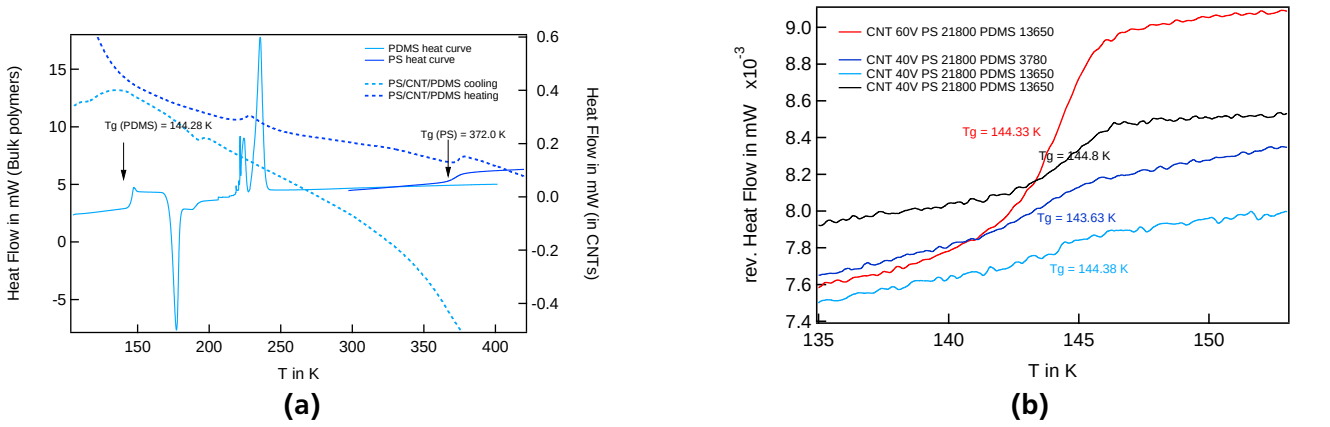

Figure 5.2.: (a) Temperature scan of PS/CNT/PDMS and bulk polymers. Heating rate 10 K/min. **(b)** Modulated temperature scan of PS/CNT/PDMS representing glass transition of PDMS in composites. Modulated parameters: amplitude 1K, period 60 sec, heating rate 0.25K/min. Curves have been shifted vertically for better visualization.

that the mobility of polymer is changed in the presence of CNTs. ΔT is also increased by 50% for PS in CNTs, which is significant enough to consider the broadening of the transition.

5.2.2 PS/CNT/PDMS composites: T_g of polymer inside and between CNTs

The glass transition temperature of polymer in the CNT array shifts to higher temperature and exhibits a broadening of the transition region. However, the CNT array is a complex system with two different shapes of surfaces that introduce two different confinements — inside the cylindrical tubes and between them. The aim of this section is to investigate the glass transition region of polymer inside and between nanotubes separately. For this aim two different polymers can be infiltrated in the array: one polymer is infiltrated inside CNTs, and a second, different polymer in the interstices between the tubes.

Polymers with well separated T_g were chosen. Polystyrene with molecular weight of 21 800 g/mol was infiltrated inside CNTs before etching the PAOX template. In this case interspaces between CNTs are closed by the template and polymer fills the tube interior only. The second polymer (PDMS) was infiltrated in the array after removing the PAOX template. Since the melting temperature of PDMS is much lower than the melting temperature of PS, PS remains solid and the tube interior is blocked for PDMS infiltration. PDMS can flow into spaces between tubes only. Therefore, we obtain the CNT array filled with two different polymers having well separated T_g ($T_g^{PS} = 372\,\mathrm{K}$, $T_g^{PDMS} = 144\,\mathrm{K}$).

The conventional temperature DSC scan is shown in figure 5.2a. Bulk polymers (solid lines) were measured separately in different scans under the same conditions. Every curve was measured three times: heating, cooling and heating again with an equilibration time of 5 minutes before every scan. The second heating curve is shown in figure 5.2a. The cooling scan does not contain extra information about polymers. Bulk PDMS has $T_g = 144.28$ K, a crystallization peak around 180 K and two melting peaks. The measured T_g of PS is 272 K which is slightly smaller than the obtained T_g in the first experiment due to different calibration settings of the instrument.

The dashed curves in figure 5.2a represent heating and cooling scans of the PS/CNT/PDMS composite. The glass transition and crystallization of PDMS are only visible in cooling scans. The melting peak of PDMS and glass transition of PS are visible in the heating scan. The melting and crystallization of PDMS will be analyzed and discussed later in chapter 5.3. Here we consider only the glass transition phenomena. It can be seen that the baseline of composites is curved. A possible explanation of this effect

		PS M_w= 21 800 g/mol				
parameter	**bulk PS**	**CNT 40V1**	**CNT 40V2**	**CNT 40V3**	**CNT 60V1**	**CNT 60V2**
T_g, K	372	374	374	371	376	374
ΔT, K	4.7	4.1	3.5	10.0	9.5	4.0

		PDMS				
parameter	**PDMS 13650**	**CNT 40V1**	**CNT 40V2**	**CNT 40V3**	**CNT 60V1**	**CNT 60V2**
T_g, K	144.3	143.6	144.8	144.4	144.3	-
ΔT, K	2.5	3.7	3.5	12.6	3.7	-

Table 5.2.: Glass transition temperature T_g and broadness of transition range ΔT of polymers in the PS/CNT/PDMS composite. Labels in table: **CNT 40V1** is CNT 40V PS 21 800 PDMS 3780 (blue line in figures 5.2b and 5.3a); **CNT 40V2** is CNT 40V PS 21 800 PDMS 13650 (black lines); **CNT 40V3** is CNT 40V PS 21 800 PDMS 13650 (light blue lines); **CNT 60V1** is CNT 60V PDMS 21 800 PDMS 13650 (red lines); **CNT 60V2** is CNT 60V PS 21 800 without PDMS (magenta line).

is the very low mass of polymer in the sample (the total sample mass is less than 2 mg). Another reason might be a weak contact of sample with pan causing losses of heat conductivity.

Comparing bulk polymers and polymers in the CNT array one observes that the thermal response of PS is stronger than the response of PDMS in the composite. This can be explained by a different amount of polymers inside and outside tubes. As was discussed in section 4.2.3 CNT arrays with 40V tubes have more volume inside CNTs than outside. The separation between tubes is around 2 nm in contrast to 40 nm diameter of the tube. It also was mentioned that arrays with 60V CNTs have the inverse situation: more polymer was observed between CNTs due to collapse of CNTs along their length. This is also seen in the thermogram of the arrays with 60V (see blue line in figure 5.4). Here the signal from PDMS is well pronounced.

Due to the deformation of the baseline and the low signal from PDMS determination of the glass transition of PDMS is not possible in the normal DSC scan. To increase the sensitivity modulated DSC was performed. The principles of modulated DSC was described in section 5.1.1. Results are shown in figure 5.2b. The main signal was modulated by an oscillation signal with 1 K amplitude and 60 sec period of modulation. The heating rate is 0.25 K/min. PS/CNT/PDMS composites with tube diameter of 40 nm (40V tubes) and 90 nm (60V tubes) with PDMS of molecular weight of 13 650 g/mol and 3780 g/mol were measured with MDSC and compared with bulk PDMS measured with the same modulated parameters. The obtained T_g of bulk PDMS in MDSC is similar to the normal DSC scan which resulted in $T_g = 144.3$ K for high molecular weight and $T_g = 143.4$ for low M_w.[3] As shown in figure 5.2b there is no shift of T_g for every chosen molecular weight of PDMS. The deviation of T_g is less than 1K.

As shown in table 5.2, there is no significant broadening of the transition temperature range. There is only one sample which shows broadening: this sample corresponds to the light blue line in figure 5.2b. One observes that this curve has a not well pronounced step at T_g probably due very low amount of PDMS in the composite. Indeed this very weak signal can cause a systematic error in determination of the transition range (see appendix B.1).

The polymer between CNTs does not show a deformation of the transition region and shows T_g and ΔT comparable with the bulk polymer. Let us now consider the polymer inside tubes. Thermograms showing the glass transition region of samples are obtained in a standard DSC scan and presented in figure 5.3a. Comparing all curves in the figure, we can observe that ΔC_p for composites is lower than for bulk PS. In the graph C_p is normalized to the total mass of the sample and not to the mass fraction of PS since it impossible to calculate. Composites now contain not only PS which contributes to the total mass, but PDMS as well. We cannot neglect the weight of PDMS and consequently not analyze ΔC_p quantitatively.

[3] Bulk PDMS is not shown in the plot since it results in the same T_g as a standard DSC scan.

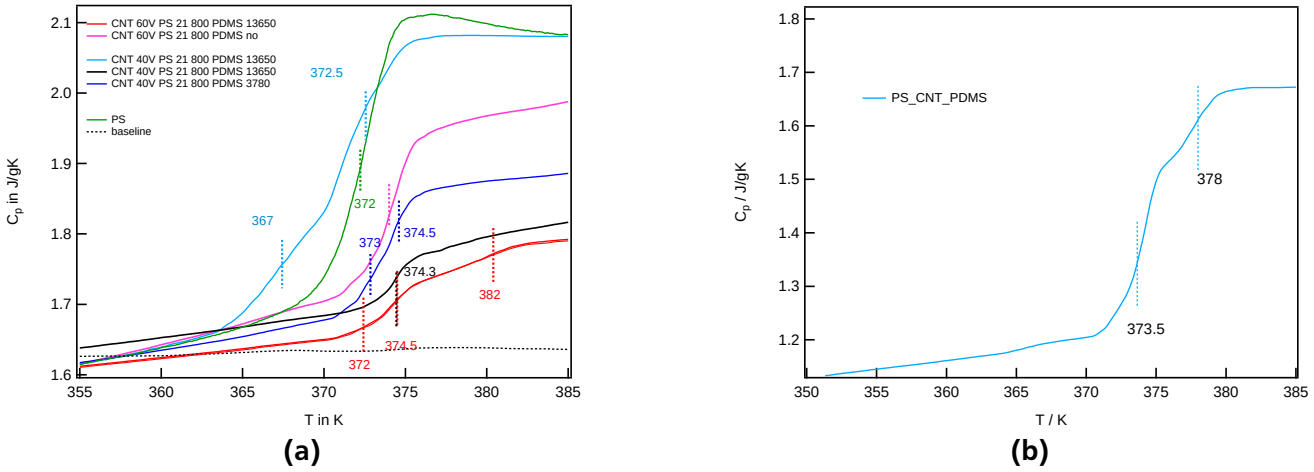

Figure 5.3.: Glass transition of PS infiltrated in the CNT interior. **(a)**: Tube diameter is 40 nm (40V) and 90 nm (60V). Heating rate 40K/min. Curves are shifted vertically for better visualization; **(b)**: Another experiment on a sample with tube diameter of 40 nm, heating rate 40 K/min.

One of the samples shown in light blue (fig. 5.3a) has step in C_p comparable to the bulk which indicates a high contribution of PS to the total mass of the sample. Comparing signals in figure 5.2b one observes that the step of the PDMS transition in this curve (light blue) is smaller than for other samples, which indicates a rather small mass of PDMS in the sample. Since the total mass of this samples is comparable to the others (around 2 mg) PS has a dominating contribution to the total mass which is shown in the large step of C_p at the glass transition.

One observes that PS in CNTs has a shift of T_g with respect to the bulk PS. In table 5.2 the average T_g is listed. One observes that almost all arrays have a T_g of 2 K higher than the bulk PS which is in agreement with results discussed in the previous section. However, the obtained T_g has a width distribution around 2K which is equal to the average shift. Moreover, one of the samples has a T_g lower than T_g of the bulk PS. A close inspection of the plot shows that some curves have a complicated shape of the transition range where we can clearly see two transition temperatures. For example, CNT 40V shown as dark blue line in figure 5.3a exhibits two transitions: 373 K and 375 K. The first transition corresponds to the bulk T_g of PS, the second one is shifted to a higher temperature. The shift is even more pronounced in the red line corresponding to 60V tubes. Here we can separate three transitions: 372K, 374.5 K and 382 K. The splitting of T_g might be caused due to confined polymer in vicinity of the CNT surface. The mobility of the polymer can be restricted. The T_g splitting is also observed in another experimental series on a PS/CNT/PDMS composite containing 40V tubes (fig. 5.3b). The thermogram is recorded with different calibration of the instrument and the absolute value of T_g can be slightly different from the one obtained before. However, the T_g of bulk PS is well reproducible within of 1 - 1.5 K. The calibration of the instrument can play an important role since we try to analyze a very small shift of T_g. Most of the curves clearly show that PS inside CNTs contains two different phases: a bulk phase and a confined phase in vicinity of CNTs with restricted mobility of chains. Going back to figure 5.3a, we see that two samples which also have positive ΔT_g (black and magenta lines) show a rather smooth transition with only one T_g. We can observe small fluctuations in the black line between 375 K and 380 K, which might correspond to a second transition, but the signal is too weak to draw a clear conclusion. Some fluctuations are visible in the magenta line between 370K and 375 K which might be interpreted as a transition around 372 K.

However, the average T_g shows a shift of 2 K. The second T_g is not reproducible from sample to sample and located in the range from 374 K to 382 K. In contrast to most of the samples, the light blue curve

exhibits the second T_g at lower temperature (around 368 K) but keeps the same structure of transition range having two steps.

One important remark concerning the determination of glass transitions are experimental errors. Usually DSC is a precise method to measure all parameters of the transition range. However, in the presented experiments we found low reproducibility of the obtained values and dependence on calibration of the instrument. It plays an important role due to the small shift of T_g which is in the range of the errors of the bulk value. Moreover, the low sample mass and structure of samples introduce another experimental error. The low signal and curvature of the thermogram make measurements sensitive to the quality of the baseline. Furthermore, the fits which are performed for the determination of T_g and ΔT can result in large uncertainties. A higher sample mass and a better contact between sample and the pan allow for higher precision of the obtained values. Nevertheless, several experiments with different samples prepared independently show the same tendency of a small increase in T_g and a complex structure of the glass transition region for PS infiltrated into the tube interior. On the other hand, PDMS infiltrated between tubes exhibits no change of T_g. Although there is a clear difference between polymer inside and outside CNTs, both polymers have a different structure. In contrast to PS, which is a glassy polymer, PDMS is semicrystalline. To study the behavior of PDMS in confinement one has to investigate the melting and crystallization as will be described in the following section.

5.3 Melting and crystallization of PDMS around CNTs in the array

Crystallization is a phase transition which defines the final properties of many technologically relevant systems. The crystallization is an important process of tailoring composite materials since the preparation from melt is a widely used technique. In principle, many common polymers with linear structure can be crystallized. Polymer crystallization has some peculiarities and is different from the crystallization of simple liquids. Due to polydispersity and cross-links polymer chains cannot form a crystal lattice in its classical meaning and can be only partially crystallized. Thus, the polymer contains crystalline and amorphous phases, the ratio between them defines the crystallinity of the polymer. Polymer crystallization involves chain ordering. From a classical point of view, chains pack in a regular manner by folding along the short direction of the growing lamellar layer. Lamellae have a constant grow rate until they impinge on each other. The polymer crystallization can be divided into two steps: nucleation and growth. First of all, nuclei are formed, this process is usually called primary nucleation. This process is necessary for homogeneous nucleation since the polymer does not have seeds to build crystals. Nucleation occurs when the polymer is supercooled. In the case of homogeneous nucleation, the number of nuclei is assumed to be a linear in time. Subsequently, layers are formed on the existing nuclei. This is secondary nucleation and growth. Polymer chain segments are adsorbed onto the surface of the primary nuclei. During this process the polymer forms spherulites. Later, the obtained spherulites can come in contact with each other and secondary crystallization between the spherulites occurs.

Strobl [129] suggested that crystallization from the entangled melt is a multi stage process. The first step is formation of a mesomorphic layer caused by density fluctuations. In this state, polymer chains keep a melt-like mobility but at the same time have a preferred orientation. The thickness of this layer grows with time and as soon as the critical thickness is reached, polymer chains transform into a granular crystal layer. Finally, granular crystal layers merge together and form a lamellar crystal.

Therefore, crystallization is a kinetically controlled process. This section resumes the discussion about thermal properties of polymers in CNT arrays and it is focused on the experimental study of melting and crystallization of PDMS in a matrix of CNT arrays. First of all the theoretical models to describe the crystallization kinetics based on the Avrami phenomenological approach will be introduced. In the next section the first observation of crystallization behavior of polymer in interstices of CNT arrays with different tube diameters will be discussed. The last two sections will deal with the isothermal and non isothermal crystallization of PDMS in bulk and in CNT arrays.

5.3.1 Description of theoretical models of polymer crystallization

Many approaches for describing kinetics of crystallization are based on the Avrami equation:

$$X_t = 1 - \exp(-K_\alpha t^n). \tag{5.11}$$

Here X_t is the relative crystallinity at time t and n is the Avrami exponent which reveals the nucleation mechanism and dimensionality of the growing crystal. For example $n = 1$ corresponds to the predetermined one dimensional crystallinity [128]. The coefficient K_α is the crystallization rate constant and characterizes the crystallization mechanism as well. The Avrami equation (eq. (5.11)) describes the isothermal crystallization of polymers. Avrami analysis does not take into account the phase transformation kinetics [36] and the second crystallization process. In real polymers the deviation from a single Avrami process can be observed at longer crystallization times. Nevertheless, the Avrami equation is widely used and suitable for describing crystallization kinetics of many polymers. For analysis of experimental data equation (5.11) can be rewritten in logarithmic form:

$$\log[-\ln(1 - X_t)] = \log K_\alpha + n \log t. \tag{5.12}$$

This representation of the Avrami equation allows to analyze the crystallization graphically using linear fit functions. For analysis of nonisothermal crystallization the Avrami equation has to be modified. The parameter K_α must be corrected for the nonisothermal case. Considering nonisothermal crystallization kinetics, Ozawa extended the Avrami equation [130] by taking into account the cooling/heating rate ϕ and incorporate it into the equation using a mathematical derivation of Evans [131]. The final form of the Ozawa equation is as follows:

$$1 - X_T = \exp\left(-\frac{K(T)}{\phi^m}\right) \tag{5.13}$$

where X_T is now temperature dependent relative crystallinity, $K(T)$ a cooling/heating function which has complex integral form [130] and m is the Ozawa exponent which has a similar meaning as the Avrami exponent and depends on the dimension of the crystal growth. This equation can be expressed in logarithmic form just as the Avrami equation above:

$$\log[-\ln(1 - X_T)] = \log K(T) - m \log \phi. \tag{5.14}$$

If Ozawa's approach is valid to describe the nonisothermal crystallization, equation (5.14) should result in a linear dependency of $\log[-\ln(1-X_T)]$ on $\log \phi$. The Ozawa equation is derived from Avrami's approach, ignores the secondary crystallization and temperature dependency of the chain folding length [36]. In order to take this into account, Mo and coworkers [132] further modified the Ozawa equation combining it with Avrami:

$$\log K_\alpha + n \log t = \log K(T) - m \log \phi \tag{5.15}$$

which can be rewritten as:

$$\log \phi = \log F(T) - b \log t \tag{5.16}$$

where

$$F(T) = (K(T)/K_\alpha)^{1/m} \tag{5.17}$$

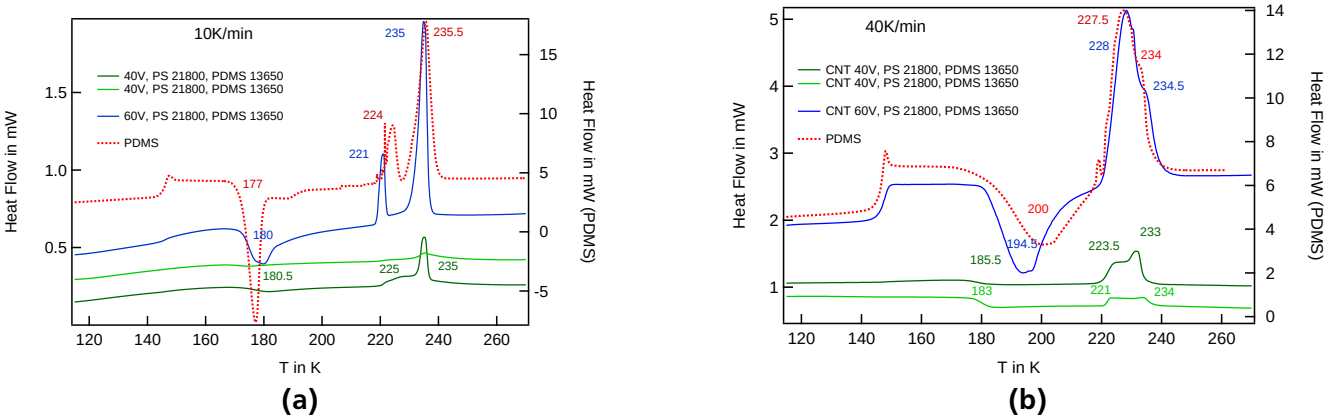

Figure 5.4.: Heating DSC scan for PS/CNT/PDMS composite with different tube diameter and molecular weight of PDMS: **(a)** rate 10 K/min; **(b)** rate 40 K/min. Blue curves correspond to the CNT 60V, both green curves represent CNT 40V, these composites were prepared independently under the same conditions.

refers to the heating/cooling rate which has to be chosen for a certain degree of the crystallinity at unit crystallization time t. $F(T)$ has a defined physical meaning and can be compared with the Avrami crystallization rate. Experimentally the time t is calculated for the chosen degree of crystallinity (20%, 40%, 60% and 80%) at the every measured scanning rate and shows how much time the polymer needs to achieve the chosen degree of crystallinity. The exponent $b = n/m$ is the ratio between the Avrami and the Ozawa exponent. A plot of $\log \phi$ vs $\log t$ at a given crystallinity gives a straight line. Parameters $F(T)$ and b can be estimated from the intercept and the slope of the line correspondingly.

The crystallization time can be calculated as follows:

$$t = \frac{|T_0 - T|}{\phi} \tag{5.18}$$

where T is the temperature at time t and T_0 is the initial onset temperature at $t = 0$ when the crystallization begins.

5.4 Effect of tube diameter and heating rate

In this section standard DSC thermograms of PDMS and CNT/PDMS composites will be considered. Samples are scanned in a cooling and subsequent heating cycle. Cooling and heating are performed with constant rate of 10 K/min and 40 K/min. A typical heating scan of PS/CNT/PDMS[4] composites at different heating rates is shown in figure 5.4. The dashed red curve corresponds to the heating scan of the bulk PDMS. One observes that the bulk PDMS has a glass transition at 145 K, one crystallization peak depending on the heating rate and two melting peaks which are almost merged at a heating rate of 40 K/min. The obtained thermogram is in agreement with literature [33, 34, 133]. At both heating rates the cooling scan of the bulk PDMS does not show any obvious features. The crystallization peak has vanished due to the relatively high cooling rate. It is well known that the crystallization during cooling is almost quenched at a rate higher than 5-7 K/min [33]. The crystallization peak in the heating scan is called cold crystallization which corresponds to a recrystallization of the metastable crystals which were formed during cooling [34]. Two melting peaks correspond to the melting of metastable

[4] In this chapter only the crystallization of PDMS is discussed. To avoid confusion further in the text the composite will be named as CNT/PDMS

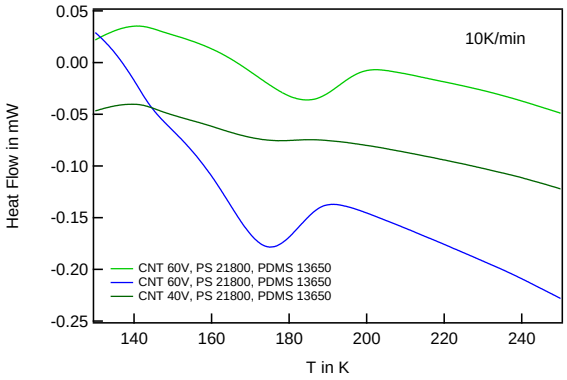

Figure 5.5: Cooling DSC scan of CNT/PDMS composites.

and stable crystals respectively. The more stable crystals melt at higher temperature, while the less perfect crystals have a lower melting point. Comparing the two heating rates, one observes that the ratio between first and second melting peak changes: at 10 K/min the second peak clearly dominates, the cold crystallization peak is very narrow which indicates that more stable crystals are formed at low heating rate. There is only a small fraction of the less perfect crystals. At the rate of 40 K/min the second melting peak decreases and first peak dominates. At this rate the polymer does not have enough time to form a lot of stable crystals and the average quality of crystals decreases. This can also be seen in significant broadening of melting and crystallization peaks.

Comparing the DSC curves of CNT/PDMS composites (solid curves) with bulk PDMS one observes the influence of the CNT diameter on the melting and crystallization behavior. PDMS around the CNT with large tube diameter (CNT 60V) has the same position of the maximum of the cold crystallization peak at 10 K/min. The peak is less pronounced than in bulk due to the smaller mass of the polymer in the CNT array. The first melting peak is shifted to lower temperatures while the position of the second peak remains unchanged. At 40 K/min the cold crystallization peak has its maximum at lower temperature than bulk PDMS, but both melting peaks have the same position compared to the bulk polymer. Thus, the cold crystallization starts earlier in the presence of CNTs. Both green curves in figure 5.4 correspond to CNT/PDMS composites with small tube diameter (CNT 40V). These two composites were prepared independently using CNT arrays with the same tube diameter and polymer of the same molecular weight. Small differences can occur in the polydispersity of the tube radius, the separation between CNTs and the filling factor. Since the CNT array has a thin layer of polymer on top the thickness of this layer can vary from sample to sample as well.

The signal shown by the light green curve (sample 2) is smaller than dark green (sample 1) which indicates that sample 1 contains less polymer than sample 2. Smaller polymer mass in the total mass of the sample is caused by two reasons: first, the bulk polymer layer on the top of the array is significantly thinner and second, less polymer is located between tubes. This can happen due to the smaller tube separation or the smaller filling factor, which lead to a lower fraction of the bulk polymer in sample 2. Decreased tube separation gives a stronger confinement and consequently increases the amount of interface per unit volume of polymer.

We do not observe cold crystallization of PDMS in the interstices of 40V CNTs. However in contrast to bulk PDMS the cooling DSC scan shown in figure 5.5 exhibits a crystallization peak called melt crystallization. This demands to consider enhanced crystallization of PDMS in the presence of CNTs. Enhanced crystallization indicates that more polymer is able to crystallize during cooling and forms more stable crystals which is corroborated by the well pronounced second melting peak in contrast to the weak first melting peak. The CNT/PDMS composite with 60V CNTs shown in the same plot has the melt crystallization peak as well. The obtained results show that in both CNT arrays (with small and big tubes) the crystallinity increases.

Now we go back to analysis of the thermogram of CNT/PDMS composites with small tubes. Similar to CNT 60V the composites with small tubes exhibit the cold crystallization peak earlier than the bulk PDMS

at 40 K/min (5.4b). Moreover, both composites with 40V CNTs have the cold crystallization peak 10 K lower than composites with large tubes. This can be a sign that crystallization of the polymer around smaller tubes is even more enhanced. There are also differences in the melt behavior. Both melting peaks are not merged anymore. While the second melting peak remains at the same position as in the bulk, the first peak has a shift of around 5K to lower temperatures. Although the second melting peak decreases with increasing heating rate, it still dominates (dark green curve) or has the same height (light green curve) as the first peak. This again indicates enhanced crystallization and better ordered crystals of the polymer in the presence of CNTs.

As was shown in this section, including the CNTs in the polymer matrix significantly affects the melting and crystallization behavior of the polymer. Analysis of heating and cooling thermograms of CNT/PDMS composites and comparing them with bulk PDMS leads to the finding of enhanced polymer crystallization in the presence of nanotubes. This effect is stronger for tubes with smaller diameter. For quantitative analysis of polymer crystallization around CNTs we will investigate kinetics of isothermal and nonisothermal crystallization of PDMS in composites in the following sections.

5.4.1 Isothermal crystallization of PDMS around CNTs in the array

The isothermal study of polymers proceeds at a certain temperature lower than the melting point but far above the glass transition. The closer the chosen temperature T_c is to the melting temperature, the slower is the crystallization process. Isothermal crystallization of PDMS is investigated on a standard DSC instrument. Polymer is equilibrated at room temperature and then cooled down as fast as possible to the chosen temperature. The cooling rate is uncontrollable and defined by the instrument itself. As soon as the sample is equilibrated at T_c the heat flow is recorded as a function of time. In the beginning the heat flow $\mathrm{d}H/\mathrm{d}t$ decreases with time, reaches a minimum, then increases and finally shows a plateau. As soon as the plateau is reached, the crystallization is finished. The obtained peak can be integrated over time in order to determine the relative crystallinity X_t:

$$X_t(t) = \frac{\int_{t_0}^{t} \frac{\mathrm{d}H}{\mathrm{d}t}\mathrm{d}t}{\int_{t_0}^{t_\infty} \frac{\mathrm{d}H}{\mathrm{d}t}\mathrm{d}t} \tag{5.19}$$

where t_0 is the beginning of the crystallization and t_∞ is the end, where the heat flow reaches the plateau. t_0 does not always correspond to the initial starting point of crystallization. Since the cooling and equilibration need some time, at low temperatures the crystallization can start before the measurement. However, the absolute crystallinity is not necessary for analysis of crystallization kinetics because relative crystallinity is the crystallinity at the time t normalized to the total peak area.

The relative crystallinity is shown in figure 5.6 as a function of time. The left plot (fig. 5.6a) shows X_t for bulk PDMS at different temperatures. The time needed for crystallization increases with increasing temperature. Increasing the temperature by 15 K leads to extending the crystallization time from 5 minutes to almost an hour. In contrast to the bulk polymer, PDMS around CNTs with large tube diameter (CNT 60V) (fig. 5.6b) has less difference between crystallization times at $T = 183$ K and $T = 198$ K. One observes that polymer around these CNTs crystallizes much faster than in the bulk. This is well observed at $T = 198$ K: crystallization in the array is completed after approximately 13 minutes while in the bulk PDMS crystallizes much longer.

Figure 5.6c illustrates isothermal crystallization of PDMS around CNTs with small tube diameter (CNT 40V). Both curves show the crystallization at $T = 188$ K, but samples were prepared independently. The dark green curve shows a slow continuous increase of the crystallinity with time without any bends. The light green curve has two clearly separated steps and polymer crystallizes faster. The same samples demonstrated a different behavior in normal DSC scans as well (see fig. 5.4, colors are corresponding). As was discussed above in the previous section, it might be due to different ratio of bulk and confined

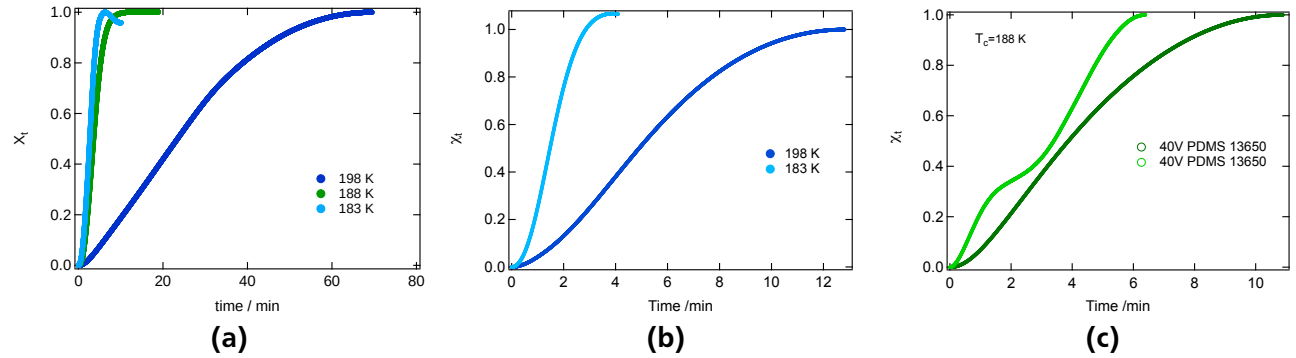

Figure 5.6.: Isothermal crystallization of PDMS around CNTs in the PS/CNT/PDMS composites: **(a)** Bulk PDMS; **(b)** PDMS in the array with 60V tubes; **(c)** PDMS in the array with 40V tubes. These composites were prepared independently under the same conditions and correspond to the composites shown in figure 5.4.

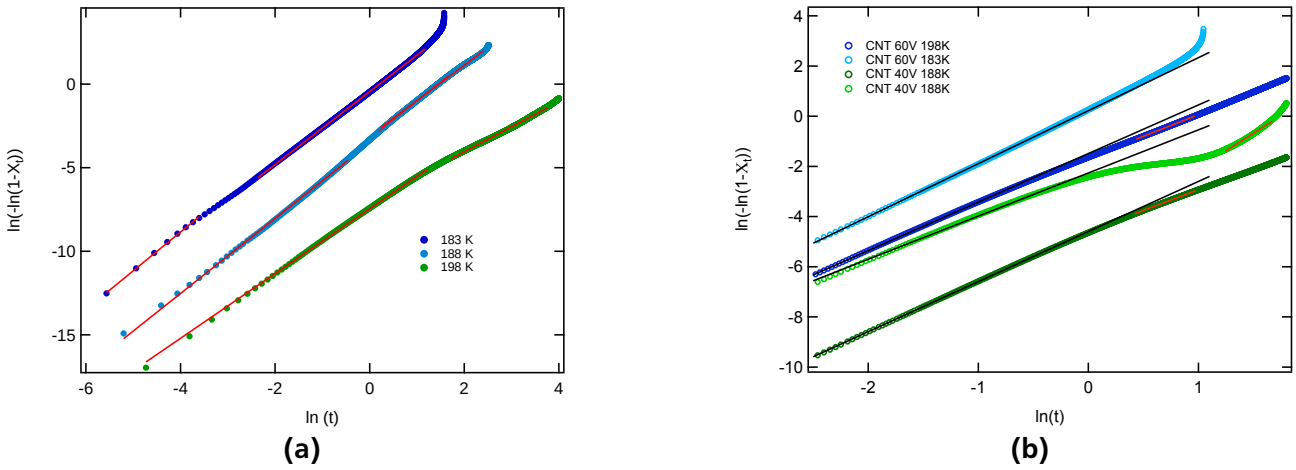

Figure 5.7.: Avrami representation of isothermal crystallization of PDMS: **(a)** Bulk PDMS; **(b)** PDMS in the CNT array.

polymer in the sample. The sample represented by the light green curve has less polymer on the top of the array and more polymer between the CNTs.

Considering the Avrami crystallization, the relative crystallinity X_t can be represented in double logarithmic form and fitted with a linear function in order to obtain parameters K_α and n in equation (5.12). These plots are shown in figure 5.7. The first plot (fig. 5.7a) shows the results for bulk PDMS. Every curve has an initial linear dependency, then subsequently changes the slope. This fact indicates that the secondary crystallization exists. In the classical crystallization theory, the secondary crystallization stage is caused by impingement of spherulites at longer crystallization times. However, in the previous section we mentioned that PDMS crystallizes in two steps: first forming metastable crystals which later transform to the stable state. We can assume that the initial linear slope which is described according to the Avrami equation is a formation of metastable crystals. It is clearly seen that the higher the temperature, the later the bend of the curve appears. Fit parameters are compiled in table 5.3. An Avrami exponent of around 2 for the primary crystallization is found. Metastable crystals are forming in all three dimensions. If we assume that metastable crystals are uniform and occur randomly in the volume the Avrami analysis is suitable in this case.

	Primary stage						
	Bulk PDMS			CNT 60V /PDMS		CNT 40V /PDMS[a]	CNT 40V /PDMS[b]
T, K	183	188	198	183	198	188	188
K_α	0.21	0.021	0.0046	-	0.05	0.075	0.28
n	2.32	2.13	1.85	-	2.0	2.0	1.72
$\tau_{1/2}$, min	1.67	5.17	12.29	-	3.88	3.04	1.69
	Secondary stage						
K_α	0.098	0.041	0.0065	0.28	0.04	0.076	0.015 - 0.058
n	2.15	2.1	1.49	2.1	1.72	1.66	3.0 - 2.0
$\tau_{1/2}$, min	2.48	3.62	22.78	1.54	5.25	3.79	3.59 - 3.26

[a] dark green curve
[b] light green curve

Table 5.3.: Avrami fit parameters of isothermal crystallization of PDMS in bulk and with CNTs of different tube diameters. Uncertainties of all listed parameters are obtained from the fit. These values are small and correspond to the minimum variation of the last shown sign after comma.

In figure 5.7a the part of the curve which does not follow the obtained linear fit is treated as the secondary crystallization stage. This range can be fitted with another linear function which again indicates Avrami type crystallization. A clear linear dependency is observed for the lowest temperature $T = 183$K. Different temperatures have a small curvature, which makes linear fits less precise and can indicate that the secondary crystallization stage deviates from Avrami crystallization. We assume the secondary crystallization to be a transformation of metastable crystals to the stable state. In this case the formed crystals do not occur randomly in the volume, they are formed from a preordered phase. In this case we indeed can expect deviation from Avrami behavior. Although, from the classical point of view, secondary crystallization does not have Avrami type behavior, many researches reported about a linear dependency of relative crystallinity with time in double logarithmic form (see eq. (5.12)). From the linear fit, the secondary crystallization has an Avrami exponent around 2 which is close to the primary stage. Comparing the crystallization rate K_α, one observes that the secondary stage is slower than the primary one. The transformation of metastable crystals is a rather slow process in contrast to their initial formation. However, PDMS at $T = 188$ K shows a different behavior: secondary crystallization is faster than the primary crystallization. The discrepancy can occur due to the thermal memory effect. If melting time is relatively short, the kinetics of the secondary crystallization depends on time and temperature of the polymer in the molten state [134]. Increasing the temperature or time results in reduction of the crystallization rate.

Parameters K_α and n give the half crystallization time, which is defined as the time at which the extent of the crystallization is 50% completed [135] and can be calculated as follows:

$$\tau_{1/2} = (\ln 2/K_\alpha)^{1/n} \tag{5.20}$$

Half crystallization times are listed in table 5.3. For $T = 183$K and $T = 198$K the secondary crystallization is almost twice slower than the primary one. As was mentioned above, due to thermal memory effect $\tau_{1/2}$ of the secondary crystallization for $T = 188$K is smaller than for the primary one. Generally, crystallization is expected to be slower at temperatures close to the melting peak. This is well shown in the table: $\tau_{1/2}$ increases with temperature for both crystallization stages.

In the presence of CNTs the kinetics of isothermal crystallization is changed. First of all, comparing the blue curves in figure 5.7b one observes that at lower temperature PDMS crystalizes in one stage only. Deviation from initial linearity is pronounced at higher temperature. In general, every stage of the crystallization is faster in CNT arrays. As we already discussed, the formation of metastable crystals is faster than their transformation. Thus, the one step crystallization of PDMS at $T = 183$K can be explained by very rapid formation of metastable crystals due to a certain equilibration time in

the beginning of the measurement. Similar to the bulk, the crystallization time of PDMS in CNT arrays increases with temperature. An extreme difference in crystallization time and speed is observed for $T = 198$ K. In the CNT array polymer crystallizes much faster although the difference between bulk and array is not so large at lower temperature. We do not observe a significant change of the exponent n.

Increasing of the crystallization rate is also observed for polymer around smaller tubes (dark green curve in fig. 5.7b). Here both stages of crystallization are faster than in the bulk and again without significant deviation of the value of the Avrami exponent for the primary crystallization stage. For the secondary crystallization stage $n = 1.66$ while for the bulk polymer $n = 2.1$. This is indicating the reduction of the dimension of crystal growth. Since we considered above that bulk PDMS exhibits a temperature memory effect at $T = 188$K , $\tau_{1/2}$ for bulk polymer and for polymer in the array is not comparable. However, the realistic $\tau_{1/2}$ for the bulk PDMS should be larger than the value given in table 5.3 and consequently larger than $\tau_{1/2}$ for PDMS in the array. This results in the enhanced crystallization of PDMS in the presence of the small CNTs.

A different situation is observed for another sample, shown in the same plot in light green color. The initial primary crystallization is twice faster than for the first sample and indeed faster than in the bulk with small decrease of n. In figure 5.7b this curve has a different behavior than others. First of all, we can see primary crystallization, then there is a slow decrease of the slope, and finally the curve again changes the slope. The secondary crystallization has not Avrami type behavior and does not show clear linear dependency. However, there is an obvious difference in crystallization kinetics between two composites with the same tube diameter.

These two samples, as is supposed, have different ratio between the bulk and the confined polymer. The second sample (light green) has more polymer between tubes, which gives rise to consider the enhancing of the crystallization in vicinity of the CNT surface. The closer polymer is to the surface, the faster it crystallizes. The amount of polymer between tubes might vary between two samples as well due to a different filling factor or a slightly different distance between CNTs. Polymer which is situated directly at the wall crystallizes faster than the bulk polymer. The rest of the polymer which is in between tubes has a slower crystallization rate due to restriction of the volume. This can explain the difference in the crystallization rate between two samples having CNTs with small tube diameter.

In summary, the presence of the CNTs in a polymer matrix speeds up crystallization of the polymer. This effect is observed for CNT arrays with tubes of 40 nm and 90 nm in diameter. The higher the chosen crystallization temperature, the more pronounced the difference of crystallization speed is between PDMS in CNT arrays and in the bulk.

5.4.2 Non isothermal crystallization of PDMS around CNTs in the array

To analyse the nonisothermal crystallization of PDMS standard DSC scans are recorded at different heating and cooling rates. Just as for the isothermal crystallization, the relative crystallinity X_T can be determined as the area under the crystallization peak up to certain time divided by the total peak area. Now X_T is considered as a function of temperature and not time:

$$X_T = \frac{\int_{T_0}^{T} \frac{dH}{dt} dT}{\int_{T_0}^{T_\infty} \frac{dH}{dt} dT} \tag{5.21}$$

T_0 and T_∞ correspond to the onset temperature at $t = 0$ and the temperature when the crystallization ends.

5.4.3 Crystallization of bulk PDMS

As was reported in literature [33, 133] PDMS shows two crystallization peaks: one peak is observed during cooling scan and the second peak during heating only. Crystallization in the cooling scan is called

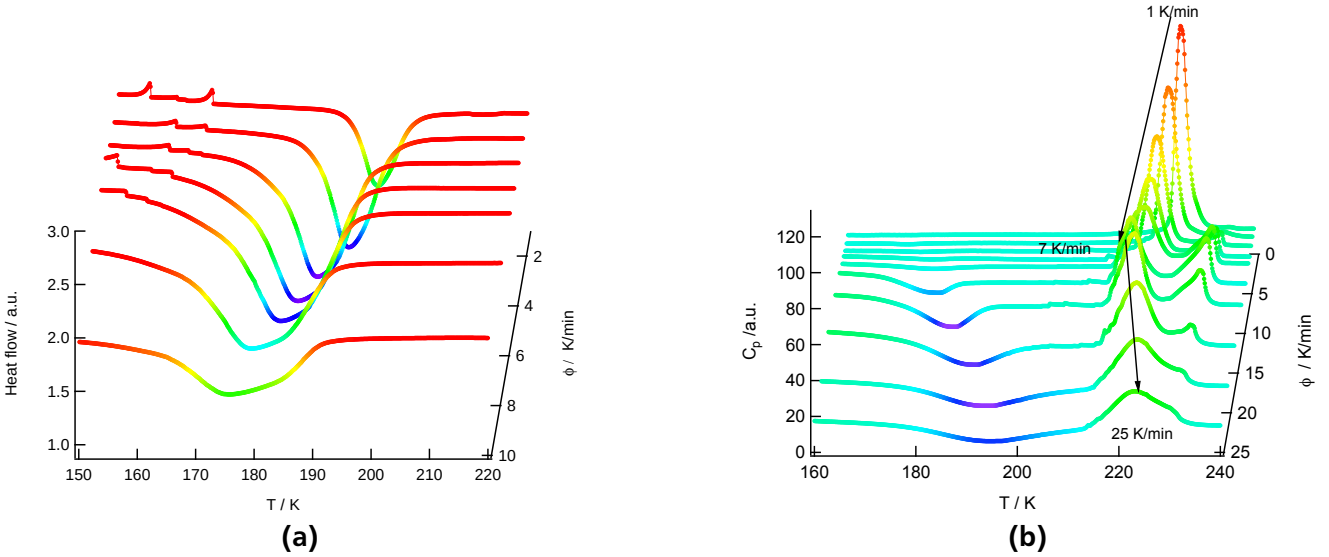

Figure 5.8.: (a) Cooling scans of PDMS with different temperature scanning rate; **(b)** Heating scans of PDMS with different temperature scanning rate.

melt crystallization and observed usually at low scanning rates. Crystallization during heating is called cold crystallization and it is quenched at low scanning rates. Both crystallizations are interdependent and in this work they will be studied together.

For investigation of nonisothermal crystallization samples are cooled from the melt to the glass transition temperature with a certain cooling rate, then subsequently heated up to the melt state with the same rate. Thermograms of different cooling/heating rates are compared. Cooling and heating DSC scans of bulk PDMS are shown in figure 5.8. Both scans exhibit a crystallization peak in the range 170-200 K depending on the heating/cooling rate. As was discussed above, PDMS forms metastable crystals during cooling which later recrystallize during heating. In figure 5.8a one observes that with increasing cooling rate the crystallization peak is getting broader and is shifted to lower temperatures. At faster cooling rates there is no time to form crystals during cooling, the crystallinity significantly decreases. This is supported by the decreasing area of the crystallization peak (see in figure 5.8a). The peak is integrated and values of the peak area are shown in table 5.4. One observes that with increasing scanning rate the area of the melt crystallization peak ΔH_C systematically decreases. The broadening of the peak corresponds to the formation of nonuniform crystals which crystallize in a broad temperature range. At cooling rates higher than 10 K/min melt crystallization is completely quenched. The opposite situation is observed for the cold crystallization shown in figure 5.8b. The area of the crystallization peak increases with heating rate. At heating rates lower than 7 K/min the cold crystallization is almost quenched. Aside from the crystallization peak, increasing the cooling/heating rate affects the melting peaks. At lowest heating rate (1 K/min) crystals are formed during cooling and melt at one temperature only. Both crystallization and melting peaks are sharp which indicates that at the low scanning rate stable uniform crystals are formed already during cooling. With increasing cooling/heating rate up to 7 K/min the melting peak moves to lower temperatures and the second melting peak arises. When the cooling rate is slow enough, metastable crystals can be transformed to stable crystals during cooling. The slower the polymer is cooled down, the more transformations can occur. For this reason the cold crystallization is quenched. When the cooling rate increases, the polymer contains stable crystals as well as metastable, that leads to the two melting peaks. A shift of the melting peak to low temperatures indicates decreasing ”quality” of obtained crystals. Up to a rate of 7 K/min polymer crystallizes mostly during the cooling scan.

At the rate of 7 K/min we can observe that both melting peaks are comparable to each other (peak area of first and second melting peaks is 17.77 J/g and 10.74 J/g respectively). Further increase of the

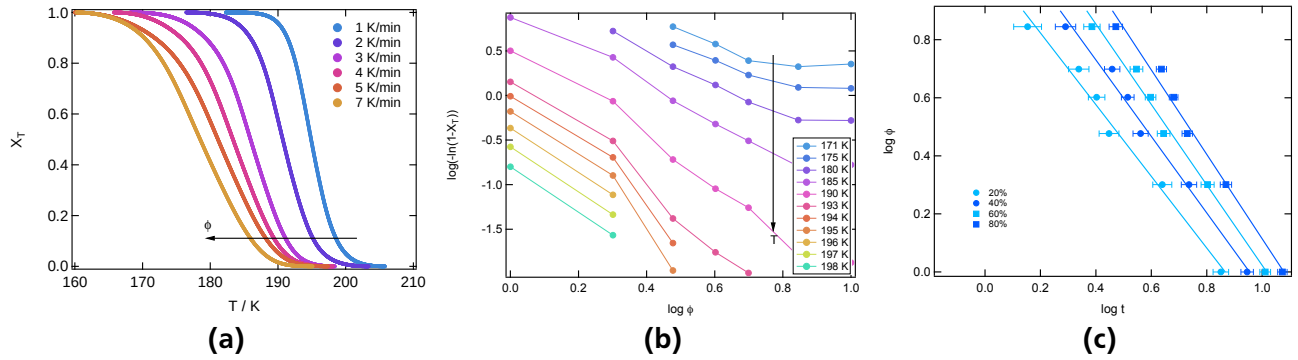

Figure 5.9.: (a) Development of relative crystallinity with temperature for non isothermal melt crystallization of PDMS; **(b)** Ozawa plot of non isothermal melt crystallization of bulk PDMS; **(c)** Plot of $\log \phi$ versus $\log t$ for melt crystallization of PDMS, where t is crystallization time calculated according equation (5.18).

cooling/heating rate leads to a shift of the first melting peak to higher temperatures while the second peak remains at the same position. At the highest rate both peaks tend to merge together. The cold crystallization peak moves to higher temperatures and broadness of the peak increases with increasing the heating rate. Similar to the melt crystallization, at high heating rates the polymer does not have enough time to form stable uniform crystals. At rates higher than 10 K/min the melt crystallization is quenched, and the cold crystallization is the dominating contribution to the crystallization process. With increasing scanning rate the amount of metastable crystals formed during cooling decreases. Moreover, the stable crystals are formed from this metastable state, which means that the formation of metastable crystals continues during heating and leads to a broad distribution of the "quality" of crystals, which are melted in a rather broad temperature range. It should be remarked that the absence of a cold or melt crystallization peak at a certain scanning rate does not mean that there is no such process. For example at high rates metastable crystals can be formed during cooling as well, but the amount of these crystals is very low which leads to a low signal in the DSC scan. In general, the cold and melt crystallizations contain both processes, the dominating component depends on the scanning rate. At an intermediate rate the formation of the metastable state mostly contributes to the melt crystallization, while the transformation to the stable state dominates in the cold crystallization.

The ratio between the two melting peaks changes with increasing heating rate. The area of the second peak decreases which indicates decrease of the fraction of stable crystals. At the same time the area of the first melting peak increases. This indicates that at high rates the polymer has a large fraction of metastable crystals. Thus, the ratio of stable and metastable crystals changes depending on the heating rate. The total area of both melting peaks decreases with increasing heating rate which shows that the total amount of crystallized polymer is getting smaller (see table 5.4).

In summary, at higher heating rate the cold crystallization has a higher contribution to the crystallinity than the melt crystallization and defines the crystallization process. At lower rate the melt crystallization is the dominating contribution. To investigate both crystallizations in detail we will perform a kinetics analysis similar to the isothermal case.

Kinetics of crystallization

Parameters of the non isothermal crystallization of PDMS such as onset temperature T_0 and peak temperature T_c, where the crystallization peak has its maximum, are listed in table 5.4. At higher cooling rates the polymer does not have enough time to align and crystallization is delayed which results in lower T_0 and T_c. Since there is no sufficient time for the polymer to form stable crystals, the polymer has a less crystalline form at high cooling rates which leads to a relatively low degree of crystallinity. The crystallinity corresponds to ΔH_C which systematically decreases at higher cooling rates. To analyze the

Melting enthalpy of PDMS

ϕ, K/min	1	2	3	4	5	7	10	15	20	25
ΔH_{m1}, J/g	36.15	35.01	29.13	24.14	20.78	17.77	21.73	23.45	19.84	26.42[a]
ΔH_{m2}, J/g	-	0.42	1.77	4.43	6.89	10.74	8.10	2.43	1.87	

PDMS melt crystallization

ϕ, K/min	1	2	3	4	5	7	10	15	20	25
T_0, K	204.4	202.5	198.0	197.8	197.1	193.9	191.9	-	-	-
T_c, K	194.4	190.2	185.6	182.8	180.9	177.5	176.6	-	-	-
ΔH_C, J/g	32.08	30.69	27.45	24.23	21.94	11.07	4.836	-	-	-

PDMS cold crystallization

ϕ, K/min	1	2	3	4	5	7	10	15	20	25
T_0, K	-	-	-	-	-	165.2	166.5	167	169.8	171.3
T_c, K	-	-	-	-	-	178.7	182.9	188.4	192.1	193.7
ΔH_C, J/g	-	-	-	-	-	8.129	19.50	23.27	21.42	15.67

CNT/PDMS melt crystallization

ϕ, K/min	1	2	3	4	5	7	10	15	20	25
T_0, K	-	-	202.1	-	199.4	-	196.4	194.3	192.6	-
T_c, K	-	-	197.8	-	195.9	-	193.3	190.8	189.2	-
ΔH_C, J/g	-	-	0.788	-	0.752	-	0.501	0.230	0.097	-
ΔH_m, J/g	-	-	0.577	-	0.579	-	0.410	0.353	0.400	-

Table 5.4.: Parameters of nonisothermal crystallization of PDMS: Φ is cooling/heating rate, T_0 is onset temperature, T_c is peak temperature and ΔH_C is enthalpy of crystallization

[a] Here the total area of both melting peaks is given. The melting enthalpy for this heating rate cannot be calculated separately for the first and second peak due to the merging of both peaks.

crystallization kinetics we do not need to know the absolute crystallinity. It is sufficient to consider the relative crystallinity which is calculated for every measured scanning rate according to equation (5.21). X_T of the melt crystallization of PDMS for different cooling rates is shown in figure 5.9a. The values of relative degree of crystallinity are analyzed in terms of the Ozawa equation (eq. (5.13)) and shown in double logarithmic form (eq. (5.14)) in figure 5.9b. This figure is obtained from figure 5.9a by taking X_T for every scanning rate ϕ at fixed temperatures. As was mentioned before, if the Ozawa analysis is valid, it is possible to describe all curves with linear functions which are parallel to each other. The slope of this linear function gives the Ozawa exponent m. One observes that at low rates and rather high temperatures curves are parallel to each other. A deviation form linearity is observed at higher cooling rates. We have a contribution of both processes during the cooling scan: formation of metastable crystals and their transformation to the stable state. Since the Ozawa analysis describes a single crystallization process, it has to be complemented by taking into account a second process in order to apply it to the present experiment. Moreover, the chain folding length is temperature dependent and indeed can cause deviation from linearity. These processes can be taken into account by combining Ozawa and Avrami methods(eq. (5.16)). We analyze the scanning rate at a certain degree of crystallinity versus time. Figure 5.9c shows this dependency of $\log \phi$ versus $\log t$ at fixed degree of relative crystallinity. Parameters $F(T)$ and b obtained by linear fitting of the data are listed in table 5.5. The only small variation of parameter b suggests that the method based on combining the Ozawa and Avrami equations is appropriate for analysis of the nonisothermal crystallization kinetics of PDMS. The value of $F(T)$ increases with increasing X_T. $F(T)$ is inversely proportional to the Avrami crystallization rate and shows how much time the system needs to achieve a certain degree of crystallinity. The smaller $F(T)$ the faster the crystallization is.

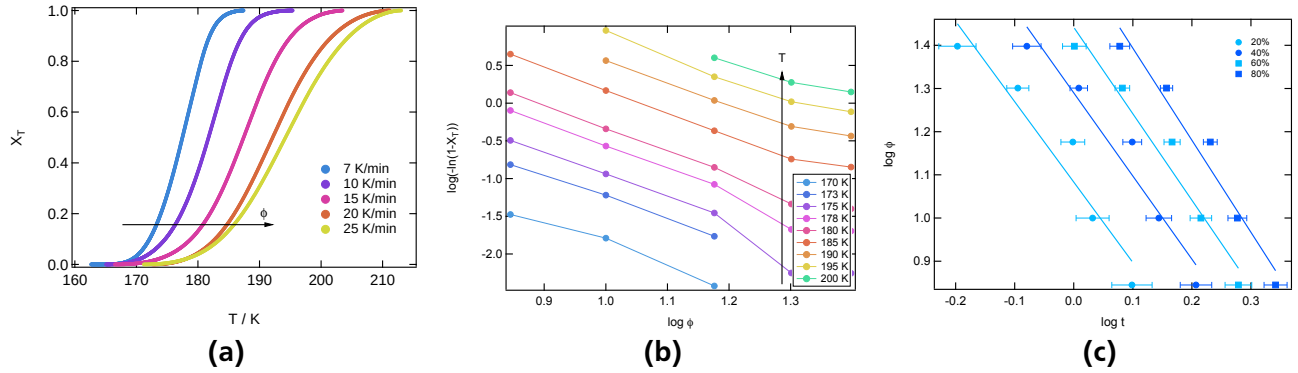

Figure 5.10.: (a) Development of relative crystallinity with temperature for non isothermal cold crystallization of PDMS; **(b)** Ozawa plot of non isothermal cold crystallization of the bulk PDMS; **(c)** Plot of $\log \phi$ versus $\log t$ for cold crystallization of PDMS.

PDMS melt crystallization

X_T, %	20	40	60	80
$F(T)$	11.8 ± 0.1	18.1 ± 0.1	25.6 ± 0.2	37.1 ± 0.2
b	1.23 ± 0.08	1.32 ± 0.07	1.38 ± 0.07	1.44 ± 0.08

PDMS cold crystallization

X_T, %	20	40	60	80
$F(T)$	12.1 ± 0.1	19.5 ± 0.2	27.6 ± 0.2	40.4 ± 0.3
b	1.9 ± 0.3	1.9 ± 0.3	2.0 ± 0.2	2.1 ± 0.3

CNT/PDMS melt crystallization

X_T, %	20	40	60	80
$F(T)$	3.15 ± 0.02	4.49 ± 0.03	5.59 ± 0.03	7.01 ± 0.03
b	1.0 ± 0.5	0.9 ± 0.5	0.9 ± 0.4	0.8 ± 0.4

Table 5.5.: Parameters $F(T)$ and b from equation (5.16) for nonisothermal crystallization of PDMS.

Uncertainties of the presented analysis have to be additionally remarked. DSC data usually contain no uncertainties, integration of the curve is very sensitive to any deformation of the thermogram and the peak area can be determined precisely. The Ozawa plot shown in figure 5.9b is just a transformation of X_T at fixed temperatures and subsequently contains no uncertainties. The data is reliable as it is plotted. A more complicated situation is in figure 5.9c since time t can contain large uncertainties resulting from the determination of the onset temperature T_0. For example, low signal in the thermogram can lead to the rather high uncertainties of T_0 which results in the high uncertainties of t (see eq. (5.18)).

The same analysis was done for investigation of the cold crystallization of PDMS. Parameters of the crystallization are listed in table 5.4. Similar to the melt crystallization, T_0 and T_C depend on the scanning rate. For the cold crystallization these temperatures are shifted to higher T. Since the cold crystallization is observed in the heating scan only, the temperature shift corresponds to crystallization at later times at high heating rates. Compared to the melt crystallization, the cold crystallization occurs at rather high temperatures. In contrast to the melt crystallization, which shows a lower crystallinity at high cooling rate, ΔH_C of the cold crystallization increases with increasing heating rate up to 15 K/min, which corresponds to increasing crystallinity with heating rate. At the highest rates (20 and 25 K/min) ΔH_C decreases. The heating rate is too fast to achieve a high degree of crystallization.

Analysis of the kinetics of the cold crystallization is shown in figure 5.10. Compared to the melt crystallization, the dependency of $\log(-\ln(1-X_T))$ versus $\log(\phi)$ (fig. 5.10b) is parallel for almost all temperatures at all heating rates; a deviation is observed only at the maximum heating rate. The

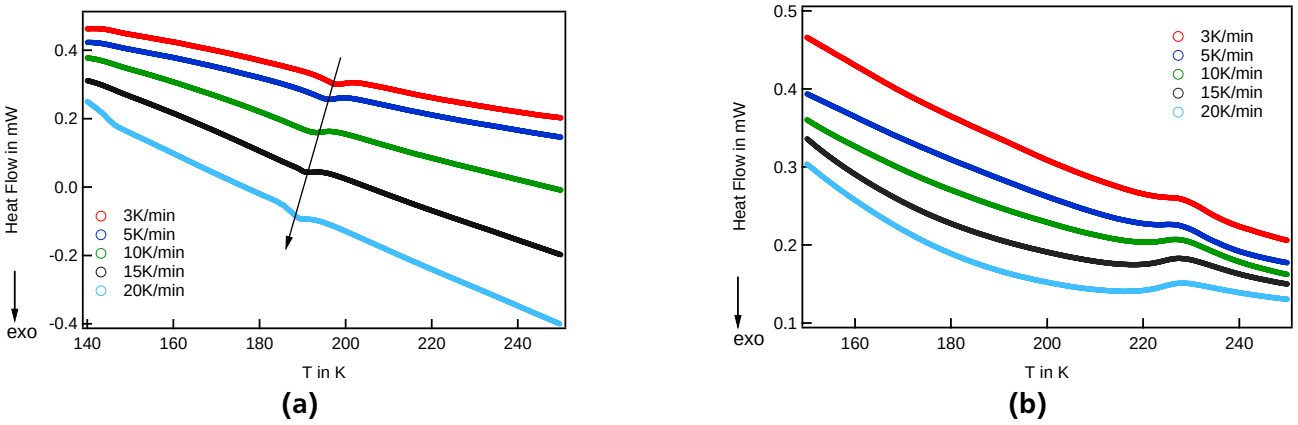

Figure 5.11.: (a) Cooling scan of PS/CNT/PDMS composites with different cooling rate; **(b)** Heating scan of PS/CNT/PDMS composite with different heating rate.

cold crystallization is a rather uniform process and corresponds to the transformation of a metastable state to a stable one since crystallization starts at low temperatures and proceeds during heating. At low temperatures formation of the metastable crystals is a very fast process. Moreover, crystals were partially formed already during cooling. The obtained slope of curves is in the range of 3.0-3.5, which is higher than for isothermal crystallization. The difference can be explained by a different mechanism of isothermal and nonisothermal crystallizations. The nonisothermal crystallization is more sensitive to the crystal growth and other temperature dependent effects since T is not constant, that might result in a different exponent. Moreover, cold crystallization is not a homogeneous crystallization as assumed in the Avrami equation due to formation of metastable crystals during cooling.

Similar to the isothermal case, we again combine Ozawa and Avrami equations in a last step of analysis. Figure 5.10c shows clear linear dependency of $\log(\phi)$ versus $\log(t)$, parameters $F(T)$ and b are listed in table 5.5. The variation of both parameters has the same tendency as for the melt crystallization.

Comparing parameters of the melt and cold crystallization of the bulk PDMS, one observes that the parameter $F(T)$ is the same for the melt and the cold crystallization. However, the crystallization rate is different due to dependency of the crystallization rate on the Ozawa exponent m (eq. (5.17)).

Crystallization of PDMS in the CNT array

To investigate the effect of the presence of the CNTs on crystallization of PDMS, the polymer was infiltrated into the CNT array with tube diameter of 40 nm (CNT 40V). The inner part of CNTs is filled by PS which has a much higher T_g and does not interfere with the measurement of melting and crystallization of PDMS. At the same time, the tube interior is blocked by PS and PDMS is located between tubes only. Heating and cooling DSC scans of the CNT/PDMS composite are shown in figure 5.11. Similar to the bulk polymer, the melt crystallization peak moves to lower temperatures with increasing cooling rate. In contrast to bulk PDMS, the CNT/PDMS composite does not show the cold crystallization at the investigated heating rates. Moreover, there is no quenching of the melt crystallization at high rates. The DSC cooling scan shows the melt crystallization peak even at the cooling rate of 20 K/min. Quenching of the cold crystallization can indicate the enhanced crystallization of polymer in the presence of CNTs. Polymer is mostly crystallized during cooling, forms stable crystals which do not exhibit recrystallization later in the heating scan. Observable melt crystallization at higher cooling rates gives evidence of faster crystallization of PDMS around CNTs. Enhanced crystallization of PDMS in the presence of nanofillers was reported before [33]. The authors observed the effect of quenching of the cold crystallization of PDMS in the presence of silica nanoparticles.

According to table 5.4, the temperature of the maximum of the crystallization peak is shifted to higher temperatures compared to the bulk PDMS. At all investigated cooling rates PDMS crystallizes earlier

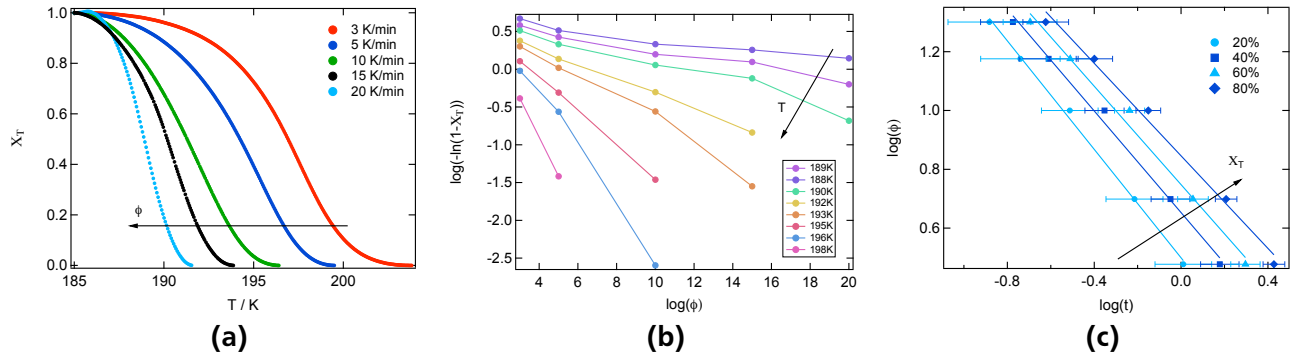

Figure 5.12.: (a) Development of relative crystallinity with temperature for non isothermal crystallization of PDMS in the CNT array; **(b)** Ozawa plot of non isothermal crystallization of the PDMS in the CNT array; **(c)** Plot of $\log \phi$ versus $\log t$ for crystallization of PDMS in the CNT array.

in the presence of CNTs. Some works have reported decreasing [35] as well as increasing [33] of T_c of PDMS in the presence of silica nanoparticles. Discrepancy of literature results can come from sample preparation and treatment of the particles which influences the interaction of polymer with the surface of nanoparticles. The shift of T_C to higher temperatures is possible evidence of the enhanced crystallization.

In the heating DSC scan one observes only one melting peak, that again supports the idea of the fast crystallization at cooling only. It is also possible that we do not observe double melting peaks due to the low mass of the sample. In this case the recorded signal is too low to distinguish between two melting peaks and the thermogram shows one broad peak. However, the peak position remains unchanged with increasing heating rate, leading to the conclusion that the second melting peak dominates at all scanning rates. Crystals formed during crystallization do not show significant increase of imperfection which would result in the shift of the melting peak. However, comparing the area under the melting and crystallization peaks (table 5.4) we can observe that ΔH_C decreases much faster than ΔH_m. It means that not all crystals which are molten later are formed during cooling at high rates. There can be recrystallization during heating like for the bulk PDMS, but due to very low signal and curvature of the base line the cold crystallization peak could be undetectable. This peak would be more pronounced at extremely high heating rates. This effect was already shown in figure 5.4 (light green line). Here the cold crystallization is observed at 40 K/min and the melting peak has two maxima in contrast to the rate of 10 K/min. As was discussed above, this sample has less bulk phase than confined phase which is also shown in the strong deviation of the isothermal crystallization. There is also a systematical decrease of ΔH_C which indicates that total crystallinity decreases at high scanning rates.

Kinetics of nonisothermal crystallization

We now consider the non isothermal melt crystallization of PDMS around CNTs in the composite. The isothermal crystallization of PDMS in CNT arrays was already discussed in section 5.4.1 and has shown two crystallization steps which are supposed to be formation of metastable crystals and their transformation to the stable state. In accordance to this picture, the nonisothermal crystallization of bulk PDMS shows the melt and cold crystallization peaks. However, the heating and cooling scans of PDMS in the CNT array shown in figure 5.11 exhibit only one melting and one crystallization peak — melt crystallization. In order to understand this phenomenon and compare the crystallization behavior of PDMS in CNT arrays and in the bulk we consider kinetics of the nonisothermal crystallization.

The experiment was performed in the same way as for the bulk polymer. Figure 5.12a shows the relative crystallinity depending on temperature. As was remarked before, the low signal in figure 5.11 do not affect the calculation of X_T, but leads to relatively high uncertainties of time t in figure 5.12c due to difficulties of determination of T_0.

Analyzing X_T according to the Ozawa equation we obtain a strong deviation from linearity of data shown in the Ozawa plot (fig. 5.12b). In the bulk PDMS we observed that the part of lines at low rates were parallel and deviation occurred at high rates only. In the CNT array even at low rates lines are not parallel. However, the first three lines from the top corresponding to low temperatures have a similar slope at low rates. The higher the temperature, the stronger is the deviation. We assume that due to enhanced crystallization the formation of metastable crystals is too fast, especially at low temperatures. In this case we observe mostly the formation of the stable crystal state. The absence of the metastable state was also observed in the isothermal crystallization at low temperatures. At high temperatures, both processes are slower and the metastable state contributes to the overall crystallization. This contribution is stronger at higher temperatures.

The combination of Ozawa and Avrami methods is shown in figure 5.12c. $\log(\phi)$ has a clear linear dependency on $\log(t)$. Thus, the crystallization of PDMS in the CNT array can be described in the same way as the crystallization of the bulk PDMS. Parameters $F(t)$ and b are recovered from a linear fit and listed in table 5.5. Comparing these parameters with parameters for the bulk PDMS, one observes a similar behavior of fit parameters: $F(T)$ for PDMS in the composite increases with relative crystallinity. However, the difference between $F(T)$ for $X_T = 20\%$ and for $X_T = 80\%$ is less than the same difference for the bulk PDMS. The polymer needs less time to achieve $X_T = 80\%$. The value of $F(T)$ is significantly smaller than for bulk PDMS which indicates faster crystallization kinetics of the polymer in the presence of CNTs since $F(T)$ is inversely proportional to the crystallization rate. However, we cannot quantitatively compare $F(T)$ for bulk PDMS and PDMS in the CNT array since $F(T)$ depends on m as well as on $K(T)$ (see equation (5.17)). These parameters could have different values for the two different systems. This could be an explanation of the dramatic difference of the obtained $F(T)$ for bulk PDMS and PDMS in the CNT array.

The parameter b is lower for polymer in CNT arrays and also lower than one, which means that the Avrami exponent is lower than the Ozawa exponent. This situation is contrary to the bulk PDMS and indicates different dimensionality of the crystal growth. It is reasonable to expect a lower dimensionality of the crystal growth in CNT arrays. Crystallization in this case in not completely homogeneous, it is heterogeneous near the surface: the chain folding mechanism can be caused not only by metastable crystals, but also by the presence of the surface. In this case the crystal growth is inhibited in certain directions which leads to the lower dimensionality of crystals.

5.5 Summary and conclusions

Using differential scanning calorimetry phase transitions of polymer in vertical aligned CNT arrays were studied. In the first step, the glass transition of polymers in CNT arrays was investigated. In the first experiment CNT arrays with two different tube diameters (40 nm and 90 nm) filled with two different molecular weights of PS were studied. Prepared by melt infiltration CNT/PS composites show a small positive shift of glass transition temperature as well as a broadening of the transition range compared to bulk PS. The decrease of the heat capacity together with shift of T_g indicates different dynamics of PS near the CNT wall, for example the immobilization of the polymer chains. The shift of T_g does not depend on the tube diameter, but it is sensitive to the molecular weight M_w. For larger M_w the shift is more pronounced.

Infiltration of two different polymers in CNT arrays in tube interior and between CNTs allows to investigate properties of polymers inside and outside tubes separately. PS infiltrated inside the tube interior has an average shift of T_g of around 2K to higher temperatures. For most samples with 40 and 90 nm tube diameter a complicated form of the transition range was found. A first glass transition was found at the T_g of bulk PS while a second transition is shifted with respect to the bulk. In most cases the shift of T_g is positive and not reproducible from sample to sample. However, the general tendency of double glass transition gives rise to consider the strong influence of the interphase on dynamical aspects of polymer in CNT arrays.

PDMS infiltrated outside tubes does not show any change in glass transition. However, it has a different melting and crystallization behavior than bulk PDMS. The combined study of isothermal and nonisothermal crystallization kinetics shows an enhanced crystallization of polymer in CNT arrays. Kinetics of crystallization was described in terms of the Avrami equation and its modifications for nonisothermal processes. We have found a deviation from Avrami's approach which is explained by a non classical mechanism of crystallization. PDMS crystallizes in two steps: the first step is formation of metastable crystals and the second is recrystallization to the stable state. In CNT arrays PDMS crystallizes in the same way, but both crystallization processes were found to be faster than in the bulk.

All DSC experiments were performed with low mass of the sample due to small size of composites and limited size of the DSC pan. This can introduce a large experimental error, which can explain the low reproducibility of data. Indeed the obtained absolute values of glass transition and crystallization temperature and other parameters should be considered in terms of large experimental errors. However, the general tendency of a complex glass transition range of polymer inside tubes and enhanced crystallization of polymer outside is clearly observed and considered as a change of polymer dynamics in CNT arrays.

6 Elastic excitations in polymer filled nanoporous templates

Dynamics of polymers can be studied with inelastic scattering, for example Brillouin light scattering (BLS). BLS spectroscopy is a powerful and non-destructive technique which allows for the direct measurement of the phonon dispersion relations along any directions in the Brillouin zone. This gives information about the sound propagation in materials. The sound propagation depends on elastic properties of the medium which result from microscopical dynamics. Changing of the dynamics of polymers can result in different elastic behavior which can be observed in Brillouin spectra.

However, investigation of CNT/polymer composites with BLS is essentially impossible due to the optical properties of carbon. A CNT array strongly absorbs the light and is heated to high temperatures during the interaction with light. The heating of CNT arrays affects the polymer inside and makes it impossible to study the polymer behavior under controllable temperatures. Moreover, keeping polymers at high temperatures for long times can result in polymer destruction, for example oxidization which changes the initial properties. For this reason we use nanoporous templates which are transparent for light and have pores similiar to the CNT array in length and diameter in order to achieve the same confinement geometry as in the interior of CNTs in arrays. However the interaction between polymer and templates is not the same as in CNT arrays.

PAOX (porous aluminum oxide) and ITPC (ion track etched polycarbonate) are used as templates. They have straight cylindrical pores of approximately 40 nm in diameter. These templates provide a confinement similar to the interior of CNTs and can be a good model for the future investigation of dynamics of polymers in CNT arrays.

This chapter will summarize the first experimental observations of elastic excitations in porous templates and show details of experiments and data evaluation.

6.1 Brillouin spectroscopy

The basic principles of light scattering are similar to X-rays and neutrons (see chapter 2.1) but have some peculiarities caused by interaction of the light with the matter which will be described here. This chapter provides a description of experimental techniques including the experimental setup and gives a short summary of the theory of Brillouin light scattering. Detailed explanation of light scattering theory and in particular Brillouin scattering can be found in literature [136, 137].

Brillouin scattering is inelastic scattering, it arises as a result of acousto-optical interactions in scattering media. Incident photons are annihilated, which together with the creation or annihilation of one phonon gives rise to inelastically scattered photons. The frequency of the scattered photons ω' is shifted with respect to the frequency of incident photons ω due to the well known Doppler effect.

6.1.1 The photoelastic effect

In contrast to X-ray and neutron scattering, light is sensitive to macroscopic properties of the media due to the longer wavelength. In order to describe light scattering, electromagnetic properties of media have to be taken into account.

We consider a nonmagnetic, nonconducting, nonabsorbing medium with average dielectric constant ε and refractive index $n = \sqrt{\varepsilon}$. Similar to equation (2.7) the incident electromagnetic wave can be expressed as

$$\mathbf{E}_i(r,t) = \mathbf{n}_i E_0 e^{i(\mathbf{k}\cdot\mathbf{r}-\omega t)} \tag{6.1}$$

where $\mathbf{n}_i$ is a unit vector in the direction of polarization of the electromagnetic wave; E_0 is the amplitude; $\mathbf{k}$ is the wave vector and ω the angular frequency. After the scattering process, the scattered wave at large distance R from the scattering medium with polarization $\mathbf{n}_s$, wave vector $\mathbf{k}'$ and frequency ω' can be written as

$$E_s(R,t) = \frac{E_0}{4\pi R\varepsilon_0} e^{ik'R} \int d^3r e^{i(\mathbf{q}\cdot\mathbf{r}-\omega t)} [\mathbf{n}_s \cdot [\mathbf{k}' \times (\mathbf{k}' \times (\delta\varepsilon(\mathbf{r},t)\cdot\mathbf{n}_i))]] \tag{6.2}$$

where $\delta\varepsilon(\mathbf{r},t)$ is the fluctuation of the dielectric constant in the scattering volume and $\mathbf{q}$ is the scattering vector defined in the same way as for X-ray scattering (eq. (2.4)): $\mathbf{q} = \mathbf{k}' - \mathbf{k}$. The magnitude of $\mathbf{q}$ can be expressed in terms of the scattering geometry where the dielectric properties of the medium have to be taken into account:

$$q = \frac{4\pi n}{\lambda} \sin\theta \tag{6.3}$$

where 2θ is the scattering angle. The scattering intensity of acousto-optical interactions strongly depends on the dielectric fluctuation related to elastic deformations of the medium. When an acoustic wave propagates through the medium, it creates a modulation of the dielectric constant and the medium has the local dielectric constant

$$\varepsilon(\mathbf{r},t) = \varepsilon_0 + \delta\varepsilon(\mathbf{r},t) \tag{6.4}$$

where the dielectric fluctuation $\delta\varepsilon(\mathbf{r},t)$ is a tensor

$$\delta\varepsilon(\mathbf{r},t)_{ij} = \sum_{kl} p_{ijkl} e_{kl} \tag{6.5}$$

where

$$e_{kl} = \frac{1}{2}\left(\frac{\partial u_k}{\partial x_l} + \frac{\partial u_l}{\partial x_k}\right) \tag{6.6}$$

is the strain tensor with u_k and u_l as k-th and l-th components of the displacement vector. p_{ijkl} is the photo-elastic tensor describing the response of the medium to the propagating wave. In general p_{ijkl} contains 21 independent coefficients. Depending on the symmetry of the medium this number can be reduced. The strain tensor e_{kl} corresponds to the elastic properties of the medium and defines the stress tensor of the medium σ_{ij}:

$$\sigma_{ij} = \lambda(\mathbf{r}) e_{ii}\delta_{ij} + 2\mu(\mathbf{r}) e_{ij} \tag{6.7}$$

where $\lambda(\mathbf{r})$ and $\mu(\mathbf{r})$ are Lame coefficients[138] which correspond to the longitudinal sound velocity v_l and transverse sound velocity v_t in the medium: for an isotropic medium we have $v_l = \sqrt{\lambda + 2\mu/\rho}$ and $v_t = \sqrt{\mu/\rho}$ with density of mass ρ. These coefficients again depend on the symmetry of the medium.

We now come back to the scattered intensity and express equation (6.2) in terms of a spatial Fourier transform of $\delta\varepsilon$:

$$E_s(R,t) = \frac{E_0}{4\pi R\varepsilon_0} e^{i(k'R-\omega t)} [\mathbf{n}_s \cdot [\mathbf{k}' \times (\mathbf{k}' \times (\delta\varepsilon(\mathbf{q},t)\cdot\mathbf{n}_i))]] \tag{6.8}$$

where

$$\delta\varepsilon(\mathbf{q},t)=\int d^3r e^{i\mathbf{q}\cdot\mathbf{r}}\delta\varepsilon(\mathbf{r},t). \tag{6.9}$$

Simplification of the vector cross products in equation (6.8) leads to

$$E_s(R,t)=\frac{-k'^2E_0}{4\pi R\varepsilon_0}e^{i(k'R-\omega t)}\delta\varepsilon_{is}(\mathbf{q},t) \tag{6.10}$$

where $\delta\varepsilon_{is}(\mathbf{q},t)=\mathbf{n}_s\cdot\delta\varepsilon(\mathbf{q},t)\cdot\mathbf{n}_i$ is the component of the dielectric constant fluctuation tensor along the initial and final polarization directions. Considering the time-averaged intensity of the scattered light, the time correlation function of E_s can be evaluated as

$$\langle E_s^*(R,0)E_s(R,t)\rangle=\frac{k'^4|E_0|^2}{16\pi^2R^2\varepsilon_0^2}\langle\delta\varepsilon_{is}(\mathbf{q},0)\delta\varepsilon_{is}(\mathbf{q},t)\rangle e^{-i\omega t}. \tag{6.11}$$

The spectral density $I_{is}(\mathbf{q},\omega',R)$ of light scattered into the detector such that $(\mathbf{n}_i,\mathbf{k},\omega)\rightarrow(\mathbf{n}_s,\mathbf{k}',\omega')$ can then be determined as

$$I_{is}(\mathbf{q},\omega',R)=\int \mathrm{d}t\langle E_s^*(R,0)E_s(R,t)\rangle e^{i\omega' t}=\frac{k'^4I_0}{16\pi^2R^2\varepsilon_0^2}\frac{1}{2\pi}\int \mathrm{d}t\langle\delta\varepsilon_{is}(\mathbf{q},0)\delta\varepsilon_{is}(\mathbf{q},t)\rangle e^{i(\omega'-\omega)t} \tag{6.12}$$

with $I_0=|E_0|^2$. Note that equation (6.12) has some characteristic features. First of all, the intensity is inversely proportional to the fourth power of wavelength (λ^4); secondly, the intensity is inversely proportional to the square of the distance for a spherical wave (R^{-2}) and depends on the frequency difference $\omega_p=\omega'-\omega$ which occurs due to time variation of the dielectric constant fluctuations. Thus, intensity (equation (6.12)) is proportional to the spectral density of the dielectric constant fluctuations I_{is}^{ε}:

$$I_{is}^{\varepsilon}(\mathbf{q},\omega_p)=\frac{1}{2\pi}\int \mathrm{d}t\langle\delta\varepsilon_{is}^*(\mathbf{q},0)\delta\varepsilon_{is}(\mathbf{q},t)\rangle e^{i\omega_p t}. \tag{6.13}$$

The scattered intensity is induced by the local fluctuations of the dielectric constant. Therefore, BLS can provide insight into dynamical processes in media.

6.1.2 Interaction of light with medium

According to the theory of soft matter a solid medium has optical and acoustic waves propagating through the medium related to the oscillations of atomic chains due to thermal fluctuations. When light travels though the medium, it is scattered by acoustic or optical phonons, and this light is subject to frequency shifts. Interaction of light with optical phonons, so called Raman scattering has a larger frequency shift than the scattering by acoustic phonons, due to the higher frequency of the optical branch. Scattering of light by acoustic waves is called Brillouin scattering.

We consider a wave of light with wavelength λ_p traveling through a medium and interacting with an elastic wave of wavelength λ_n. The elastic wave can be understood as a moving pattern of periodic density modulations. Similar to the Bragg reflection of X-rays in crystals we can describe acousto-optical interaction as light scattering on a lattice with lattice constant λ_n and can express it in terms of the Bragg condition as

$$\frac{2\pi}{\lambda_n}=\frac{4\pi n}{\lambda_p}\sin\theta=q \tag{6.14}$$

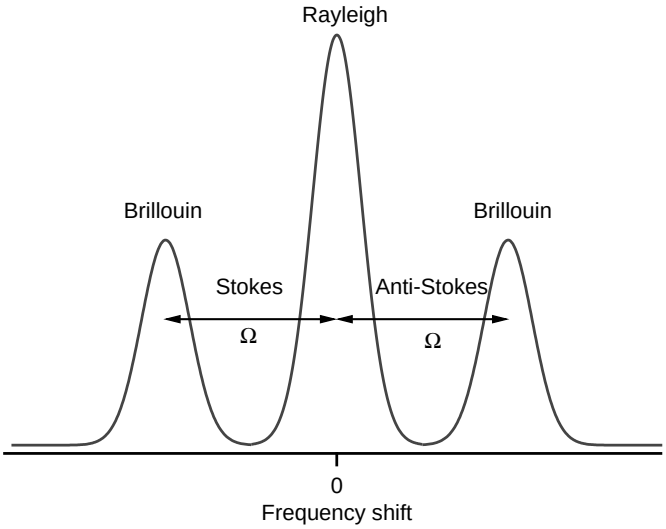

Figure 6.1.: Schematic brillouin spectrum

where $\mathbf{k_n} = 2\pi/\lambda_n$ is the wave vector of the elastic wave. Therefore, the scattering vector relates to the wave vector of the elastic wave. This equation shows that the wave vector of the elastic wave is equivalent to the scattering vector. Thus $\mathbf{k}' = \mathbf{k} \pm \mathbf{k_n}$ and multiplying this expression by $\hbar$ leads to the law of momentum conversation

$$\hbar\mathbf{k}' = \hbar\mathbf{k} \pm \hbar\mathbf{k_n}. \tag{6.15}$$

Also, the energy is conserved during the scattering process:

$$\hbar\omega' = \hbar\omega \pm \hbar\Omega \tag{6.16}$$

where Ω is the frequency shift schematically shown in figure 6.1. The process shifted to higher frequencies corresponds to the absorption of a phonon and is known as anti-Stokes component of the scattered radiation. The process shifted to lower frequencies is called Stokes component and corresponds to the process in which a phonon is emitted. The shift of frequency can be expressed as

$$\Omega = \frac{4\pi n\omega\upsilon}{c}\sin\theta = \upsilon q \tag{6.17}$$

where υ is the phonon phase velocity and c is the speed of light. By measuring the frequency shift Ω, it is thus possible to calculate the sound propagation velocity in the sample medium.

6.1.3 Fabry-Perot interferometer

In order to achieve the high resolution needed to measure the small frequency shift in BLS, a Fabry-Perot (FP) interferometer is used. The inelastic component of light corresponding to Stokes and anti-Stokes processes is much weaker than the elastic contribution. To be able to extract the BLS signal a high resolution spectrometer is needed.

We first consider a single pass FP interferometer. It consists of two parallel dielectric mirrors with highly reflecting inner surfaces in order to induce multiple reflections of light between the mirrors. In scattering experiments, slightly divergent monochromatic light enters the interferometer perpendicular

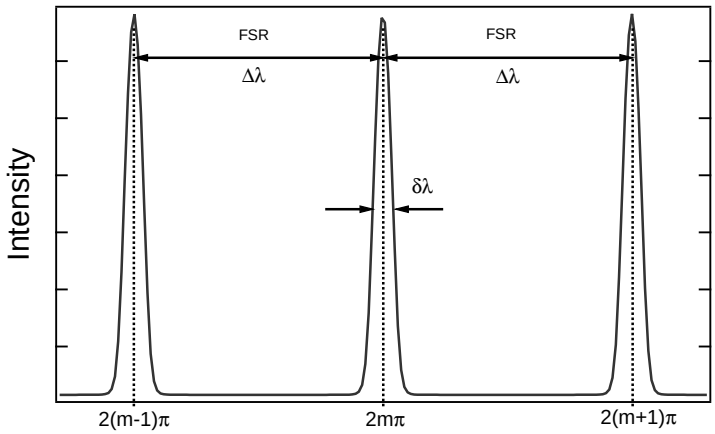

Figure 6.2.: Optical transmission function of a single pass Fabry-Perot interferometer

to the mirrors and is reflected back and forth in the interferometer cavity. Only waves for which an integer number of half wavelengths fit into the cavity interfere constructively:

$$d = \frac{m\lambda}{2} \tag{6.18}$$

where m is an integer number referring to the order of the transmission peak, d the mirror spacing and λ the wavelength. The mirrors are only partially reflecting and the transmitted wave contains only these allowed wavelengths. The single pass optical transmission function T of a FP interferometer is the so-called Airy function:

$$T = \frac{T_0}{1 + (4F^2/\pi^2)\sin^2(2\pi d/\lambda)} \tag{6.19}$$

where T_0 is the overall transmission and F the effective finesse which will be defined later. The optical transmission function is illustrated in figure 6.2.

If the incident light contains many wavelengths of varying intensities, we can analyze its spectrum by scanning the distance d in the FP interferometer because for a given separation d, the interferometer transmits only the wavelength which satisfies equation (6.18). This is usually done by physically moving the mirrors piezoelectrically.

If we vary the distance between mirrors, the wavelength of the transmission maximum will change. Therefore, if d changes by an amount δd, the wavelength transmitted will be

$$\lambda + \delta\lambda = \frac{2(d + \delta d)}{m}. \tag{6.20}$$

If the mirror separation will be increasing further, at some point, when the separation will be increased by an amount Δd, the original wavelength will be transmitted again with a different m

$$\lambda = \frac{2(d + \Delta d)}{m + 1}. \tag{6.21}$$

In other words, $m+1$ half wavelengths of λ and m half wavelengths of $\lambda + \Delta\lambda$ fit into the cavity of the interferometer simultaneously and we would not be able to distinguish between these two wavelengths. The value $\Delta\lambda$ is called free spectral range (FSR) and can be calculated to

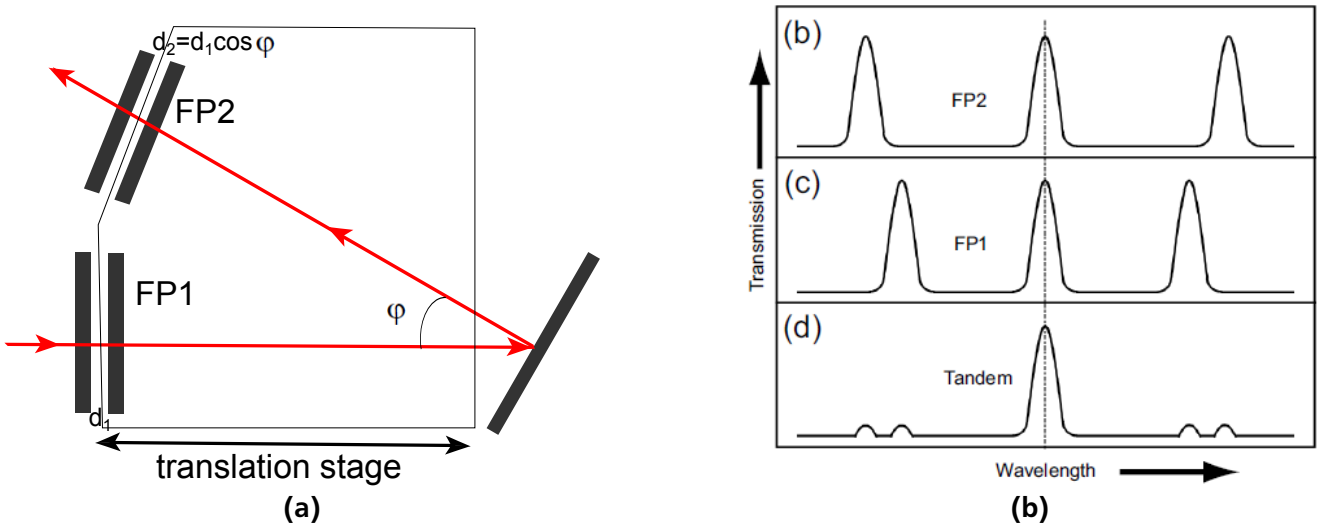

Figure 6.3.: (a) Schematic view of a tandem Fabry-Perot interferometer; **(b)** Effect of increasing of free spectral range (FSR) due to suppression of overlapping orders in a tandem Fabry-Perot interferometer

$$\Delta\lambda = \frac{\lambda^2}{2d}. \tag{6.22}$$

The FSR corresponds to the wavelength range between adjacent cavity modes. Usually in BLS spectroscopy the FSR is expressed as a frequency range

$$\mathrm{FSR} \equiv \Delta\nu = \frac{c}{2nd}. \tag{6.23}$$

Another important parameter characterizing FP interferometers is the finesse. As shown in figure 6.2 the peaks have finite width because the surfaces of the mirrors are not perfectly reflecting. The value describing the instrumental resolution is called finesse F. It is defined as the maximum number of resolvable peaks within the FSR (see fig. 6.2)

$$F = \frac{\Delta\lambda}{\delta\lambda} \tag{6.24}$$

where $\delta\lambda$ is the full width at half maximum of the peak. Therefore, it is necessary to optimize the mirror separation for each experiment depending on lowest and highest frequencies to be measured in order to achieve the best combination of finesse and FSR.

Multi pass tandem Fabry-Perot interferometer

A Fabry-Perot interferometer is a well established spectroscopic instrument for the investigation of thermally excited phonons in media. However, the standard FP interferometer has a low contrast and problems with the overlapping of the neighboring orders to allow weak Brillouin signals to be observed in the presence of the elastic signal. Increased contrast, resolution and FSR can be achieved by using two FP interferometers with slightly different mirror spacing [140]. Using the second interferometer allows to suppress overlapping modes and to increase FSR. At the same time the contrast and the resolution can be improved by routing the beam sequentially through two different optical paths [141]. In this case the FP interferometer is called multi pass interferometer. Combination of tandem FP interferometer and

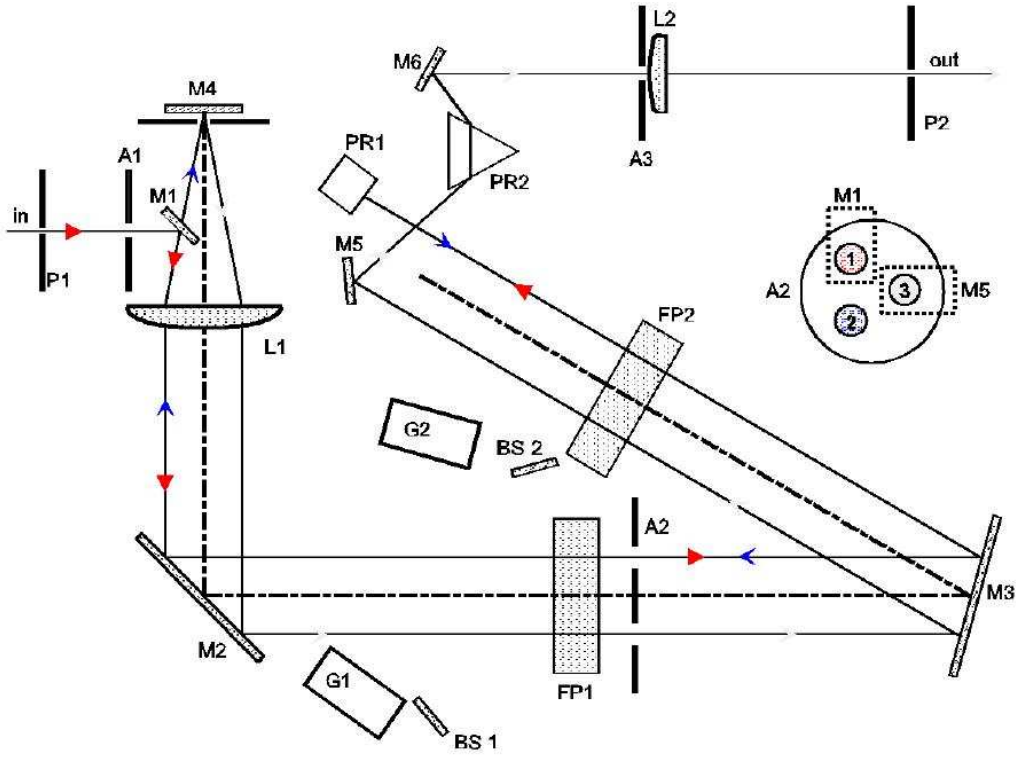

Figure 6.4.: The optical path inside the used tandem Fabry-Perot interferometer [139].

multi pass FP interferometer is often used in Brillouin spectroscopy. In this section the principles of both interferometers will be shortly explained.

The tandem FP interferometer is schematically shown in figure 6.3. Two interferometers FP1 and FP2 with mirror separation of d_1 and d_2 correspondingly are arranged at the angle ϕ between their axes. The scanning mirrors of both interferometers are mounted on the same translational stage (fig. 6.3a). When these two interferometers transmit light simultaneously, a change Δd in the mirror separation satisfies the following condition:

$$\frac{\Delta d_1}{\Delta d_2} = \frac{d_1}{d_2} = \frac{1}{\cos\phi} \tag{6.25}$$

The transmitted wavelength λ through tandem arranged interferometers fits simultaneously into the cavity of both interferometers according to equation (6.18):

$$d_1 = \frac{m_1\lambda}{2} \tag{6.26}$$

and

$$d_2 = \frac{m_2\lambda}{2} \tag{6.27}$$

Since the mirror spacing of FP1 and FP2 is slightly different, the interferometers have different FSR. When all conditions above are satisfied the neighboring orders are suppressed and the transmitted signal looks as shown in figure 6.3b.

As was mentioned above, combination of the tandem interferometer with the multi pass interferometer allows to achieve high contrast, large FSR and increase the resolution. In this work a six pass tandem Fabry-Perot interferometer designed by JRS Scientific instruments [139] is used. The optical path inside this interferometer is shown in figure 6.4.

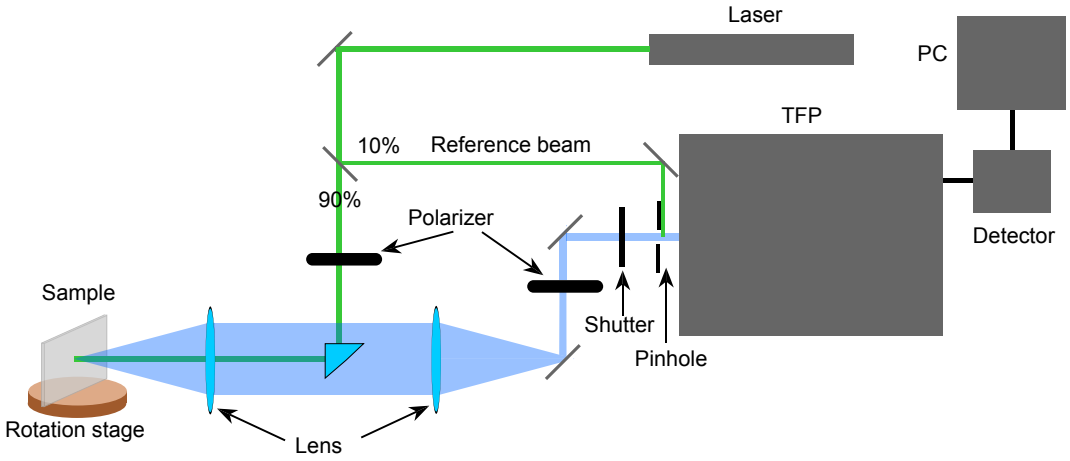

Figure 6.5.: Sketch of experimental setup.

The scattered light enters the interferometer at the pinhole P1. The aperture A1 then defines the cone of light which is accepted. The mirror M1 reflects the light towards the lens L1 where it is collimated and directed via mirror M2 to FP1. After FP1 the beam passes through the upper aperture 1 of mask A2 (red arrows) and is directed via mirror M3 to FP2.

After transmission through FP2 the light hits the 90° prism PR1 where it is reflected back and returning towards FP2 (blue arrows). It continues through the lower aperture 2 of A2 to FP1. Then it passes through lens L1, underneath mirror M1, and is focussed onto mirror M4. This mirror returns the light through lens L1 where it is again collimated and directed through FP1.

The combination of lens L1 and mirror M4 lying at its focus is known as a catseye, and is optically equivalent to a cornercube but has the advantage that it also acts as a spatial filter which filters out unwanted beams such as the beams reflected from the rear surfaces of the interferometer mirrors.

After the final pass through the interferometers, through the right aperture 3 of A2, the light hits the mirror M5 where it is directed to the prism PR2. This prism, in combination with the lens L2 and the output pinhole P2, forms a bandpass filter with a width determined by the size of the pinhole. The mirror M6 sends the light to the output pinhole and will have to be adjusted whenever the laser wavelength is changed.

Beamsplitters BS1 and BS2 and glass blocks G1 and G2 are used for alignment of the interferometer.

6.1.4 Experimental setup and scattering geometry

The experimental setup is shown in figure 6.5. The Nd:YAG laser provides monochromatic light with a wavelength of 532 nm. The beam is split in two parts. The first part is a reference beam having 10% of the primary beam intensity and goes directly to the entry pinhole of the spectrometer. The main part of the beam passes through a polarizer and is turned by a prism towards to the sample. The light scattered from the sample is collected and focused by two lenses backwards to the incident beam. Thus, the angle between incident and scattered beam is 180°; this is so-called backscattering geometry. After focusing the scattered beam passes the second polarizer and goes into the interferometer through the pinhole.

The scattering geometry defines the direction of propagation of the measured elastic wave. In thin films we can analyze the signal parallel or perpendicular to the surface of the film. The scattering vector $\mathbf{q}$ has two components: $q_{\parallel}$ parallel to the surface and $q_{\perp}$ normal to the film surface (fig. 6.6). Rotation of the template with respect to the incident laser beam increases and decreases the contribution of either of the components.

Since the experimental setup has backscattering alignment the wave vectors of incident and scattered beams have the opposite direction but the same absolute value of scattering vectors: $|k| = |k'|$. In this case the scattering vector q is

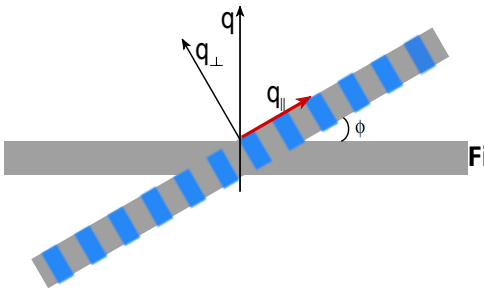

Figure 6.6: Orientation of the sample in BLS. The porous template is installed perpendicular to the incident laser beam. In this case $q_{\parallel} = 0$. The template can be tilted to angle ϕ ($q_{\parallel} = q \sin \phi$)

$$q = \frac{4\pi}{\lambda} n_{\text{eff}} \tag{6.28}$$

where is n_{eff} is the effective refractive index of the medium. The effective refractive index can be calculated according to the Maxwell-Garnet approximation [142].

The porous template to be investigated is installed perpendicular to the incident laser beam, so that $q_{\parallel} = 0$. The template can be tilted to angles $\phi = 0° - 80°$ leading to $q_{\parallel} = q \sin \phi = 0 - 0.98q$. Spectra at different ϕ are recorded and compared.

6.2 Acoustic excitations in porous templates

Porous materials exhibiting variations in their density and elastic properties can show modified propagation of sound waves with respect to the bulk material. Due to the large mismatch in elastic contrast between the air in pores and the template material thermally excited surface waves as well as bulk phonons can be significantly changed. In this section we will compare results of phonon propagation in empty and polymer filled porous templates with different porosity. Ion track etched polycarbonate membranes (ITPC) of low porosity and highly porous PAOX with the same pore radius were filled with polydimethylsiloxane (PDMS).

Since the surface effects in the thin films cannot be neglected, the surface modes of Brillouin spectra arise and significantly contribute to the spectrum. In the present section we will analyze the surface excitations of porous templates and compare them before and after polymer infiltration.

6.2.1 Bulk and surface waves

Thermally excited elastic waves can propagate in a medium in any direction independent of the medium being isotropic or anisotropic. In the bulk three different waves, the so-called bulk modes can propagate in a given direction. One of them describes the displacement along the propagation direction and is called longitudinal bulk mode (P). The remaining two waves have displacement transverse to the direction of propagation and are called transverse bulk modes [137, 143]. The mode with horizontal particle displacement is called shear horizontal mode (SH) and the mode with vertical particle displacement is the shear vertical mode (SV). All bulk modes are schematically shown in figure 6.7a.

Now we consider the dispersion relation $q(\omega)$ for each exited wave[1]. In the general case equation (6.7) can be rewritten as

$$\sigma_{ij} = \sum_{kl} c_{ijkl} e_{kl} \tag{6.29}$$

[1] Later in the discussion of the experimental results we will plot q vs ν since ν is directly observable in experiment. Here we use $\omega = 2\pi\nu$ in order to avoid the coefficient 2π in equations.

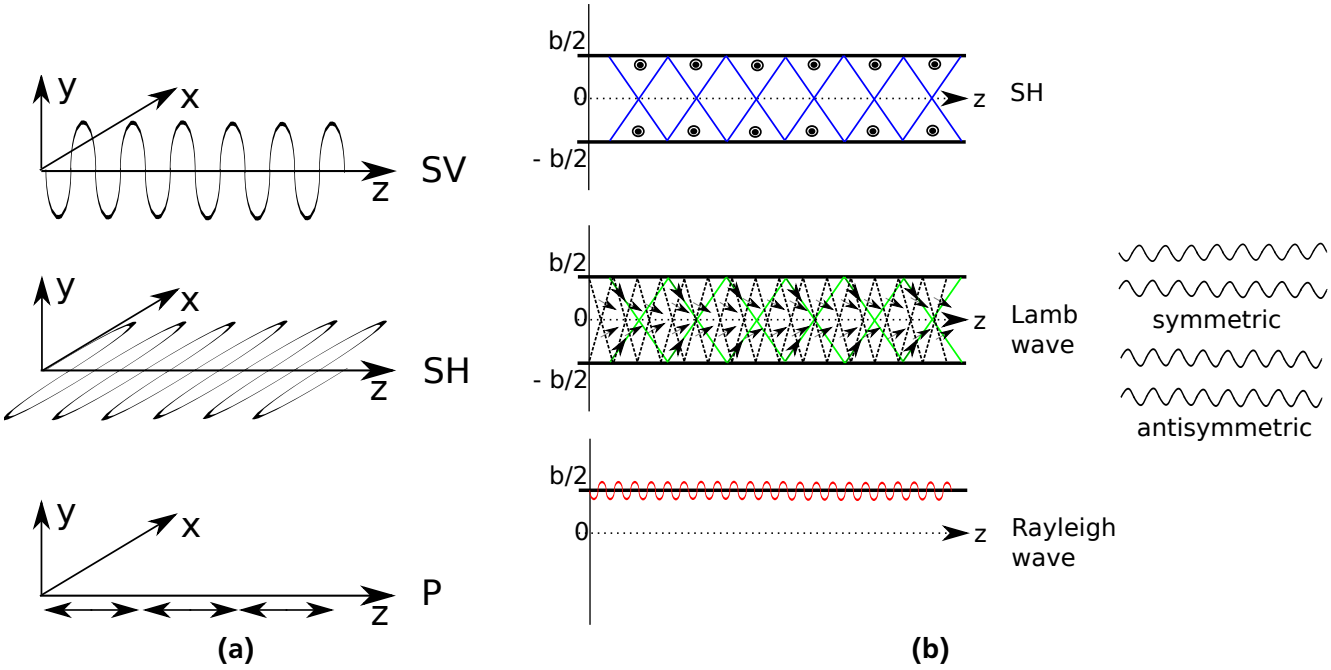

Figure 6.7.: Schematic view of **(a)** bulk waves: SV – shear vertical mode, SH – shear horizontal mode and P – longitudinal mode. z is the direction of propagation; **(b)** surface modes. SH is polarized in plane of the surface (blue lines). Green lines correspond to SV mode and dashed black lines to P mode. Arrows show polarization of waves.

where c_{ijkl} is the stiffness tensor. The acoustic wave equation[2] can be expressed in terms of the Christoffel matrix $Q_{ik} = \chi_j c_{ijkl} \chi_l$ (χ_j and χ_l are normalized vectors):

$$q^2 Q_{ik} \cdot U_k = \rho \omega^2 U_i \tag{6.30}$$

where ρ is the density of the medium and $\mathbf{U}$ is eigenvector. In an isotropic medium, wave solutions are the same for all directions of propagation and we can take a direction that reduces the analysis to its simplest term. Assume that waves propagate along z direction. In this case the Christoffel matrix is a purely diagonal matrix:

$$[Q] = \begin{pmatrix} c_{44} & 0 & 0 \\ 0 & c_{44} & 0 \\ 0 & 0 & c_{11} \end{pmatrix} \tag{6.31}$$

Thus equation (6.30) can be separated into three independent equations:

$$\begin{aligned} q^2 c_{44} U_x &= \rho \omega^2 U_x \\ q^2 c_{44} U_y &= \rho \omega^2 U_y \\ q^2 c_{11} U_z &= \rho \omega^2 U_z. \end{aligned} \tag{6.32}$$

Solving each of the equations above we obtain that the longitudinal wave (having particle motion in z direction) satisfies the dispersion relation

[2] The acoustic wave equation describes the propagation of the acoustic waves in media. A detailed description and transformations of the equation can be found in the literature [137, 144]. Here we give only equations directly leading to the dispersion relation, which will be used for analysis of propagating waves later.

$$q^2 c_{11} = \rho\omega^2. \tag{6.33}$$

The other two modes are transverse with polarization in x and y directions correspondingly and satisfy the dispersion relation

$$q^2 c_{44} = \rho\omega^2. \tag{6.34}$$

Both transverse waves propagate with the same velocity in the medium, they only differ in polarization. The sound velocity then can be found as

$$\begin{aligned} v_l &= \sqrt{\tfrac{c11}{\rho}} \\ v_t &= \sqrt{\tfrac{c44}{\rho}}. \end{aligned} \tag{6.35}$$

As was mentioned in section 6.1 the phase velocities in an isotropic medium can also be expressed through Lame coefficients:

$$\begin{aligned} v_l &= \sqrt{\lambda + 2\mu/\rho} \\ v_t &= \sqrt{\mu/\rho}. \end{aligned} \tag{6.36}$$

Depending on the scattering symmetry we can observe only longitudinal or only transverse modes, or all modes together. For example, only longitudinal modes can be observed when the sample surface is perpendicular to the incident beam in backscattering geometry [137]. In 90°-configuration only transverse modes are observed. In our experiments we use backscattering geometry, where transverse modes are not visible. However, if the sample is tilted to an arbitrary position, the scattering symmetry is broken and transverse modes can appear.

In 1885 Lord Rayleigh observed that elastic waves can propagate along the surface of solids. In this case most of the energy is localized near the surface within a depth of about one wavelength [145]. Bulk longitudinal and transverse modes of an isotropic medium are independent of the rotation of the sample and propagate in any directions. In contrast to bulk modes, surface modes are sensitive to the surface orientation in respect of the incident beam. Surface modes are also limited in volume and have to fulfill boundary conditions which require that the displacement amplitude vanishes at $z = \pm b/2$, where b is the thickness of the template (see fig. 6.7b).

The easiest case is propagation of the SH mode. The SH mode reflects from the surface of the template without changing the polarization and stays independent from the other two modes (P and SV). This mode propagates under the condition $\omega > \omega_{cf}$ where ω_{cf} is the frequency at which the mode changes from propagating to nonpropagating, the so-called cutoff frequency. It is defined as

$$\omega_{cf} = \frac{m\pi}{b} v_t, \quad m = 0, 1, 2... \tag{6.37}$$

The dispersion relation of this wave is

$$\frac{q}{\omega} = \frac{1}{v_t}\left[1 - \left(\frac{m\pi v_t}{b\omega}\right)^2\right]^{1/2} \tag{6.38}$$

In case when $m = 0$ the dispersion relation of the SH mode satisfies equation (6.34).

The situation is more difficult with P and SV modes. In thin templates these modes do not exist individually, but they are coupled. The boundary conditions lead to

$$\frac{\tan(k_{zt}b/2)}{\tan(k_{zl}b/2)} = -\frac{4q^2k_{zt}k_{zl}}{(k_{zt}^2 - k_{zl}^2)^2} \quad \text{(symmetric)} \tag{6.39}$$

and

$$\frac{\tan(k_{zt}b/2)}{\tan(k_{zl}b/2)} = -\frac{(k_{zt}^2 - k_{zl}^2)^2}{4q^2k_{zt}k_{zl}} \quad \text{(antisymmetric)} \tag{6.40}$$

where k_{zt} and k_{zl} are wave vector components of transverse and longitudinal modes correspondingly. The mode frequencies are given by

$$\begin{aligned} k_{zl}^2 &= \left(\frac{\omega}{v_l}\right)^2 - q^2 \\ k_{zt}^2 &= \left(\frac{\omega}{v_t}\right)^2 - q^2 \end{aligned} \tag{6.41}$$

There are three frequency regimes [146]: (a) $\omega/q > v_l$. In this case k_{zl} and k_{zt} are real and the solutions are normal bulk modes. (b) $v_l > \omega/q > v_t$ leads to real k_{zt} and imaginary k_{zl}. These are Lamb waves, which represent the combination of SV and P modes and are strongly located at the surface. Figure 6.7 schematically shows symmetric and antisymmetric lamb waves. Symmetrical Lamb waves, or so-called "extensional" modes, move in a symmetrical fashion with respect to the median plane of the solid film. The wave is "stretching" and "compressing" the film in the propagation (longitudinal) direction. Wave motion in the symmetrical mode is most efficiently produced when the exciting force is parallel to the film. Antisymmetrical Lamb waves, or "flexural" modes, exhibit average displacement in the transverse direction. The third possible solution is (c) $\omega/q < v_t$. In this case, both transverse and longitudinal components are localized at the surfaces. These are Rayleigh modes which are the surface modes of a semi-infinite solid when $qb \to \infty$. Loudon [147] showed mathematically that velocity v_R of the Rayleigh surface wave is slightly below the velocity of the transverse bulk mode v_t: $v_R/v_t = 0.933$.

Another possible type of surface waves is scattering on surface ripples. The reflection of light is sensitive to irregularities of the surface and the inelastic surface effect can play a significant role. For example Mishra and Bray [148] and later Sandercock [149] observed contributions at relatively high frequencies compared to Rayleigh surface waves. This surface mode corresponds to the reflection from surface ripples. The exact form of the Brillouin spectrum depends on the ratio v_t/v_l. Similar to the previous case described above three regions can be specified: (a)$\omega/q > v_l$, (b) $v_l > \omega/q > v_t$ and (c) $\omega/q < v_t$ which correspond to scattering from bulk phonons, Lamb waves and Rayleigh waves. Since these waves are reflected waves they do not propagate through the film and thus do not depend on the refractive index n. Therefore, they can be observed in scattering experiments on opaque materials.

Surface waves can also propagate along the interface between two media. We consider a thin layer with thickness b on a substrate. Depending on the ratio of transverse velocities v_t/v_t' in the layer (v_t) and in the substrate (v_t') several possibilities can exist [144, 146]: (a) $v_t' > v_t$, in this case the wave is trapped in the thin layer on the substrate, corresponding to total internal reflection with only an evanescent wave extending into the substrate. This is a horizontally polarized surface wave and often called the Love wave. The second case (b) $v_t' \ll v_t$ corresponds to only one vertically polarized wave. In the limit $qb \to 0$ this wave becomes the Rayleigh wave on the substrate. If (c) $v_t' \gg v_t$ there are two families of modes which can be excited: symmetric M_{1i} and antisymmetric M_{2i} modes. These modes have special properties. In the limit $qb \to 0$ only the M_{11} mode is trapped and corresponds to the Rayleigh wave on the substrate surface. As the thickness increases, the next mode M_{21} is trapped which is called the Sezawa wave. In the limit $qb \to \infty$ the Sezawa mode becomes the Rayleigh mode on the upper boundary of the layer. Under specific conditions $v_t' \sim v_t$ the mode M_{21} becomes a bound interface mode known as the Stoneley wave with velocity v_s which must satisfy the condition: $v_R' < v_s < v_t'$ where v_R' is the Rayleigh wave in the substrate.

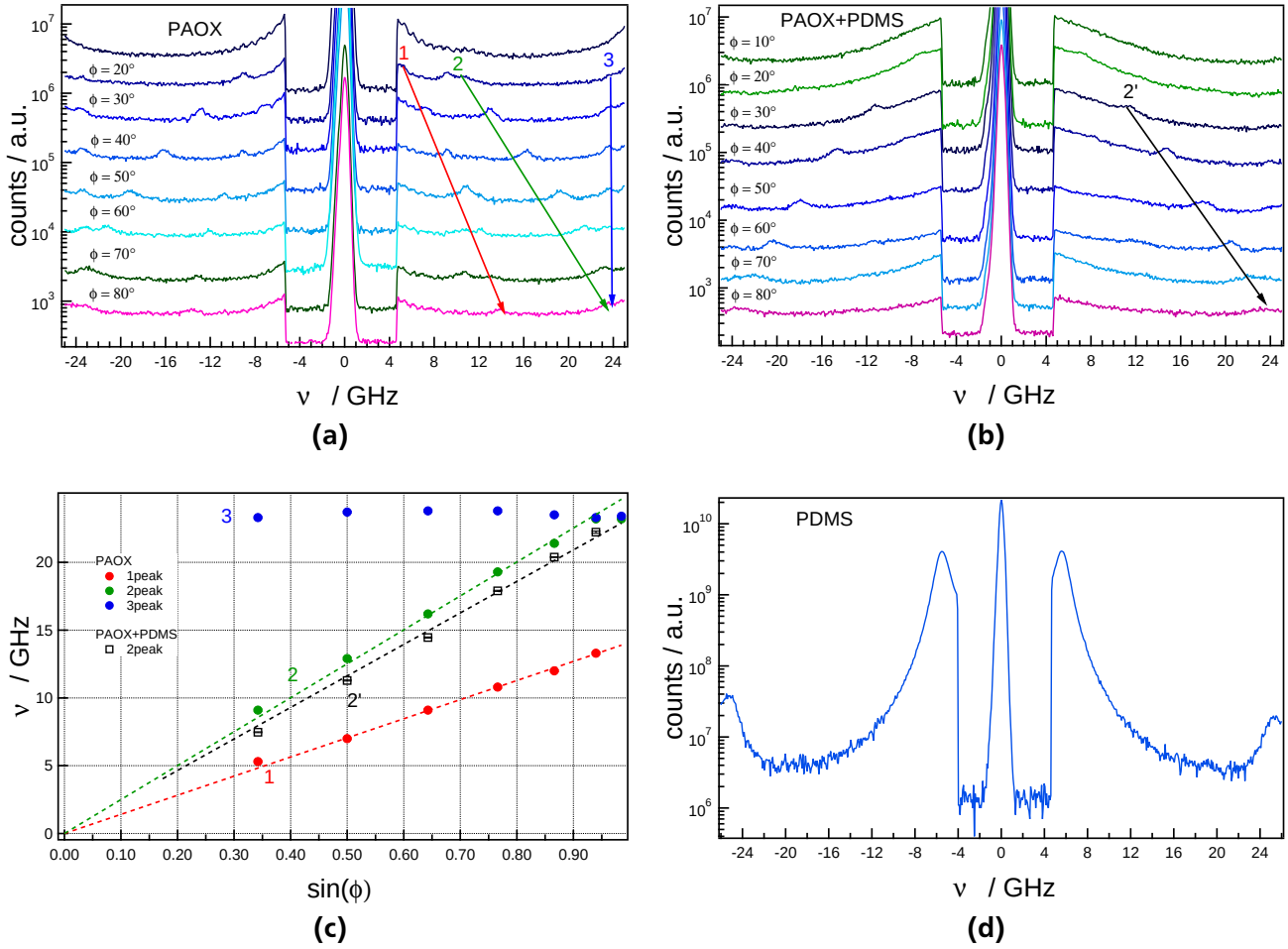

Figure 6.8.: BLS spectra of PAOX membrane: (a) empty pores;)b) filled with PDMS; (c) Dispersion relation of empty and PDMS filled PAOX templates; (d) BLS spectrum of bulk PDMS.

6.2.2 Sound propagation in PAOX templates

In this section the elastic excitations in PAOX templates will be discussed. Properties and structure of the PAOX template were described in chapter 3.1. Here we use the template with pore radius of 20 nm and a porosity of around 60%. PDMS of M_w=13 650 g/mol was placed on the open surface of the PAOX template and infiltrated into pores at room temperature within 2 hours. A polymer layer formed on the membrane surface during infiltration and was mechanically removed. The presence of PDMS in the pores of the membrane was verified using SAXS.

The PAOX templates are transparent for light which makes them suitable for investigations using Brillouin light scattering. The sample was fixed on a rotation stage. Every sample was measured in the angular range from $\phi = 0°$ corresponding to perpendicular alignment of the surface to the laser beam (see fig. 6.6) and $q_{\parallel} = 0$, up to $\phi = 80°$ when the incident beam is close to being parallel to the surface of the template. In this case the scattering vector almost corresponds to $q_{\parallel}$, and $q_{\perp}$ is close to zero.

Figure 6.8a shows the measured intensity $I(\nu)$ scattered from the empty PAOX template for different rotation angles ϕ. The spectra displays two distinct regions. The first region in the center of the spectrum around $\nu = 0$ shows the elastic peak which is attenuated in order to decrease the maximum intensity of the elastic peak. The second region is outside the elastic peak and represents the Brillouin lines, which show different behavior depending on rotation angle. Peak positions are recovered from the fit according to superposition of normalized lorentzian functions:

$$f(\nu) = A \cdot \frac{1}{\pi}\left(\frac{\Gamma/2}{(\Gamma/2)^2+(\nu-\nu_0)^2} + \frac{\Gamma/2}{(\Gamma/2)^2+(\nu+\nu_0)^2}\right) + \\ +B \cdot \frac{1}{\pi}\left(\frac{\Gamma'/2}{(\Gamma'/2)^2+(\nu-\nu_0')^2} + \frac{\Gamma'/2}{(\Gamma'/2)^2+(\nu+\nu_0')^2}\right) \tag{6.42}$$

where A and B are areas of the peaks, Γ and Γ' are the broadness of the corresponding peaks and ν_0 and ν_0' are peak positions.

First of all, the empty template exhibits three very small peaks. One of the peaks – mode (3) – does not change position with the rotation angle and thus corresponds to the bulk longitudinal mode of PAOX [150].

The other modes (mode 1 and 2) depend on the rotation angle and shift to higher frequencies with increasing rotation angle. As shown in figure 6.8c modes (1) and (2) have linear variation with $q_{\|}$, and therefore propagate along the surface of the template. These modes can be either surface modes or transverse modes. Due to rotation of the template with respect to the incident beam the transverse mode propagates with $q_{\|}$ which results in the linear dependency of $\nu(q_{\|})$. The sound velocity of the transverse mode is expected to be $\upsilon_t = 3750$ m/s [150], which corresponds to a frequency of 18.4 GHz at $\phi = 90°$ and 6.3 GHz at $\phi = 20°$. One observes that mode (1) has a different sound velocity[3] which is equal to $\upsilon_1 = 2850 \pm 30$ m/s if we assume that the mode propagates inside the template. This mode is much slower than the expected transverse mode, moreover it is slower than the expected Rayleigh wave ($\upsilon_R = 0.933\upsilon_t$). It means that this mode does not propagate though the PAOX template and can arise due to scattering on surface ripples. In this case mode (1) is independent on the refractive index n and propagates with velocity $\upsilon_1 = 3730 \pm 30$ m/s.

Mode (2) obviously has higher velocity than the transverse mode ($\upsilon_2 = 5240 \pm 40$ m/s in the template). The ratio between velocities of mode (2) and mode (1) is $\upsilon_2/\upsilon_1 = 1.4 \pm 0.2$ which is slightly above the refractive index of PAOX ($n_{\text{eff}} = 1.31$). This mode might be scattering on surface ripples on the back side of the template. This mode propagates inside the template.

After polymer infiltration the Brillouin spectrum shows only one angle dependent peak (2') which is shifted to lower frequencies compared to mode (2) of empty PAOX (fig. 6.8b). The shift ratio is $\nu_2/\nu_{2'} = 1.17$ which corresponds to the expected change of the refractive index and the bulk modulus of the effective medium (the calculation is shown in appendix B.2). Since mode (2) propagates through the template it is sensitive to the change of the elastic properties of the template. The corresponding sound velocity is $\upsilon_{2'} = 3870 \pm 40$ m/s. Modes (1) and (3) have vanished. The reason for the disappearance of mode (1) might be the strong contribution of the broad peak of PDMS which shows in figure 6.8b as ν-dependent background. The frequency of the longitudinal bulk mode of PDMS is expected to be around 4.5 GHz which is near the limit of the FSR and not visible in the spectra. However, since the PAOX template has 60% of volume fraction filled with polymer and might have an extra polymer layer on the surface[4] the scattering from PDMS could dominate in the spectrum and cover the surface mode (1).

6.2.3 Ion track etched polycarbonate templates (ITPC)

ITPC is a nanoporous template containing strictly parallel pores similar to the already presented PAOX template. These membranes are produced by the irradiation of PC foils with heavy ions and subsequent chemical etching of the tracks. By varying parameters of the ion beam and the etching conditions templates with different pore size and porosity can be obtained. Compared to PAOX, ITPC has no regular arrangement of pores, the pores are statistically distributed and the porosity of this template is much

[3] The sound velocity is calculated from the slope a of the experimental curve in figure 6.8c as $\upsilon = 2\pi a/q$. Error bars are estimated in the same manner.

[4] It is impossible to completely remove the polymer layer from the template surface mechanically. The thin layer of PDMS might remain on the surface.

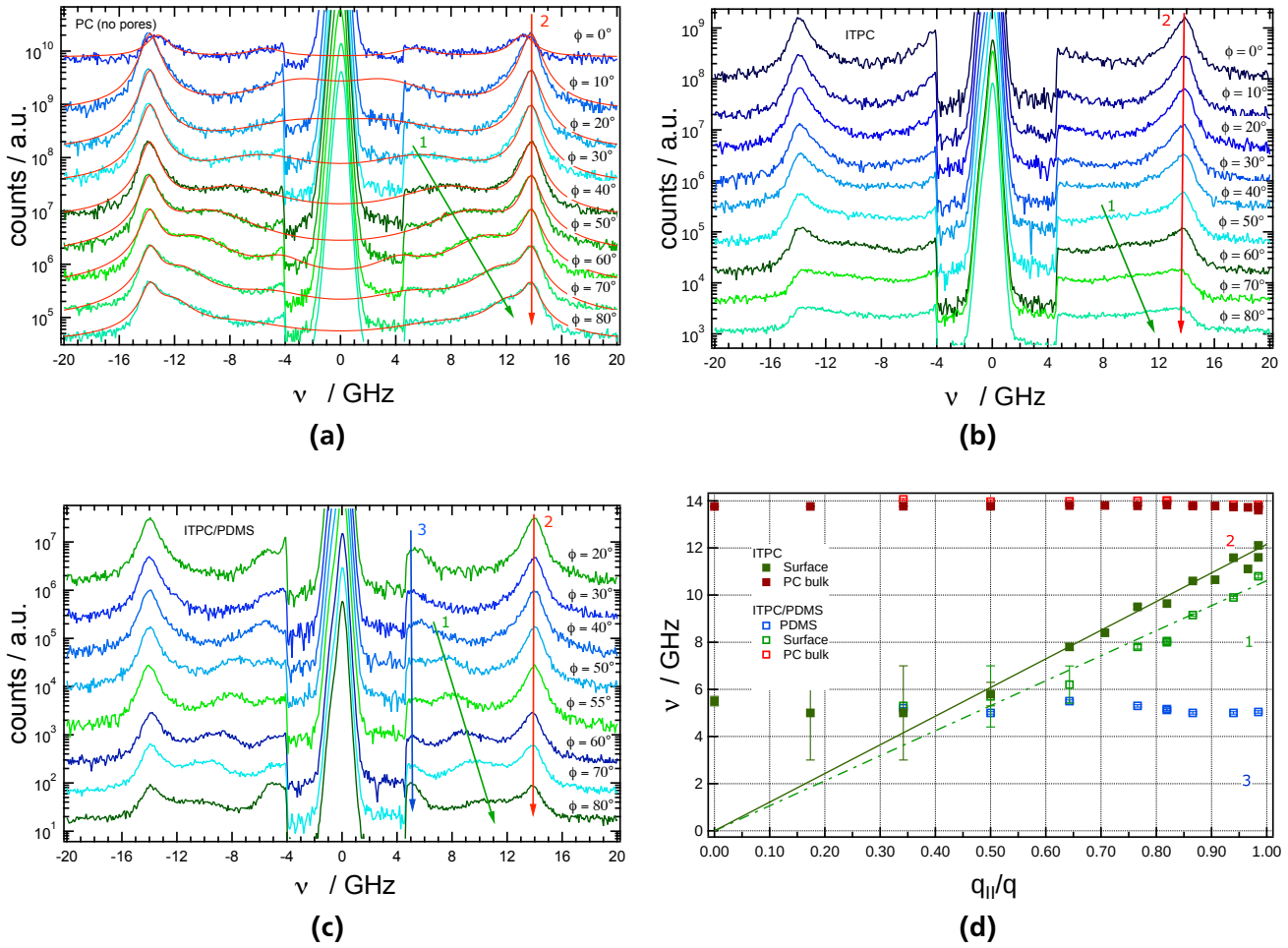

Figure 6.9.: BLS spectra of PC membrane: (a) PC membrane without pores with fit according to equation (6.42) ; (b) ITPC, (c) ITPC filled by PDMS; (d) Dispersion relation of empty and PDMS filled ITPC membrane. Mode (1) is the bulk mode of PC, mode (2) shows the surface mode of PC and mode (3) corresponds to the bulk mode of PDMS.

lower than for PAOX. Pore distribution can influence the propagation of sound waves due to changing of the opto-elastical response of the medium.

Amorphous polycarbonate foil (Macrofol, Bayer) with a thickness of 15 μm was irradiated with swift heavy ions at the linear accelerator UNILAC (GSI). To produce membranes, a metallic mask with circular aperture was placed in front of the PC foil [151]. The foil was further treated with UV light in order to increase the track etching selectivity. Then the foil was etched with a solution of 6 mol/ml NaOH at 50 °C within 80 sec. The pore density is $N_p = 1 \times 10^9$ pores/cm^2 and the porosity is $f = \pi R^2 N_p = 0.013$. The pore radius $R = 18$ nm was determined by SAXS [92].

Sound propagation in empty and polymer filled ITPC template

The important difference between ITPC and PAOX templates is the fact that ITPC has low porosity and change of the effective medium due to polymer infiltration does not affect the sound propagation. Empty and PDMS filled ITPC membranes are measured under the same conditions as PAOX templates. The rotation angle varies within $0° < \phi < 80°$.

The Brillouin spectra of the empty ITPC membrane is shown in figure 6.9a. First of all, all spectra exhibit one peak at 13.8 GHz (mode 2). The position of the maximum does not depend on the rotation and corresponds to the longitudinal bulk mode [152].

The spectra also contain a broad shoulder – mode (1) – which is a ϕ-dependent mode and is only visible at high rotation angles ($\phi > 30°$). As shown in figure 6.9d this mode has linear variation[5] with $q_{\parallel}$, and therefore propagates along the surface of the template with velocity of $v_1 = 1970 \pm 20$ m/s (in the template). The sound velocity is higher than the expected velocity of the transverse wave ($v_t = 1100$ m/s [152]), thus this mode is not transverse or the Rayleigh mode. This mode might be identified as a surface mode caused by surface ripples which can be on the top or bottom side of the template. If mode (1) corresponds to the scattering from ripples on the bottom side of the template, the mode propagates through the medium and depends on n. In case when the mode occurs due to scattering from ripples on the top side, the mode does not depend on n and then has a velocity of 3090 ± 30 m/s.

Another possibility is that the observed surface mode arises not due to surface ripples, but due to coupling of P and SV modes, which is the Lamb wave. The strong indication for the existence of Lamb waves is the thickness of the template which is only 15 μm. Since $v_t < v_1 < v_l$ is satisfied, the Lamb wave can exist. However, mode (1) shows very broad shape. The broad shape of the mode can be explained by overlapping of different surface modes [152]. For example, the peak (1) could contain two acoustic modes: the surface mode which arises from the surface ripple inelastic scattering and the Lamb wave having the same $q_{\parallel}$ component of the scattering vector.

The same modes are observed in figure 6.9b displaying the ITPC membrane with empty pores. The bulk longitudinal mode (2) propagates with the same speed (v_1) as in the amorphous PC film and only the shape of the peak becomes broader. The surface mode (1) is less pronounced than in amorphous PC but is clearly observed at angles higher than 50°. Low resolution of the surface mode can be explained by birefringence of the PC membrane. Birefringence affects the intensity of the surface mode. Rotation of the membrane in plane perpendicular to the incident beam decreases or increases the intensity of the observed surface mode.

Now we consider the ITPC membrane filled with PDMS. After infiltration of PDMS in the nanopores of the ITPC membrane we observe three modes (fig. 6.9c). The low frequency mode (3) corresponds to the acoustic wave propagating through PDMS. It is independent of the rotation angle and corresponds to the longitudinal bulk mode of PDMS. Now we do not observe the ν-dependent background caused by PDMS due to very low fraction of PMDS in the total sample volume. The bulk mode of PC (2) does not shift after polymer infiltration. A broadening of the observed peak between amorphous PC film, empty and polymer filled ITPC can occur due to birefringence of the polycarbonate film. However, the surface mode (1) becomes narrower than for empty ITPC and amorphous PC films and is shifted to lower ν. The ratio of sound propagation velocity for this mode between polymer filled and unfilled ITPC is $v_{\text{empty}}/v_{\text{filled}} = 1.22$. In contrast to the PAOX templates, where the change of sound velocity was explained as a change in effective refractive index n_{eff} or effective bulk modulus k_{eff}, ITPC is a low porous template and the effective medium does not change so strong to cause the observed shift (this can be seen from the calculation in appendix B.2).

The changing of the frequency of the surface mode is probably caused by the presence of a thin PDMS film on the ITPC surface which could not be completely removed. In this case, the surface wave can propagate along the interface of PDMS and PC and along the free surface of the PDMS film [143, 153]. However, the sound velocity of PDMS is too low ($v_l = 1050$ m/s [154]) and PDMS surface modes are not visible in our experiment. The observed mode propagates along the interface of ITPC and PDMS films. Since $v_t^{PDMS} < v_t^{ITPC}$ the excited mode might be the Sezawa or the Love wave. Therefore, the PDMS layer on the top surface of the ITPC membrane can modify the structure of Brillouin spectra. The original mode is not visible anymore, instead we observe another surface mode which arises due to change of the boundary conditions.

Actually the polymer layer is expected to be on top of the filled PAOX template as well and should cause the same effect as in the case of the ITPC membrane in principle. However, we do not observe an extra mode on the surface of the PAOX template. First of all, Brillouin spectra of PAOX/PDMS show

[5] The frequency at low ϕ differs from the linearity due to bad resolution of the mode at this angles. The peak is expected to be lower the FSR and cannot be properly fitted. We exclude these points in data analysis.

ν-dependent background increasing at low ν. All modes which are expected to be in the low frequency range can be hidden. On the other side, the PAOX template has almost four times the thickness of the ITPC template (PAOX 50 μm, ITPC 15 μm). This means that four times the number of wavelengths fit into the thickness of the PAOX template and for example Lamb waves do not exist or have very low frequency close to the expected frequency of the Rayleigh wave.

6.3 Summary and conclusions

Using Brilloun light scattering thin templates with cylindrical pores were investigated. We compared two types of templates having high and low porosity. Brillouin spectra in both cases show a combination of bulk and surface modes. Surface modes are identified by their linear dependency of peak position on the parallel component of the scattering vector.

Amorphous PC and ITPC show a longitudinal bulk mode and one surface mode. After polymer infiltration the surface mode of the ITPC membrane is shifted to lower frequencies. The shift cannot be explained by a change of the effective medium due to the low porosity of the membrane. However, it might be caused by the PDMS layer on top of the template which changes the boundary condition and modifies Brillouin spectra.

The empty PAOX template shows one longitudinal bulk mode and two surface modes which probably arise due to the surface ripples. In the PAOX/PDMS system one of the surface modes disappears due to a strong overlapping signal from the bulk PDMS. The second mode shows a shift to lower frequencies by a factor similar to the one found for ITPC membranes. However, the shift in PAOX fully corresponds to the change of the effective medium. Due to a different thickness of PAOX and ITPC templates different surface modes can be visible in the Brillouin spectrum.

However, we do not have enough information to identify modes propagating parallel to the surface without a doubt. The experiment contains many difficulties, for example the birefringence of ITPC templates influences the resolution of surface modes and makes analysis more complex. The variety of the possible surface waves which fulfill the propagation conditions can be overlapping in Brillouin spectra making the identification even more difficult. Moreover, we used only one experimental geometry which does not provide full information about elastic excitations in the investigated templates. More experiments at different scattering geometries, polarization as well as with templates of different thickness should be performed in order to obtain more robust conclusions.

7 Thesis summary

In this work polymers were investigated under cylindrical confinement, in particular in composite materials based on carbon nanotube (CNT) arrays. For this purpose we used CNT arrays consisting of well ordered, vertically aligned CNTs with tube diameter in the range of 40-100 nm. The first part of the work was focused on the investigation of the structure of CNT arrays and their composites. The second part of the thesis described the imbibition of the polymer into CNT arrays and focused on properites of polymers in arrays like chain conformation and dynamical aspects of polymers. In the last part of this work we described the elastic properties of thin porous templates filled with polymers.

This work was started with the characterization of CNT arrays at every step of the preparation process. In the first step, the porous alumina (PAOX) templates were investigated by small angle X-ray scattering (SAXS). PAOX templates having hexagonally ordered cylindrical pores were described in terms of the model function of core-shell cylinders arranged in a two dimensional hexagonal lattice. Parameters of anodization of PAOX influence the structure of templates: changing the voltage, acid concentrations and steps of the anodization process result in different pore diameters and distances between pores. All these effects can be taken into account by the mentioned model function. The resulting parameter values are in good agreement with the values obtained by scanning electron microscopy (SEM). CNTs of 40 nm and 90 nm in diameter were used in this work. The average distance between pores of 40 nm in diameter was found to be around 100 nm.

Having information about PAOX templates, we described CNTs grown inside these templates by the chemical vapor deposition (CVD) technique. Analysis of the structure of CNTs enclosed in PAOX was performed in the same way as for pure PAOX templates with the same scattering model function. During the deposition of carbon in the pores of PAOX amorphous carbon layers are formed on the top and bottom surfaces of the templates. Depending on the time of the synthesis two different situations can be achieved: one with the carbon layer on only one side of the array and a completely closed array (with two carbon layers). The carbon layer can be removed by plasma etching, which results in the third possible structure — freestanding CNT arrays. It was shown that the presence of carbon layers affects the final structure of the CNT arrays. CNTs in freestanding arrays are bundled by van der Waals forces and the average distance between centers of two nearest tubes almost equals the tube diameter. In these arrays CNTs form clusters which are well resolved in SEM. In the case where two carbon layers remain on both sides of the CNT array this dramatic decrease of the tube-to-tube distance with respect to the pores of PAOX was found as well. Due to the high flexibility of CNTs along their length tubes are curved in the middle. One side closed arrays have shown parameters similar to freestanding arrays, but the carbon layer prevents tubes from bundling.

In the next step the structure of CNT/polymer composites was investigated. Two ways of polymer infiltration were considered. First, CNT arrays were filled with polymeric solutions. We used polystyrene (PS) and polymethylmetacrylate (PMMA) of various concentrations of solutions. A SAXS study has shown that in freestanding arrays polymers adsorb from the solution inside CNTs and between clusters of bundled tubes. The higher the concentration of solutions is, the faster the adsorption proceeds and correspondingly less polymer was found in the composites. In the case of two remaining carbon layers the infiltration of the tube interior is prevented. The Polymer solution can fill the array perpendicular to the long axis of tubes and can flow between CNTs only. We have found no evidence of polymer deposition in both sides closed arrays for any concentration of the polymeric solution.

The second possible method is polymer infiltration from the melt. This was studied on two types of arrays: freestanding and one side closed arrays. In all cases polymer flows into CNT arrays due to capillary forces. However, the structure of CNTs plays an important role. Freestanding arrays were filled

in the tube interior and between clusters of CNTs. The structure of arrays did not change after the polymer infiltration. One side closed arrays showed increase of the distance between CNTs of around 3 nm after the polymer infiltration. Polymer flow into these arrays improves the arrangement of tubes. At the same time the polymer fills the inner part of CNTs as well.

Combining SAXS and microscopy (TEM and AFM) we investigated the structure of CNT/polymer composites on a wide range of scales. Thus, composites with CNTs of 40 and 90 nm in diameter were considered. The AFM study has shown that the big tubes (90 nm) are not stable along their length. CNTs are collapsed and form small tube-like arrangements with a diameter of 15-20 nm. Comparing the arrays with two different diameters, we found that depending on tube diameter the efficiency of the filling inside and outside tubes is different. Thus, in arrays with large tube diameter polymer fills the inner part of CNTs more effectively than the interstices between tubes. The opposite situation was observed for arrays with small tube diameter: the tube interior is less filled than the volume around CNTs.

Up to this point we have obtained information about the structure of CNT/polymer composites, the influence of the tube diameter, presence of carbon layers and different methods of polymer infiltration. It was shown that CNT/polymer composites can be successfully studied by SAXS and described by the chosen model function. After this detailed description of the structure of composites we can get access and focus on the polymer properties in CNT arrays.

The investigation of the structure of composites was followed by the study of the filling kinetics. The obtained difference in "quality" of polymer infiltration inside tubes and between them gave rise to consider the imbibition process of polymers into CNT arrays in detail. Using time-resolved SAXS we have found that the filling of PS into CNT arrays with tube diameter of 40 nm proceeds on two separate time scales. They are related to formation of a precursor film and filling of the volume. The filling kinetics deviates from the well-known Lucas-Washburn flow and was described by compressed exponentials with exponents 1.7 ± 0.1 and 3.5 ± 0.1 which correspond to the dimensionality of the expansion of the polymer filled areas in the array.

The investigation of filling kinetics of PS in the tube interior only has shown that in uniform straight cylindrical tubes the imbibition proceeds in one step only which can be described with exponent 1.5 ± 0.1. However, the overall kinetics can be separated in two stages. The early stage is the polymer flow into tubes which can be described by the Lucas-Washburn equation. The later stage of kinetics corresponds to reorganization of the polymer inside tubes. A depletion layer is formed in the vicinity of the CNT surface. The thickness of this layer is found to be around 7-8 nm. Based on the presented experiment and theoretical studies of polymers at interfaces we assume a complex structure of the interphase near the CNT surface consisting of a rather thin adsorbed polymer layer on the surface, then the thick depletion layer with radially stretched chains and finally the bulk polymer in the center of the tube. The conformation of polymer chains in the CNT interior was studied by small angle neutron scattering (SANS). Experiments have shown that investigation of polymer chain conformation in CNT arrays is difficult due to the structure of composites and incomplete filling of the arrays.

The existence of the interphase near CNT walls in composites suggested different mobility of polymer in these composites. The dynamical aspects of polymer behavior in CNT arrays were probed by the investigation of phase transitions of polymers. Using differential scanning calorimetry (DSC) we studied the glass transition of PS in CNT arrays. Arrays with tube diameter of 40 and 90 nm were filled with PS of molecular weight of 21 000 and 88 000 g/mol. We have found a small positive shift of the glass transition temperature T_g. For the small molecular weight of PS the shift was found to be 2K and 4K for the larger polymer. The tube diameter does not affect T_g. Taking into account the different confinement inside and outside tubes in arrays we investigated the glass transition inside and outside tubes separately. This was achieved by infiltration of two different polymers: one in the tube interior and a second one into the interstices between tubes. PS infiltrated into tubes demonstrated a complex glass transition. Two different T_g can be recovered: one corresponds to the T_g of the bulk polymer and the second one is shifted with respect to the bulk. In most cases we observed a positive shift of T_g.

We have not found a shift of T_g for polydimethylsiloxane (PDMS) infiltrated between CNTs. However, differences in melting and crystallization were observed. Isothermal and nonisothermal crystallization of PDMS was investigated. In the beginning we have analyzed the crystallization of bulk PDMS. PDMS crystallizes in two steps: the first step is a formation of metastable crystals and the second one is recrystallization of these crystals to the more stable state. We have found that in CNT arrays PDMS crystallizes in the same way: formation of stable crystals via the metastable state. Both processes were found to be faster than in the bulk. Thus, crystallization of PDMS around CNTs in the array is enhanced.

In the last part of the work the elastic properties of thin porous templates filled with polymer were investigated. Two templates with low and high porosity were studied by Brillouin light scattering (BLS). Ion tracked etched polycarbonate membranes (ITPC) and PAOX having a pore diameter around 40 nm and a film thickness of 15 and 50 μm respectively were filled with PDMS. In both cases Brillouin spectra contained bulk and surface modes which arise due to surface ripples. The surface modes are affected by the polymer infiltration while the bulk modes remain unchanged. The ITPC membrane representing a low porous system showed a shift of the surface mode to lower frequencies after polymer infiltration which cannot be explained in terms of the effective medium approximation. The surface mode of the PAOX template is also shifted to lower frequencies after polymer infiltration. However this shift is well explained by the changing of elastic properties of the effective medium. No evidence of elastic deformation due to an interphase was found. However, further systematic experiments with different polarization and variation of the q vector have to be done.

A Data evaluation for SAXS and SANS experiments

A.1 Multi shell cylindrical form factor

For describing SAXS scattering profiles of polymer filled CNTs embedded into the PAOX template or to consider the precursor layer near the CNT surface (see section 4.4.3) the form factor with more than one shell is applied.

The form factor of the cylinder with multiple shells (see figure A.1) can be derived similar to form factor of the core-shell cylinder. For this purpose the equation for the solid cylinder (2.17) can be rewritten as

$$F(q) = b_e\rho_{\text{core}} \int_{-L/2}^{L/2}\int_{0}^{R_{\text{inner}}}\int_{0}^{2\pi} e^{-i\mathbf{qr}} r' d\phi dr' dz + b_e\rho_{\text{shell}_1} \int_{-L/2}^{L/2}\int_{R_{\text{inner}}}^{R_{\text{outer}_1}}\int_{0}^{2\pi} e^{-i\mathbf{qr}} r' d\phi dr' dz + \\ + b_e\rho_{\text{shell}_2} \int_{-L/2}^{L/2}\int_{R_{\text{outer}_1}}^{R_{\text{outer}_2}}\int_{0}^{2\pi} e^{-i\mathbf{qr}} r' d\phi dr' dz + \ldots \tag{A.1}$$

where R_{inner}, R_{outer_1} and R_{outer_2} are radii of inner cylinder (core) and first and second shell correspondingly. The integrals over z and ϕ can be calculated in the same way as for solid cylinders and the form factor of a multi-shell cylinder can be expressed as a superposition of single cylinders. The solution of every integral over r' results in the Bessel function $J_1(qR)$. Solving integrals over r' for every term in equation (A.1) in the respective limits results in the form factor of a multi-shell cylinder $F(\mathbf{q})$:

$$F(\mathbf{q},R) \propto R_{\text{inner}}(\rho_{\text{core}} - \rho_{\text{shell}_1})\frac{J_1(R_{\text{inner}}q)}{q} + R_{\text{outer}_1}(\rho_{\text{shell}_1} - \rho_{\text{shell}_2})\frac{J_1(R_{\text{outer}_1}q)}{q} + \\ + R_{\text{outer}_2}(\rho_{\text{shell}_2} - \rho_{\text{matrix}})\frac{J_1(R_{\text{outer}_2}q)}{q} \tag{A.2}$$

Following the same procedure the form factor for three, four and more shells can be derived.

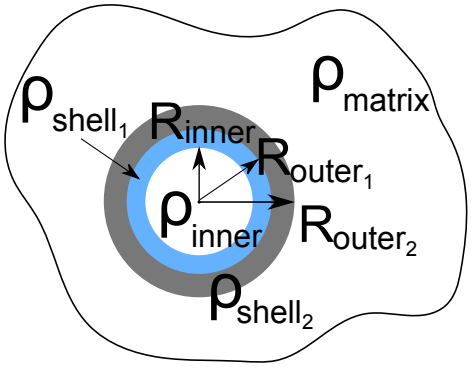

Figure A.1: Sketch of a multi-shell cylinder

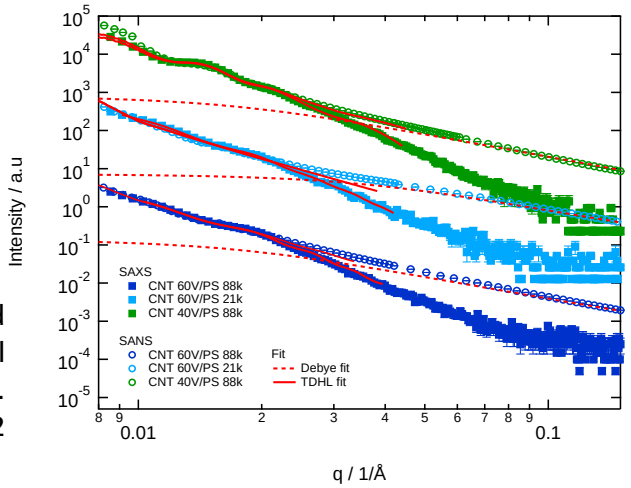

Figure A.2: SANS and SAXS profiles of PS filled CNT arrays with fit of the TDHL model and approaching the Debye function. SANS profiles were recorded by the D22 diffractometer.

A.2 SANS scattering profiles and data correction

D22 experiment: choice of the optimal tube diameter and molecular weight of polymer

As was discussed in the beginning of section 4.3.3, the purpose of the D22 experiment was to find the combination of tube diameter and molecular weight of polymer in order to separate scattering from polymer chains and CNT structure for future SANS experiments.

Figure A.2 is complementary for figure 4.14b and shows polymer filled CNT 60V (blue curves) and CNT 40V (green curves) fitted with the two dimensional hexagonal (TDHL) model function with core-shell cylindrical form factor (solid red line). Structure parameters like inner and outer radii of CNTs, polydispersity and distance between tubes are obtained from fitting SAXS profiles and the model function is then approximated to SANS data by replacing the scattering length densities (SLD). SANS profiles cannot be fitted directly due to the arbitrary orientation of the CNTs with respect to the incident beam. Nevertheless, as shown in figure A.2 the structure peak observed in SANS curves at low q range remains the same as in SAXS profiles.

The Debye function shown in figure A.2 is obtained from the fit of bulk polymer film and shown together with SANS profiles of CNT/PS composites[1]. It shows that the high q range contains a contribution of the scattering from the polymer coils. The best separation between scattering from the CNT structure and the polymer is observed for CNT 60V and PS 21 800 (light blue curves). This data is shown in figure 4.14b in section 4.3.3. For this combination of the CNT radius and the polymer radius of gyration the scattering from polymer is more pronounced at high q and exhibits evidence of the plateau around 0.35 $Å^{-1}$ which is typical for the Debye function. The observed plateau will make a fit of the polymer scattering component more precise. Smaller tube diameter as well as larger M_w of the polymer produces overlapping of the scattering from CNT structure and the scattering from the polymer chain.

D11 experiment: Contrast situation of CNT/PAOX structure

During the SANS experiment on CNT arrays filled with PS in tube interior only (sec. 4.3.3) which was carried at D11 diffractometer we observed a broad shoulder at q around 0.1 $Å^{-1}$. Figure A.3a shows this shoulder for all investigated samples with small (40V) and big (60V) tube diameter. One observes that the shoulder position as well as the shape does not depend on the tube diameter and the polymer filling. Figure A.3b shows the polymer filled CNT 40V together with the TDHL model function plotted with adequate parameters. The SLD of CNT walls is assumed to be around $5 \cdot 10^{-6}$ $Å^{-2}$, SLD of PAOX $4.5 \cdot 10^{-6}$ $Å^{-2}$ [155], SLD of PS is close to $1 \cdot 10^{-6}$ $Å^{-2}$. Direct fitting is not possible due to arbitrary orientation of CNT with respect to the primary beam. The model suggests a broad shoulder in the high

[1] The Debye curve is only vertically shifted to the level of SANS profiles of CNT arrays

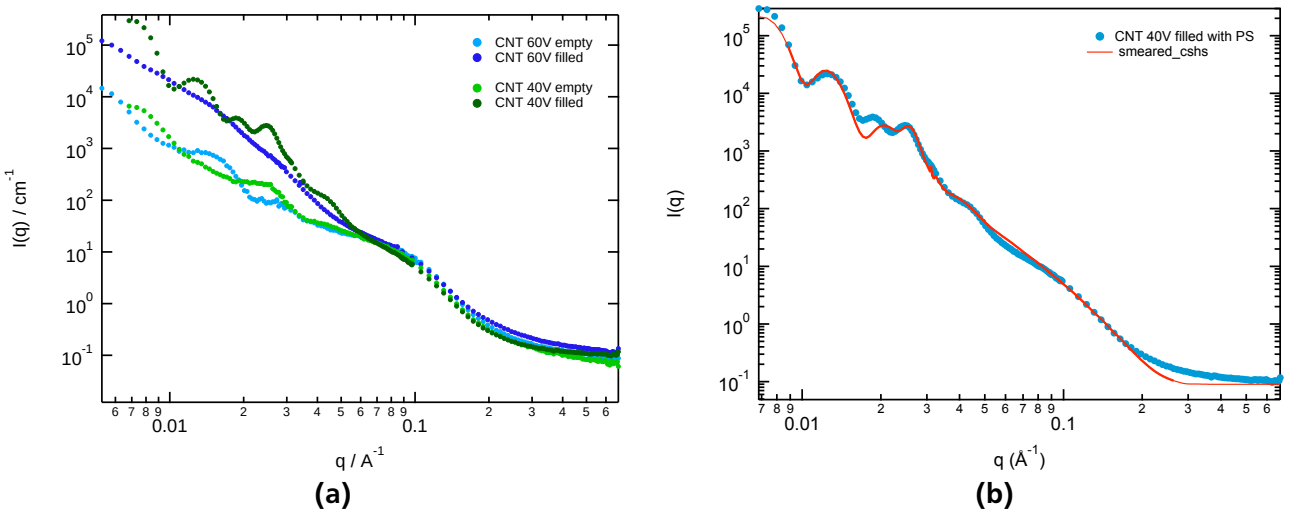

Figure A.3.: (a) SANS profiles of empty and polymer filled CNT 40V and 60V in the PAOX template representing the shoulder at high q range; **(b)** SANS profile of CNT 40V in the PAOX template with TDHL model function

q range similar to the one observed in experimental data. This shoulder can be considered as a feature arising due to SLD contrast between PAOX and CNT.

A.3 Branch fitting procedure of the filling kinetics

Data series of the filling kinetics presented in sections 4.4.2 and 4.4.3 were fitted one by one in a programmed automatic procedure. First of all, the scattering profile of the empty CNT with a solid polymer film on top (the first profile in the experimental series) is fitted by the model function. All obtained parameters except electron densities of core and shell/matrix are fixed since the sample is kept in the vacuum sample chamber without changing its position. In the experiment described in section 4.4.2, when the tube separation increased right after beginning of polymer infiltration, the scattering profiles in the beginning were fitted manually in order to define a new structure factor and keep it fixed during the automatic fit procedure. Since the measuring time is several days, the fluctuation of the primary beam intensity should be taken into account. Any fluctuations of the intensity are included in the prefactor. It has to be corrected before fitting. Correction was done by measuring the photodiode intensity at the primary beam. This intensity corresponds to the primary beam intensity transmitted by the sample. Since the sample volume in the beam does not change, the photodiode intensity shows the fluctuation of the primary beam. The photodiode intensity is shown in figure A.4b. The fluctuation of the photodiode intensity is around 10%. Before fitting every scattering profile was divided by the photodiode intensity. After this the prefactor was determined by fit of the first scattering profile (before infiltration) and then fixed to the obtained value during the automatic fit procedure.

Therefore, scattering profiles are fitted one by one starting from the second (as soon as the temperature reaches 180°C) to the last one with two (in the section 4.4.3 three) free fit parameters - the electron density of core and matrix in section 4.4.2 and the electron density of core and shell, and the core radius in section 4.4.3. For the data presented in section 4.4.2 the fitting procedure was subjected to constraints for the electron densities: $\rho_{i-1} \leq \rho_i \leq 340$ e/nm^3 where i is the number of the scattering profile to be fitted. This restriction of the electron density results in rather small uncertainties of obtained electron densities. For the data in section 4.4.3 electron densities were less restricted in order to avoid unexpected errors of the fit procedure caused by the zero radius at the first steps and simultaneous fitting of core radius and electron densities. Constraints were chosen as $0 < \rho \leq 340$ e/nm^3 and for the radius

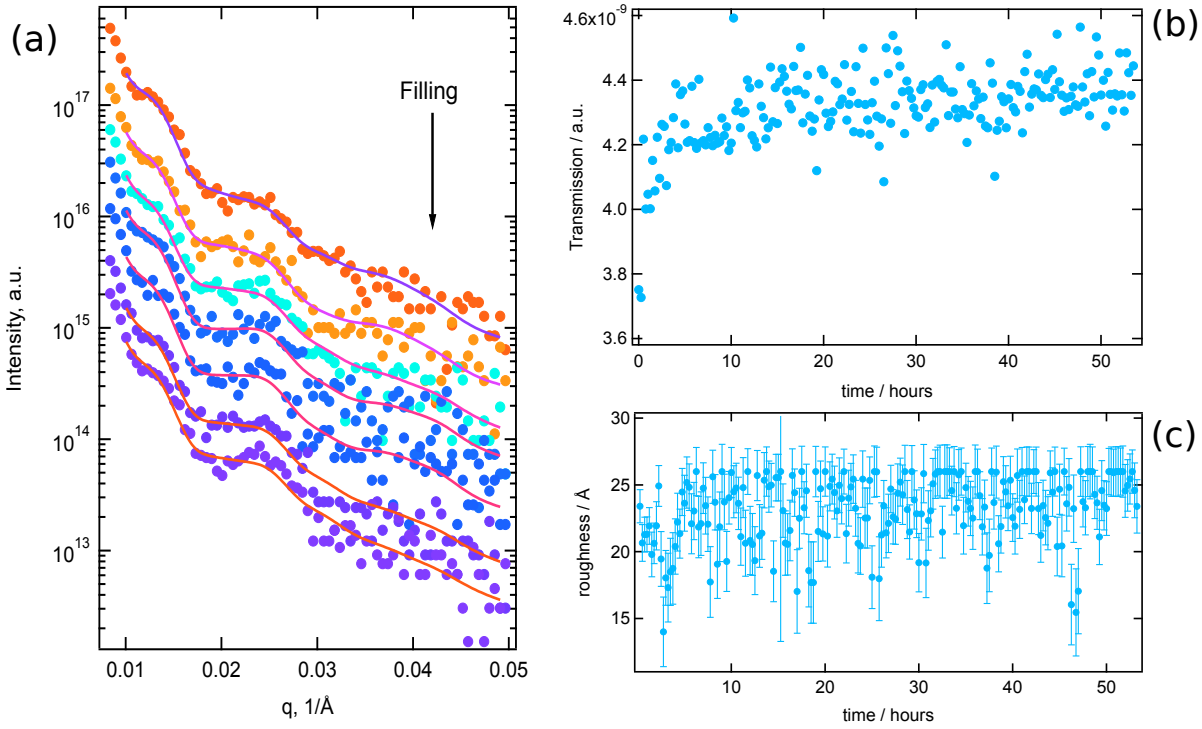

Figure A.4.: (a) Evaluation of the scattering profile during infiltration. Every 30th measurement is shown. Curves are vertically shifted; **(b)** The photodiode intensity at the beam-stop, which corresponds to the transmission of the sample; **(c)** Roughness of the CNT wall obtained from the fit.

$0 < R_{\text{core}} \leq R_{\text{inner}}$ where R_{inner} is inner radius of the CNT. Simultaneous fitting of electron densities and the radius results in the larger uncertainties of electron densities and the radius.

For the fitting of the kinetics in section 4.4.3 the double-shell form factor was used. Evaluation of the scattering profiles during infiltration is shown in figure A.4a. The first curve from the top represents the empty CNT array with solid polymer layer on the top and last curve in this sequence corresponds to the last scattering profile in the total experimental series. During the infiltration time the scattering profile was slowly changing. One observes the increase of the intensity of the second observed maximum.

In order to improve the fit procedure and better adjust the fitting curve the roughness of the CNT wall was kept as a free fit parameter with narrow constraints: $15 < \sigma_D < 26$ Å. These values were found experimentally by the manual fit of scattering profiles. The fitted roughness of the CNT wall for every scattering profile is shown in figure A.4c. The mean value of σ_D is around 24 Å. In the model function increase of the roughness provides an extra decay in high q-range. High q-range contains large uncertainties which arises due to the short measuring time which is preferable for investigation of filling kinetics. Variation of this parameter lets us better adjust the model function for bad statistics in the high q-range.

Technically, the roughness models the smooth transition of the electron density between core and shell or shell and matrix. The mean roughness in the experiment is around 2.5 nm which is of the range of two segment lengths of PS. This is a possible explanation why we did not observe the thin precursor layer at the wall which is expected to be in order of 1-2 monolayers. Anyway, the model function contains 15 fitting parameters in total and the investigated CNT arrays have very high polydispersity and deviation from an ideal hexagonal arrangement which strongly affects the quality of the fit. Introducing more fit parameters can lead to unphysical or uncertain values of electron densities and structural parameters of CNTs.

B Thermal analysis of polymers and Brillouin scattering

B.1 Calculation of T_g, ΔT and ΔC_p

For the discussion of glass transition of polymers in CNT arrays described in chapter 5.2 we need to specify the method of determination of the glass transition temperature T_g, the broadness of the transition range ΔT and the difference of heat capacity of the glass transition ΔC_p.

The principle of calculation of the glass transition is shown in figure B.1. The linear range of the thermogram below and above the glass transition is fitted with linear functions ($y1$ and $y2$). The average of these two linear functions $y3$ crosses the transition range in the middle. The intersection point is taken as glass transition temperature T_g. The difference between line $y1$ and line $y2$ at the point of T_g is taken as difference of heat capacity of the glass transition ΔC_p.

In order to obtain the broadness of the transition range ΔT, the slope of the heat flow is approximated at T_g with a linear function $y4$. The intersection points of $y4$ with lines $y1$ and $y2$ give the high and low limits of the transition range correspondingly. The difference between these points is the broadness of the glass transition.

B.2 Calculation of change of the speed of sound in porous media

The speed of sound propagating through a porous medium can be modified by porosity causing variation of the elastic contrast between pores and matrix and change of the effective bulk modulus or the effective refractive index of the medium.

As was discussed in chapter 6 the phonon phase velocity υ (speed of sound in a medium) depends on frequency ν of the acoustic mode and q vector:

$$\upsilon = \frac{2\pi\nu}{q} \tag{B.1}$$

where for the backscattering experiment q is defined according to equation (6.28):

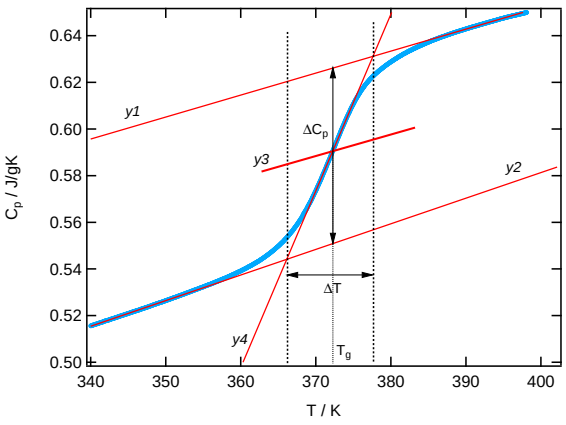

Figure B.1: Principle of calculation of parameters of the glass transition range

$$q = \frac{4\pi}{\lambda} n_{\text{eff}} \tag{B.2}$$

where n_{eff} is effective refractive index of the medium.

At the same time the speed of sound in a medium depends on elastic properties of this medium: k_{eff} — effective bulk modulus and mass density of the effective medium ρ_{eff}.

$$\upsilon = \sqrt{\frac{k_{\text{eff}}}{\rho_{\text{eff}}}} \tag{B.3}$$

Here we compare calculation of speed of sound for PAOX and ITPC templates before and after polymer infiltration.

ITPC

We first consider the ITPC membrane with porosity $f = 1.2\%$. The refractive index of PC is $n = 1.57$, bulk modulus $k = 3.1$GPa and mass density $\rho = 1.22$ g/cm^3. In the case of the empty membrane the pores are filled with air, so the effective refractive index of ITPC/air can be calculated using the Maxwell-Garnet approximation:

$$\varepsilon = \frac{\varepsilon_{\text{matrix}} \left(1 + 2f \frac{\varepsilon_{\text{pore}} - \varepsilon_{\text{matrix}}}{\varepsilon_{\text{pore}} + 2\varepsilon_{\text{matrix}}}\right)}{2 - f \frac{\varepsilon_{\text{pore}} - \varepsilon_{\text{matrix}}}{\varepsilon_{\text{pore}} + 2\varepsilon_{\text{matrix}}}} \tag{B.4}$$

where $n_{\text{eff}}^{\text{empty}} = \sqrt{\varepsilon} = 1.5629$. In the case of PDMS filled pores ($n = 1.41$, $\rho = 0.98$g/cm^3, $k = 1{\cdot}10^7$Pa) $n_{\text{eff}}^{\text{filled}} = 1.5679$. Therefore $n_{\text{eff}}^{\text{empty}} / n_{\text{eff}}^{\text{filled}} \approx 1$ and $\upsilon^{\text{filled}} = \upsilon^{\text{empty}}$.

The effective bulk modulus can be calculated according to the following equation:

$$k_{\text{eff}} = f \cdot k^{\text{pores}} + (1 - f) \cdot k^{\text{PC}} \tag{B.5}$$

The effective density is calculated in the same way. Again due to low porosity $k_{\text{eff}}^{\text{empty}} = k_{\text{eff}}^{\text{filled}} = 3.06$GPa and thus $\upsilon^{\text{filled}} = \upsilon^{\text{empty}}$.

PAOX

Similar to ITPC membranes in the previous paragraph the speed of sound in PAOX and PAOX/PDMS template can be calculated. We consider the PAOX template with porosity $f = 60\%$ and $n = 1.77$, $\rho = 3.95$g/cm^3, $k = 164 \cdot 10^9$Pa.

The resulting values for empty PAOX are: $n_{\text{eff}} = 1.31$, $k_{\text{eff}} = 65.6 \cdot 10^9$ Pa, $\rho_{\text{eff}} = 1.58$ g/cm^3.

According to equation (B.1) speed of sound is $\upsilon_n^{\text{empty}} = 6588$ m/s and according to equation (B.3) $\upsilon_k^{\text{empty}} = 6445$ m/s, where indices n and k correspond to the calculation with equation (B.1) and (B.3) respectively.

Similar calculations can be performed for PDMS filled PAOX. The resulting values are $n_{\text{eff}} = 1.55$, $k_{\text{eff}} = 65.6 \cdot 10^9$ Pa, $\rho_{\text{eff}} = 2.17$ g/cm^3 and $\upsilon_n^{\text{filled}} = 5562$ m/s and $\upsilon_k^{\text{filled}} = 5501$ m/s.

The change in speed of sound due to changing elastic properties of the medium is $\upsilon_n^{\text{empty}} / \upsilon_n^{\text{filled}} = 1.18$ and $\upsilon_k^{\text{empty}} / \upsilon_k^{\text{filled}} = 1.17$ which corresponds to the experimental findings in section 6.2.2.

Bibliography

[1] Janaky, C., and Visy, C. Conducting polymer-based hybrid assemblies for electrochemical sensing: a materials science perspective. *Analytical and Bioanalytical Chemistry 405*, 11 (2013), 3489–3511.

[2] Shalwan, A., and Yousif, B. In state of art: Mechanical and tribological behaviour of polymeric composites based on natural fibres. *Materials & Design 48*, 0 (2013), 14 – 24. Materials, Design and Tribology.

[3] Suckeveriene, R. Y., Zelikman, E., Mechrez, G., and Narkis, M. Literature review: conducting carbon nanotube/polyaniline nanocomposites. *Reviews In Chemical Engineering 27*, 1-2 (Sept. 2011), 15–21.

[4] Plank, H., Guentner, R., Scherf, U., and List, E. J. W. Structural and electronic properties of the first monolayers of spin-cast poly(fluorene)-based conjugated-polymer films. *Advanced Functional Materials 17*, 7 (May 2007), 1093–1105.

[5] Lin, E. K., Kolb, R., Satija, S. K., and Wu, W. L. Reduced polymer mobility near the polymer solid interface as measured by neutron reflectivity. *Macromolecules 32*, 11 (June 1999), 3753–3757.

[6] Meth, J. S., and Lustig, S. R. Polymer interphase structure near nanoscale inclusions: Comparison between random walk theory and experiment. *Polymer 51*, 18 (Aug. 2010), 4259–4266.

[7] Krutyeva, M., Martin, J., Arbe, A., Colmenero, J., Mijangos, C., Schneider, G. J., Unruh, T., Su, Y., and Richter, D. Neutron scattering study of the dynamics of a polymer melt under nanoscopic confinement. *The Journal of chemical physics 131*, 17 (Nov. 2009), 174901–174901.

[8] Mattia, D., and Gogotsi, Y. Review: static and dynamic behavior of liquids inside carbon nanotubes. *Microfluidics and Nanofluidics 5*, 3 (Sept. 2008), 289–305.

[9] Rahmat, M., and Hubert, P. Carbon nanotube-polymer interactions in nanocomposites: A review. *Composites Science and Technology 72*, 1 (Dec. 2011), 72–84.

[10] Iijima, S. Helical microtubules of graphitic carbon. *Nature 354*, 6348 (Nov. 1991), 56–58.

[11] Mohammed, H. A.-S., and Uttandaraman, S. Review of the mechanical properties of carbon nanofiber/polymer composites. *Composites Part A: Applied Science and Manufacturing 42*, 12 (2011), 2126 – 2142.

[12] Thostenson, E. T., Ren, Z. F., and Chou, T. W. Advances in the science and technology of carbon nanotubes and their composites: a review. *Composites Science and Technology 61*, 13 (2001), 1899–1912.

[13] Schneider, J. J., and Engstler, J. Carbon and polymer filaments in nanoporous alumina. *European Journal of Inorganic Chemistry -*, 9 (May 2006), 1723–1736.

[14] Huczko, A. Synthesis of aligned carbon nanotubes. *Applied Physics A-materials Science & Processing 74*, 5 (May 2002), 617–638.

[15] Reilly, R. M. Carbon nanotubes: Potential benefits and risks of nanotechnology in nuclear medicine. *Journal of Nuclear Medicine 48*, 7 (July 2007), 1039–1042.

[16] Odom, T. W., Huang, J. L., Kim, P., and Lieber, C. M. Atomic structure and electronic properties of single-walled carbon nanotubes. *Nature 391*, 6662 (Jan. 1998), 62–64.

[17] Wong, E. W., Sheehan, P. E., and Lieber, C. M. Nanobeam mechanics: Elasticity, strength, and toughness of nanorods and nanotubes. *Science 277*, 5334 (Sept. 1997), 1971–1975.

[18] Kim, P., Shi, L., Majumdar, A., and McEuen, P. L. Thermal transport measurements of individual multiwalled nanotubes. *Physical Review Letters 87*, 21 (Nov. 2001), 215502.

[19] Treacy, M. M. J., Ebbesen, T. W., and Gibson, J. M. Exceptionally high young's modulus observed for individual carbon nanotubes. *Nature 381*, 6584 (June 1996), 678–680.

[20] Ajayan, P. M. Nanotubes from carbon. *Chemical Reviews 99*, 7 (1999), 1787–1800.

[21] Barrera, E., Corral, E., Shofner, M., and Simien, D. Fundamentals of carbon-based nanocomposites. In *Polymer Nanocomposites Handbook*. CRC Press, July 2009, pp. –.

[22] Bose, S., Khare, R. A., and Moldenaers, P. Assessing the strengths and weaknesses of various types of pre-treatments of carbon nanotubes on the properties of polymer/carbon nanotubes composites: A critical review. *Polymer 51*, 5 (2010), 975 – 993.

[23] Alig, I., Poetschke, P., Lellinger, D., Skipa, T., Pegel, S., Kasaliwal, G. R., and Villmow, T. Establishment, morphology and properties of carbon nanotube networks in polymer melts. *Polymer 53*, 1 (Jan. 2012), 4–28.

[24] Byrne, M. T., and Gun'ko, Y. K. Recent advances in research on carbon nanotube-polymer composites. *Advanced Materials 22*, 15 (Apr. 2010), 1672–1688.

[25] Haggenmueller, R., Gommans, H. H., Rinzler, A. G., Fischer, J. E., and Winey, K. I. Aligned single-wall carbon nanotubes in composites by melt processing methods. *Chemical Physics Letters 330*, 3-4 (Nov. 2000), 219–225.

[26] Oliva-Aviles, A. I., Aviles, F., and Sosa, V. Electrical and piezoresistive properties of multi-walled carbon nanotube/polymer composite films aligned by an electric field. *Carbon 49*, 9 (Aug. 2011), 2989–2997.

[27] Duong, H. M., Yamamoto, N., Bui, K., Papavassiliou, D. V., Maruyama, S., and Wardle, B. L. Morphology effects on nonisotropic thermal conduction of aligned single-walled and multi-walled carbon nanotubes in polymer nanocomposites. *Journal of Physical Chemistry C 114*, 19 (May 2010), 8851–8860.

[28] Choi, E. S., Brooks, J. S., Eaton, D. L., Al-Haik, M. S., Hussaini, M. Y., Garmestani, H., Li, D., and Dahmen, K. Enhancement of thermal and electrical properties of carbon nanotube polymer composites by magnetic field processing. *Journal of Applied Physics 94*, 9 (Nov. 2003), 6034–6039.

[29] Yang, Z., Dong, B., Huang, Y., Liu, L., Yan, F. Y., and Li, H. L. A study on carbon nanotubes reinforced poly(methyl methacrylate) nanocomposites. *Materials Letters 59*, 17 (July 2005), 2128–2132.

[30] Meier, J. G., Crespo, C., Pelegay, J. L., Castell, P., Sainz, R., Maser, W. K., and Benito, A. M. Processing dependency of percolation threshold of mwcnts in a thermoplastic elastomeric block copolymer. *Polymer 52*, 8 (Apr. 2011), 1788–1796.

[31] Mahanandia, P., Schneider, J. J., Khaneft, M., Stühn, B., Peixoto, T. P., and Drossel, B. Polymer confinement effects in aligned carbon nanotubes arrays. *Physical Chemistry Chemical Physics 12*, 17 (2010), 4407–4417.

[32] Boncel, S., Koziol, K. K. K., Walczak, K. Z., Windle, A. H., and Shaffer, M. S. P. Infiltration of highly aligned carbon nanotube arrays with molten polystyrene. *Materials Letters 65*, 14 (July 2011), 2299–2303.

[33] Dollase, T., Wilhelm, M., Spiess, H. W., Yagen, Y., Yerushalmi-Rozen, R., and Gottlieb, M. Effect of interfaces on the crystallization behavior of pdms. *Interface Science 11*, 2 (Apr. 2003), 199–209.

[34] Aranguren, M. I. Crystallization of polydimethylsiloxane: effect of silica filler and curing. *Polymer 39*, 20 (Sept. 1998), 4897–4903.

[35] Klonos, P., Pandis, C., Kripotou, S., Kyritsis, A., and Pissis, P. Interfacial effects in polymer nanocomposites studied by dielectric and thermal techniques. *Ieee Transactions On Dielectrics and Electrical Insulation 19*, 4 (Aug. 2012), 1283–1290.

[36] Shi, X., Wang, J., Jiang, B., and Yang, Y. Influence of nanofiller dimensionality on the crystallization behavior of hdpe/carbon nanocomposites. *Journal of Applied Polymer Science 128*, 6 (2013), 3609–18.

[37] Keddie, J. L., Jones, R. A. L., and Cory, R. A. Interface and surface effects on the glass-transition temperature in thin polymer-films. *Faraday Discussions 98* (1994), 219–230.

[38] Forrest, J. A. Veress, K., Stevens, J. R., and Dutcher, J. R. Effect of free surfaces on the glass transition temperature of thin polymer films (vol 77, pg 2002, 1996). *Physical Review Letters 77*, 19 (Nov. 1996), 4108–4108.

[39] Bansal, A., Yang, H. C., Li, C. Z., Cho, K. W., Benicewicz, B. C., Kumar, S. K., and Schadler, L. S. Quantitative equivalence between polymer nanocomposites and thin polymer films. *Nature Materials 4*, 9 (Sept. 2005), 693–698.

[40] Freed, K. F., Dudowicz, J., Stukalin, E. B., and Douglas, J. F. General approach to polymer chains confined by interacting boundaries. *Journal of Chemical Physics 133*, 9 (Sept. 2010), 094901.

[41] Martin, J., Krutyeva, M., Monkenbusch, M., Arbe, A., Allgaier, J., Radulescu, A., Falus, P., Maiz, J., Mijangos, C., Colmenero, J., and Richter, D. Direct observation of confined single chain dynamics by neutron scattering. *Physical Review Letters 104*, 19 (May 2010), 197801.

[42] Pitsa, D., and Danikas, M. G. Interfaces features in polymer nanocomposites: A review of proposed models. *Nano 6*, 6 (Dec. 2011), 497–508.

[43] Butt, H.-J., Graf, K., and Kappl, M. *Physics and Chemistry of Interfaces*. Willey-VCH GmbH & Co. KGaA, Weinheim, 2006.

[44] Israelachvili, J. N. *Intermolecular and Surface Forces*. Elsevier Inc., 2011.

[45] Müller, M., MacDowell, L. G., and Yethiraj, A. Short chains at surfaces and interfaces: A quantitative comparison between density-functional theories and monte carlo simulations. *The Journal of Chemical Physics 118*, 6 (2003), 2929–2940.

[46] Arnold, A., Bozorgui, B., Frenkel, D., Ha, B.-Y., and Jun, S. Unexpected relaxation dynamics of a self-avoiding polymer in cylindrical confinement. *Journal of Chemical Physics 127*, 16 (Oct. 2007), 164903.

[47] Jancar, J. Review of the role of the interphase in the control of composite performance on micro- and nano-length scales. *Journal of Materials Science 43*, 20 (Oct. 2008).

[48] Krutyeva, M., Wischnewski, A., Monkenbusch, M., Willner, L., Maiz, J., Mijangos, C., Arbe, A., Colmenero, J., Radulescu, A., Holderer, O., Ohl, M., and Richter, D. Effect of nanoconfinement on polymer dynamics: Surface layers and interphases (vol 110, 108303, 2013). *Physical Review Letters 110*, 11 (Mar. 2013), 119901.

[49] Guinier, A. *X-ray difraction in crystals, imperfect crystals, and amorphous bodies*. Dover Publications, INC, New York, 1994.

[50] Roe, R.-J. *Methods of X-Ray and Neutron Scattering in Polymer Science*. Oxford university press, 2000.

[51] Sivia, D. *Elemental Scatteing Theory for X-ray and Neutron Users*. Oxford university press, 2011.

[52] Engel, M., Stühn, B., Schneider, J. J., Cornelius, T., and Naumann, M. Small-angle x-ray scattering (saxs) off parallel, cylindrical, well-defined nanopores: from random pore distribution to highly ordered samples. *Applied Physics A-materials Science & Processing 97*, 1 (Oct. 2009), 99–108.

[53] Mittelbach, P., and Porod, G. Zur röntgenkleinwinkelstreuung verdünnter kolloider systeme - die berechnung der streukurven von parallelepipeden. *Acta Physica Austriaca 14* (1961), 185.

[54] Ruland, W., and Smarsly, B. Saxs of self-assembled nanocomposite films with oriented two-dimensional cylinder arrays: an advanced method of evaluation. *Journal of Applied Crystallography 38* (Feb. 2005), 78–86.

[55] Grillo, I. *Small-Angle Neutron Scattering and Applications in Soft Condensed Matter*. 2008, p. 723.

[56] Rinzler, A. G., Hafner, J. H., Nikolaev, P., Lou, L., Kim, S. G., Tomanek, D., Nordlander, P., Colbert, D. T., and Smalley, R. E. Unraveling nanotubes - field-emission from an atomic wire. *SCIENCE 269*, 5230 (Sep 1995), 1550–1553.

[57] Wong, S. S., Harper, J. D., Lansbury, P. T., and Lieber, C. M. Carbon nanotube tips: High-resolution probes for imaging biological systems. *Journal of the American Chemical Society 120*, 3 (Jan 1998), 603–604.

[58] Niu, C. M., Sichel, E. K., Hoch, R., Moy, D., and Tennent, H. High power electrochemical capacitors based on carbon nanotube electrodes. *Applied Physics Letters 70*, 11 (Mar 1997), 1480–1482.

[59] Huang, S., Li, L., Yang, Z., Zhang, L., Saiyin, H., Chen, T., and Peng, H. A new and general fabrication of an aligned carbon nanotube/polymer film for electrode applications. *Advanced Materials 23*, 40 (Oct 2011), 4707.

[60] Sandler, J., Shaffer, M. S. P., Prasse, T., Bauhofer, W., Schulte, K., and Windle, A. H. Development of a dispersion process for carbon nanotubes in an epoxy matrix and the resulting electrical properties. *Polymer 40*, 21 (Oct. 1999), 5967–5971.

[61] Cho, J., Boccaccini, A. R., and Shaffer, M. S. P. Ceramic matrix composites containing carbon nanotubes. *Journal of Materials Science 44*, 8 (Apr. 2009), 1934–1951.

[62] Barrau, S., Demont, P., Peigney, A., Laurent, C., and Lacabanne, C. Dc and ac conductivity of carbon nanotubes-polyepoxy composites. *Macromolecules 36*, 14 (July 2003), 5187–5194.

[63] Ren, Z. F., Huang, Z. P., Xu, J. W., Wang, J. H., Bush, P., Siegal, M. P., and Provencio, P. N. Synthesis of large arrays of well-aligned carbon nanotubes on glass. *Science 282*, 5391 (Nov 1998), 1105–1107.

[64] Huczko, A. Template-based synthesis of nanomaterials. *Applied Physics A-materials Science & Processing 70*, 4 (Apr 2000), 365–376.

[65] Andrews, R., Jacques, D., Rao, A., Derbyshire, F., Qian, D., Fan, X., Dickey, E., and Chen, J. Continuous production of aligned carbon nanotubes: a step closer to commercial realization. *Chemical Physics Letters*

303 (1999), 467 – 474.

[66] Keller, T. M., and Qadri, S. B. Ferrocenylethynylbenzenes as precursors to in situ synthesis of carbon nanotube and fe nanoparticle compositions. *Chemistry of Materials 16*, 6 (2004), 1091–1097.

[67] Schneider, J. J., Maksimova, N. I., Engstler, J., Joshi, R., Schierholz, R., and Feile, R. Catalyst free growth of a carbon nanotube-alumina composite structure. *Inorganica Chimica Acta 361*, 6 (May 2008), 1770–1778.

[68] Schneider, J. J., Engstler, N., Budna, K. P., Teichert, C., and Franzka, S. Freestanding, highly flexible, large area, nanoporous alumina membranes with complete through-hole pore morphology. *European Journal of Inorganic Chemistry*, 12 (June 2005), 2352–2359.

[69] Martin, C. R. Membrane-based synthesis of nanomaterials. *Chemistry of Materials 8*, 8 (1996), 1739–1746.

[70] Steinhart, M. Supramolecular organization of polymeric materials in nanoporous hard templates. *Self-assembled Nanomaterials II: Nanotubes 220* (2008), 123–187.

[71] Parthasarathy, R. V., Phani, K. L. N., and Martin, C. L. R. Template synthesis of graphitic nanotubules. *Advanced Materials 7*, 11 (Nov. 1995), 896–&.

[72] Schneider, J. J., Engstler, J., Franzka, S., Hofmann, K., Albert, B., Ensling, J., Gutlich, P., Hildebrandt, P., Dopner, S., Pfleging, W., Gunther, B., and Müller, G. Carbon nanotube bags: Catalytic formation, physical properties, two-dimensional alignment and geometric structuring of densely filled carbon tubes. *Chemistry-a European Journal 7*, 13 (2001), 2888–2895.

[73] Kyotani, T., Tsai, L. F., and Tomita, A. Preparation of ultrafine carbon tubes in nanochannels of an anodic aluminum oxide film. *Chemistry of Materials 8*, 8 (Aug. 1996), 2109–2113.

[74] Bose, S., and Bragg, R. H. Small-angle x-ray-scattering from oriented ellipsoidal voids in pyrolytic-graphite. *Journal of Applied Physics 49*, 5 (1978), 2916–2918.

[75] Qian, D., Dickey, E. C., Andrews, R., and Rantell, T. Load transfer and deformation mechanisms in carbon nanotube-polystyrene composites. *Applied Physics Letters 76*, 20 (May 2000), 2868–2870.

[76] Tibbetts, G. G., and McHugh, J. J. Mechanical properties of vapor-grown carbon fiber composites with thermoplastic matrices. *Journal of Materials Research 14*, 7 (July 1999), 2871–2880.

[77] Garcia, E. J., Hart, A. J., Wardle, B. L., and Slocum, A. H. Fabrication of composite microstructures by capillarity-driven wetting of aligned carbon nanotubes with polymers. *Nanotechnology 18*, 16 (Apr. 2007), 165602.

[78] Potschke, P., Brunig, H., Janke, A., Fischer, D., and Jehnichen, D. Orientation of multiwalled carbon nanotubes in composites with polycarbonate by melt spinning. *Polymer 46*, 23 (Nov. 2005), 10355–10363.

[79] Patro, D., Bhattacharyya, S., and Jayaram, V. Flow kinetics in porous ceramics: Understanding with non-uniform capillary models. *Journal of the American Ceramic Society 90*, 10 (Oct. 2007), 3040–3046.

[80] Brandrup, J., Immergut, E., and Grulke, E., Eds. *Polymer handbook*. A Willey-interscience publication, 1999.

[81] Chopra, N. G., Benedict, L. X., Crespi, V. H., Cohen, M. L., Louie, S. G., and Zettl, A. Fully collapsed carbon nanotubes. *Nature 377*, 6545 (Sept. 1995), 135–138.

[82] Muthukumar, M. Polymers under confinement. *Advances In Chemical Physics, Vol 149 149* (2012), 129–196.

[83] Dhont, J. K., Gompper, G., and Richter, D. *Lecture manuscripts of the 33th IFF winter school*. Forschungszentrum Jülich GmbH Institut für Ferstkörperforschung, 2002.

[84] Dhont, J. K., Gompper, G., Nägele, G., Richter, D., and Winkler, R. G. *Lecture notes of the 39th Spring School: Soft Matter from synthetic to biological materials*. Forschungszentrum Jülich GmbH Institut für Ferstkörperforschung, 2008.

[85] Higgins, J. S., and Benoit, H. C. *Polymers and Neutron Scattering*. Oxford university press, 2002.

[86] de Gennes, P. G. Conformations of polymers attached to an interface. *Macromolecules 13*, 5 (1980), 1069–1075.

[87] Lovell, R., Mitchell, G. R., and Windle, A. H. Wide-angle x-ray-scattering study of structural parameters in non-crystalline polymers. *Faraday Discussions 68* (1979), 46–57.

[88] Starov, V. M., Velarde, M. G., and Radke, C. J. *Wetting and Spreading Dynamics*. CRC Press, 2007.

[89] Whitby, M., and Quirke, N. *Handbook of Nanophysics: Nanotubes and Nanowires*. CRC Press, 2010, ch. Fluid Flow in Carbon Nanotubes, pp. 11–1:11–22.

[90] Lucas, R. über das zeitgesetz des kapillaren aufstiegs von flüssigkeiten. *Kolloid-Z 23* (1918), 15.

[91] Washburn, E. W. Note on a method of determining the distribution of pore sizes in a porous material. *Proceedings of the National Academy of Sciences of the United States of America 7*, 4 (Apr. 1921), 115–6.

[92] Engel, M., and Stühn, B. In situ small angle x-ray scattering measurements of the filling process of poly-isobutylene and poly-epsilon-caprolactone in ion track etched polycarbonate nanopores. *Journal of Chemical Physics 132*, 22 (June 2010), 224502.

[93] Lavi, B., and Marmur, A. The exponential power law: partial wetting kinetics and dynamic contact angles. *Colloids and Surfaces A-physicochemical and Engineering Aspects 250*, 1-3 (Dec. 2004), 409–414.

[94] Kraus, J., Müller-Buschbaum, P., Kuhlmann, T., Schubert, D. W., and Stamm, M. Confinement effects on the chain conformation in thin polymer films. *Europhysics Letters 49*, 2 (Jan. 2000), 210–216.

[95] Lum, K., Chandler, D., and Weeks, J. D. Hydrophobicity at small and large length scales. *Journal of Physical Chemistry B 103*, 22 (June 1999), 4570–4577.

[96] Peixoto, T. P., and Drossel, B. Density profile and polymer configurations for a polymer melt in a regular array of nanotubes. *New Journal of Physics 13* (July 2011), 073030.

[97] Müller, M. 1.15 - polymers at interfaces and surfaces and in confined geometries. In *Polymer Science: A Comprehensive Reference*. Elsevier, Amsterdam, 2012, pp. 387 – 416.

[98] Gobrecht, H., Hamann, K., and Willers, G. Complex plane analysis of heat capacity of polymers in glass transition region. *Journal of Physics E-scientific Instruments 4*, 1 (1971), 21–&.

[99] Gill, P. S., Sauerbrunn, S. R., and Reading, M. Modulated differential scanning calorimetry. *Journal of Thermal Analysis 40*, 3 (1993), 931–939.

[100] Reading, M., Elliott, D., and Hill, V. L. A new approach to the calorimetric investigation of physical and chemical-transitions. *Journal of Thermal Analysis 40*, 3 (1993), 949–955.

[101] Reading, M., Luget, A., and Wilson, R. Modulated differential scanning calorimetry. *Thermochimica Acta 238* (June 1994), 295–307.

[102] Schawe, J. E. K. A comparison of different evaluation methods in modulated temperature dsc. *Thermochimica Acta 260* (Aug. 1995), 1–16.

[103] Schawe, J. E. K. Principles for the interpretation of modulated temperature dsc measurements .1. glass-transition. *Thermochimica Acta 261* (Sept. 1995), 183–194.

[104] Garden, J. L. Macroscopic non-equilibrium thermodynamics in dynamic calorimetry. *Thermochimica Acta 452*, 2 (Jan. 2007), 85–105.

[105] Jackson, C. L., and McKenna, G. B. The glass-transition of organic liquids confined to small pores. *Journal of Non-crystalline Solids 131* (June 1991).

[106] Liu, G., Li, Y., and Jonas, J. Confined geometry-effects on reorientational dynamics of molecular liquids in porous silica glasses. *Journal of Chemical Physics 95*, 9 (Nov. 1991), 6892–6901.

[107] Hall, D. B., and Torkelson, J. M. Small molecule probe diffusion in thin and ultrathin supported polymer films. *Macromolecules 31*, 25 (Dec. 1998), 8817–8825.

[108] Forrest, J. A., and Mattsson, J. Reductions of the glass transition temperature in thin polymer films: Probing the length scale of cooperative dynamics. *Physical Review E 61*, 1 (Jan. 2000), R53–R56.

[109] Priestley, R. D., Ellison, C. J., Broadbelt, L. J., and Torkelson, J. M. Structural relaxation of polymer glasses at surfaces, interfaces and in between. *Science 309*, 5733 (July 2005), 456–459.

[110] Park, J. Y., and McKenna, G. B. Size and confinement effects on the glass transition behavior of polystyrene/o-terphenyl polymer solutions. *Physical Review B 61*, 10 (Mar. 2000), 6667–6676.

[111] Jackson, C. L., and McKenna, G. B. Vitrification and crystallization of organic liquids confined to nanoscale pores. *Chemistry of Materials 8*, 8 (Aug. 1996), 2128–2137.

[112] Fryer, D. S., Peters, R. D., Kim, E. J., Tomaszewski, J. E., de Pablo, J. J., Nealey, P. F., White, C. C., and Wu, W. L. Dependence of the glass transition temperature of polymer films on interfacial energy and thickness. *Macromolecules 34*, 16 (July 2001), 5627–5634.

[113] Kawana, S., and Jones, R. A. L. Character of the glass transition in thin supported polymer films. *Physical Review E 63*, 2 (Feb. 2001), 021501.

[114] Clough, A., Peng, D., Yang, Z., and Tsui, O. K. C. Glass transition temperature of polymer films that slip.

Macromolecules 44, 6 (Mar. 2011), 1649–1653.

[115] Boucher, V. M., Cangialosi, D., Yin, H., Schoenhals, A., Alegria, A., and Colmenero, J. T-g depression and invariant segmental dynamics in polystyrene thin films. *Soft Matter 8*, 19 (2012), 5119–5122.

[116] Efremov, M. Y., Kiyanova, A. V., Last, J., Soofi, S. S., Thode, C., and Nealey, P. F. Glass transition in thin supported polystyrene films probed by temperature-modulated ellipsometry in vacuum. *Physical Review E 86*, 2 (Aug. 2012), 021501.

[117] Keddie, J. L., Meredith, P., Jones, R. A. L., and Donald, A. M. Film formation of acrylic latices with varying concentrations of non-film-forming latex particles. *Langmuir 12*, 16 (Aug. 1996), 3793–3801.

[118] Forrest, J. A., DalnokiVeress, K., and Dutcher, J. R. Interface and chain confinement effects on the glass transition temperature of thin polymer films. *Physical Review E 56*, 5 (Nov. 1997), 5705–5716.

[119] Koh, Y. P., McKenna, G. B., and Simon, S. L. Calorimetric glass transition temperature and absolute heat capacity of polystyrene ultrathin films. *Journal of Polymer Science Part B-polymer Physics 44*, 24 (Dec. 2006), 3518–3527.

[120] Langhe, D. S., Murphy, T. M., Shaver, A., LaPorte, C., Freeman, B. D., Paul, D. R., and Baer, E. Structural relaxation of polystyrene in nanolayer confinement. *Polymer 53*, 9 (Apr. 2012), 1925–1931.

[121] Grady, B. P., Paul, A., Peters, J. E., and Ford, W. T. Glass transition behavior of single-walled carbon nanotube-polystyrene composites. *Macromolecules 42*, 16 (Aug. 2009), 6152–6158.

[122] Paul, A., Ford, W. T., and Grady, B. P. Polystyrene grafted single-walled carbon nanotube composite. *Abstracts of Papers of the American Chemical Society 242* (Aug. 2011), Amer Chem Soc (ACS).

[123] McCoy, J. D., and Curro, J. G. Conjectures on the glass transition of polymers in confined geometries. *Journal of Chemical Physics 116*, 21 (June 2002), 9154–9157.

[124] Reiter, G. Dewetting as a probe of polymer mobility in thin-films. *Macromolecules 27*, 11 (May 1994), 3046–3052.

[125] Putz, K. W., Mitchell, C. A., Krishnamoorti, R., and Green, P. F. Elastic modulus of single-walled carbon nanotube/poly(methyl methacrylate) nanocomposites. *Journal of Polymer Science Part B-polymer Physics 42*, 12 (June 2004), 2286–2293.

[126] Yang, Y. K., Xie, X. L., Wu, J. G., and Mai, Y. W. Synthesis and self-assembly of polystyrene-grafted multi-walled carbon nanotubes with a hairy-rod nanostructure. *Journal of Polymer Science Part A-polymer Chemistry 44*, 12 (June 2006), 3869–3881.

[127] Miaudet, P., Derre, A., Maugey, M., Zakri, C., Piccione, P. M., Inoubli, R., and Poulin, P. Shape and temperature memory of nanocomposites with broadened glass transition. *Science 318*, 5854 (Nov. 2007), 1294–1296.

[128] Sperling, L. *Introduction to the physical polymer science*. John Wiley & Sons, Inc., 1992.

[129] Strobl, G. From the melt via mesomorphic and granular crystalline layers to lamellar crystallites: A major route followed in polymer crystallization? *European Physical Journal E 3*, 2 (Oct. 2000), 165–183.

[130] Ozawa, T. Kinetics of non-isothermal crystallization. *Polymer 12*, 3 (1971), 150–&.

[131] Evans, U. R. The laws of expanding circles and spheres in relation to the lateral growth of surface films and the grain-size of metals. *Transactions of the Faraday Society 41*, 7 (1945), 365–374.

[132] Liu, T. X., Mo, Z. S., Wang, S. G., and Zhang, H. F. Nonisothermal melt and cold crystallization kinetics of poly(aryl ether ether ketone ketone). *Polymer Engineering and Science 37*, 3 (Mar. 1997), 568–575.

[133] Lund, R., Alegria, A., Goitandia, L., Colmenero, J., Gonzalez, M. A., and Lindner, P. Dynamical and structural aspects of the cold crystallization of poly(dimethylsiloxane) (pdms). *Macromolecules 41*, 4 (Feb. 2008), 1364–1376.

[134] Alfonso, G., and Ziabicki, A. Memory effects in isothermal crystallization ii. isotactic polypropylene. *Colloid and Polymer Science 273*, 4 (1995), 317–323.

[135] Xiao, J., Zhang, H. L., Wan, X. H., Zhang, D., Zhou, Q. F., Woo, E. M., and Turner, S. R. Crystallization kinetics of new copoly(ethylene terephthalate-imide)s. *Polymer 43*, 13 (June 2002), PII S0032–3861(02)00192–1.

[136] Berne, B. J., and Pecola, R. *Dynamic Light Scattering*. Dover Publications, INC, New York, 2000.

[137] Blachowicz, T. *Brillouin Spectroscopy in Crystal Lattices*. Wydawnictwo Politechniki Slaskiej, Gliwice, 2003.

[138] Landau, L., and Lifshitz, E. *Theory of elasticity*. Elsevier, 1986.

[139] *Tandem Fabry-perot-interferometer TFP-1. Operator manual*.

[140] Lindsay, S. M., Anderson, M. W., and Sandercok, J. R. Construction and alignment of a high-performance multipass vernier tandem fabry-perot-interferometer. *Review of Scientific Instruments 52*, 10 (1981), 1478–1486.

[141] Dil, J. G., Vanhijningen, N. C. J. A., Vandorst, F., and Aarts, R. M. Tandem multipass fabry-perot-interferometer for brillouin-scattering. *Applied Optics 20*, 8 (1981), 1374–1381.

[142] Choy, T. C. *Effective Medium Theory*. Oxford: Clarendon press, 1999.

[143] White, R. M. Surface elastic waves. *Proceedings of the Institute of Electrical and Electronics Engineers 58*, 8 (1970), 1238.

[144] Auld, B. *Acoustic Fields and waves in solids*. Krieger publishing company, Malabar, Florida, 1973.

[145] Hess, P. Surface acoustic waves in materials science. *Physics Today 55*, 3 (Mar. 2002), 42–47.

[146] Sandercock, J. R. *Topics in Applied Physics: Light Scattering in Solids III*. Springer Berlin / Heidelberg, 1982, ch. Trends in Brillouin Scattering: Studies of Opaque Materials, Supported Films, and Central Modes, pp. 173–206.

[147] Loudon, R. Theory of surface-ripple brillouin-scattering by solids. *Physical Review Letters 40*, 9 (1978), 581–583.

[148] Mishra, S., and Bray, R. Surface-ripple mechanism for brillouin-scattering of reflected light from bulk acoustic-waves. *Physical Review Letters 39*, 4 (1977), 222–225.

[149] Sandercock, J. R. Light-scattering from surface acoustic phonons. *Bulletin of the American Physical Society 23*, 3 (1978), 387–388.

[150] Sato, A., Knoll, W., Pennec, Y., Djafari-Rouhani, B., Fytas, G., and Steinhart, M. Anisotropic propagation and confinement of high frequency phonons in nanocomposites. *Journal of Chemical Physics 130*, 11 (Mar. 2009), 111102.

[151] Chtanko, N., Toimil Molares, M. E., Cornelius, T., Dobrev, A., and Neumann, R. Etched single-ion-track templates for single nanowire synthesis. *Journal of Physical Chemistry B 108*, 28 (July 2004), 9950–9954.

[152] Tommaseo, G., Lescanne, M., Steffen, W., Fytas, G., and Stamm, M. Elastic excitations in polycarbonate membranes. *Journal of Polymer Science Part B-polymer Physics 42*, 18 (Sept. 2004), 3311–3317.

[153] Yu, Z., and Boseck, S. Propagation of surface waves in deformed, anisotropic thin layered solids. *Nondestructive Testing and Evaluation 18*, 2 (2002), 51–73.

[154] Sato, A., Pennec, Y., Shingne, N., Thurn-Albrecht, T., Knoll, W., Steinhart, M., Djafari-Rouhani, B., and Fytas, G. Tuning and switching the hypersonic phononic properties of elastic impedance contrast nanocomposites. *Acs Nano 4*, 6 (June 2010), 3471–3481.

[155] Marchal, D., and Deme, B. Small-angle neutron scattering by porous alumina membranes made of aligned cylindrical channels. *Journal of Applied Crystallography 36* (June 2003), 713–717.

[156] Khaneft, M., Stühn, B., Engstler, J., Tempel, H., Schneider, J. J., Pirzer, T., and Hugel, T. Imbibition of polystyrene melts in aligned carbon nanotube arrays. *Journal of Applied Physics 113*, 7 (2013), 074305.

Curriculum vitae

Personal Data

Name:	Marina Khaneft (born Gontsova)
Date of Birth:	15 May 1985
Place of Birth:	Kurgan (Russian Federation)
Nationality:	Russian

Education

2009 – 2013	PhD at Darmstadt University of Technology / Darmstadt
2005 – 2008	Diploma (Engineer-physicer) at National Research Nuclear University (former Moscow Engineering Physics Institute) / Moscow, Russia
2002 – 2005	Physics study at Samara State University / Samara, Russia
1992 – 2002	General Education School / Roschinsky, Russia

Research Experience

2009 – 2013	Researcher at Darmstadt University of Technology, Darmstadt
2008 – 2009	Probationer-researcher at Shemyakin-Ovchinnikov Institute of Bioorganic Chemistry (Russian Academy of Sciences)
2007 – 2008	Laboratory assistant at Shemyakin-Ovchinnikov Institute of Bioorganic Chemistry (Russian Academy of Sciences)
2007 – 2008	Industrial researcher, Center of new technologies / Moscow, Russia

Publications

1. Khaneft, M.; Stühn, B., Engstler, J., Tempel, H., Schneider, J. J., Pirzer, T. and Hugel, T. *Imbibition of polystyrene melts in aligned carbon nanotube arrays* Journal of Applied Physics, AIP, 2013, 113, 074305

2. Mahanandia, P., Schneider, J. J., Khaneft, M., Stühn, B., Peixoto, T. P. and Drossel, B. *Polymer confinement effects in aligned carbon nanotubes arrays* Physical Chemistry Chemical Physics, 2010, 12, 4407-4417

Acknowledgements

I would like to thank all people who help me and support me last years, without them my study would not be possible.

First of all, I would like to express my sincere gratitude to my PhD advisor Prof. Dr. Bernd Stühn for continuous support of my PhD study and research, for his patience, motivation and knowledge, for everything what I have learned during my study.

I also would like to thank my colleagues for fruitful discussion of my research work and friendly working atmosphere, especially Tinka Spehr for teaching and helping me with neutron scattering experiments. She also helped me to adapt in Germany in the beginning of my study. I am thankful to Martin Kraska for his advises which helped me to improve my PhD thesis.

I also would like to thank our secretary Heike Neumann for her kindness and attention to my working and personal problems.

I would like to acknowledge Prof. Dr. Jörg J.Schneider and his working group especially Hermann Tempel, Thorsten Heilein and Jörg Engstler for close collaboration and providing samples for our research projects.

I would like to thank my parents, my sister and my grandparents for their sympathy and believing in me. They were always supporting, encouraging me with best wishes.

Finally, I would like to thank Markus Appel for his open heart and unconditional support in every possible way. His patience, ideas and advices enabled me to complete work and his inspiration was my driving force.